International

Agreement Report

Data Base on the Behavior of High Burnup Fuel Rods with Zr-1%Nb Cladding and UO$_2$ Fuel (VVER Type) under Reactivity Accident Conditions

Description of Test Procedures and Analytical Methods

Prepared by
L. Yegorova, V. Asmolov, G. Abyshov, V. Malofeev, A. Avvakumov, E. Kaplar, K. Lioutov, A. Shestopalov
Nuclear Safety Institute of Russian Research Centre "Kurchatov Institute"
Kurchatov Square 1, Moscow 123182, Russia

A. Bortash, L. Maiorov, K. Mikitiouk, V. Polvanov
Institute of Nuclear Reactors of Russian Research Centre "Kurchatov Institute"
Kurchatov Square 1, Moscow 123182, Russia

V. Smirnov, A. Goryachev, V. Prokhorov
State Research Centre "Research Institute of Atomic Reactors"
Dimitrovgrad 433510, Russia

V. Pakhnitz, A. Vurim
Institute of Atomic Energy of National Nuclear Centre of Kazakhstan Republic
Semipalatinsk 490021, Kazakhstan

Office of Nuclear Regulatory Research
U.S. Nuclear Regulatory Commission
Washington, DC 20555-0001

July 1999

AVAILABILITY NOTICE

Availability of Reference Materials Cited in NRC Publications

NRC publications in the NUREG series, NRC regulations, and *Title 10, Energy,* of the *Code of Federal Regulations,* may be purchased from one of the following sources:

1. The Superintendent of Documents
   U.S. Government Printing Office
   P.O. Box 37082
   Washington, DC 20402–9328
   <http://www.access.gpo.gov/su_docs>
   202–512–1800

2. The National Technical Information Service
   Springfield, VA 22161–0002
   <http://www.ntis.gov/ordernow>
   703–487–4650

The NUREG series comprises (1) brochures (NUREG/BR-XXXX), (2) proceedings of conferences (NUREG/CP-XXXX), (3) reports resulting from international agreements (NUREG/IA-XXXX), (4) technical and administrative reports and books [(NUREG-XXXX) or (NUREG/CR-XXXX)], and (5) compilations of legal decisions and orders of the Commission and Atomic and Safety Licensing Boards and of Office Directors' decisions under Section 2.206 of NRC's regulations (NUREG-XXXX).

A single copy of each NRC draft report is available free, to the extent of supply, upon written request as follows:

Address: Office of the Chief Information Officer
Reproduction and Distribution
  Services Section
U.S. Nuclear Regulatory Commission
Washington, DC 20555–0001
E–mail: <DISTRIBUTION@nrc.gov>
Facsimile: 301–415–2289

A portion of NRC regulatory and technical information is available at NRC's World Wide Web site:

   <http://www.nrc.gov>

All NRC documents released to the public are available for inspection or copying for a fee, in paper, microfiche, or, in some cases, diskette, from the Public Document Room (PDR):

NRC Public Document Room
2120 L Street, N.W., Lower Level
Washington, DC 20555–0001
<http://www.nrc.gov/NRC/PDR/pdr1.htm>
1–800–397–4209 or locally 202–634–3273

Microfiche of most NRC documents made publicly available since January 1981 may be found in the Local Public Document Rooms (LPDRs) located in the vicinity of nuclear power plants. The locations of the LPDRs may be obtained from the PDR (see previous paragraph) or through:

   <http://www.nrc.gov/NRC/NUREGS/
   SR1350/V9/lpdr/html>

Publicly released documents include, to name a few, NUREG-series reports; *Federal Register* notices; applicant, licensee, and vendor documents and correspondence; NRC correspondence and internal memoranda; bulletins and information notices; inspection and investigation reports; licensee event reports; and Commission papers and their attachments.

Documents available from public and special technical libraries include all open literature items, such as books, journal articles, and transactions, *Federal Register* notices, Federal and State legislation, and congressional reports. Such documents as theses, dissertations, foreign reports and translations, and non-NRC conference proceedings may be purchased from their sponsoring organization.

Copies of industry codes and standards used in a substantive manner in the NRC regulatory process are maintained at the NRC Library, Two White Flint North, 11545 Rockville Pike, Rockville, MD 20852–2738. These standards are available in the library for reference use by the public. Codes and standards are usually copyrighted and may be purchased from the originating organization or, if they are American National Standards, from—

American National Standards Institute
11 West 42nd Street
New York, NY 10036–8002
<http://www.ansi.org>
212–642–4900

International

Agreement Report

Data Base on the Behavior of High Burnup Fuel Rods with Zr-1%Nb Cladding and UO$_2$ Fuel (VVER Type) under Reactivity Accident Conditions

Description of Test Procedures and Analytical Methods

Prepared by
L. Yegorova, V. Asmolov, G. Abyshov, V. Malofeev, A. Avvakumov, E. Kaplar, K. Lioutov, A. Shestopalov
Nuclear Safety Institute of Russian Research Centre "Kurchatov Institute"
Kurchatov Square 1, Moscow 123182, Russia

A. Bortash, L. Maiorov, K. Mikitiouk, V. Polvanov
Institute of Nuclear Reactors of Russian Research Centre "Kurchatov Institute"
Kurchatov Square 1, Moscow 123182, Russia

V. Smirnov, A. Goryachev, V. Prokhorov
State Research Centre "Research Institute of Atomic Reactors"
Dimitrovgrad 433510, Russia

V. Pakhnitz, A. Vurim
Institute of Atomic Energy of National Nuclear Centre of Kazakhstan Republic
Semipalatinsk 490021, Kazakhstan

ABSTRACT

This volume of the report contains the following information on test conditions and basic procedures used to develop the data base:

- objects and conditions of the IGR reactor tests;

- test parameters of fuel rods before, during and after the RIA tests;

- parameters of fuel rods during RIA tests calculated by FRAP-T6 and SCANAIR computer codes;

- measured mechanical properties of Zr-1%Nb cladding obtained due to special tests;

- parameters of Zr-1%Nb cladding failure of the ballooning type measured under the burst test conditions;

- input data with original material properties of Zr-1%Nb cladding for the MATPRO package and SCANAIR code.

TABLE OF CONTENTS

LIST OF FIGURES

LIST OF TABLES

ACKNOWLEDGMENTS

LIST OF ACRONYMS

ANL	Argonne National Laboratory (USA)
AO MZ	AO Mashinostroitelny Zavod (Electrostal, Russia)
CABRI	name of the test reactor (France)
CE-Saclay	Research Centre Saclay (France)
FGR	fission gas release
FRAP-T6	fuel rod analysis program, transient version 6 (USA)
IAE KI	Institute of Atomic Energy "Kurchatov Institute" (former name of RRC KI)
IAE NNC	Institute of Atomic Energy of National Nuclear Centre of Kazakhstan Republic (Kazakhstan)
IGR	Impulse Graphite Reactor (Kazakhstan)
IPSN/CEA	Institute for Protection and Nuclear Safety of Commissariat of Atomic Energy (France)
LOCA	loss-of-coolant accident
NSI RRC KI	Nuclear Safety Institute of Russian Research Centre "Kurchatov Institute" (Russia)
NSRR	Nuclear Safety Research Reactor (Japan)
NV NPP	NovoVoronezh nuclear power plant
PCMI	pellet–cladding mechanical interaction
PWR	pressurized–water reactor
RIA	reactivity–initiated accident
RIAR	State Research Centre "Research Institute of Atomic Reactors" (Russia)
RRC KI	Russian Research Centre "Kurchatov Institute" (Russia)
SCANAIR	code for describing the fuel behavior under an RIA transient (France)
VNIINM	All-Russian Research Scientific Institute for Inorganic Materials (Russia)
VVER	Russian type of pressurized–water reactor

1. EXECUTIVE SUMMARY

1.1. Introduction

As it was noted in Volume 1, this Report summarizes the development of the data base under the long-term research program aimed at investigating the behavior of high burnup VVER fuel rods under RIA conditions. Fig. 1.1 presents the structural diagram of the basic investigations conducted under this program.

The analysis of the diagram enables two important statements:

- there is a direct relation between quality of the obtained results and quality of analytical and experimental tools used to produce these results;

- practical value of the developed data base and many original procedures goes far beyond the scope of this work.

These statements lead to a conclusion that it is appropriate to describe in detail the used test procedures, analytical methods and obtained data base. That is why this volume of the Report is intended to provide an overview of corresponding information. The following main approaches were therewith taken in preparation of this volume:

- standard well known procedures are described very schematically;

- main emphasis in description of new or modified methods is placed on justification of procedures, including verification investigations;

- complex and essential procedures are described in individual original reports which have been made specifically for this purpose.

1.2. The IGR/RIA tests with VVER high burnup fuel rods

The main purpose of testing fuel rods of VVER-1000 type at IGR reactor was comparative studies of the behavior of preirradiated and unirradiated fuel rods under conditions simulating reactivity initiated accidents. These tests were conducted at IGR impulse research reactor (Semipalatinsk, Kazakhstan) in 1991.

The program of the tests provided for the solution of the following problems:

- determination of failure thresholds of VVER-1000 fuel rods as a function of the burnup;

- determination of failure mechanisms of fuel rods versus test parameters.

Three types of fuel rods were prepared for tests at IGR reactor:

- 13 re-fabricated fuel rods, manufactured from commercial fuel elements of VVER-1000 type (C-type fuel rods);

- 10 re-fabricated fuel rods containing irradiated cladding of commercial fuel elements of VVER-1000 type and unirradiated fuel of VVER-1000 type (D-type fuel rods);

- 20 unirradiated fuel rods of VVER-1000 type (E-type fuel rods).

Taking into account the world experience of testing LWR fuel under conditions simulating RIA and corresponding experience of testing unirradiated VVER-1000 fuel rods, the following conditions were selected to test fuel rods of C, D, E type:

- test type is the reactor capsule test;

- mode of changing the reactor power is the power pulse;

- coolant in the capsule is the water, air;

- initial coolant parameters are atmospheric pressure, ambient temperature, no flow rate;

- number of fuel rods in the capsule are 2 (with the exception of 3 tests performed with 1 rod).
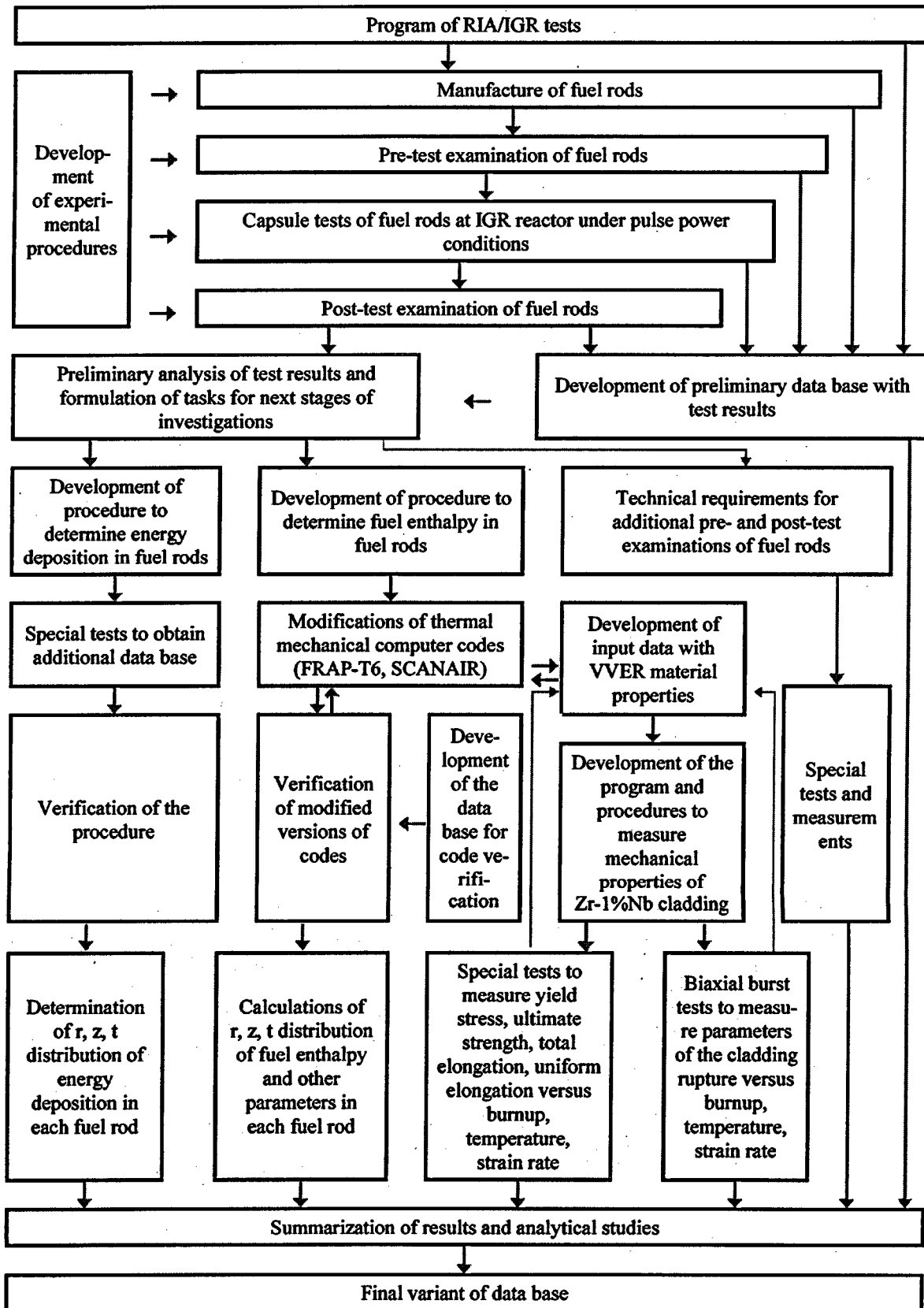
Fig. 1.1. Structure of researches

The air was selected as the second type of the coolant in the capsule because of the desire to obtain the data base for the analysis and computer simulation of the fuel rod behavior, in rather simple boundary conditions of the heat exchange between fuel rods and the coolant. Besides this obtained data base can be used to analyze the behavior of fuel rods under LOCA conditions.

The technical requirements on test modes were developed taking into account the following factors:

- absence, in the world data base, of experimental results on failure thresholds of high burnup fuel rods under RIA conditions (as of the beginning of 1991);

- absence, by the beginning of these tests, of reliable data on ratios between the energy deposition in the fuel of high burnup fuel rods and the energy deposition in IGR reactor;

- absence of technical devices that would allow to determine directly at IGR reactor whether a high burnup fuel rod is intact or destroyed after the test.

A special scoping test was conducted at MIR research reactor (Dimitrovgrad, Russia) to obtain input data characterizing the ratio between number of fissions in the unirradiated fuel of VVER-1000 type and in the high burnup fuel of VVER-1000 type under the same irradiation conditions in the stationary mode. The results were used to determine the operating ratio connecting the energy deposition in IGR reactor with the energy deposition in unirradiated fuel rods and the energy deposition in high burnup fuel rods. Unfortunately, later it turned out that the experimental coefficient obtained in the scoping test at MIR reactor was determined with a large error (about 30%); this circumstance affected some results of testing fuel rods in IGR reactor.

In the final form, the following logic was used as the basis of the development of specific technical requirements on the tests:

1. The number of high burnup fuel rods tested in capsules with the water coolant is 8.

2. The number of high burnup fuel rods tested in capsules with the air coolant is 5.

3. The number of fuel rods with the preirradiated cladding and the fresh fuel tested in capsules with the water coolant is 5.

4. The number of fuel rods with the preirradiated cladding and the fresh fuel tested in capsules with the air coolant is 5.

5. 20 unirradiated fuel rods were used as reference rods tested under the same conditions as preirradiated fuel rods. Thus, each of these fuel rods was installed in capsules in addition to the main fuel rod of C or D type.

6. The total number of tests was 23.

7. All fuel rods of the same type for each coolant type are to be tested in the conditions when only one integral parameter is varied, namely, the energy deposition in the fuel rod. The power pulse half width must remain more or less constant. This requirement was satisfied using automatic power regulator of IGR reactor.

8. The entire test cycle was divided into two stages. At the first stage 12 tests were performed, which included tests of three types of fuel rods for two coolant types. The series of tests of fuel rods of the same type (for the same coolant type) was conducted with a gradual increase in the energy deposition from one rod to another by step-by-step method for a selected energy deposition range. After the first stage of tests was completed, twelve capsules with tested fuel rods were sent to hot cells in RIAR (Dimitrovgrad, Russia), where the capsules were opened and the fuel rods were visually examined to determine the scale of destruction. According to the results of the visual examination of fuel rods, the test program of the second stage was developed; the main task of the second stage was to adjust of fuel rod failure thresholds.

9. Special scoping tests were to be conducted at IGR reactor to obtain experimental coefficients connecting the energy deposition in the unirradiated fuel sample with the energy deposition in IGR reactor.

10. Based on safety considerations, it was necessary to ensure the absolute leak-tightness of the capsules with the high burnup fuel rods at all technological stages of the tests including the railway transportation of the capsule devices (~2500 km) from the place of their assembly to IGR reactor and back. Due to this

requirement the idea of measuring thermo-physical parameters of fuel rods in the test process was rejected (i.e. there were no instrument penetrations through the capsules with high burnup fuel rods).

In general, the technological scheme of the tests included the following stages:

- manufacturing of E-type fuel rods and fuel pellets of D-type fuel rods in AO MZ "Electrostal" (Electrostal, Russia);

- manufacturing of re-fabricated fuel rods of C, D types, capsules for them, assembly of capsules with fresh and irradiated fuel rods in RIAR (Dimitrovgrad, Russia);

- transportation of capsules with fuel rods to IGR reactor and back by RIAR, Dimitrovgrad, Russia);

- fuel rod tests at IGR reactor in IAE NNC (Semipalatinsk, Kazakhstan);

- post-test examinations of commercial fuel elements of NV NPP, pre- and post-test examinations of fuel rods of C, D types in RIAR (Dimitrovgrad, Russia).

The program of post-test examinations of commercial fuel elements was coordinated with programs implemented within the framework of other studies and provided for the conduct of only those measurements which were necessary for supplementing the data base on input characteristics of re-fabricated fuel rods of C, D types.

The program of pre- and post-test examinations of C, D types fuel rods included a set of studies to solve problems of this project.

The management of this project as a whole, coordination of all types of studies, development of the program and methodological documentation, development of the procedure to determine r, z, t distribution energy deposition, validation of the tests, consolidation and analysis of test results were carried out by RRC "Kurchatov Institute" (Moscow, Russia).

1.3. Experiments to measure mechanical properties of Zr-1%Nb cladding

It is evident that the full-scope analysis of the data base obtained during testing of the VVER fuel rods in IGR reactor can be done only by computer codes. Therefore original input data characterizing mechanical properties of VVER fuel rods are to be prepared. Still, the assessment of the existing data base with mechanical properties of Zr-1%Nb claddings has demonstrated that it was necessary to perform new special tests in order to get mechanical properties of irradiated claddings. Besides, some additional tests were to be performed to complete the data base with the properties of unirradiated Zr-1%Nb claddings.

The testing program worked out by NSI RRC KI called for the performance of two types of tests:

- testing of the plain ring specimens fabricated of the commercial VVER tubes and of irradiated claddings of commercial VVER high burnup fuel elements;

- burst tests of pressurized specimens fabricated of the commercial VVER tubes and of irradiated claddings of commercial VVER high burnup fuel elements.

The first type of tests was performed to measure yield stress, ultimate strength, uniform elongation, total elongation versus temperature and strain rate. The objective of the second type of tests was to measure burst parameters of the claddings versus temperature and strain rate, as well as the number of specific characteristics of the ballooning type cladding deformation. The set of special procedures was developed for these tests by the specialists of RRC KI and RIAR. The experimental part of work was performed in RIAR, and analytical part of work was carried out in NSI RRC KI.

1.4

1.4. Computational analysis of VVER fuel rod behavior under IGR/RIA test conditions

Two computer codes were used for computational analysis of VVER fuel rod behavior under IGR test conditions:

- FRAP-T6 code [1];

- SCANAIR code [2].

Neither of the codes was intended to calculate behavior of the VVER fuel rods. Therefore, special attention was paid to develop the data base with original mechanical properties of the VVER fuel rods. Besides, preliminary verification of the codes for the IGR test conditions has demonstrated that it was necessary to modify some of the code's models prior to using them as the tools to analyze VVER fuel rod behavior. That is why code modification was a separate stage of the work. After that the final verification of the codes was performed, and the boundaries of their applicability to analyze IGR test results were determined. Final stage of this research included computer analysis of 25 fuel rods tested in IGR reactor and processing of these results as the computational data base. The whole complex of work in this direction was performed by the specialists of RRC KI.

1.5. Structure of the generalized data base for IGR/RIA tests of VVER fuel rods

The generalized data base is included into Volumes 2, 3 of this Report. The data base of Volume 3 consists of the following main sub-bases:

- Test data to characterize parameters of VVER fuel elements prior to irradiation at NPP (Appendix A);

- Test data to characterize the irradiation history of VVER fuel elements at NPP (Appendix B);

- Test data to characterize parameters of fuel rods fabricated of VVER fuel elements prior to IGR tests (Appendixes C, D, E);

- Test data to characterize IGR test conditions (Appendix F);

- Test and calculated (by FRAP-T6 and SCANAIR codes) data to characterize fuel rod behavior during IGR tests and after IGR tests (Appendixes G, H, I);

- Test data to characterize the results of tests on the measurement of mechanical properties of VVER claddings using ring specimens (Appendix J);

- Test data to characterize the results of burst tests with Zr-1%Nb claddings (Appendix K).

The data base of Volume 2 includes the material properties of VVER fuel rods.

The main objective of the present Volume of the Report is to describe, justify, and analyze the whole set of experimental and calculational procedures used to obtain the data base presented in Volume 3.

1.6. References

[1] L. Siefken, Ch. Allison, M. Bohn, S. Peck "FRAP-T6: Computer code for the transient analysis of oxide fuel rods." *NUREG/CR-2148 EGG-2104, May 1981.*

[2] F. Lamare, J.C. Latche, "SCANAIR. A Computer Code for Reactivity Initiated Accidents in LWRs", *Rapport Technique SEMAR 95/01*

2. OBJECTIVES AND CONDITIONS OF THE IGR REACTOR TESTS

2.1. Test objects

Refabricated high burnup fuel rods (fuel rods of C-type)

Refabricated C-type fuel rods were manufactured from commercial fuel elements #317 and #22 of fuel assembly #1114 removed from power unit No5 of NovoVoronezh Nuclear Power Plant (NV NPP-5). Operating cycles of VVER-1000 fuel elements took place from June 25, 1984 to June 25, 1987.

Characteristics of commercial fuel elements before the irradiation are presented in Appendix A, Volume 3 of the Report [1]. Characteristics of operating cycles [2] and characteristics of commercial fuel elements after the irradiation are presented in Appendix B, Volume 3 of the Report. Procedures used to obtain characteristics are described in section 3.1. The general appearance of the refabricated C-type fuel rod is presented in Fig. 2.1.
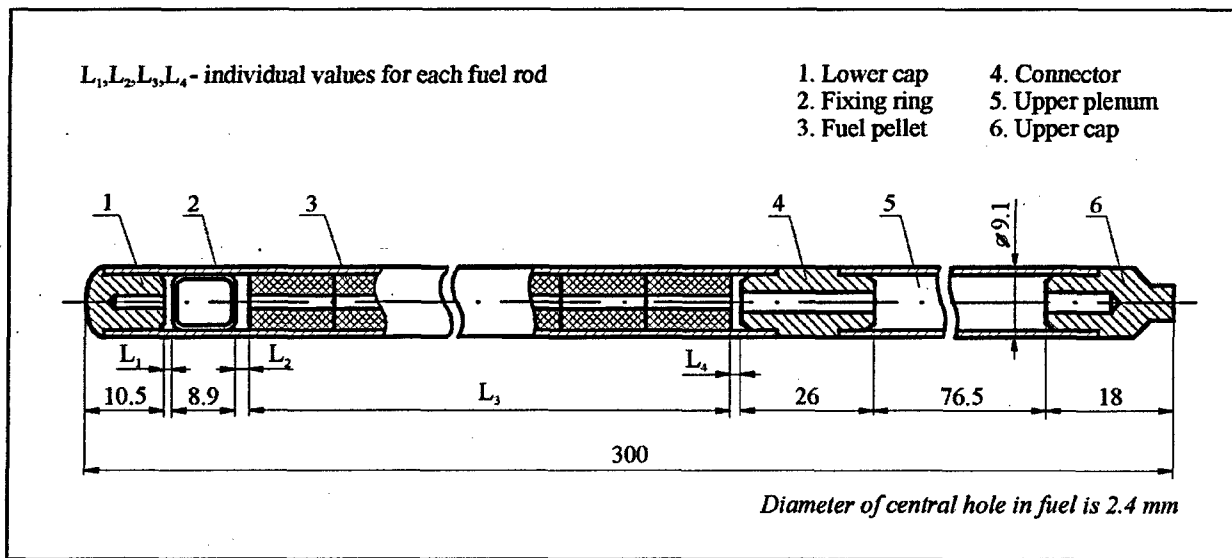
Fig. 2.1. Scheme of high burnup fuel rod

The refabricated C-type fuel rod contains the active part (fuel stack and cladding), which was a part of one out of two commercial fuel elements, and technological components (top and bottom caps), the fixing ring which fixes the fuel stack in the axial direction, the connector and the cladding that forms the upper gas plenum. All technological components of the fuel rod were made of unirradiated materials. The procedure to manufacture refabricated fuel rods is described in section 3.3 of the present Volume.

The material of the C-type fuel rod cladding is Zr-1%Nb alloy, fuel rod pellets are of cylindrical form, there is a hole along the axis of the pellet. The source fuel material is UO_2. The average fuel burnup in C-type fuel rods is 48 MWd/kg U. The internal plenum of the fuel rod is filled with helium under the pressure of 1.7 MPa. Characteristics of C-type fuel rods before tests in IGR reactor are presented in Appendix C, Volume 3 of the Report. Procedures to obtain these characteristics are described in section 3.1 of the present Volume.

Refabricated fuel rods with fresh fuel and irradiated cladding (fuel rods of D-type)

Refabricated D-type fuel rods contain, in the fuel rod active part, a segment of the cladding of commercial fuel element #22 (see description of C-type fuel rod), a stack of unirradiated fuel pellets of VVER-1000 type and technological components similar to those of C-type fuel rods. The general appearance of D-type fuel rod is presented in Fig. 2.2.

2.1
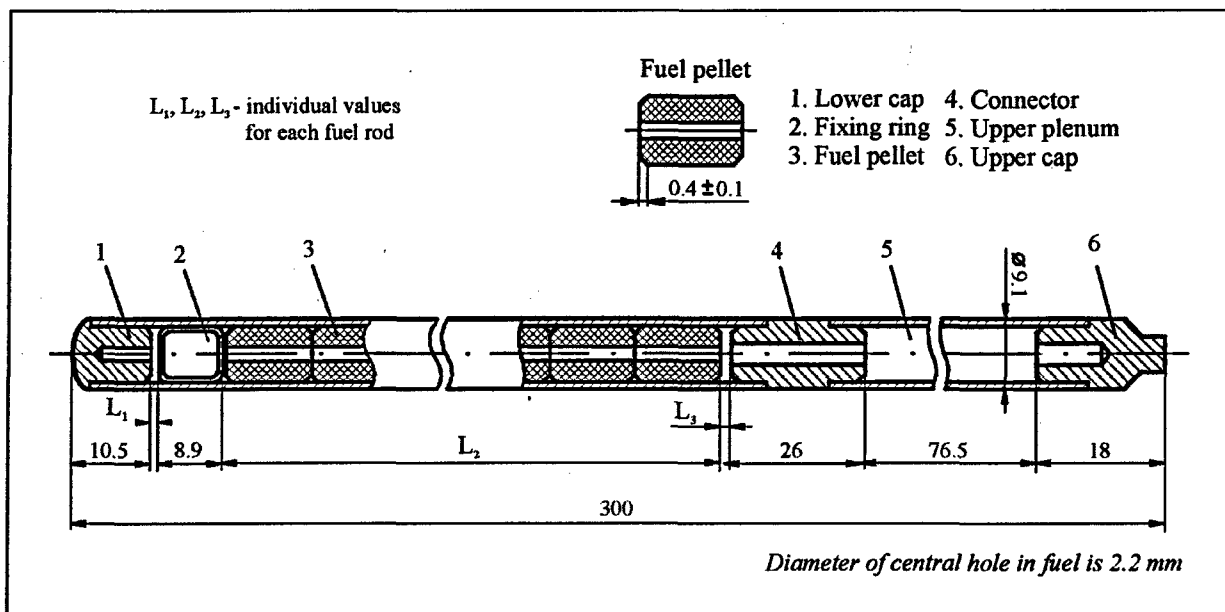
Fig. 2.2. Scheme of fuel rod with preirradiated cladding and fresh fuel

The fuel rod cladding material is Zr-1%Nb alloy; the fuel material is UO_2 with the average enrichment of 4.4%. D-type fuel rod pellets are of cylindrical form with facets at external edge parts, there is a hole along the pellet axis. The internal environment of the fuel rod is helium under the pressure of 1.7 MPa.

Characteristics of D-type fuel rods before tests in IGR reactor are presented in Appendix D, Volume 3 of the Report. Procedures to obtain these characteristics are described in section 3.2 of the present Volume.

Fresh fuel rods (fuel rods of E-type)

The procedure of manufacturing unirradiated E-type fuel rods is described in section 3.3 of the present Volume. The general appearance of E-type fuel rods is presented in Fig. 2.3.
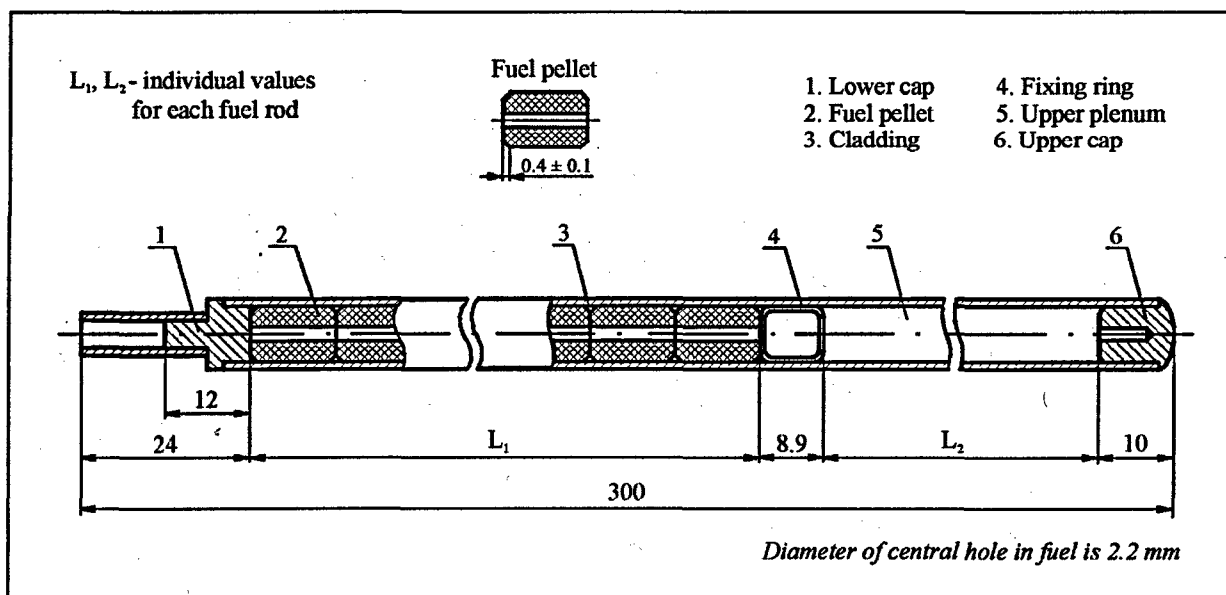
Fig. 2.3. Scheme of unirradiated fuel rod

The fuel rod contains the cladding made of Zr-1%Nb alloy, the fuel stack about 150 mm long, the upper plenum, the fixing ring and caps. The fuel rod is filled with helium to the pressure of about 2–2.5 MPa.

2.2

E-type fuel rod pellets are of cylindrical form with facets at edges. Fuel pellet material is UO_2 with the enrichment of about 4.4%; there is a hole in the pellet centre. Characteristics of E-type fuel rods are presented in Appendix E, Volume 3 of the Report. Procedures to obtain these characteristics are described in section 3.2 of the present Volume.

2.2. Test conditions

As it has already been noted, 23 leak-tight capsules with test fuel rods were delivered to IGR reactor before the beginning of pulse tests. 20 capsules contained two fuel rods – one of them was refabricated, the other one was unirradiated. The three capsules contained one refabricated fuel rod. The load scheme of fuel rods in capsules and the coolant type in each capsule are presented in the Table of Appendix F, Volume 3 of the Report. Before the installation of the capsule with fuel rods into IGR reactor, special fuel samples were positioned in the capsule. These samples, the capsule and IGR reactor are described below.

Special fuel samples

Two special fuel samples were installed in the capsule with fuel rods before the beginning of the tests at IGR reactor.

After the completion of the test at IGR reactor the fuel samples were removed from the capsule, and number of fissions in them was measured. Results of these measurements were used as the input data for the procedure of determining the energy deposition in fuel rods of C-, D-, E- types tested at IGR reactor (see sections 4.1, 4.3). The design scheme of special fuel samples is presented in Fig. 2.4.

1. Guide tube
2. Special fuel samples
3. Aluminium box
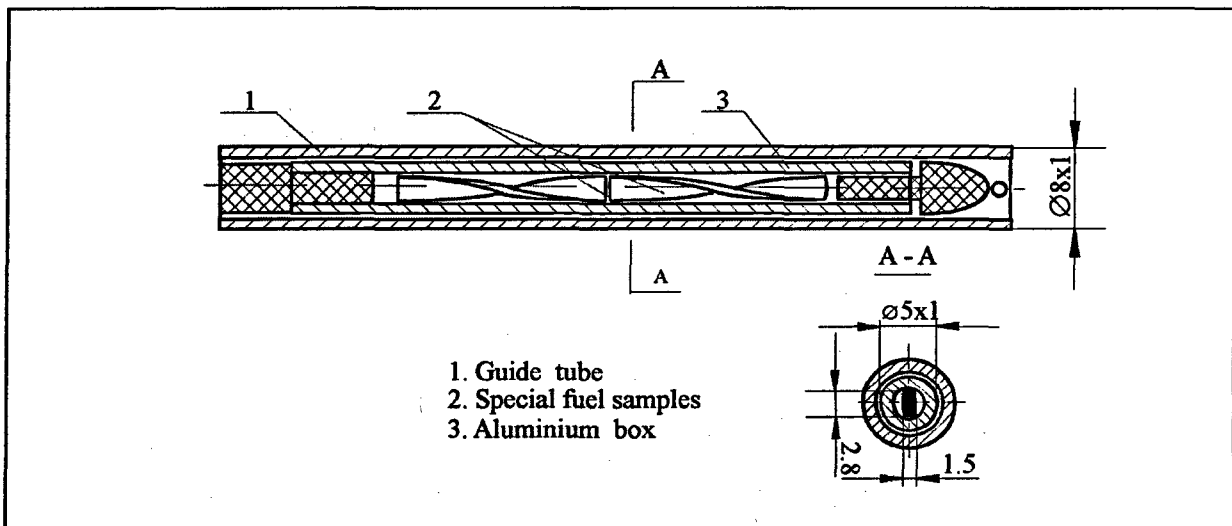
Fig. 2.4. Axial and cross-sections of the guide tube with special fuel samples

There was a guide tube in each capsule, intended for installing the aluminum box with two fuel samples. Each fuel sample was about 20 mm long and represented a spiral-rod fuel element of two-blade profile, 1.5 mm thick. The fuel element was in the cladding Zr-1%Nb alloy, 0.3 mm thick. Each special fuel element had a certification of the manufacturing plant and was qualified regarding its fuel composition [3]. Before the installation in capsules, all special fuel samples were subjected to input spectrometric monitoring of U^{235} content.

Experimental capsule

The geometric scheme of the capsule with fuel rods is presented in Fig. 2.5.

2.3
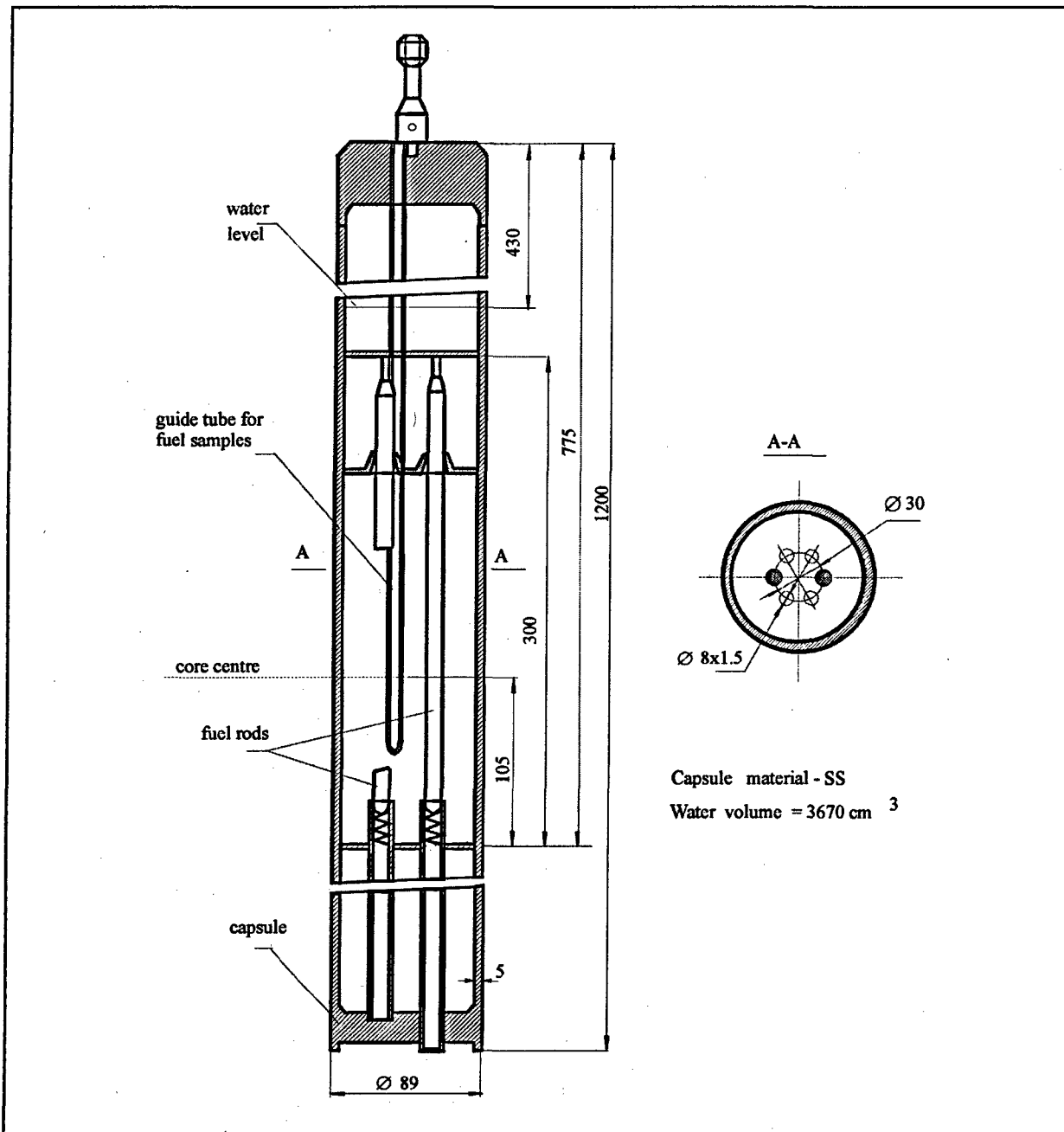
Fig. 2.5. Scheme of the experimental capsule

The capsule represented a steel leak-tight vessel filled with the coolant and equipped with structural elements intended for the installation of fuel rods to be tested in them. The capsule design provided for a free axial movement of fuel rods during the test process due to thermal expansion. The fixation of fuel rods in a certain position during transportation and handling was provided by springs. The capsules were filled with water and had an air-filled gas plenum in the upper part. Each capsule had four guide tubes intended for positioning special fuel samples. The axes of two fuel rods and of four guide tubes were located along the circumference with a uniform angular step.

Initial thermo-physical parameters in the capsule were as follows:

- atmospheric pressure;
- ambient temperature;

2.4

- no flow rate;

- water or air as coolant.

IGR reactor

IGR reactor is a pulse uranium-graphite self-quenching reactor of thermo-capacity type [4]. Fig. 2.6, Fig. 2.7 show cross and axial sections of IGR reactor.

1. Water tank
2. Reactor vessel
3. Thermal shield
4. Reactor core
5. Side reflector
6. Ionization chamber channel
7. Temperature sensor channel
8. Control rod channel
9. Central experimental channel
10. Side experimental channel
11. Physical measurement channel
12. Neutron source channel
13. In-core monitoring detector channel
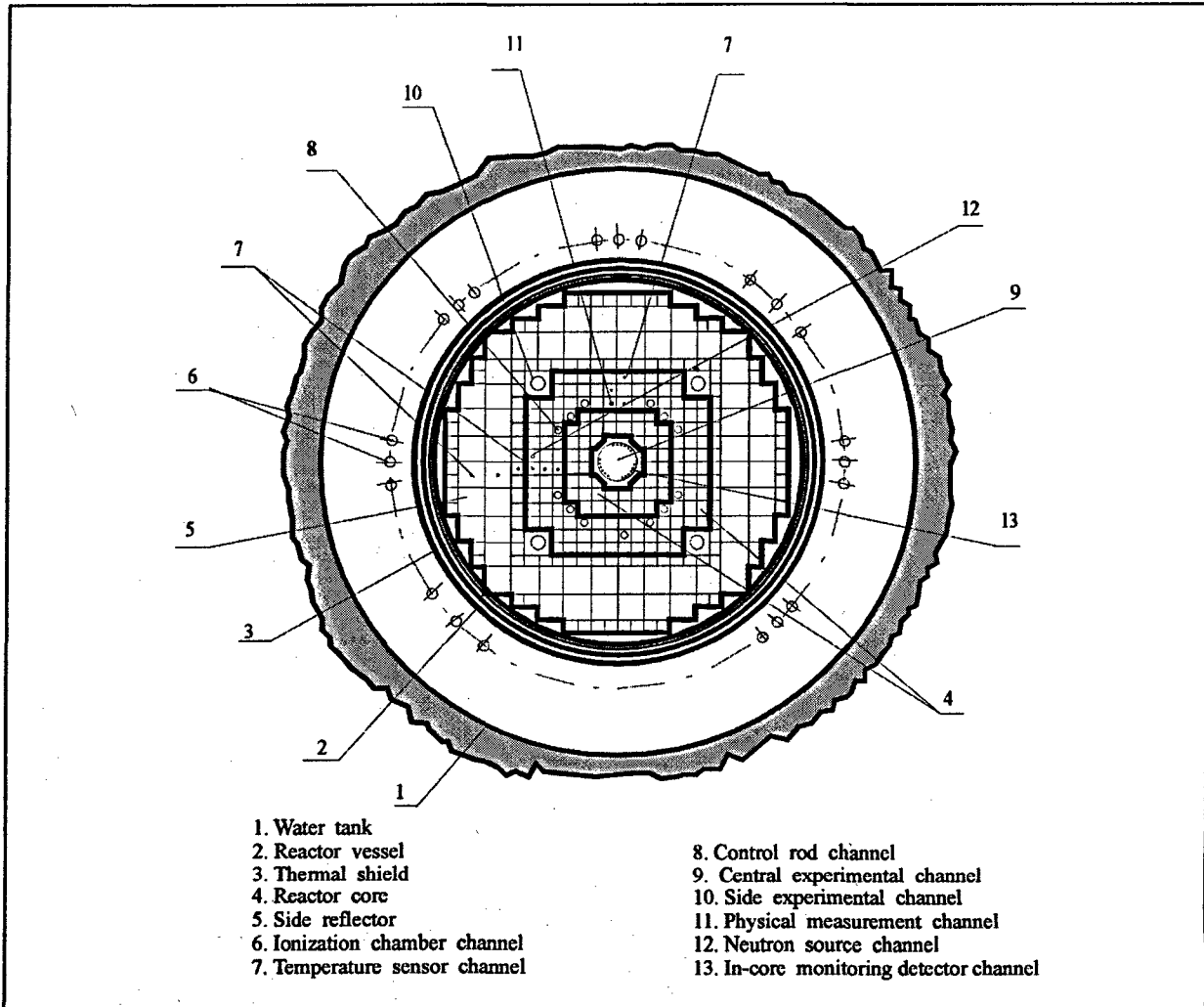
Fig. 2.6. Cross-section of IGR reactor

The reactor core consists of graphite blocks impregnated with uranium salt. The reactor core includes two parts: immovable part and movable part of the core, which can move in the axial direction using a special device. The side reflector, top and bottom edge reflectors consist of the same graphite blocks (but without uranium). The reactor core is located in the leak-tight reactor vessel filled with helium. The reactor vessel with the core is located in the water-filled tank. Therefore, the heat generated during the reactor operation is accumulated in the reactor core, and then is gradually transferred to the coolant circulating in the water tank. The reactor power is controlled using control rods positioned in special holes of the reactor core. In addition to control rods there are four lateral rods in the reactor, which are also located in the holes of the reactor core. The reactor power is monitored using a group of ionization chambers installed at a certain angle along the circumference in the water tank. In addition, in-core sensors of the neutron flux are used in some cases. These sensors are installed in the central plenum of the reactor. Cross and axial sections of the reactor central part are presented in Fig. 2.8, Fig. 2.9.

2.5

Fig. 2.7. Axial section of IGR reactor

1. Water tank
2. Reactor vessel
3. Thermal shield
4. Reactor core
5. Side reflector
6. Ionization chamber channel
7. Temperature sensor channel
8. Control rod channel
9. Central experimental channel
10. Biological shield
11. Ceiling

1.   Graphite insert
2, 3, 4. Three shrouds of reactor
           capsule
5.   In-core neutron detector
6.   Protective shroud
7.   Capsule
8, 9.   Fuel rods
10.   Tube for fuel samples
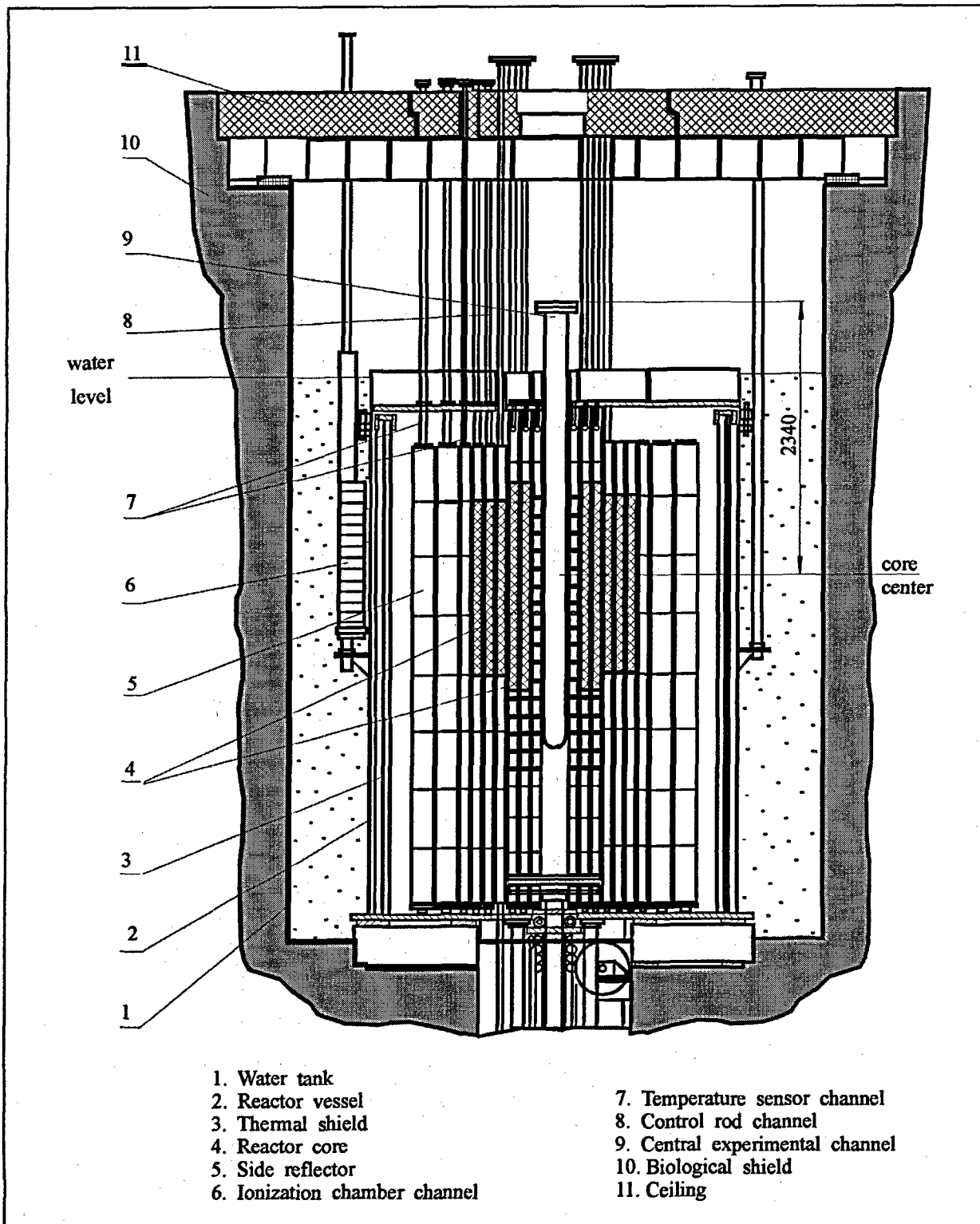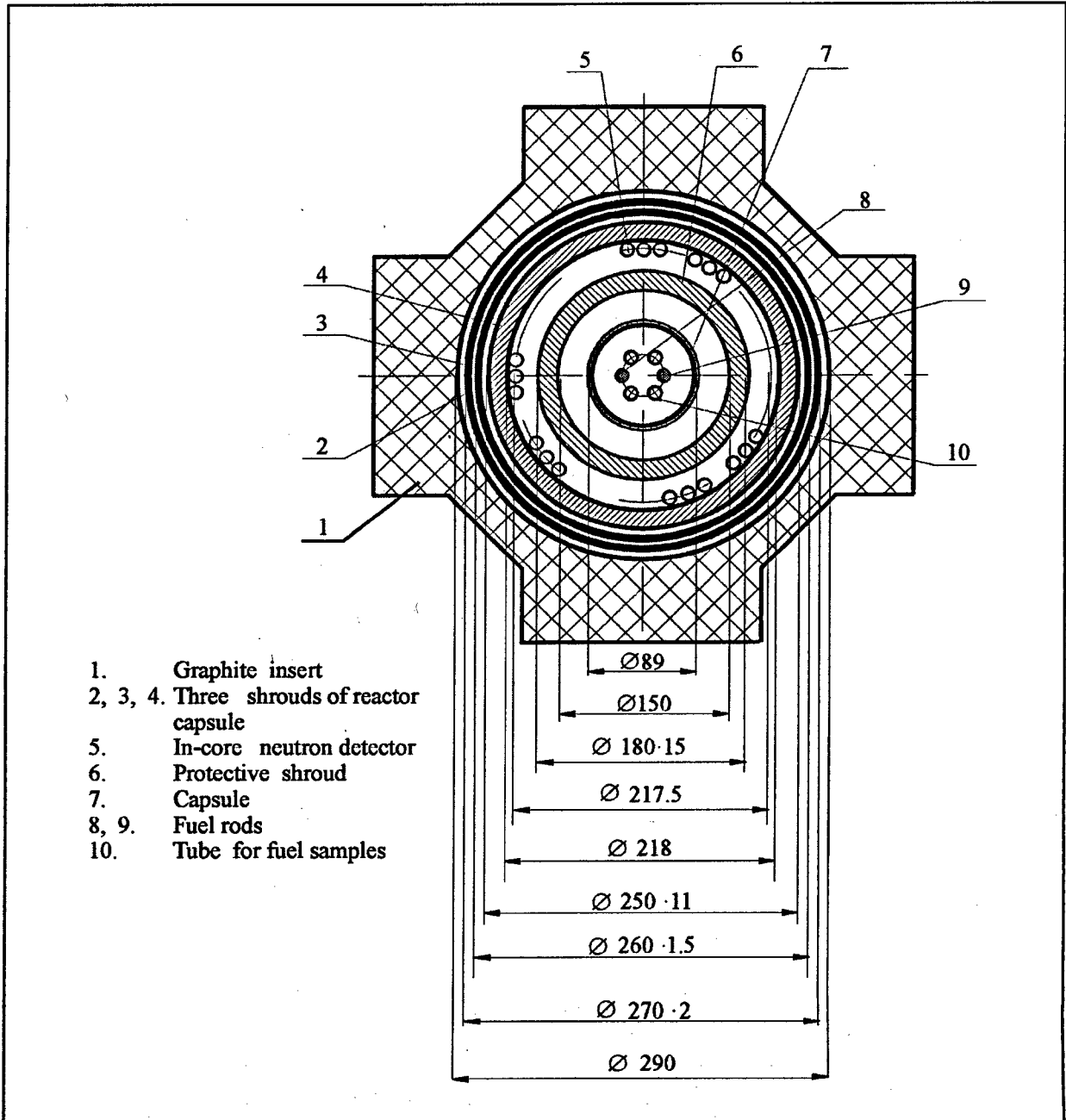
Fig. 2.8. Cross-section of the IGR reactor central part
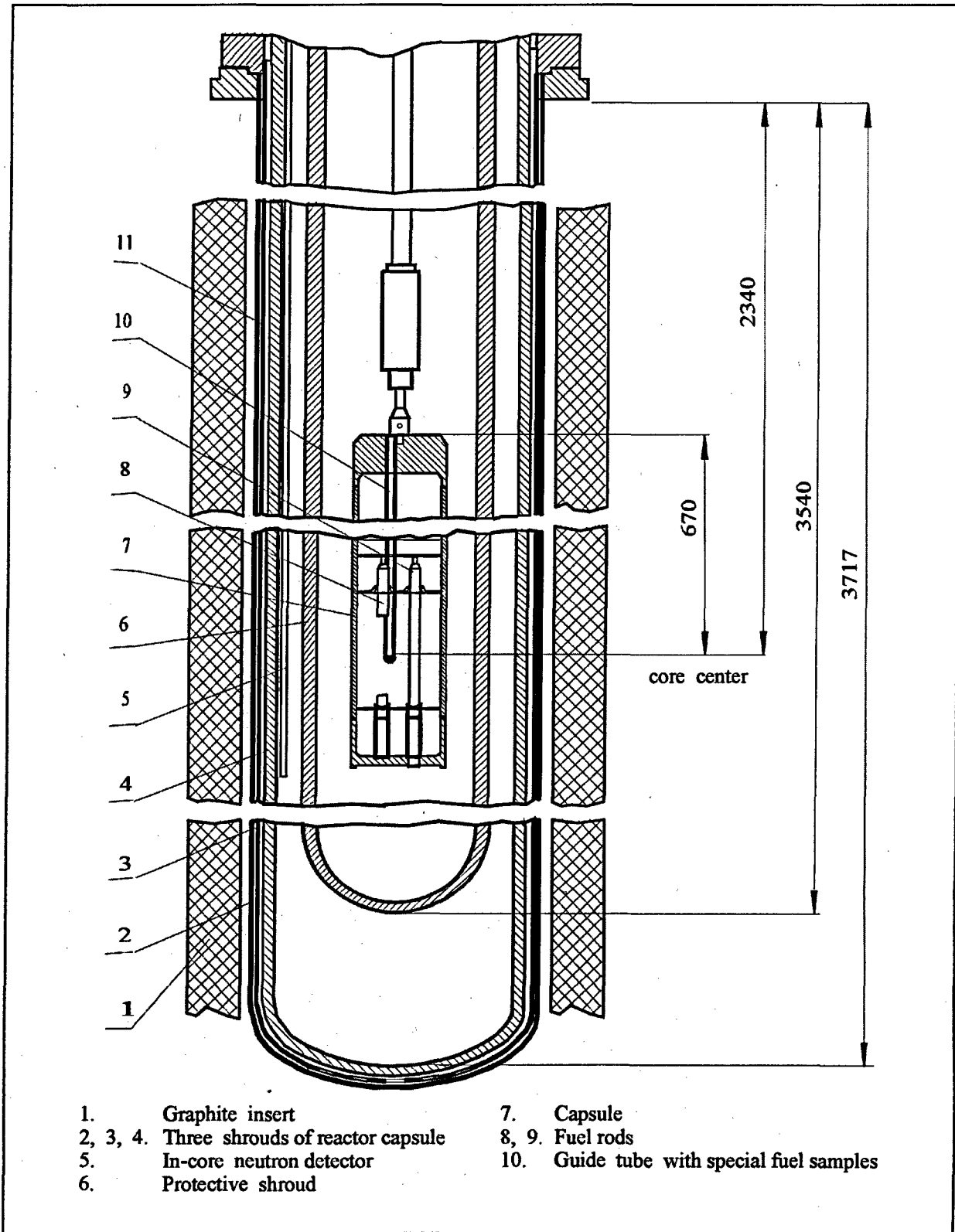
Fig. 2.9. Axial section of IGR reactor central part

1.   Graphite insert
2, 3, 4. Three shrouds of reactor capsule
5.   In-core neutron detector
6.   Protective shroud

7.   Capsule
8, 9. Fuel rods
10.   Guide tube with special fuel samples

This part consists of the graphite insert with the central hole, in which the central experimental channel of the reactor is located. The central experimental channel of the reactor consists of the following elements:

- reactor capsule consists of three shrouds, water circulates in the gap between two of them to provide protection of the internal plenum of the central experimental channel against the heat generated in the reactor core;

- protective shroud intended to protect reactor structural components in case of the destruction of test objects;

- central cavity 150 mm in diameter intended for positioning test object at IGR reactor.

Test objects (in our case, the capsule with fuel rods) are positioned in the central cavity of the central experimental channel.

There are two main types of the reactor power mode:

- uncontrolled power pulse;

- controlled power pulse.

The uncontrolled power pulse mode is implemented by withdrawing a required group of control rods to a required height. This results in the introduction of the initial positive reactivity in the range up to 10 β_{eff} and, thus, in the formation of the forward front of the reactor power pulse. The reactor quenching, i.e. reduction of the positive reactivity, is carried out without control rods due to the negative temperature reactivity coefficient.

The controlled power pulse mode is implemented using the automatic regulator of the reactor power. It is possible to implement practically any reactor power profile as a function of time, including the stationary one. In this case the only limitation is the reactor core temperature. It must not exceed certain values provided for in the safety requirements,

Main characteristics of IGR reactor are presented in Table 2.1. During the tests of fuel rods of C-, D-, E-types the reactor operated in the controlled power pulse mode with the pulse half width of about 700 ms. A more detailed description of reactor operating modes during these tests is contained in section 4.6.

Table 2.1. Main characteristics of IGR reactor

Characteristic	Value
1. Approximate overall dimensions of the reactor core (mm)	1400·1400·1400
2. Outer diameter of the central experimental channel (mm)	270
3. Material of fuel elements of the reactor core	graphite impregnated with uranyl nitride
4. U^{235} mass in the reactor core (kg)	9
5. Fuel enrichment in U^{235} (%)	90
6. Nuclear ratio (carbon/uranium)	8040
7. Moderator material	graphite
8. Reflector material	graphite
9. Maximum thermal neutron flux density in the reactor central experimental channel (n/cm^2·sec)	$7 \cdot 10^{16}$
10. Maximum thermal neutron fluence in the central experimental channel (n/cm^2)	$3.7 \, 10^{16}$
11. Excess reactivity (β_{eff})	31.6
12. Effective fraction of delayed neutrons (β_{eff})	0.00685
13. Temperature reactivity coefficient (β_{eff}/K)	-0.03
14. Maximum permissible temperature of the reactor core (K)	1400

2.3. References

[1] V.Zhitelev, B.Kanashov, V.Polenoc, A.Smirnov. "Data Base and Postirradiation Examination Results of Spent VVER-1000 Fuel Elements and Assemblies", BNES Conference-Fuel Management and Handling, Edinburg, England, 20-22 March, 1995.

[2] Yu.Vikhorev, V.Voznesensky, V.Goncharov et.al "Fuel Assembly Operation Experience in VVER-1000 Reactor of Unit 5 of NV NPP", Rus., At. Energia, Vol. 54, Iss.3, 1983.

[3] "Passport for Special Fuel Samples", Rus., Scientific and Industrial Association "LUCH", Passport No. 837.5.02.00.03ET, Podolsk, 1990.

[4] I.Kurchatov, S.Feinberg, N.Dollegal et.al "IGR Pulse Graphite Reactor", Report No. 322A, Proceedings of the 3-rd International Conference on the Peaceful Uses of Atomic Energy, Geneva, Vol. 7, p. 461-472, UN Press, New-York, 1965.

3. CHARACTERISTICS OF FUEL RODS BEFORE AND AFTER IGR TESTS

3.1. High burnup commercial fuel elements of power unit No 5 of NV NPP

Procedures described in this section were developed in RIAR (Dimitrovgrad, Russia) and were used to determine characteristics of commercial fuel elements, which are presented in Appendix B, Volume 3 of the present Report.

3.1.1. Geometric and thermo-physical characteristics of fuel elements [1, 2]

Average pellet outer diameter

The outer diameter of fuel pellets was determined by direct measurements at metallographic specimens of fuel elements #22 and #307 using metallographic microscope (fuel element #307 is practically the analog of fuel element #317 regarding the whole set of important irradiation parameters).

Length of fuel stack

The length of the fuel stack was determined by processing a statistically representative series of results of gamma spectrometric scanning of fuel elements #22 and #317 along their length.

Pellet-cladding gap

The gap was determined by direct measurements at several metallographic specimens made of fuel element sections with different axial coordinates.

Pressure inside fuel element

The gas pressure inside fuel elements was measured using the manometer method after the cladding was punched with the laser. Since the accuracy of determining the pressure by this method is about 7%, the average gas pressure in a group of fuel elements of the same type is presented as measurement results.

Fuel density

The fuel density for a series of axial coordinates was measured by the immersion method for fuel element #307.

3.1.2. Burnup, fuel isotopic composition and chemical composition of the gas inside the fuel element

Determination of the element cross-section-average burnup and the fuel isotopic composition

These characteristics were measured at fixed axial sections of fuel element #317 by the mass-spectrometric method [3]. The procedure included the following stages:

- cutting the sample and fuel removal from the sample;

- fuel dissolution in the nitric acid;

- separation of isotope fractions of uranium, plutonium, americium, cerium, neodymium by methods of ion exchange and extraction chromatography;

- determination of the isotopic composition of elements;

- determination of the quantitative composition of isotopes by methods of isotopic dilution and alpha spectrometry.

Measurements were conducted using two possible variants of the mass-spectrometric method, namely:

- method of heavy atoms;

- method of determining the accumulation of fission products.

The mass-spectrometric method is a qualified procedure, and its error is about 4.4%.

Determination of the burnup axial distribution [1]

The processing of results of γ-scanning of the irradiated fuel element for Cs^{137} isotope forms the basis of the method to determine the burnup axial distribution. The experimental part of the procedure consists of two stages:

- γ-scanning of commercial VVER-1000 fuel element;

- γ-scanning of the reference sample calibrated for the burnup by the mass-spectrometric method.

The comparison of Cs^{137} gamma line intensity in VVER-1000 fuel element and in the reference sample forms the basis of the calculation procedure to determine the burnup axial distribution in absolute units of burnup measurements. In general, this procedure is qualified; its burnup determination error does not exceed 7%.

Determination of the burnup radial distribution and the fuel isotopic composition

These characteristics were determined by the mass-spectrometric method. The measurements were performed for five fuel micro-samples taken from the cross-section of fuel element # 317. The arrangement of these samples is presented in Fig. 3.1.

1. Cladding
2. Fuel
3. Microsample for analysis
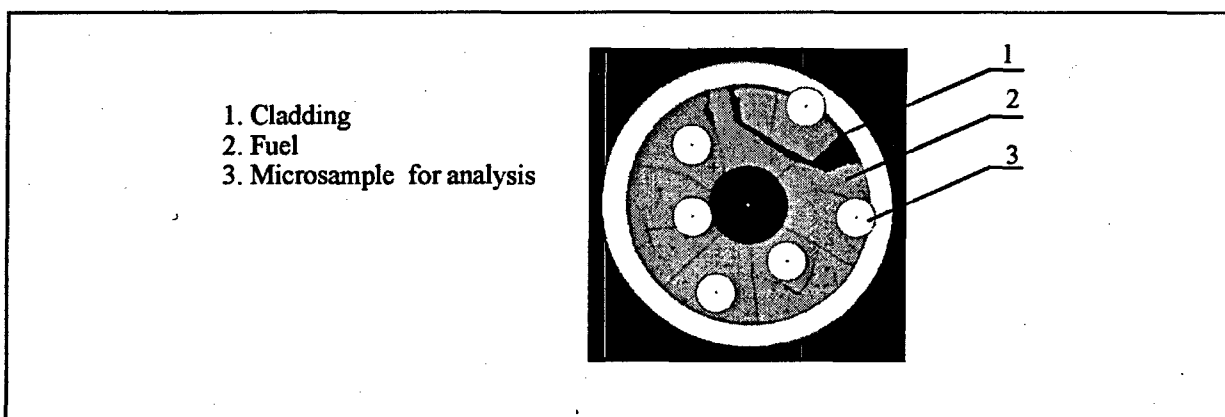
Fig. 3.1. Arrangement of fuel samples taken from the cross-section of fuel element #317 to measure the burnup radial distribution and the fuel isotopic composition

The samples were taken using a tube-type sampler connected to the generator of ultrasonic oscillations. The diameter of a sample was 0.5 mm. The error in determining of the radial coordinate of the sample centre did not exceed 5 %.

Gas composition inside fuel element.

The gas composition inside fuel elements was determined after punching the cladding with the laser, taking the gas sample and mass-spectrometric measurements of its composition. Taking into account the error of a single measurement, this procedure was implemented for a group of fuel elements, which were in similar irradiation conditions. Average measurement values are presented as the measurement results.

3.2. Characteristics of refabricated fuel rods before IGR tests

All measured characteristics of fuel rods of C and D types (with the exception of the fuel of D-type fuel rods) were obtained within the framework of corresponding procedures in RIAR (Dimitrovgrad, Russia). All measured characteristics of D-type fuel rods were obtained in AO MZ "Electrostal" (Electrostal, Russia). All calculation procedures to determine axial distribution of free gas volume, fuel mass etc. were developed in the Russian Research Centre "Kurchatov Institute" (Moscow, Russia).

Results obtained using procedures described in this section are presented for C-type fuel rods in Appendix C, Volume 3; for D-type fuel rods in Appendix D, Volume 3; and for E-type fuel rods in Appendix E, Volume 3.

3.2.1. High burnup fuel rods

Representative values of initial characteristics for C-type fuel rods

Characteristics of this group were not determined individually for each fuel rod. They are typical for the whole batch of fuel rods. A majority of characteristics of this group for C-type fuel rods are completely identical to corresponding characteristics of commercial fuel elements in Appendix B, Volume 3. The following characteristics were additionally measured for a batch of several metallographic samples using standard procedures:

- grain size;

- corrosion thickness of cladding;

- H_2 content in cladding;

The outer diameter of fuel rod cladding and the free gas volume of fuel rods were determined as the arithmetic mean for a group of corresponding measurements performed for each fuel rod.

The initial gas pressure was determined by averaging the results of manometer pressure measurements conducted in the chamber where the fuel rods were filled with helium and sealed. The composition of the gas in the fuel rod was determined under the same conditions using the mass-spectrometric method.

Consolidated characteristics for C-type fuel rods

Procedures to determine characteristics, which either do not depend on r, z coordinates in the fuel rod or are average values, are presented here.

Axial coordinates of the top and the bottom of the fuel stack of each fuel rod, as well as coordinates of undamaged sections of the fuel stack (i.e. which were not fragmented in the process of the fuel rod refabrication) were determined within the framework of a specially developed calculation procedure used to analyze and process the results of the axial γ-scanning of fuel rods and X-ray photographs of fuel rods.

The average burnup in each fuel rod was obtained by the mathematical processing of measurement results of the burnup axial distribution at the section of the commercial fuel element used for refabrication of this fuel rod.

The procedure to determine the total free gas volume is described in section 3.2.6.

The geometric dimensions L_1, L_2, L_3, L_4 were determined by processing the results of γ-scanning of each fuel rod and X-ray photographs of the fuel rod; the outer diameter of the fuel rod cladding was determined as an average value based on fuel rod profilometry results.

Individual measured r, z distributions of C-type fuel rod characteristics

Z distribution of the cladding outer diameter of each fuel rod was obtained by the profilometry in two azimuth positions using the converter of magnet scale type. The scanning step was 2 mm, the measurement error was ±0.01 mm. The radiation intensity of isotopes Cs^{134}, Cs^{137}, Ru^{106} along the fuel rod length was measured by the gamma spectrometric method using Ge (Li) detector. The width of the spectrometer collimator was 5 mm, the scanning step was 5 mm (in three cases – 10 mm). Fuel rod cladding quality was checked using the standard eddy current method at two different frequencies. The burnup axial distribution was determined by tying the file of burnup measured distributions in fuel elements to axial coordinates of the fuel stack in each C-type fuel rod.

Calculation procedures to determine r, z distribution of fissile isotopes in the fuel rod, r distribution of the burnup, z distribution of the fuel mass and z distribution of the gas free volume are described in sections 3.2.2, 3.2.3, 3.2.6.

3.2.2. Axial distribution of the fuel mass in high burnup fuel rods

The determination of the fuel mass distribution in C-type fuel rods was a rather complex methodological problem. This was related to the fact that direct measurements of the mass of each fuel pellet were not performed because it was impossible to remove the fuel from fuel rods without the risk of damaging it. An additional complicating factor was the consequences of the fuel rod refabrication procedure. These were the

consequences of the process of the fuel removal from the upper and lower parts of the commercial fuel element which resulted in a destruction of a part of fuel pellets used to form the fuel stack of the refabricated fuel rod. That is why it was impossible to assess the fuel stack mass in refabricated fuel rods on the basis of data on the mass of a corresponding section of the commercial fuel element. Thus, a special procedure was developed to determine the fuel mass in refabricated fuel rods.

Main provisions of the procedure

Results of spectrometric measurements of Cs^{137}, Cs^{134} and Ru^{106} activity in the fuel were used as basic measurements to determine the mass axial distribution in refabricated C-type fuel rods.

The count rate of the spectrometer during the γ-scanning of the axial section of the irradiated fuel rod was determined using the following expression:

$$S = \varepsilon \cdot \eta \; \lambda \; k_s \; n \; m,$$

where S= the count rate in the photopeak while recording gamma quanta of a certain energy (1/s);

ε = the photo-efficiency of recording gamma quanta of a certain energy with the spectrometer (per-unit);

η = the quantum yield of gamma quanta (per-unit);

λ = the decay constant of a given isotope (1/s);

k_s = the coefficient of self absorption of gamma quanta of a certain energy in the fuel pellet (per-unit);

n = the average concentration of a given isotope in the fuel (1/g);

m = the fuel mass in this axial section (g).

The above expression can be written in another form:

$$S = C \; k_s \; n \; m,$$

where C= the coefficient which does not depend on the fuel mass in the section and on fuel irradiation conditions (1/s).

Thus, the fuel mass in a given axial section can be determined if S, C, κ_s, n values are known. However, only S value is the result of spectrometric measurements in this section of the fuel. To determine other parameters, it is possible to use the data base describing characteristics the commercial fuel element from which this fuel rod was refabricated.

The following expressions for spectrometer count rates can be written for two axial sections of the commercial fuel element:

$$S_{fe,i} = C \; k_{s,fe,i} \; n_{fe,i} \; m_{fe,i},$$

$$S_{fe,o} = C \; k_{s,fe,o} \; n_{fe,o} \; m_{fe,o},$$

where fe = the index for the fuel element;

i, o = indexes of axial sections of the fuel element.

According to corresponding measurements, the fuel density of commercial fuel elements after irradiation at power unit No 5 of NV NPP is not changed along the height of the fuel element (with the exception of upper and lower parts of the fuel element). Thus, $m_{fe,i} = m_{fe,o}$ expression will be valid for any axial section of the commercial fuel element. In this case the following expression will also be valid:

$$\frac{n_{fe,i}}{n_{fe,o}} = \frac{S_{fe,i}}{S_{fe,o}},$$

Let us further assume that these are the ith and the oth sections of the commercial fuel element that were subjected to the procedure of the gamma scanning for the second time, but within the composition of the refabricated fuel rod. In this case the following expressions are valid:

$$S_{fr,i} = C \; k_{s,fr,i} \; n_{fr,i} \; m_{fr,i},$$

$$S_{fr,o} = C \; k_{s,fr,o} \; n_{fr,o} \; m_{fr,o},$$

3.4

while:

$$\frac{S_{fr,i}}{S_{fr,o}} = \frac{S_{fe,i}k_{s,fr,i}m_{fr,i}}{S_{fe,o}k_{s,fr,o}m_{fr,o}} ,$$

where fr = the index of the fuel rod.

If the selection of the refabricated fuel rod section with the index "o" was made in accordance with the condition that $m_{fe,o} = m_{fe,i}$, the following formula can be obtained to determine the fuel mass in the ith section of the refabricated fuel rod:

$$m_{fr,i} = m_{fe,o} \frac{S_{fe,o}S_{fr,i}k_{s,fe,o}}{S_{fe,i}S_{fr,o}k_{s,fr,i}} .$$

In this formula all spectrometer count rates are the results of direct measurements. The fuel mass in the commercial fuel element ($m_{fe,o}$) is determined by the following expression:

$$m_{fe,o} = \frac{M\Delta L}{L} ,$$

where M = the total fuel mass in the fuel element (g);

L = the effective fuel stack length of the fuel element, i.e. without gas gaps (cm);

ΔL = is the gamma scanning section length (cm).

Corresponding values $m_{fe,o}$ were determined for fuel elements #22 and #317 on the basis of measured values of M and L.

The last stage of this procedure is to determine coefficients of gamma quanta self absorption of Cs^{137}, Cs^{134} and Ru^{106} in the fuel of the refabricated fuel rod for the ith section of the gamma scanning. Coefficients of self absorption for commercial fuel elements were calculated according to standard procedures.

The fuel of the ith section of the refabricated fuel rod can be in two states:

- undamaged, i.e. in conditions similar to fuel conditions in the commercial fuel element (in this case $k_{s,fr,i} = k_{s,fe,o}$);

- damaged, i.e. fragmented.

Coefficient k_s for the damaged section of refabricated fuel rod was calculated for two extreme variants in which the fuel can theoretically exist:

- fuel is homogeneously distributed in the entire section volume;

- fuel with the density of the commercial fuel rod occupies a local cylindrical volume.

The mass of the refabricated fuel rod was calculated for each of the two variants. Taking into account that $k_s = f(m)$, the calculations were performed by the iteration method. The average mass value obtained on the basis of two calculation variants was taken as the final mass value in the ith section.

The above procedure was used to calculate the mass in refabricated fuel rods of C type using individual sets of spectrometric measurement results for isotopes Cs^{137}, Cs^{134}, Ru^{106}. The average weighted value of three measurements was used as the final mass value.

Verification of the procedure

A special test was conducted in RIAR (Dimitrovgrad, Russia) to verify the procedure of determining the fuel mass in C-type fuel rods. The schematics of the test can be described as follows:

1. A sample of commercial fuel element 70 mm long was cut from commercial fuel element #295 removed from fuel assembly No 1114, irradiated at power unit No 5 of NV NPP.

2. The fuel burnup in the sample was determined (48.1 MWd/kg U).

3. X-ray photographs of the sample were taken; according to them, the cut-out sample had the undamaged fuel stack.

3.5

4. γ-scanning of the cut-out sample for Cs^{134}, Cs^{137}, Zr^{95} was performed with 1 mm step (collimator width of 1 mm), with 5 mm step (collimator width of 5 mm), with 10 mm step (collimator width of 10 mm),

5. Then the fuel was removed from the cladding and weighed. A careful monitoring was provided to ensure the complete removal of the fuel from the cladding. The fuel weight in the sample was $29.2^{\pm 0.005}$ g.

6. The removed fragmented fuel was placed in the unirradiated cladding of VVER-1000 type. The fuel stack length in this cladding was 120 mm (according to the data of X-ray radiography).

7. γ-scanning of the unirradiated cladding with irradiated fuel was performed in the same modes as in item 4.

Results of this test were used to verify the indirect procedure of mass determination in fuel rods of C-, D-, E-types. All parameters used in the verification are presented in Table 3.1.

Table 3.1. Verification results for procedure to determine
fuel mass in high burnup fuel rods

Parameter	Measured	Calculated
Value of mass (g)	29.2	28.55
Total error (%)	0.02	2.4
Relative discrepancy (%)	2.2	

Procedure error assessment

The error analysis of this procedures was carried out in a number of areas:

- assessment of spectrometric measurement errors;
- assessment of the error in determining the fuel mass in the ith section of the commercial fuel element;
- assessment of the error in determining the self-absorption coefficient for damaged and undamaged sections of the refabricated fuel rod;
- assessment of the error in determining the axial coordinates of ith sections in the commercial fuel element and in the refabricated fuel rod.

Results of error calculations of the fuel mass in each C-type fuel rod are presented in Table 3.2.

Table 3.2. Errors in determining the total fuel mass in C-type fuel rods

Number of fuel rod	Mass (g)		Relative error of mass (%)	
	in fuel rod	in undamaged section	standard deviation	systematic error
H1T	60.4	53.4	0.43	0.75
H2T	61.2	61.2	0.44	0.87
H3T	60.6	51.1	0.43	1.05
H4T	59.8	56.7	0.43	0.84
H5T	57.0	39.5	0.43	0.89
H6T	49.2	16.6	0.42	1.90
H7T	56.8	42.6	0.43	1.25
H8T	56.2	30.7	0.42	1.20
B9T	58.9	56.1	0.44	0.87
B10T	55.9	43.5	0.45	0.95
B11T	57.7	38.5	0.43	1.24
B12T	47.9	10.2	0.42	2.07
B13T	59.7	56.2	0.43	0.81

3.2.3. Isotopic composition of the high burnup fuel rods

Purpose of the procedure

The purpose of the procedure was the calculation determination of the axial and radial distribution of main isotopes in C-type fuel rods.

Input data

The following characteristics were selected as the input data:

- isotopic composition of the fuel of commercial fuel elements before the irradiation at NovoVoronezh Nuclear Power Plant (NV NPP);

- geometry and material composition of fuel elements and fuel assemblies, scheme of the fuel element arrangement in the fuel assembly;

- NV NPP operational characteristics;

- load schedule of fuel elements ##317, 22 in the fuel assembly;

- thermo-hydraulic parameters of fuel cycles;

- schedule of boron control in the primary circuit;

- cooling time of fuel elements #317 and #22 after the end of operating cycles.

Selection and validation of computer codes and description of the numeric method

The selection of the computer code to determine the spatial distribution of the isotopic composition in refabricated C-type fuel rods manufactured from irradiated commercial fuel elements was made taking into account the following requirements on the simulation of these processes:

- consideration of the non-uniformity of nuclide formation and burnup along the radius of fuel pellets of the commercial fuel element during operating cycles (consideration of the rim-zone formation);

- consideration of the scenario of the boron control during operating cycles of power unit No 5 of NV NPP;

- consideration of real conditions of the fuel irradiation to adjust the neutron spectrum hardness as a function of time and z-coordinate;

- possibility of ensuring consistent information transfer procedures in the system of interconnected calculations, using different codes, of neutronics characteristics of C-type fuel rods.

Taking into account the above requirements, TRIFOB code was selected to calculate the spatial r,z distribution of the burnup and isotopic composition versus time for commercial fuel elements of NV NPP-5 [4].

TRIFOB code provides a flexible scheme of isotopic transitions and allows to change it depending on the conditions of the problem. The data base of the code can be expanded to cover the data base on nuclides which are included into the transition scheme in addition to the main nuclides.

Isotopic composition calculations with TRIFOB code were carried out using the calculation cell of VVER-1000 reactor, which represented the fuel pellet with the central hole, surrounded with the zirconium cladding and the coolant layer. The spatial and energy calculations of this reactor cell were performed with TRIFON code by solving the multi-group integral transport equation using the collision probability method [5].

TRIFON code allows to take into account the detailed resonance structure of neutron cross-sections. Neutron thermalization models are used for the thermal energy region. The isotropic return of neutrons at the cell boundary is used as the boundary condition. TRIFON code was used to calculate process rates, which were subsequently used as the input data for TRIFOB code to simulate the kinetics of nuclide burnup and accumulation.

The calculations were conducted for discrete time intervals into which the fuel cycle was divided. Process rate calculations taking into account discrete changes in the cell nuclide composition were performed for each of time intervals.

TRIFOB code used the standard scheme of nuclide transformations. This scheme includes 16 heavy nuclides from U^{234} through Cm^{244} and 8 main fission products (Xe^{135}, Rh^{105}, Sm^{149}, Sm^{151}, Pm^{149}, Pm^{151}, Cd^{113}, Gd^{157}). Other fission products are presented in the form of four effective fission fragments for U^{235}, U^{238}, Pu^{239} and Pu^{241}. Each fragment is presented together with its precursor according to the known procedure [6].

TRIFOB code was improved to solve a specific problem. The improved version of TRIFOB code was expanded to include the module that adjusts the neutron spectrum in the cell of VVER-1000 reactor during the fuel cycle. The adjustment was made using parameter γ, which takes into account the degree of the neutron spectrum hardness. In the general form, the rates of neutronics processes taking into account parameter γ are presented as follows:

$$S = S_{th} + \gamma \, S_f ,$$

where S = the identifier of a corresponding process rate (per-unit);

S_{th}, S_f = identifiers of rate components for the thermal and fast energy regions, respectively (per-unit);

γ = the spectrum hardness parameter (per-unit).

Parameter γ is determined as a function of time of the fuel cycle in the following form:

$$\gamma(t) = \frac{\gamma_0 \, vF_{th}(t)}{vF_0 - \gamma_0 vF_f(t)} ,$$

where γ_0 = the initial value of the spectrum hardness parameter (per-unit);

vF_0 = the initial rate of neutron generation (per-unit);

$vF_{th}(t)$, $vF_f(t)$ = rates of neutron generation versus time for the thermal and fast energy regions, respectively (per-unit).

The spectrum hardness parameter is a global characteristic of the fuel cycle. Its value were determined on the basis of the analysis of isotopic composition measurement results of fuel elements ## 61, 257, 317 of the fuel assembly #1114 of NV NPP-5.

Special verification procedures for TRIFOB code

TRIFOB code was carefully verified using results of mass-spectrometric measurements of the isotopic composition in the fuel of VVER-type reactors [7]. Within the framework of this work, special verification procedures were implemented, which included three stages:

1. TRIFON code verification using Monte Carlo code;

2. TRIFOB code verification using Monte Carlo code;

3. TRIFOB code verification using experimental data obtained as a result of measurements of neutronics characteristics of commercial fuel elements irradiated in NV NPP.

1. TRIFON code verification was conducted on the basis of results of benchmark calculations of LWR- and VVER-type reactor cells using MCU code (see section 4.7) and MCNP code [8]. Both codes are of Monte Carlo type. According to results of comparative calculations, the error in calculating the multiplication factor K_{eff} and neutronic process rates does not exceed 0.5 and 5%, respectively, i.e. the error in calculating K_{eff} using TRIFON code is comparable with the error of Monte Carlo code calculations.

2. An additional verification of TRIFOB code using a code of Monte Carlo type was performed for conditions of this problem. The burnup and nuclide composition were calculated for the standard cell of VVER-1000 as a function of time [9]. Calculations were carried out without taking into account the boron poisoning and without spectrum hardness control. In the calculation scheme, the fuel pellet with the initial enrichment of 4.4% was divided into several layers; 0.1 mm rim layer was separated. Results of comparative calculations are presented in Fig. 3.2 and Fig. 3.3. According to the results of the analysis, the maximum difference in concentrations of the main nuclides, obtained using two computer codes, does not exceed 5% for the burnup range up to 50 MWd/kg U. Radial distributions of main nuclide concentrations for fuel with the burnup of 50 MWd/kg U, obtained using two computer codes, are in good agreement with the exception of Pu^{241} and Pu^{242} isotopes. The maximum difference in concentration values for these isotopes was in the rim layer (about 10%).
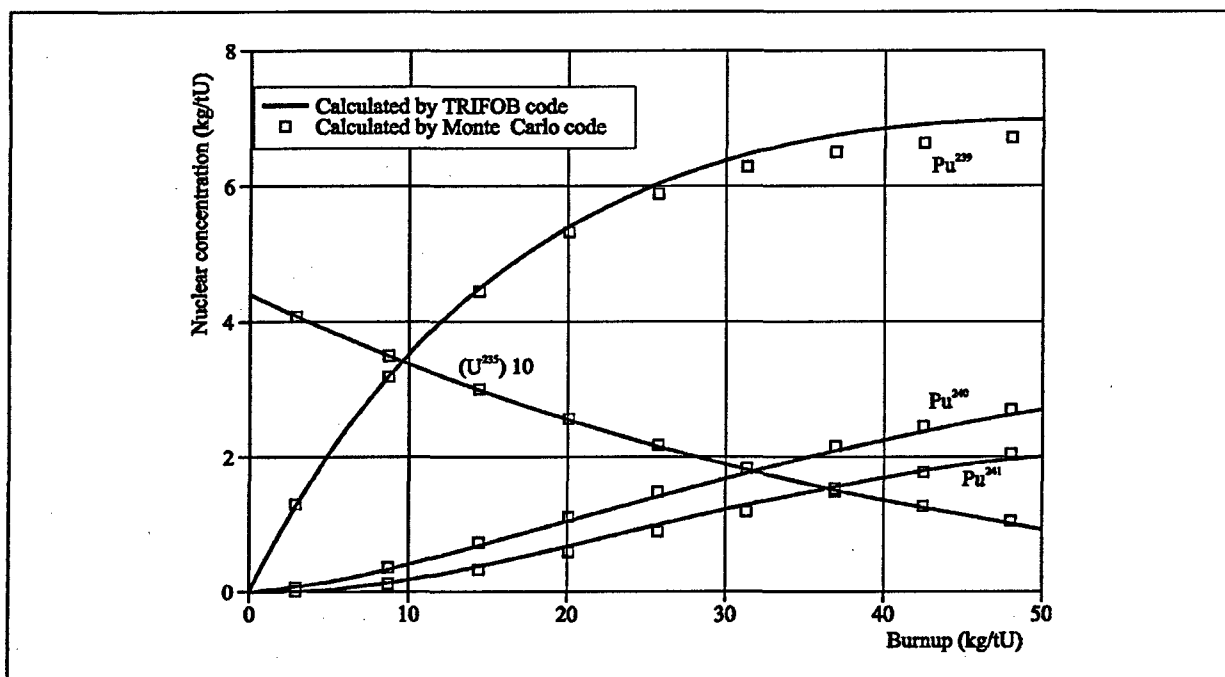
Fig. 3.2. TRIFOB verification versus burnup using Monte Carlo code

3. TRIFOB code verification on the basis of the original data was carried out in accordance with the requirements of the present work. The verification was performed using results of mass-spectrometric measurements of the nuclide composition of fuel samples taken from the middle part of fuel columns of commercial fuel elements ## 61, 257, 317, irradiated in the fuel assembly of NV NPP-5. At the first stage of the verification procedure, calculations of the standard VVER-1000 cell were performed with TRIFOB code for fuel elements #61 and #257 taking into account the boron poisoning during 3 fuel cycles. According to the analysis of the results, TRIFOB code calculations agree with experimental results within 3-5% (the statistical experimental error 3σ is 5%). Verification results for U^{235}, Pu^{239}, Pu^{240} and Pu^{241} are presented in Fig. 3.4. At the second stage of the verification procedure, cell calculations of fuel element #317 were conducted. The cell of this fuel element has another effective radius and another enrichment. In this case the agreement between the calculated and experimental data was within 5% for the main nuclides with the exception of Pu^{240}, for which the difference is 7%. Results of this verification procedure are presented in Table 3.3 and Fig. 3.4. The verification of calculated values of the radial distribution of the nuclide composition of fuel element #317, obtained using TRIFOB code, was performed on the basis of corresponding experimental data. The procedure to obtain experimental data is described in sections 3.1, 3.2. Verification results are presented in Fig. 3.5.

Table 3.3. Calculated and measured isotopic concentrations and burnups for fuel element #317

Method	Burnup (kg/t U)	Isotopic concentration (kg/t U)							
		U^{235}	U^{236}	U^{238}	Pu^{238}	Pu^{239}	Pu^{240}	Pu^{241}	Pu^{242}
Experiment	52.4(11)*	4.35(3)	4.92(3)	928(1)	0.31(2)	5.00(5)	2.62(3)	1.64(2)	1.12(1)
Calculated by TRIFOB	52.4	4.52	4.97	926	0.29	5.22	2.80	1.57	1.10

* Here and below the statistical error of the experiment is indicated in brackets (error of determining the last digit).
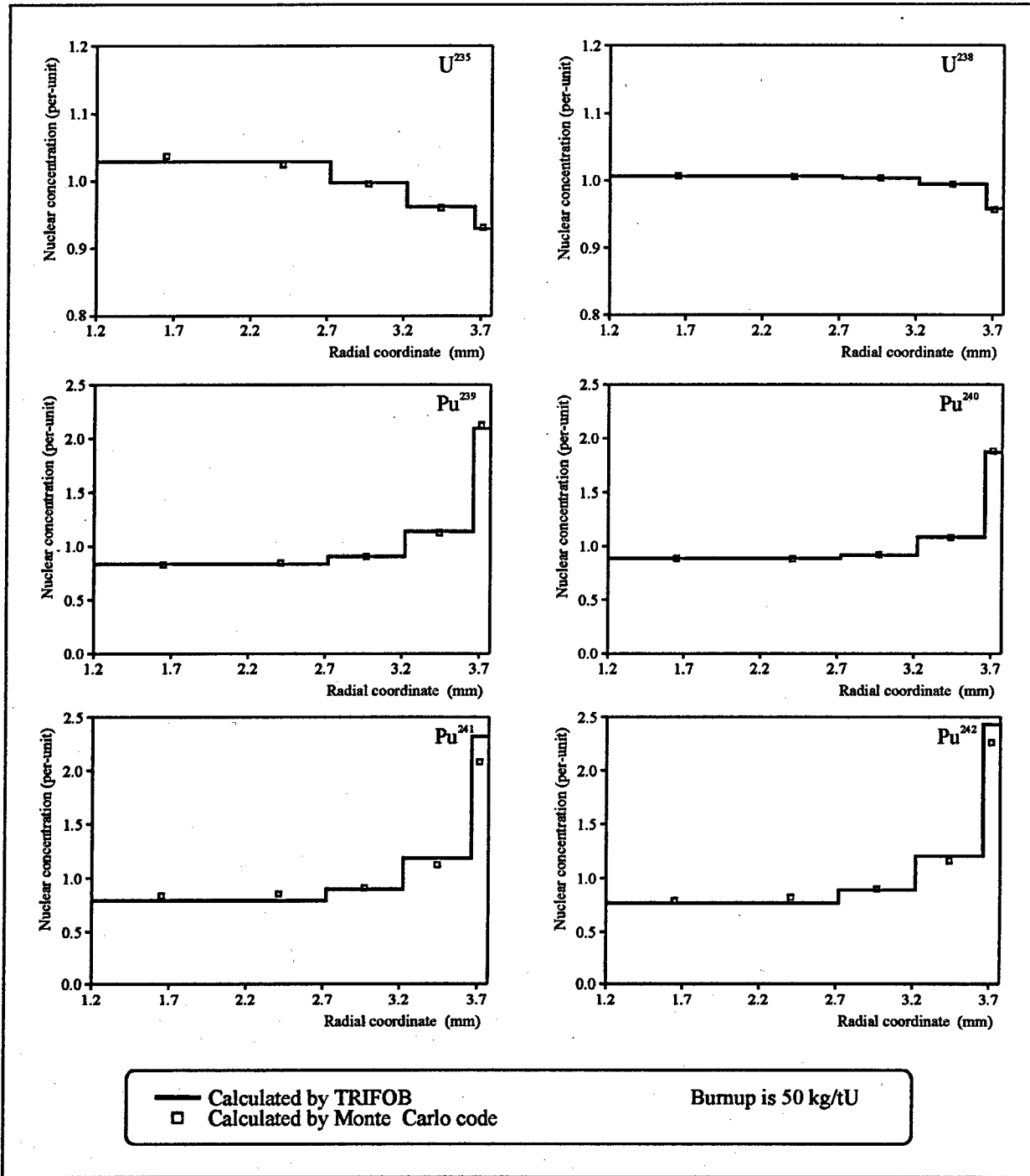
Fig. 3.3. TRIFOB verification vs. radial isotope distribution using Monte Carlo code
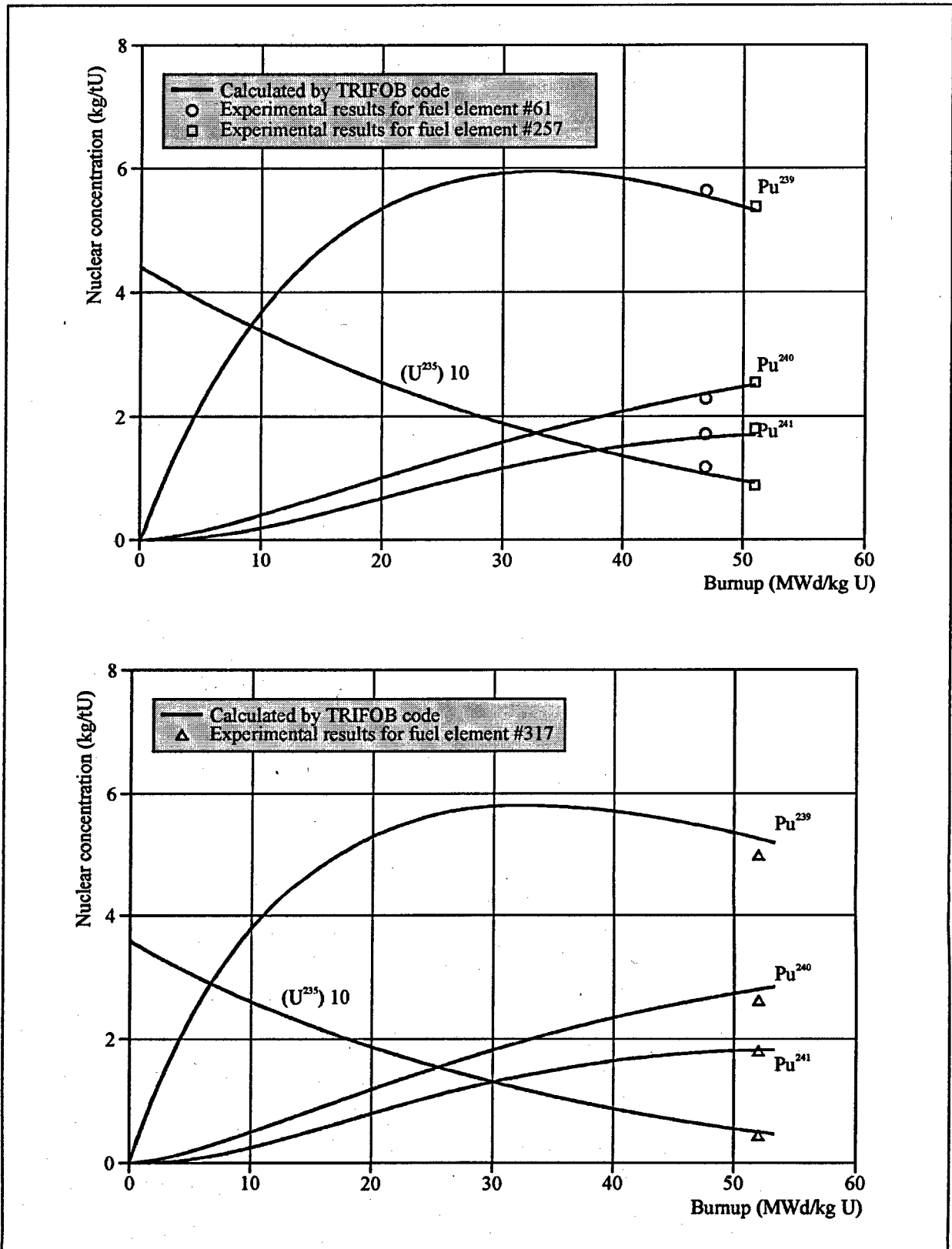
Fig. 3.4. Special TRIFOB verification vs. burnup using NV NPP fuel elements
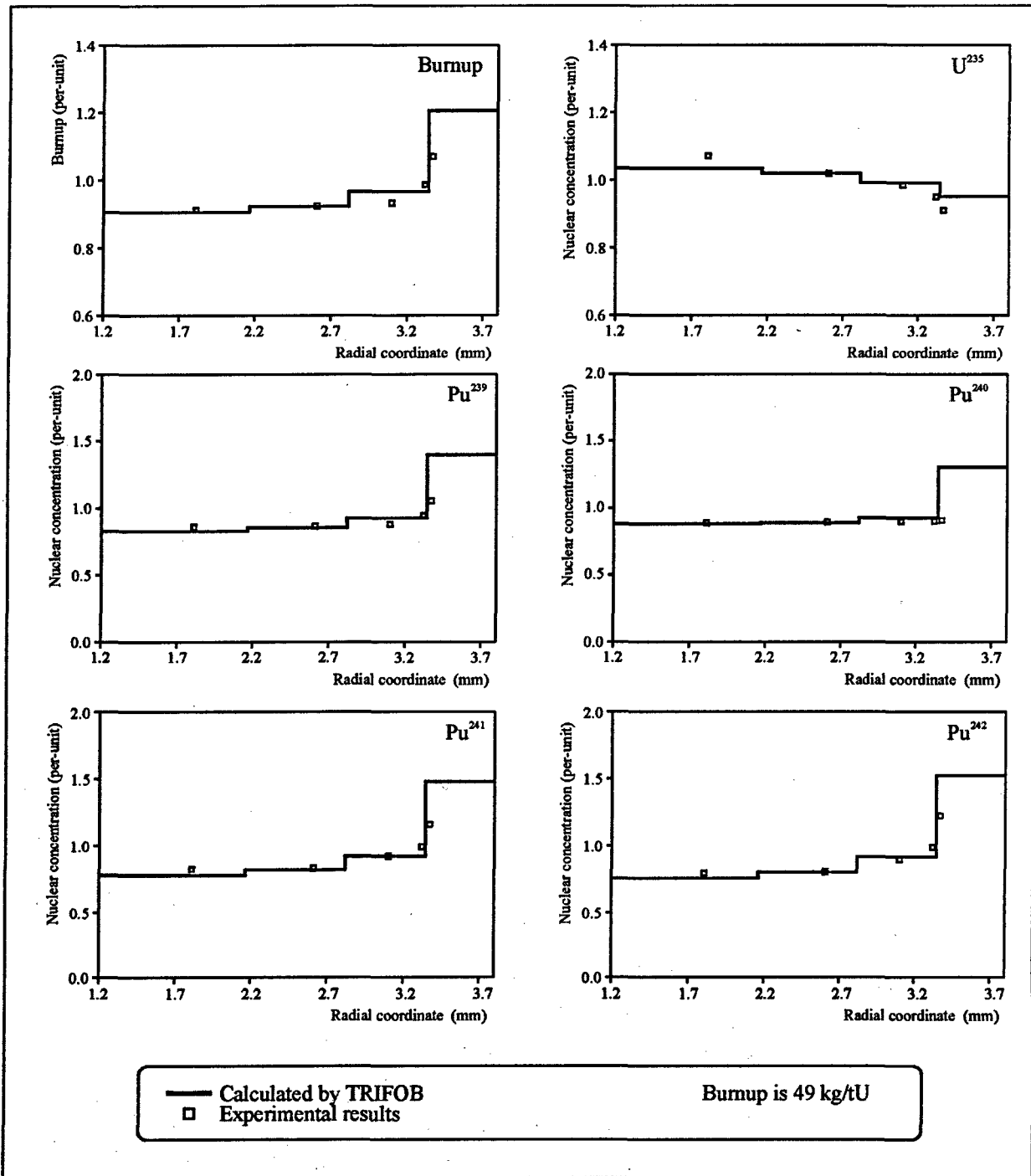
Fig. 3.5. Special TRIFOB verification vs. radial isotope distribution using NV NPP fuel element #317

<u>Calculation scheme for C-type fuel rods and results</u>

Calculations of the nuclide composition of C-type fuel rods were carried out taking into account the coordinates of cutting these fuel rods from commercial fuel elements #22 and #317. The calculation procedure took into account the dependence of the coolant density in the commercial reactor on the axial coordinate. This was done with the aim of preventing an additional error in burnup calculations, which can exceed 5% for U^{235} and Pu^{239} if this effect is ignored (there are 10% changes in the coolant density along the reactor core height for this fuel cycle). This effect was taken into account by introducing the following approximating dependence for the coolant temperature:

$$T(z) = T_{in} + 1.47\ z + 7.04\ z^2 - 1.38\ z^3,$$

where $T(z) =$ the coolant temperature as a function of the axial coordinate z (K);

$T_{in} =$ the coolant temperature at the reactor core inlet (K);

$z =$ the axial coordinate (m).

In the final form, the procedure of variant calculations of 13 refabricated C-type fuel rods included:

• calculations of r,z distribution of the isotopic composition in each fuel rod with the step of 5 mm along the coordinate z for four radial zones which corresponded to the following set of fuel volume ratios 0.5, 0.3, 0.15, 0.05 (volume ratio of 0.05 corresponds to 0.086 mm thick rim layer).

• adjustment of the calculated set of r, z distribution of the isotopic composition taking into account experimental data in Table 3.3 within the limits of 3–5 %.

Results of variant calculations of the isotopic composition of C-type fuel rods using TRIFOB code are presented in Appendix C, Volume 3 of the Report.

3.2.4. Fuel rods with fresh fuel and irradiated cladding

<u>Representative values of initial characteristics for D-type fuel rods</u>

Fuel characteristics presented in this group were determined by the manufacturing plant in accordance with standard procedures for VVER-1000 fuel [10]. All cladding characteristics of D-type fuel rods correspond to cladding characteristics of C-type fuel rods and were obtained within the framework of the same procedures. This is also true for the initial gas pressure, its composition and volume.

<u>Consolidated characteristics for D-type fuel rods</u>

All parameters characterizing the refabrication process of D-type fuel rod cladding were obtained according to procedures similar to those for C-type fuel rods.

All fuel parameters were determined by the manufacturing plant in accordance with standard procedures for VVER-1000 fuel [10].

Individual geometric dimensions L_1, L_2, L_3 were determined by the mathematical processing of results of fuel rod X-ray photographs.

<u>Individual r,z distributions of D-type fuel rod characteristics</u>

The manufacturing plant presented a set of individual characteristics of fuel pellets, that were obtained within the framework of standard VVER-1000 procedures [10].

This set includes the following measurements:

• outer diameter of each fuel pellet, measured in two azimuth planes;

• fuel mass in each pellet.

Using a specially developed mathematical procedure, this set was converted to data files for z distributions of corresponding characteristics.

z distributions of the cladding outer diameter were obtained as a result of the mathematical processing of profilometry results, which was carried out using the same method as for C-type fuel rods.

3.13

z distributions of the free volume in fuel rods were obtained according to the procedure described in section 3.2.6.

3.2.5. Fresh fuel rods

All input data on characteristics of E-type fuel rods were provided by the fuel rod manufacturing plant [10]. The input data include the following measured parameters:

- fuel and cladding composition;
- fuel enrichment;
- gas composition and pressure inside the cladding;
- fuel stack length in each fuel rod;
- cladding outer diameter in two azimuth planes as a function of fuel rod length;
- cladding wall thickness as a function of fuel rod length;
- average fuel-cladding gap for each fuel rod;
- outer diameter of each fuel pellet measured in two azimuth planes;
- mass of each fuel pellet;
- fuel mass in the fuel rod;
- characteristics of the thermal treatment of fuel rod cladding.

The following parameters were obtained on the basis of the input data using corresponding mathematical procedures:

- representative values of characteristics for the fuel rod set;
- consolidated characteristics for each fuel rod;
- individual distributions of characteristics for each fuel rod.

3.2.6. Axial distribution of the gas volume in fuel rods

Individual measurements of the total free gas volume were not conducted for each fuel rod of C-, D-, E-types. The total free gas volume was measured selectively; these measurements were used for the verification of the indirect procedure to determine the axial distribution of the free gas volume for each fuel rod. This procedure included the following main stages:

1. Determination of the axial distribution of the free gas volume inside the fuel rod without taking into account the volume occupied by the fuel and the fixing ring. Fuel rod drawings and X-ray photographs of each fuel rod were used for this purpose.

2. Determination of the axial distribution of the volume occupied by the fuel and the fixing ring. The axial distribution of the fuel mass was used in this case.

3. Determination of the axial distribution of the free gas volume taking into account the fuel and the fixing ring was carried out by subtracting the data set under item 2 from the data set under item 1.

4. The total free gas volume was determined by summing up the data under item 3 for each fuel rod.

According to the verification of the procedure using results of direct measurements of the total free gas volume, the Relative standard deviation for calculated characteristics of the volume does not exceed 2%.

3.3. Procedure to manufacture the fuel rods

C-type fuel rods

A batch of C-type fuel rods was manufactured in RIAR (Dimitrovgrad, Russia) by refabricating commercial fuel elements of VVER -1000 type, that were irradiated at power unit No 5 of NV NPP. The refabrication procedure included the following stages:

1. Manufacturing fuel rod blanks by cutting commercial fuel elements into samples of a required length and with fixed axial cutting coordinates.

2. Fuel removal from the upper and lower parts of each blank by drilling.

3. Manufacturing structural components of the fuel rod, top and bottom caps, the fixing ring, the connector, the cladding (for the upper plenum).

4. Installation of the fixing ring in the blank, welding of the bottom cap and the connector with the fuel rod blank.

5. Welding of the top cap with the unirradiated cladding.

6. Welding of the upper and lower parts of the fuel rod.

7. Filling the fuel rod with helium through the hole in the top cap under the conditions of a special chamber filled with helium at the initial helium pressure in the fuel rod.

8. Gas evacuation from the fuel rod and repeated filling with helium under the same conditions.

9. Welding the hole in the top cap.

10. Fuel rod tightness testing using helium leak detector.

D-type fuel rods

Refabricated D-type fuel rods were manufactured in RIAR (Dimitrovgrad, Russia), unirradiated fuel pellets were manufactured in AO MZ "Electrostal" (Electrostal, Russia).

The manufacturing procedure of D-type fuel rods was similar to that of C-type fuel rods. However, in this case all fuel of the commercial fuel element was removed from the fuel rod blank and was replaced with unirradiated fuel pellets of VVER-1000 type. Fuel pellets for D-type fuel rods were manufactured in accordance with the technology, the main provisions of which correspond to the standard technology of fuel manufacturing for VVER-1000 reactors.

E-type fuel rods

Unirradiated E-type fuel rods were manufactured in AO MZ "Electrostal" (Electrostal, Russia).

Standard blanks for fuel elements of commercial VVER-1000 reactors were used for the manufacturing. The fuel for E-type fuel rods was manufactured in accordance with the technology similar to that of fuel manufacturing for D-type fuel rods.

Standard procedures used for manufacturing commercial fuel elements were applied for the thermal treatment of fuel rod cladding and the monitoring of the fabrication quality.

3.4. Post test examinations of fuel rods

The following set of non-destructive and destructive post-test examinations was implemented for fuel rods of C-, D-, E- types in RIAR (Dimitrovgrad, Russia):

1. Taking photographs of the fuel rod appearance.

2. Taking X-ray photographs of each fuel rod that preserved its structural integrity.

3. Outer diameter measurements of all fuel rods that preserved their structural integrity and had minor cladding deformation.

4. Preparation of cross-sectional metallographic specimens for each fuel rod.

5. Taking macro- and micro-photographs of metallographic specimens.

3.15

6. Measurements of the oxide film thickness and the thickness of α-Zr on the fuel rod cladding.

7. Measurements of the H_2 concentration in the cladding and hydride orientation.

8. Measurements of Kr, Xe concentrations in the gas of fuel rods after the test.

9. Measurements of the Kr concentration in the high burnup fuel after the test.

Results of these studies are presented in Appendixes G, H, I, Volume 3 of the Report.

3.5. References

[1] "Post-Irradiation Examinations of Fuel Assembly No. 4436001114, which was Used at Unit 5 of NV NPP within 3 Fuel Cycles up to Average Burnup of 44.7 MW days/kg U", Rus., Report No. O-4011, Research Institute of Atomic Reactors, Dimitrovgrad, 1991.

[2] A.Scheglov, V.Proselkov, A.Yenin. "Statistic Processing Results of Structural and Technological Parameters of VVER-1000 Reactor Fuel Element", Rus., IAE "Kurchatov Institute", Report No. 5334/4, Moscow, 1991.

[3] A.Chetverickov, V.Borisenkov, V.Chistiackov et.al "Identification of Nuclide Composition and Burnup Degree of Spent Fuel of VVER-1000 Reactor", Rus., Report No. 21240014, Research Institute of Atomic Reactors, 1991.

[4] M.Vostrikov, B.Kochurov. "TRIFOB - the Code for Calculation of Isotopic Composition in a Cylindrical Reactor Cell Taking into Account Neutron Spatial-Energy Distribution", Rus., Report ITEP-106, Moscow, 1981.

[5] A.Burmistrov, B.Kochurov, A.Kvaratshely. "The Code TRIFON Abstract", Rus., VANT, Ser. Nuclear Reactor Physics and Engineering, Vol.4, p.35, 1985.

[6] A.Galanin. "Introduction to the Theory of Thermal Neutron Nuclear Reactor", Rus., Moscow, Energoatomizdat, 1990.

[7] A.Gerasimov, T.Zaritskaya, A.Rudik. "Handbook on Build-up of Nuclides in Nuclear Reactors", Rus., Moscow, Energoatomizdat, 1989.

[8] J.Briesmeister, "MCNP - a General Monte Carlo Code for Neutron and Photon Transport", LA-7396-M-Rev.2, 1987.

[9] A.Avvakumov. "Method for Calculation of Isotopic Composition of High Burnt-out VVER Fuel Taking into Account Radial Heterogeneous Burnup and Buildup of Nuclides", Rus., Report No. 90/1-16-95, Nuclear Safety Institute of Russian Research Centre "Kurchatov Institute", 1995.

[10] "VVER-1000 Experimental Fuel Rods", Rus., Passport No. AB.01.021.000PS, AO MZ "Electrostal", 1990.

4. ENERGY DEPOSITION, POWER OF FUEL RODS AND FUEL ENTHALPY UNDER IGR REACTOR TEST CONDITIONS

The main purpose of this procedure is to determine the two-dimensional energy deposition and power field (r, z geometry) of fuel rods as a function of time. It is impossible to directly measure these parameters in the reactor test process. Therefore, special procedures are developed to implement this type of experimental programs, which combine a set of calculation and experimental methods and take into account specific features of the research reactor and the test objects.

In this case the following was used as the basic experimentally determined parameters:

- number of fissions in a fixed section of the fuel column (the section length is about 13 mm) of E-type fuel rods (fresh fuel, fresh cladding) over the entire test;

- number of fissions in special fuel samples located in a fixed point inside the capsule.

In a schematic form, the procedure of determining the energy deposition and power of fuel rods included the following stages:

- determination of the reactor power profile versus time using the results of the reactor power measurements by the ionization chamber and the results of adjusting the measured power profile near the zero values;

- measurements of the number of fissions in fixed sections of the fuel of E-type fuel rods (fresh fuel, fresh cladding);

- measurements of the number of fissions in special fuel samples;

- implementation of calculation neutronics codes to perform calculations of the system "IGR reactor - capsule - fuel rods - special fuel samples";

- code verification using special reactor experiment;

- performance of the neutronics calculations of the system "reactor - capsule - fuel rods - special fuel samples" to determine the ratio between the number of fissions in special fuel samples and fission reaction fields for each fissile isotope in tested fuel rods;

- determination of isotope fission rates in rod fuel in r, z geometry as a function of time;

- determination of fuel rod energy deposition and power fields using thermal equivalents of one fission event of various isotopes taking into account specific features which depend on the contribution of prompt and delayed radiation components in fuel rods and in the reactor.

4.1. Main provisions of the procedure

Fuel rod power profile versus time

Readings of standard ionization chambers of IGR reactor were used as the input data (see section 4.2), which were adjusted to take into account the contribution of delayed neutrons using the calculation procedure (see section 4.6).

Numbers of fissions in central (along the column length) fuel pellets of E-type fuel rods and in special fuel samples

Results of radiometric measurements of number of fissions in central fuel pellets of non-failed fuel rods of E-type, results of radiometric measurements of number of fissions in special fuel samples and measurement results of the energy deposition in the reactor in units of ionization chamber readings were used as the input data.

The standard mathematical procedure is applied to determine the regression coefficients that characterize ratios between the above parameters for two types of the coolant in the capsule. The obtained coefficients are used to determine the numbers of fissions in central fuel pellets of E-type fuel rods and in special fuel samples (see sections 4.3, 4.4).

4.1

Determination of neutronics parameters of fuel rods of C-, D-, E- types

It will be demonstrated in section 4.7 that the spatial-time distribution of fission rate R (r, z, t) in test fuel rods can be obtained based on the spatial distribution of the number of fissions in the fuel rod n (r, z) determined by solving the stationary problem.

The purpose of this procedural stage was to determine n (r, z) for each of the tested fuel rods. The set of n (r, z) values is determined based on the stationary calculations of the reactor at a fixed temperature of the reactor core, the coolant and fuel rods (see section 4.7).

This approach to determine R (r, z, t) was selected because of the complexity of the geometric and material structure of the capsule with fuel rods and the necessity of obtaining R (r, z, t) values with the accuracy not less than that of experimental methods of measuring the number of fissions in fuel pellets of rods of C-, D-, E- types. Due to these circumstances it was necessary to use accurate neutronics models, such as Monte Carlo type, to calculate the distribution of the number of fissions in fuel rods. However, the full-scale simulation of the "reactor–capsule–fuel rod" using precision codes is beyond the scope of the present work. Thus, the problem of optimizing the calculation simulation was initially solved, and the capabilities of using the above approach were demonstrated (see section 4.7).

Energy deposition and power fields of C, D, E - type fuel rods

The first stage of this procedure covered the adjustment of sets of fission density in fuel rods n(r, z), that were calculated using Monte Carlo code. The adjustment was performed using norming coefficients determined on the basis of the procedure of comparing calculated and experimental values of fission densities in central fuel pellets of E-type fuel rods and in special fuel samples.

Sets of neutron fission rates R (r, z, t) in fuel rods were determined during the next step. This set was formed using the normalized (on the basis of experimental data) set of fission densities n_m (r, z), the set of values characterizing the reactor power as a function of time P (t), and temperature adjusting coefficients to take into account the kinetics of neutron gas temperature changes in the capsule.

The final stage of the procedure was the determination of fields of the energy deposition E (r, z, t) and fuel rod power P (r, z, t). These characteristics were determined by calculating the energy released in each fission event from the value set R (r, z, t). The following components of the energy deposition were taken into account within the framework of this procedure:

- fission fragment energy;

- energy due to the prompt neutron and gamma radiation of the reactor and fuel rods;

- energy due to the delayed beta and gamma radiation.

The procedure to determine the energy deposition and the power of fuel rods is described in detail in sections 4.8, 4.9.

4.2. IGR reactor power versus time

IGR reactor profile is recorded in the process of each test using standard ionization chambers of the reactor installed in the water tank (Fig. 4.1). The ionization chambers are arranged with a certain angular step. The measurement ranges of chambers are different. A specific set of chambers for recording the reactor power profile are selected in accordance with the program of the experiment taking into account the maximum reactor power values, was implemented. For the present test series, the calibration of ionization chamber measurement channels was performed at the stage of the scoping tests. The validation of IGR reactor power profile identity in the locations of ionization chambers and IGR reactor power profile in the central reactor plenum was carried out repeatedly. An additional experimental check was performed within this series of tests using in-core neutron detectors arranged along the external perimeter of the capsule with fuel rods.

Corresponding studies showed that the reactor power profile does not depend also on the azimuth angle, at which the ionization chamber is located. Fig. 4.1 presents results of a typical experiment.
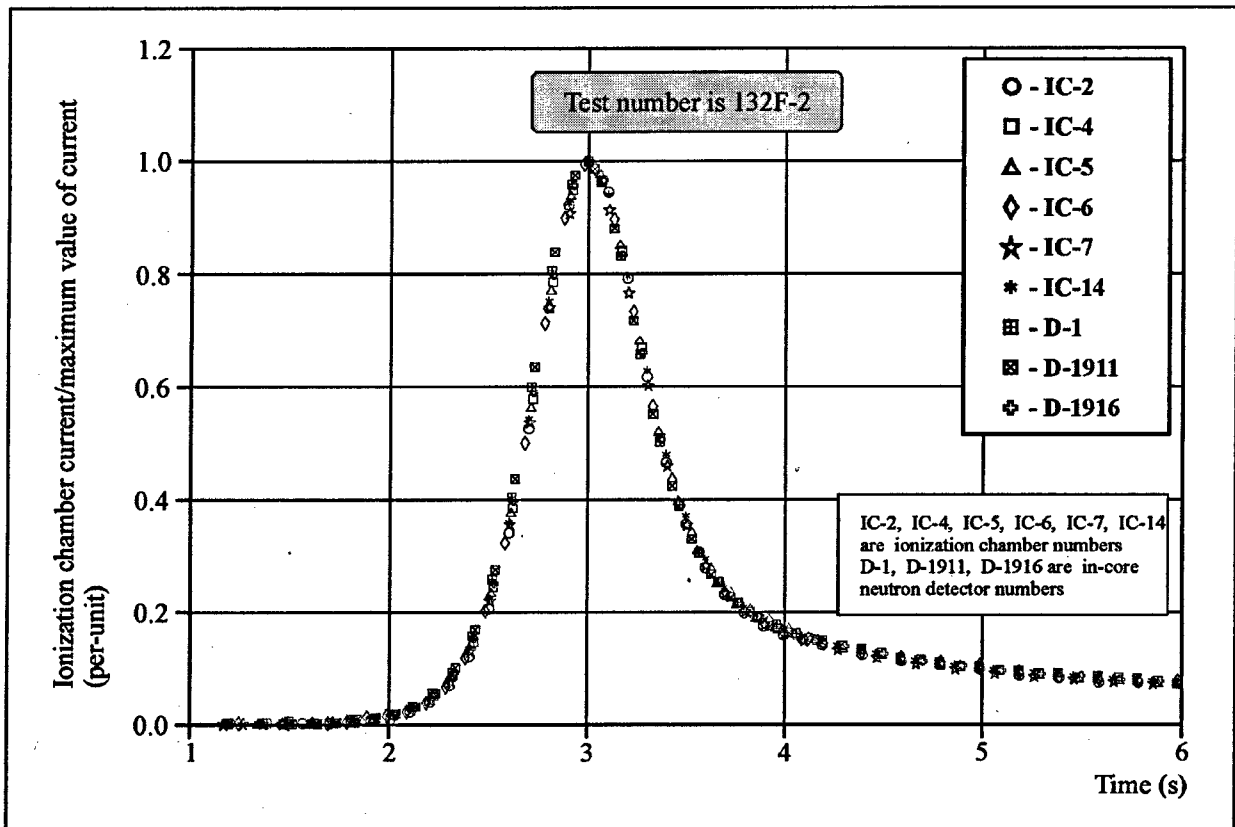
Fig. 4.1. The reactor power profile measured by ionization chambers and in-core neutron detectors

The measurement error for standard ionization chambers of IGR reactor is ± 2.5 % of the signal value for the operating measurement area.

In addition, it should be noted that, since the range of reactor power changes is wide during the pulse tests, there is a problem of reconstructing the reactor power profile near the zero values at the back front of the pulse. This problem is related to the fact that the reactor power level turns out to be lower than the parasite signal initiated in the ionization chamber by the reactor gamma field. This is typical mainly for the time interval when the process takes place only due to delayed neutrons. An approach to solve this problem within a specific series of tests is described in section 4.6.

4.3. Number of fissions in special fuel samples

Measurement of number of fissions in special fuel samples

In 16 tests out of 23, special fuel samples were placed in the capsule with fuel rods before the capsule was installed in IGR reactor and were removed from the capsule after the tests were completed (see section 4.6).

The La^{140} activity was measured by recording gamma quanta with the energy of 1596 keV emitted by the fuel sample. The measurements were performed using the semiconductor Ge (Li) gamma spectrometer [1].

The number of fissions in the special fuel sample was determined as:

$$n_s = \frac{Ak_s}{t_i \eta \varepsilon_\gamma m f_i},$$

where n_s = the number of fissions in the sample (fiss./g U^{235});

A = the photopeak area for a corresponding gamma quantum with the energy of 1596 keV (counts);

4.3

k_s = the coefficient of the self absorption of gamma quanta with the energy of 1596 keV in the special fuel sample (per-unit);

m = the mass of U^{235} isotope in the special fuel sample (g);

t_l = the live time of recording the gamma quanta in the spectrometer (s);

η = the quantum yield of gamma quanta with the energy of 1596 keV per one decay of La^{140} (per-unit) [2];

ε_γ = the efficiency of recording the gamma quanta with the energy of 1596 keV by the spectrometer (per-unit);

f_t = the coefficient connecting the La^{140} activity at the time of measurements with the accumulated uranium number of fissions in the special fuel sample over the total time of its irradiation (1/s).

The effect of the cascade summation of gamma quanta in this case was not taken into account since the special fuel sample was located at the distance of about 100 mm from the spectrometer detector. The number of repeated measurements performed for each fuel sample is 8 or more. This allowed to determine the activity of each sample and the statistical measurement error.

The values of gamma quanta self absorption coefficient in the special fuel samples were calculated taking into account the real geometry of samples and their material composition. Linear coefficients of gamma quanta absorption were taken from [3]. The efficiency of recording the gamma quanta with the energy of 1596 keV was determined using the empirical dependence. The dependence was obtained on the basis of experimental data characterizing the ratio between the spectrometer efficiency and gamma quanta energy for the real geometry of fuel samples. The spectrometer was calibrated using reference standard gamma-radiation sources of the first order qualified on the basis of the gamma yield with the error not exceeding 1.5 %.

The mass of U^{235} isotope in each of the special fuel samples was taken from the sample passport data [4]. In addition, the checks of U^{235} mass in samples were carried out using a reference sample and radiometric measurement procedure.

The value of coefficient f_t is:

$$f_t = \lambda_{La} e^{-\lambda_{La} t_0} \left\{ y_{Ba} \frac{\lambda_{Ba}}{\lambda_{La} - \lambda_{Ba}} \left[e^{(\lambda_{La} - \lambda_{Ba}) t_0} - 1 \right] + y_{La} \right\},$$

where λ_{La}, λ_{Ba} = decay constants of La^{140} and Ba^{140}, respectively (1/s) [2];

y_{Ba} = the cumulative yield of Ba^{140} for U^{235} fissions by thermal neutrons (per-unit) [5];

y_{La} = the independent yield of La^{140} for U^{235} fissions by thermal neutrons (per-unit) [5];

t_0 = the time interval from the beginning of the fuel rod irradiation till the beginning of this measurement using the gamma spectrometer (s).

Table 4.1 presents number of fissions values in special fuel samples, obtained on the basis of the above procedure.

Table 4.1. Measured number of fissions in central fuel pellets of E-type fuel rods, special fuel samples, measured integrals of current readings of the ionization chamber and integrals of corrected readings of the ionization chamber

Test number	Number of refabricated fuel rod	Measured integral of current readings (μAs)	Integrals of corrected current readings (μAs)	$n_s \, 10^{-14}$ $\left(\dfrac{fiss}{gU^{235}}\right)$	$n_E \, 10^{-14}$ $\left(\dfrac{fiss}{gU^{235}}\right)$
103F-1	H14T	19210	19860	4.36	3.31
103F-2	H17T	29730	30870	6.69	5.04
103F-3	H16T	41290	42660	9.37	6.92
103F-4	B21T	38550	39920	5.66	4.51
103F-5	H8T	45910	47240	10.8	7.58
103F-6	B20T	49200	50790	7.36	5.81
103F-7	H6T	68920	71040	15.7	11.13
103F-8	H4T	89820	92890	20.6	-
103F-9	H5T	109490	113300	-	-
103F-10	H7T	111090	116700	-	-
103F-11	B11T	158450	164200	-	-
103F-12	B13T	224540	231300	-	-
103F-13	H1T	120860	125100	-	-
103F-14	H2T	150970	157100	-	-
103F-15	H3T	185430	193700	-	-
103F-16	B10T	79740	82810	12.0	9.92
103F-17	H15T	65660	67980	15.4	11.5
103F-18	B9T	109720	114300	16.8	-
103F-19	B12T	123250	128700	17.3	-
103F-20	B19T	70060	72500	9.71	8.24
103F-21	B23T	97720	101700	14.0	-
103F-22	B22T	31400	32690	4.46	3.69
103F-23	H18T	51460	53400	10.8	-

Table 4.2 presents error values for parameters of the formula for the determination of the number of fissions in special fuel samples. The procedure used to determine the error in the number of fissions in special fuel samples is described in section 4.10.

Table 4.2. Errors in characteristics in the formula to determine number of fissions in the special fuel samples

Legend	Standard deviation (%)	Systematic error (%)
A	1	0.5
k_s	0*	0.5
t_i	0*	0.5
η	0*	0.1
m	1	1
ε_γ	1	1.5
f_t	0*	1.5

* Errors in characteristics which were calculated or taken from the literature were considered as systematic errors

4.5

Adjustment of the set of measured values of the reactor power profile versus time

The data files of standard ionization chambers readings of IGR reactor were the input data to determine the reactor power versus time. Results of these measurements are presented in Tables, Appendix F, Volume 3 of the present Report.

The analysis of this set of results shows that their direct use will lead to an additional systematic error related to a large error in recording low power levels of the reactor. The special procedure described in section 4.6 made it possible to adjust ionization chamber readings in this area. The corrected power measurement results are presented in Tables, Appendixes G, H, I, Volume 3 of the Report.

Energy deposition in IGR reactor

The standard integration procedure was applied for each of 23 adjusted reactor power data files. The obtained integrals characterize the energy deposition in IGR reactor and, thus, in special fuel samples, in the measurement units of ionization chamber (μA s). Table 4.1 presents integration results. For comparison, reactor power integrals before the adjustment are also presented.

Ratio between the energy deposition in IGR reactor and the number of fissions in special fuel samples

Multiple studies performed earlier at IGR reactor show that, for reactor power pulses used at this series of tests, the ratio between the energy deposition in the reactor and the number of fissions in the special fuel sample (fiss./g·U^{235}) does not depend on the value of the positive reactivity introduced, but is determined only by the material composition of the capsule, of the sample and their geometry. The proof of this statement is outside the framework of this Report, however the below results can be used for its verification.

Taking into account the above considerations, the standard methods of determining the linear regression coefficients were used to process data sets of number of fissions in special fuel samples and of the energy deposition in IGR reactor. Its own regression equation was obtained for each type of the coolant.

These equations are:

$$n_{sm} = 2.2 \ 10^{10} \ E_r \qquad \text{for the variant with water in the capsule,}$$

$$n_{sm} = 1.4 \ 10^{10} \ E_r \qquad \text{for the variant with air in the capsule,}$$

where n_{sm} = the number of fissions in the special fuel sample (fiss./g U^{235}),

E_r = the corrected energy deposition in the reactor in the measurement units of the ionization chamber (μAs).

The obtained results are presented in the graphical form in Fig. 4.2.
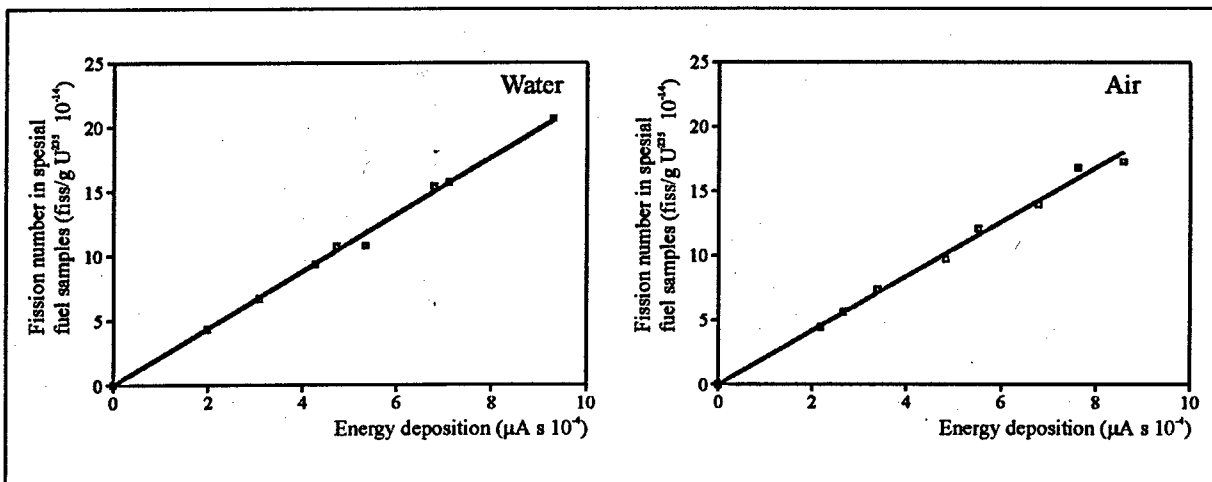
Fig. 4.2. Number of fissions in the special fuel samples vs. the energy deposition in the reactor

Number of fissions in special fuel samples

The above regression equation and the reactor energy deposition data were used to determine 23 values of number of fissions in special fuel samples (for 7 tests, in which there were no fuel samples, the notion of a conditional fuel sample was introduced). Out of 23 values, 20 were the final values, and three values were additionally adjusted. This was done because in three tests there was no E-type fuel rod, therefore, there were changes in the ratio between the number of fissions in the special fuel sample and the reactor energy deposition. The inclusion of this effect using MCU (see section 4.7) and WIMS-4D computer codes shows that the number of fissions in special fuel samples in this case increases by $8^{\pm 0.5}$ %.

4.4. Number of fissions in central fuel pellets of fresh fuel rods

Measurement of number of fissions in non-failed fuel rods of E-type

One fuel pellet was removed from the centre (along the length) of the fuel column of each non-failed fuel rod. Each pellet was crashed to powder, the resulting mass was thoroughly mixed. Then three powder samples with the weight of 0.1 g each were taken from each crashed pellet. Fuel samples were placed in the form of a thin layer on organic glass plates. Then Zr^{95} isotope activity was measured for each fuel sample. The activity was measured in gamma radiation with the energy of 724 keV using gamma spectrometer [6]. Several measurements were performed for each sample.

The duration of one measurement was about one hour, since the measurements were performed after the completion of the cycle of non-destructive and destructive post-test examinations of fuel rods, i.e. several months after the tests. The number of fissions in the fuel sample is:

$$n_E = \frac{A k_s e^{\lambda_{Zr} t_0}}{y_{Zr} t_1 \eta \varepsilon_\gamma m \lambda_{Zr}},$$

where n_E = the number of fissions in the central pellet of E-type fuel rod (fiss./g U^{235});

A = the area of the photopeak that corresponds to gamma quanta with the energy 724 keV (counts);

k_s = the self absorption coefficient of gamma quantum with the energy of 724 keV in the fuel sample (per-unit);

y_{Zr} = cumulative yield of Zr^{95} for U^{235} thermal neutron fission (per-unit) [3];

t_0 = the time interval from the beginning of the fuel rod irradiation to the beginning of this measurement using the gamma spectrometer (s);

η = the quantum yield of gamma quanta with the energy of 724 keV for Zr^{95} decay (per-unit) [2];

m = the mass of U^{235} isotope in the fuel sample (g);

ε = the efficiency of recording the gamma quanta with the energy of 724 keV by the spectrometer (per-unit);

λ_{Zr} = the decay constant of Zr^{95} (1/s) [2];

t_1 = the live time of recording the gamma quanta with the energy of 724 keV by the spectrometer (s).

Procedures similar to those described in section 4.3 were used to calculate the self absorption coefficient and the spectrometer efficiency. The mass of U^{235} isotope in the fuel sample was determined using the measured mass of the fuel sample and the uranium enrichment (data of the fuel rod manufacturing plant).

Table 4.1 presents measurement results of number of fissions in fuel pellets of E-type fuel rods. Errors in characteristics that were used to determine the numbers of fissions are presented in Table 4.3. The procedure of the measurement error calculation of the number of fissions in fuel pellets is described in section 4.10.

Table 4.3. Errors in characteristics in the formula to determine the number of fissions in fuel pellets of E-type fuel rods

Legend	Standard deviation (%)	Systematic error (%)
A_p	1.5	0.5
k_s	0^*	0.5
t_1	0^*	0.5
η	0^*	0.5
m	1.2	0.5
ε_γ	1	1.5
λ_{Zr}	0^*	0.06
t_o	0^*	0.01
y_{Zr}	0	1.0

* Errors in characteristics, which were calculated or taken from the literature, were considered as systematic errors.

Fission numbers in central fuel pellets of E-type fuel rods

The procedure for determining the number of fissions in central fuel pellets of E-type fuel rods was similar to the procedure of determining the number of fissions in special fuel samples described in section 4.3.

The regression equations for central fuel pellets of E-type fuel rods is:

$$n_{Em} = 1.62 \; 10^{10} \; E_r \qquad \textit{for the variant with water in the capsule,}$$

$$n_{Em} = 1.16 \; 10^{10} \; E_r \qquad \textit{for the variant with air in the capsule,}$$

where n_{Em} = the number of fissions in the central fuel pellet of E-type fuel rod (fiss./g U^{235});

E_r = the energy deposition in the reactor in the measurement units of the ionization chamber (μAs).

Fig. 4.3. presents these results in the graphical form.
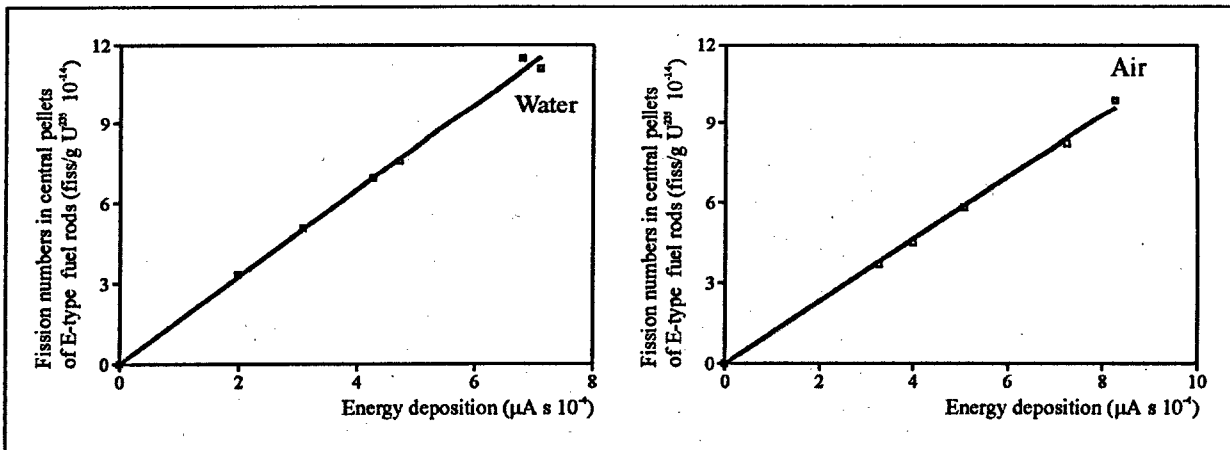
Fig. 4.3. Number of fissions in fuel pellets of E-type fuel rods vs. the energy deposition in the reactor

In addition regression equations were obtained, that connect the number of fissions in central fuel pellets of E-type fuel rods and the number of fissions in special fuel samples. These equations are:

$$n_{Em} = 0.73 \; n_{sm} \qquad \textit{for the variant with water in the capsule,}$$

$$n_{Em} = 0.82 \; n_{sm} \qquad \textit{for the variant with air in the capsule,}$$

Where n_{Em} = is the number of fissions in the central fuel pellet of E-type fuel rod (fiss./g U^{235});

n_{sm} = is the number of fissions in the special fuel sample (fiss./g U^{235}).

The final values of number of fissions in central fuel pellets of E-type fuel rods were determined using coefficients from regression equations and energy deposition values in IGR reactor.

4.5. Input data on the geometry and the material composition of the reactor, the capsule, fuel rods and special fuel samples

The data base, described in Chapter 2 of the present Volume of the Report and presented in Appendixes to Volume 3 of the Report, was used as the input data characterizing the geometry and the material composition of fuel rods, the capsule and special fuel samples. The set of input data characterizing IGR reactor was formed using corresponding special reports [7, 8].

General characteristics from this set are presented in Table 4.4.

Table 4.4. Main characteristics of IGR reactor

Parameter	Value
1. Reactor core	
• overall dimensions:	
horizontal cross-section (cm)	140·140
height of immovable part (cm)	133
height of movable part (cm)	146
2. Fuel element	
• shape	parallelepiped
• composition	U-impregnated graphite
• horizontal cross-section (cm)	9.8·9.8
• height (cm)	13.3
• enrichment (%)	90
• U^{235} density (g/cm^3)	$4.7\ 10^{-3}$
• graphite density (g/cm^3)	1.72
3. Control rod	
• shape	double-layer cylinder
• composition of the external absorbing layer	Gd_2O_3 and graphite
• Gd_2O_3 content in graphite (% by weight)	2
• thickness of external absorbing layer (cm)	0.8
• rod outer diameter (cm)	50
• internal rod material	graphite
• internal rod density (g/cm^3)	1.72
• absorbing layer height in the control rod (cm)	170

Table 4.4. Main characteristics of IGR reactor

Parameter	Value
4. Lateral rod	
• shape	multi-layer cylinder
• height (cm)	150
• outer diameter (cm)	10
• composition of the external absorbing layer	Gd_2O_3 and graphite
• absorbing layer thickness (cm)	0.8
• composition of the gap between the absorbing layer and the internal rod	air
• internal rod material	steel
• internal rod diameter (cm)	0.8
5. Reflectors	
• material	graphite
• density (g/cm³)	1.67
• maximum thickness of the side reflector (cm)	50
• maximum height of the top end reflector (cm)	79.5
• maximum height of the bottom end reflector (cm)	227.5
6. Central experimental channel	
6.1 Cross-like insert with the internal hole	
• material	graphite
• maximum dimensions in the cross-section (cm)	40·40
• hole diameter (cm)	29
6.2 Gap	
• material	He
• thickness (cm)	1
6.3 External shroud	
• material	Zr alloy
• outer diameter (cm)	27
• thickness (cm)	0.2
6.4 Gap	
• material	H_2O
• thickness (cm)	0.3
6.5 Separating shroud	
• material	Al-Mg alloy
• outer diameter (cm)	26
• thickness (cm)	0.15
6.6 Gap	
• material	H_2O
• thickness (cm)	0.35

Table 4.4. Main characteristics of IGR reactor

Parameter	Value
6.7 Internal casing • material • outer diameter (cm) • thickness (cm)	 Al-Mg alloy 25 1.1
6.8 Gap • material • thickness (cm)	 air 2.4
6.9 Protective shroud • material • outer diameter (cm) • thickness (cm)	 Al-Mg alloy 18 1.5
6.10 Experimental cavity • material • outer diameter (cm)	 air 15
7. Side experimental channel	
7.1 External shroud • material • outer diameter (cm) • thickness (cm)	 steel 10.2 0.1
7.2 Gap • material • thickness (cm)	 water 0.2
7.3 Separating shroud • material • outer diameter (cm) • thickness (cm)	 steel 9.6 0.1
7.4 Gap • material • thickness (cm)	 water 0.2
7.5 Internal shroud • material • outer diameter (cm) • thickness (cm)	 Al 9.0 0.4
7.6 Experimental cavity • material • diameter (cm)	 air 8.2

4.6. Procedure to adjust the input data characterizing the power profile of IGR reactor

Purpose and tasks of the procedure

The adjustment of the input data characterizing the power profile of IGR reactor versus time was performed with the aim of the calculation reconstruction of the reactor power profile in the area of small power values, below 2.5 % of the maximum power.

The following problems were solved to reconstruct the lacking information on the power profile of IGR reactor:

- special scoping tests were conducted in 1995 at IGR reactor (132F series) with the aim of obtaining a corresponding experimental data base using sensitive measurement channels of the neutron flux [9];

- 3D dynamic computer code DINAR was improved to take into account the temperature feedback as applied to specific features of IGR reactor [10];

- the three-dimensional full-scale computer simulation of IGR reactor power pulses was performed for 23 tests of fuel rods of C-, D-, E- types;

- IGR reactor power profile was corrected.

Validation of computer code selection.

During the controlled power pulse in IGR reactor the following takes place: increase in the reactor core temperature, increase in the leakage of thermal neutrons, changes in the insertion depth of control rods. The process is accompanied by the spatial deformation of the neutron flux distribution and by changes in the control rod efficiency due an increased temperature in the reactor core. Such a complex process can be only described with an acceptable accuracy using a full-scale neutronics model. Therefore, the non-stationary reactor calculations were carried out using the 3D dynamic code DINAR [11], which was improved to take into account the temperature feedback of IGR reactor [10].

DINAR code is intended for 3D simulation of fast transients in the reactor taking into account reactivity feedbacks. The model of DINAR code, that describes reactor neutronics characteristics in space and time, is based on the generic theory of the heterogeneous reactor [11–13]. Within the framework of this model the reactor is divided into a number of cells. Non-stationary boundary conditions that connect neutron fluxes and currents through cell interface matrixes are set for the surface of each cell. In this case there is no need in the validity of the diffusion approximation for the entire volume of the reactor. It is assumed that the diffusion equation describes the process only at the boundaries of selected cells. Unlike traditional finite difference algorithms, the heterogeneous method allows to correctly calculate heterogeneous reactor components such as control rods, content of the central reactor plenum, etc., without using the cell homogenization.

The spatial neutron flux distribution in DINAR code is calculated by TREC code in the few-group approximation [14]. IGR reactor calculations used 4-group energy division. The neutron flux distribution for TREC code is constructed in the form of Green's functions. The amplitudes of Green's functions are determined through cell interface matrix using the difference approximation [15]. The axial distribution of the neutron flux is described by expanding the axial component of the flux into Fourier series (i.e. without using the axial discretization).

The cell interface matrix calculations for reactor geometric components were performed using TRIFON code described in section 3.2.3.

Within the framework of the present work the improvement of DINAR code was carried out as applied to requirements on the code with the aim to describe IGR reactor The code was supplemented with the module to calculate the non-stationary temperature distribution in the reactor core; 3D calculations of temperature changes in the reactor core were performed using heat balance equations. To determine the amplitude function, a strong negative energy deposition feedback was explicitly introduced into the calculation module. This procedure resulted in a considerable reduction of the calculation efforts in the process of the pulse development dynamics simulation.

Input data for calculation modeling

In addition to the input data presented in section 4.5, the following input data were used for DINAR code:

- insertion depth of each of the control rods in the critical conditions of the reactor before the power pulse (measured values for each of 23 tests);

- initial temperature of the reactor core (measured values for each test);

- geometry and material composition of the capsule with fuel rods;

- insertion depth of each of the control rods versus time for each test (measured values).

The input data are described in more detail in [10].

Calculation scheme and main assumptions

Cross- and axial sections of the calculation geometrical model of IGR reactor are presented in Fig. 4.4, Fig. 4.5.

1	Tank water	6	Control rod
2	Reactor vessel and thermal shield	7	Lateral rod
3	Side experimental channel	8	Side reflector
4	Central experimental channel	9,10	Reactor core (movable and immovable parts)
5	Graphite insert		
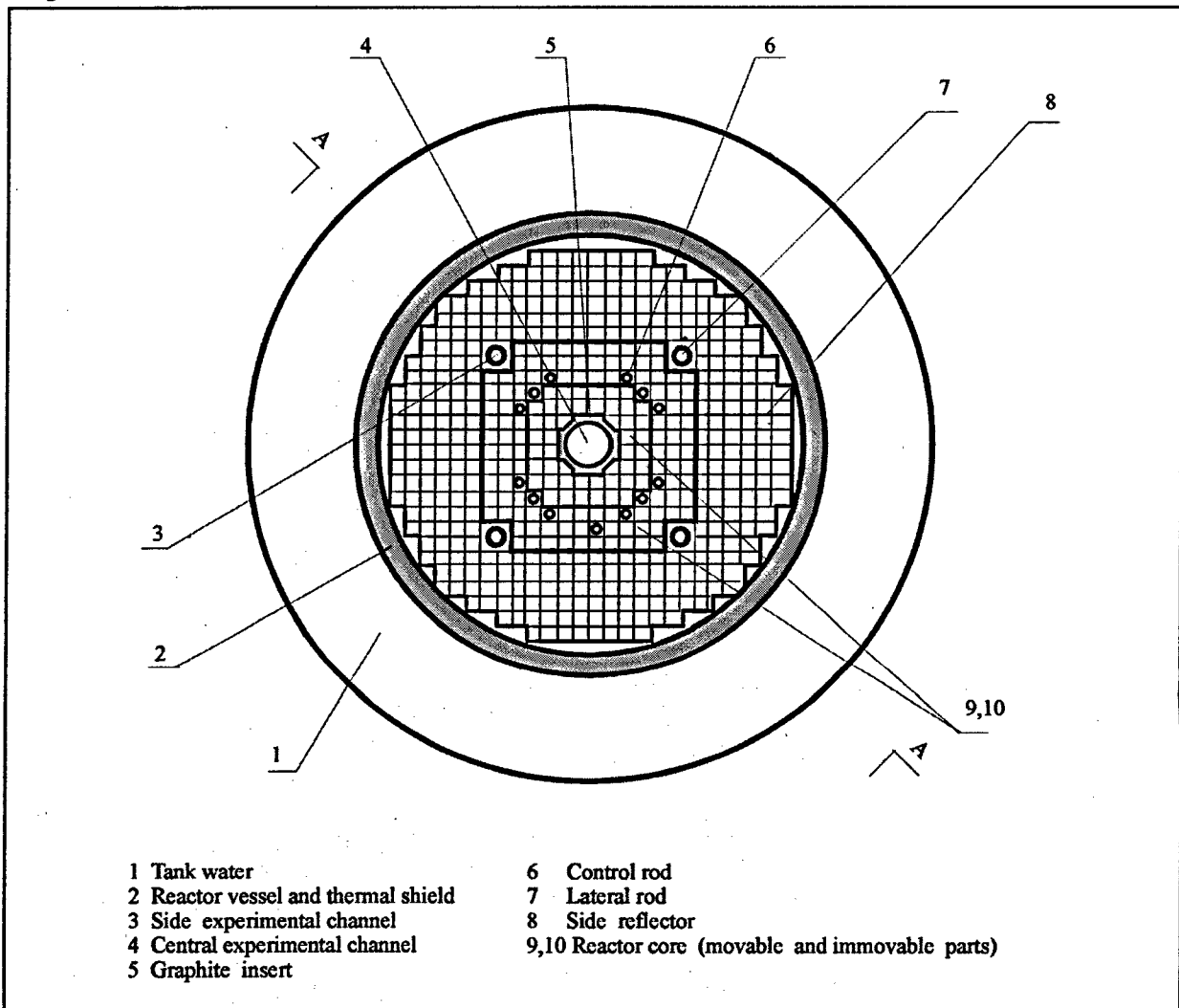
Fig. 4.4. Cross-section of the calculation geometrical model of IGR reactor for DINAR computer code

4.13
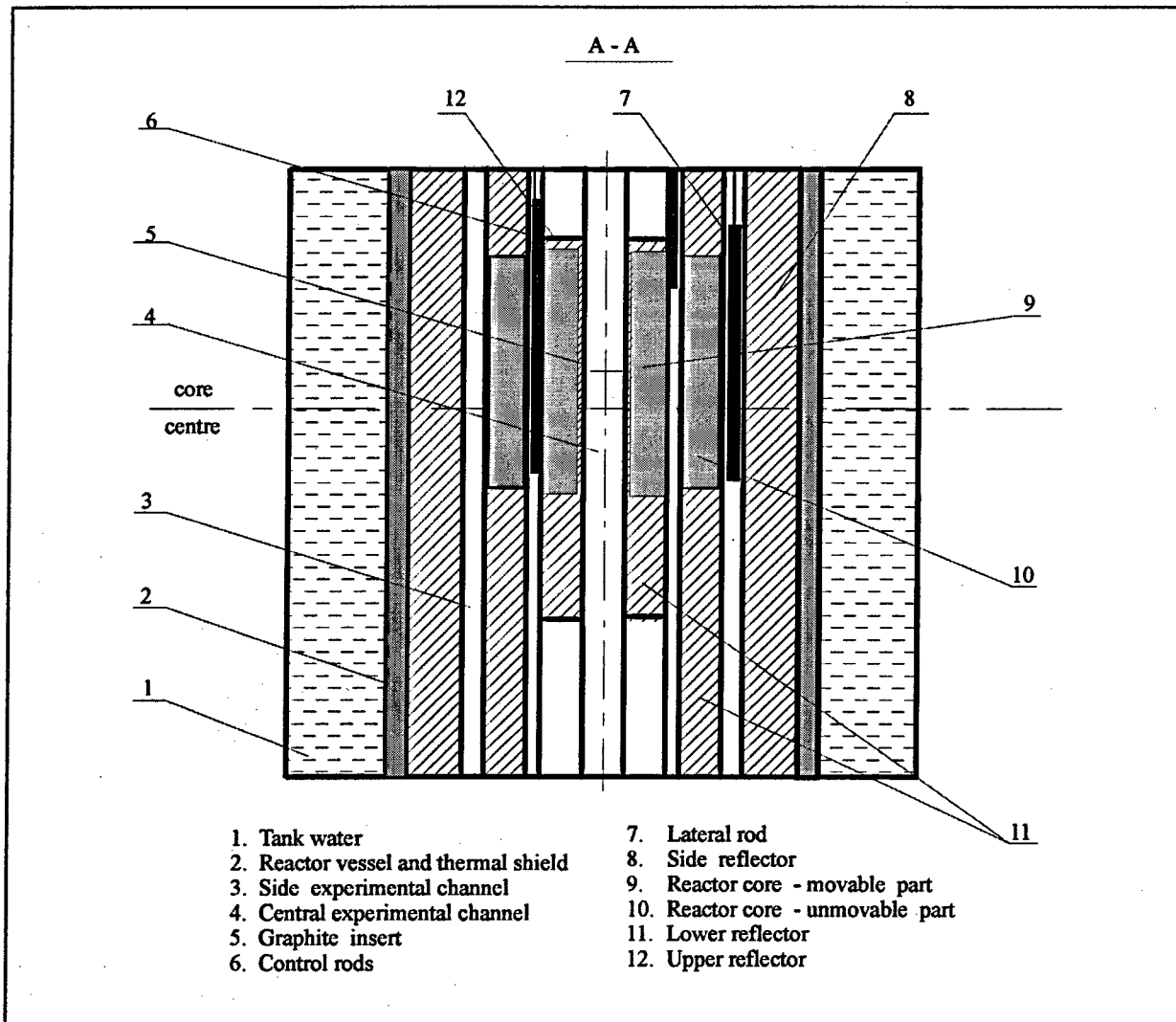
Fig. 4.5. Axial section of the calculation geometrical model of IGR reactor for DINAR computer code

The calculation model includes the following main elements:

- reactor fuel elements (graphite columns impregnated with the uranium salt);

- graphite columns of the reactor core with control rods;

- graphite columns of the reflector and graphite columns of the reactor core, non impregnated with the uranium salt;

- graphite columns of the reflector with lateral rods;

- central reactor plenum with all its internals;

- side experimental channel;

- tank water.

The total number of calculation elements in the cross-section equals 1900. The cell interface matrix of fuel rods of the reactor core was calculated as the temperature function in the range of 290-560 K, which is characteristic for these tests. Gaps-between elements of the reactor core were taken into account by reducing the graphite density by 3-4%. The non-uniformity of the uranium concentration in the graphite was not taken into account because of the absence of adequate input data. Due to a small duration of the neutron pulse and

the presence of gaps between fuel elements of the reactor core, the heat exchange between them was not taken into account. The capsule with fuel rods was described for these calculations approximately in the cylindrical r, z geometry.

<u>Verification of DINAR computer code</u>

Results of special scoping tests performed at IGR reactor were used to verify the results of reconstructing the pulse shape of IGR reactor using DINAR computer code.

The following features characterize the series of scoping tests at IGR reactor (series 132F):

- total number of tests – 7;
- tests were conducted without the installation of the capsule with fuel rods into the reactor central test channel;
- IGR reactor power profile was recorded by six standard ionization chambers and by three in-core neutron detectors; high sensitivity channels were connected to two out of six ionization chambers to provide correct recording of the back front on the reactor power pulse;
- one test was performed in the uncontrolled power pulse mode; other tests – in controlled pulse mode;
- modes of the controlled pulse corresponded to test modes of fuel rods of C-, D-, E- types in 103F series;
- the controlled pulse was formed by a group of 8 control rods;
- the introduction of the initial positive reactivity in the range of 0.9–1.8 β_{eff} was provided by the withdrawal of 1 start-up rod.

The verification of DINAR code was carried out in the following two areas:

(a) Checks of the quality of the code simulation of IGR reactor power pulses starting from the initial time till the moment when the power value of the pulse back front is 2.5 % of the maximum.

(b) Checks of the quality of the code simulation of IGR reactor small power levels (less than 2.5 % of the maximum).

The following characteristic of the energy deposition in the reactor as a function of time t was used as the verification criterion:

$$E(t) = \frac{1}{P_{max}} \int_0^t P(t)dt,$$

where E(t) =   the energy deposition in the reactor in relative units (per-unit s);

     P(t) =   the reactor power (MW for calculations), (μA for measurements);

    P_{max} =   the maximum reactor power in this test (MW for calculations), (μA for measurements).

For each test in 132F series, the set of relative deviations of calculated and experimental values E(t) was determined:

$$\delta_{E(t)} = \frac{E_c(t) - E_m(t)}{E_{m,max}} 100,$$

where $\delta_{E(t)}$ =   the relative deviation of calculated and experimental values E(t) (%);

$E_m(t)$, $E_c(t)$ =   the measured and calculated values of the relative energy deposition in the reactor as a function of time (per-unit s);

   $E_{m,max}$ =   the measured values of the relative energy deposition for t=∞ (per-unit s).

The typical $\delta_{E(t)}$ error distribution is presented in Fig. 4.6 ($\delta_{E(t)}$ error characterizes the integral error of the "experiment-calculations" system).

The results of IGR pulse simulating by DINAR code are presented in Fig. 4.7, Fig. 4.8.

4.15
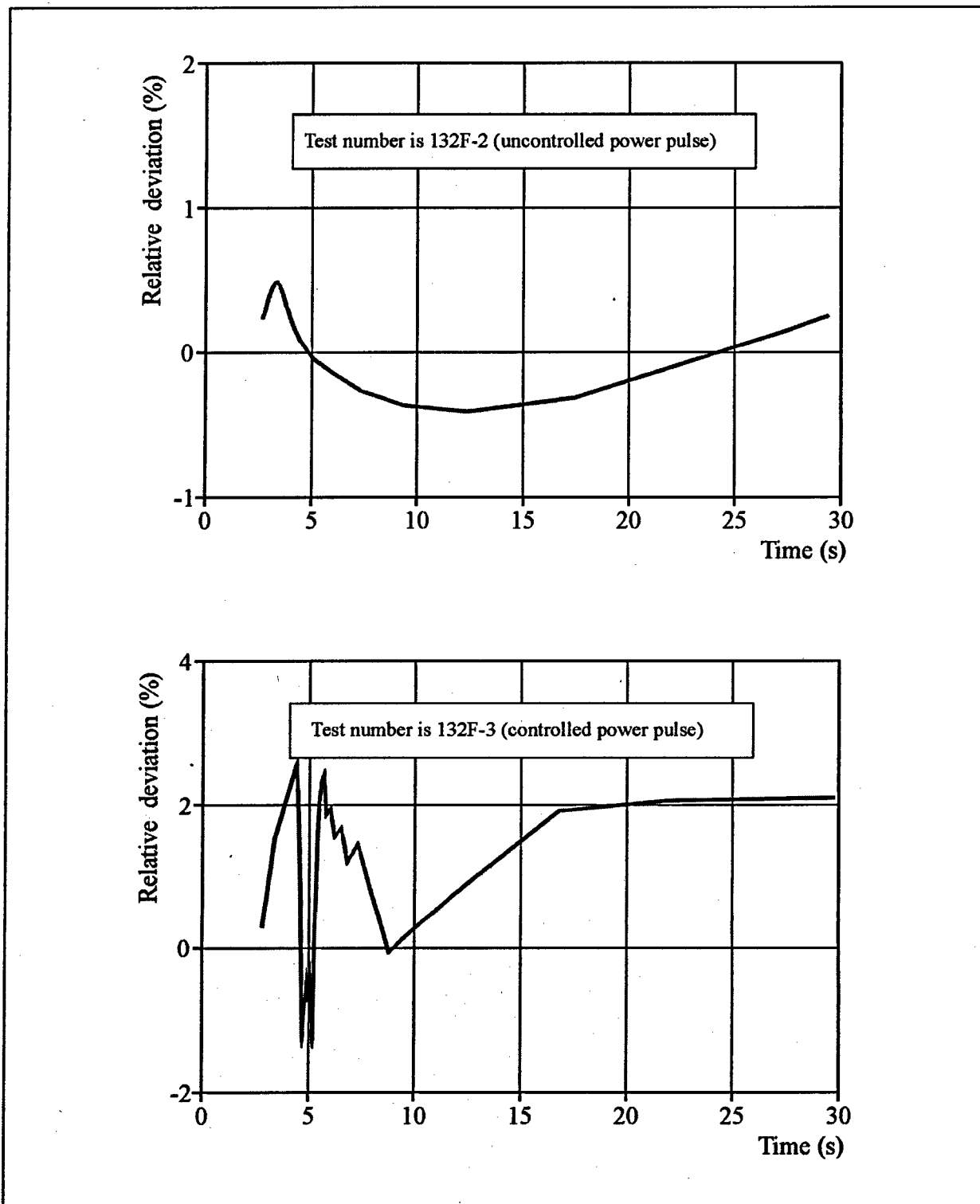
Fig. 4.6. Total relative error in determining IGR reactor energy deposition by the ionization chamber and DINAR code
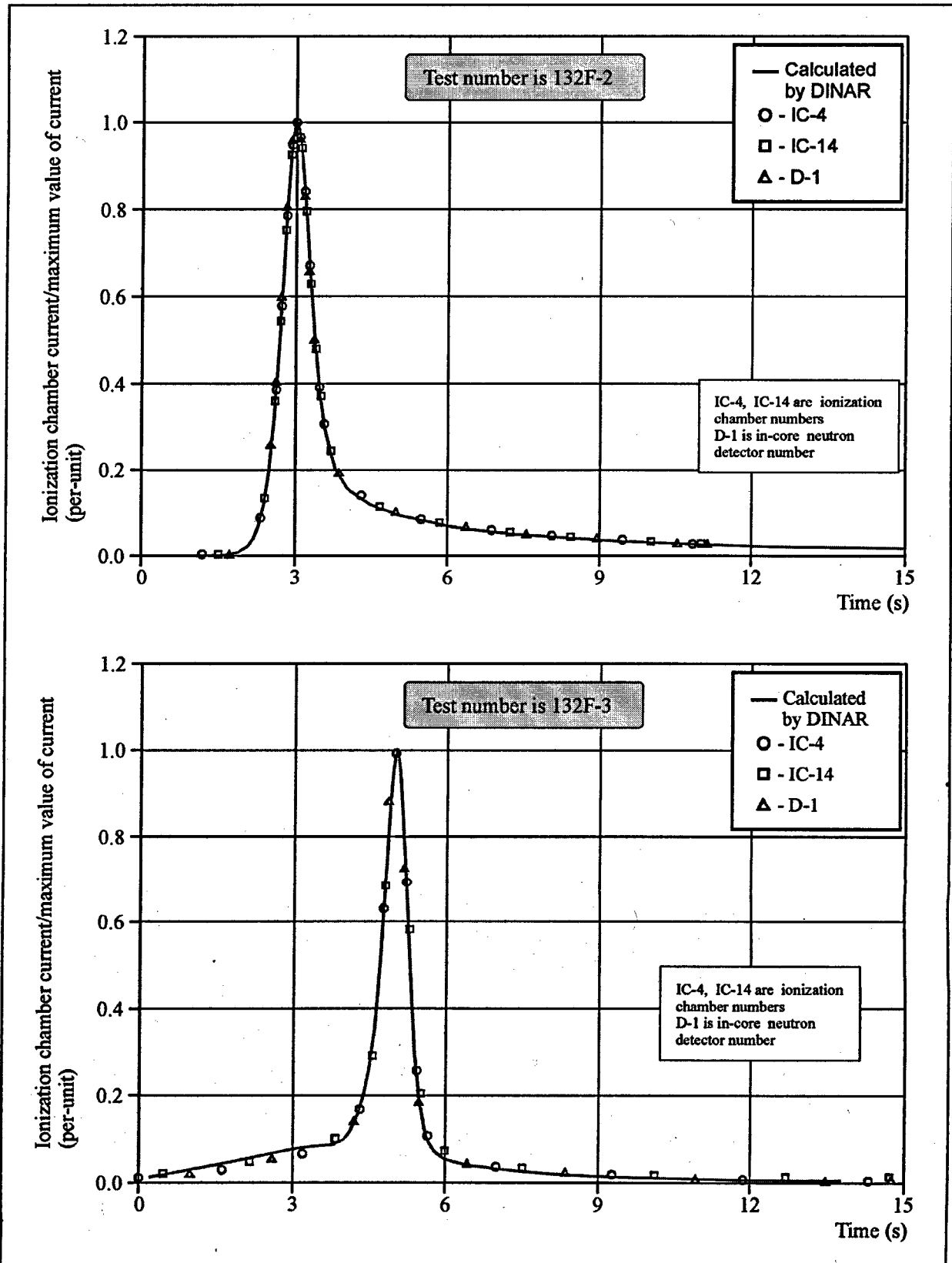
Fig. 4.7. Relative IGR reactor power profile measured by ionization chambers and calculated with DINAR code
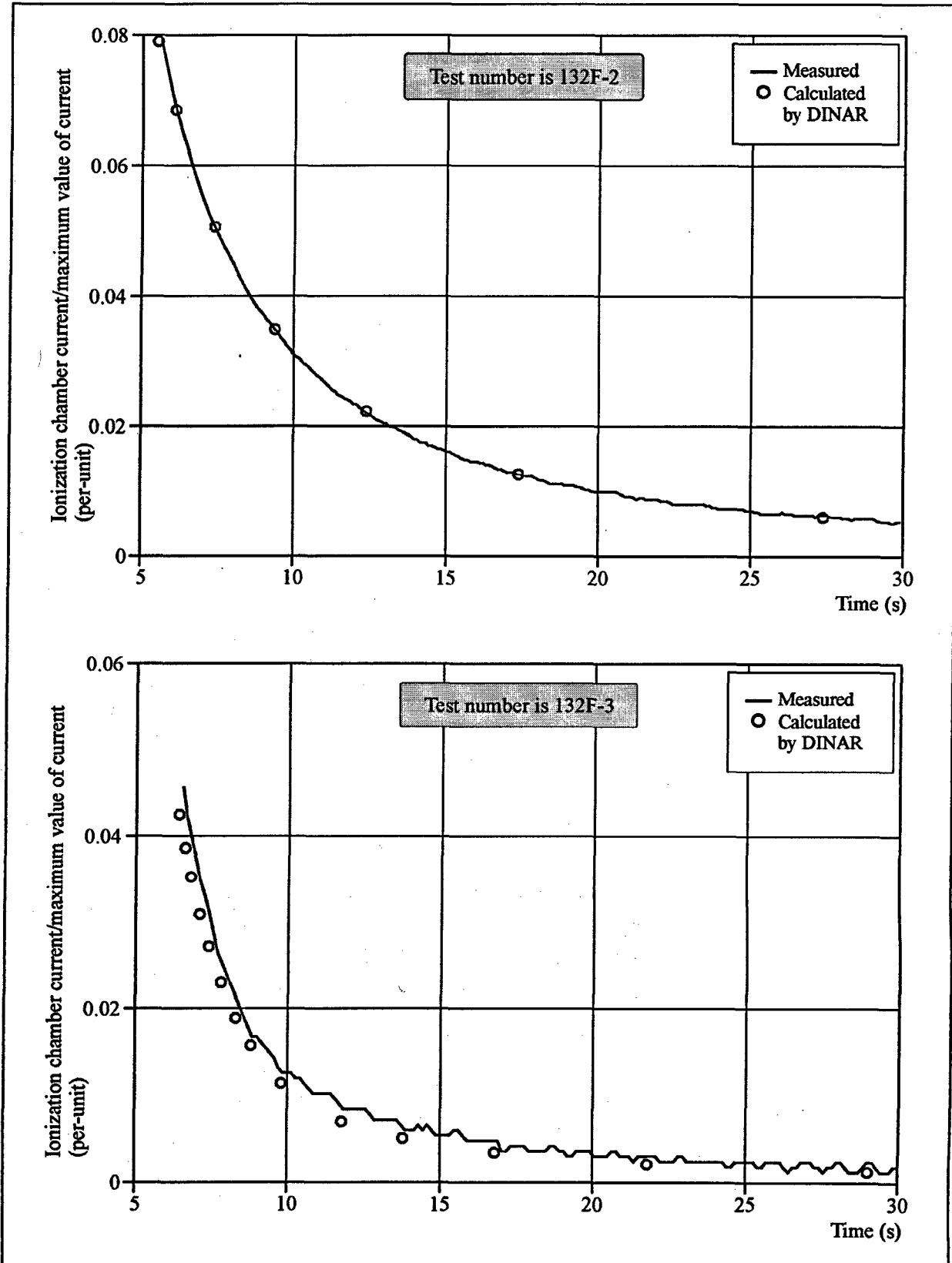
Fig. 4.8. Verification of the DINAR code simulation quality of small power levels of IGR reactor

Algorithm of adjusting the back front of IGR reactor power pulse

The adjustment of the input data for all 23 tests of C-, D-, E- types was carried out using the readings of the ionization chamber No 6 (IC-6). The adjustment was performed for the power pulse section starting at 2.5% of the maximum power (according to readings of the chamber IC-6). Starting with this value and later, DINAR code calculation results were used as the time-dependent IGR reactor power profile. The adjustment procedure was implemented individually for each of 23 tests. Fig. 4.9 contains an example illustrating specific results of applying this procedure for tests 103F-19.
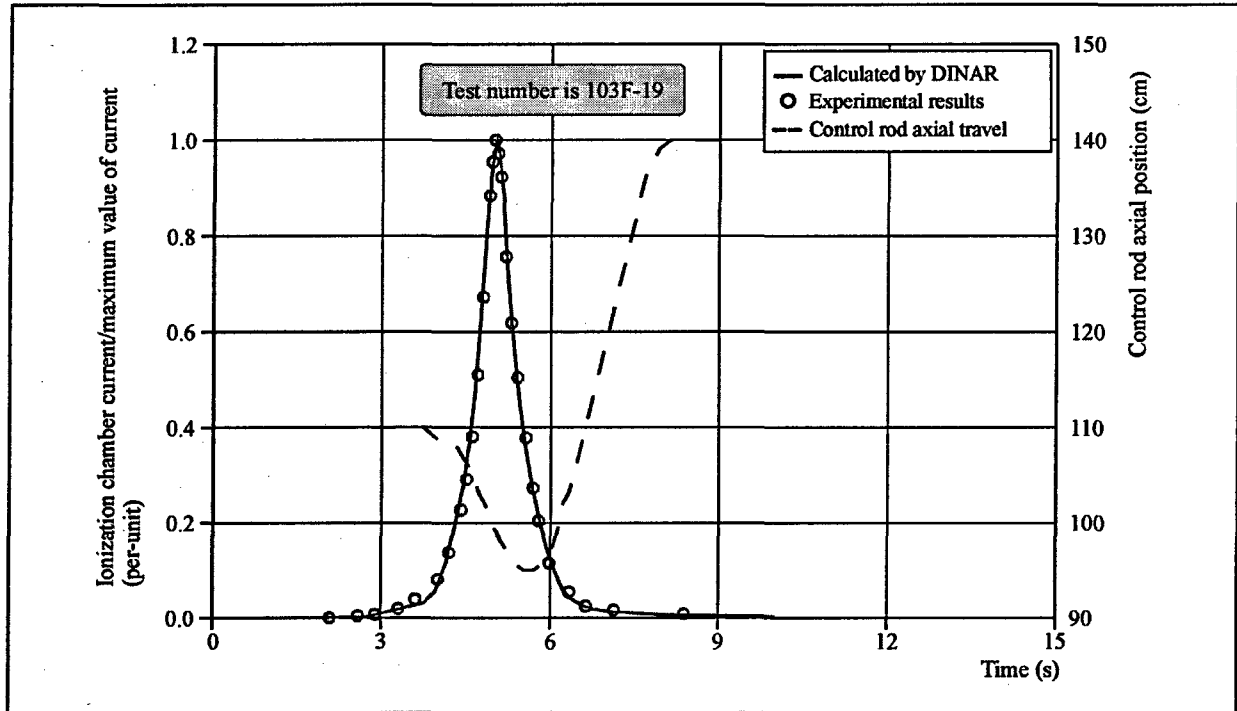
Fig. 4.9. IGR reactor power simulating by DINAR code

4.7. Neutronics parameters of fuel rods

Purpose and tasks of the procedure

The purpose of this procedure is to calculate the time integral function of the spatial distribution of the number of fissions in fuel rods of C-, D-, E- types and in special fuel samples.

The main tasks of this research area included the following:

- conduct of a series of full-scale neutronics dynamic calculations of IGR-type reactor using DINAR code to determine the axial distribution of IGR reactor power at the external surface of the central experimental channel of the reactor as a function of time for each of 23 tests of fuel rods of C-, D-, E- types;

- conduct of the stationary calculation simulation of IGR reactor including the capsule and fuel rods for 23 tests of fuel rods of C-, D-, E- types.

Input data

The following was used as the input data:

- geometry and material composition of IGR reactor (see sections 4.5, 4.6);

- geometry and material composition of fuel rods, the capsule, special fuel samples (see Chapter 2).

Procedure validation and computer code selection

Since the geometric and material structure of the capsule with fuel rods is complex, adequate calculation simulation of such object with the aim of determining the number of fissions in fuel rods requires a rather accurate neutronics model using, for example, Monte Carlo method. However the use of precision calculation methods based on Monte Carlo for detailed non-stationary full-scale calculations of IGR reactor is an extremely effort-intensive procedure which is beyond the capabilities of the present work. Therefore, the problem of searching for the ways to simplify the calculation method without affecting the accuracy of the results was solved at the first stage of the procedure development to determine the neutronics parameters of fuel rods of C-, D-, E- types. This problem was solved by conducting detailed calculations of IGR reactor using 3D dynamic code DINAR (see section 4.6). The analysis of the obtained results allowed to identify an important feature of the spatial neutron distribution in IGR reactor in the tests with the controlled power pulse. It was found out that the axial power profile of IGR reactor at the outside surface of the graphite insert of the central experimental channel depends slightly on the reactor core heating up.

On the other hand, because of similar schedules of control rod movement with small changes in the insertion depths, this axial power profile depends slightly on the position of control rods in the reactor (these statements are valid for the test series under consideration).

Thus, in this case the axial profile of the neutron flux to the capsule depends mainly on the geometry and the material composition of the reactor and the capsule with fuel rods. This circumstance results in two conclusions:

- using the three-dimensional dynamic code, IGR reactor can be simulated in all 23 tests, and it is possible to obtain axial profiles of the neutron flux to the central experimental channel;

- the solution of the stationary criticality problem can be used to find the detailed spatial distribution of the number of fissions in fuel rods of C-, D-, E- types.

These conclusions form the basis of the procedure to determine the number of fissions in fuel rods of C-, D-, E- types.

Using DINAR code, the first stage of the procedure covered the three dimensional dynamic simulation of IGR reactor for tests of fuel rods of C-, D-, E- types. The time-average axial profile of IGR reactor power, obtained as a result of the calculations, was used as the boundary condition for the second stage of the procedure.

During the second stage of the procedure calculations by Monte Carlo method were performed using model in which the reactor core was described approximately, and its characteristics did not depend on time. All other reactor elements, primarily its central part, including the central experimental channel, the capsule and fuel rods, were accurately described.

The variant for the approximate reactor description was selected on the basis of the optimization procedure, during which neutronics characteristics of the reactor core (its absorbing properties) were selected in such way as to obtain the identical boundary conditions for MCU and DINAR codes on the axial profile of the reactor power. The criticality problem was solved within the framework of this computer model. Taking into account the requirements on results of the calculations performed at the second stage, Monte Carlo MCU computer code was selected for calculations. The use of this code provides the solution of the problem on the neutron transfer with the accuracy which is limited only by the accuracy of nuclear data libraries.

MCU-RFFI code description

MCU-RFFI code is of modular structure and is written in FORTRAN-77 [16-19]. Three dimensional elements of the reactor, the capsule and fuel rods are described in the code by methods of the combinatorial geometry as Boolean combinations of a simple body set. Various options of MCU-RFFI program are generated from MCU program modules. MCU-RFFI has a number of optional physical modules, which are different in model types used to describe the interaction of neutrons with the matter and in libraries of constants.

The simulation of the interaction of neutrons with nuclei of the environment in physical models can be carried out using the model of continuous energy changes at collisions or the model in the multi-group approximation. A combination of these two models is possible for different energy regions. The pointwise and stepwise presentation of cross-sections can be used in the continuous slowing-down model.

4.20

Taking into account the accuracy requirements on the calculation simulation, the most verified option of the physical module and the corresponding library of constants were selected for the use within the framework of this task. The main features of the selected module are described below.

Neutron slowing down is simulated taking into account continuous changes in their energy at collisions. In the unresolved resonance region the cross-sections are calculated in the subgroup approximation or using Bondarenko's f-factors. In the resolved resonance region the subgroup and pointwise descriptions are used. For the most important nuclides, cross-sections are described by infinite number of points, i.e. cross-sections in each energy point are calculated directly in the simulation process on the basis of the resonance parameter library. This approach allows to perform calculations taking into account Doppler cross-section broadening without a prior tabulation of cross-sections. Cross-section approximation with step functions is used for less important isotopes. Collision simulation in the thermalization area is carried out either in the multi-group approximation, or on the basis of the model of continuous energy changes taking into account the correlation between the energy changes and the scattering angle.

Chemical bonds, thermal movement of nuclei, coherent effects for elastic scattering are considered in both cases.

Constants for the above version of MCU-RFFI physical module are provided by DLC/MCUDAT - 1.0 bank of neutronics data which includes the following libraries:

- ABBN/MCU expanded and modified version of 26-group of ABBN system of constants [20];

- LIPAR, containing resonance parameters of nuclides in the resolved resonance region [21];

- TEPCON, containing multi-group cross-sections for the thermalization region [19];

- VESTA library to simulate neutron collisions with nuclei taking into account continuous changes in the neutron energy in the thermalization region, arranged in the form of probability tables obtained from S (α,β) scattering laws [19].

DLC/MCUDAT-1.0 bank and MCU-RFFI program, with the above physical module, were verified using results of more than 300 integral benchmark experiments and results of the comparison with calculations using MCNP program with constants calculated on the basis of ENDF/B-V files [22, 23]. The verification results demonstrated that the critical benchmark experiment calculation error of MCU-RFFI code is not worse than 0.2-0.4 % in K_{eff}. The reliability of this code was tested as a result of thousands of applied calculations of various types of reactors conducted in Russia during 15 years. The documentation on MCU code verification is contained in [19-27].

Calculation schemes and main assumptions

The calculation scheme of IGR reactor and main assumptions for DINAR code are described in section 4.6. The present section describes of the calculation scheme of MCU-RFFI code.

The stage of selection and validation of the calculation scheme of IGR reactor for MCU-RFFI code revealed a specific difficulty of this problem. It is related to the fact that the ratio between the volume of the fuel rod and of the special fuel sample, and the reactor volume is less than 10^{-6} for the special fuel sample. Due to this fact, the direct simulation of the reactor is impossible. A series of attempts were directed at reducing the variance using standard methods such as splitting and the Russian roulette. However these procedures turned out to be not very efficient, for example, the statistical error of calculations for the capsule with the air could not be reduced below 25-50 %, despite of the simulation of several millions of histories. That is why it was necessary to modify MCU-RFFI code as applied to the condition of this problem.

The code modification was carried out by developing the corresponding procedure [28, 29]. This procedure enables to solve the problem in two stages.

During the first stage, the criticality problem is solved. For this purpose, a relatively small object V, which contains fuel rods, is separated in the capsule (Fig. 4.10 - Fig. 4.12), and neutron fluxes to the surface of this volume are calculated. In other words, all neutrons, that cross the surface V, are recorded and stored in the disk during the simulation of the critical reactor.
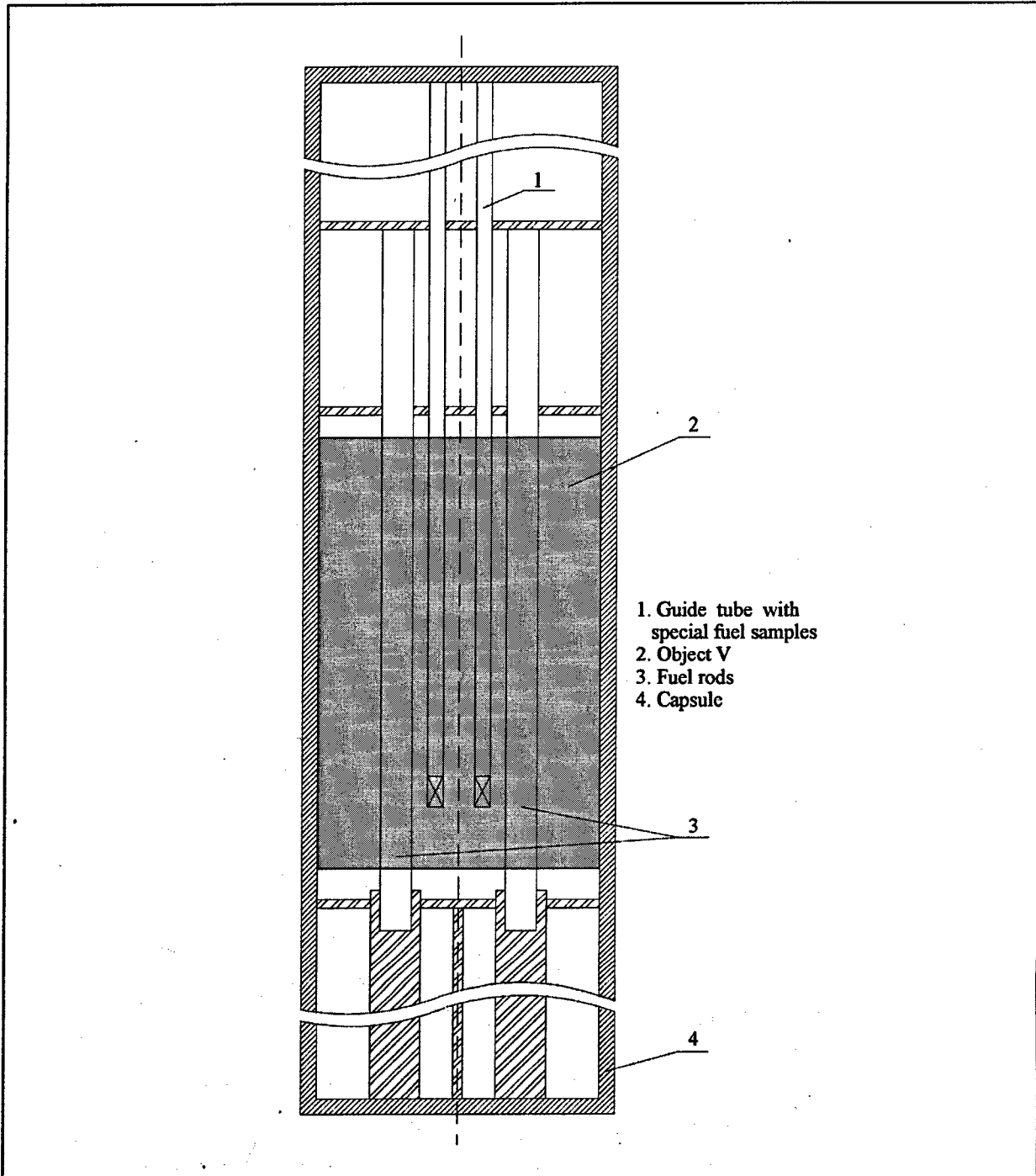
Fig. 4.10. Axial section of calculation geometrical model of object V for MCU computer code

During the second stage, neutrons recording are treated as surface sources. The non-uniform problem of the neutron field distribution inside the volume V, surrounded by the black absorber, is solved using these sources. This problem is mathematically equivalent to the original problem of the neutron distribution inside the capsule placed in the critical reactor.

This algorithm, which provides for the calculations in two stages, allowed to reduce significantly the tally variance and to shorten the count time.

1. Guide tube with special samples   3. Boundary of volume V
2. Fuel rod   4. Capsule
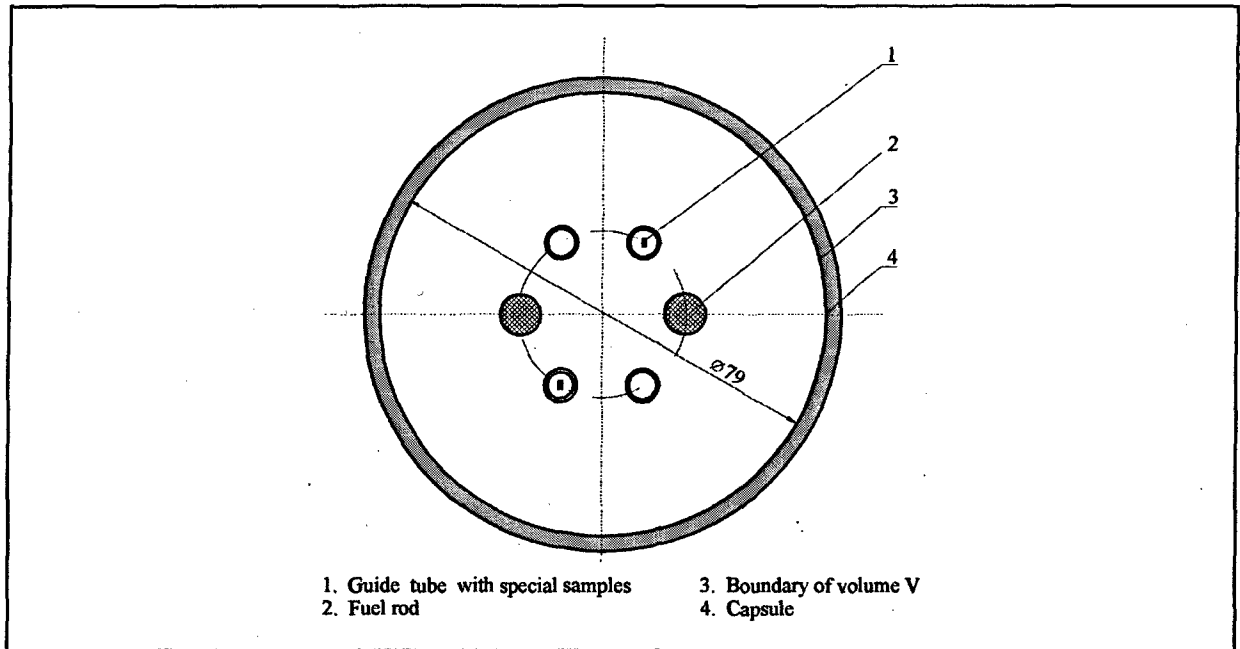
Fig. 4.11. Cross-section of the calculation geometrical model of object V for MCU computer code

1. Protective shroud   4. Thre e shrouds of reactor capsule
2. Object V   5. Reactor core
3. Capsule   6. Reflector
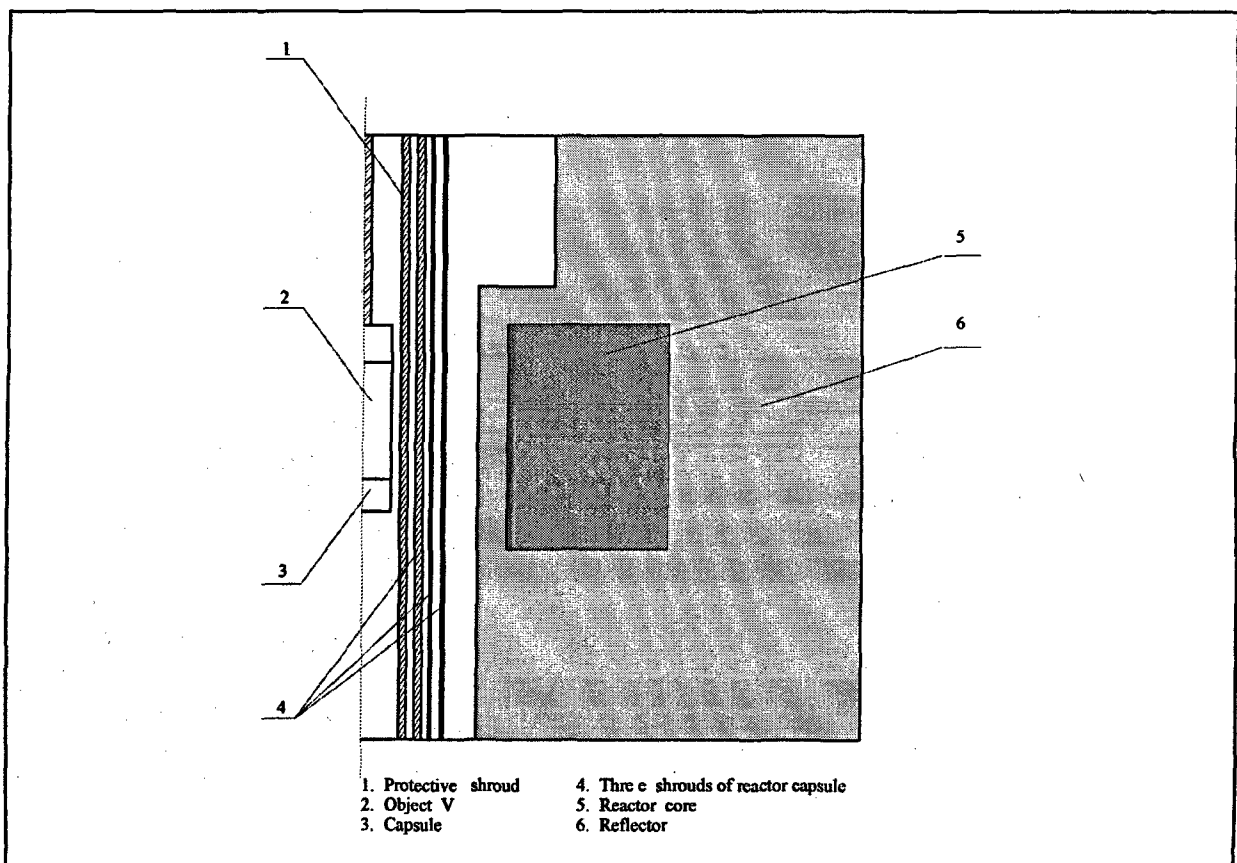
Fig. 4.12. Axial section of calculation geometrical model of IGR reactor for MCU computer code

4.23

A number of additional methods were applied to increase the count efficiency:

1. Each neutron entering the volume V was split into a number of neutrons with corresponding changes in the weight during calculations at the second stage. The combination of the splitting method with the single reactor calculations greatly improved the efficiency of procedure.

2. The hypothesis on the smooth nature of the neutron flux on the surface of the object V was used. This allowed in a random manner to shift within certain limits the coordinate and the vector of the direction for each split neutron entering the volume V. The use of this method resulted in a considerable reduction of the estimate tally variance and in an improved efficiency of the calculations.

The practical implementation of this algorithm within the framework of the specific problem required a series of optimization calculations with the aim of the final selection of the calculation scheme. The following problems were solved during the optimization calculations:

a) The shape and dimensions of the object V were selected;

b) Effects of the model type of IGR reactor on the calculation accuracy were assessed;

c) Effects of the material composition and the geometry of fuel rods in the capsule on the distribution function of the surface neutron flux at object V boundaries were assessed;

d) Splitting parameters and parameters of coordinate and the velocity vector shift, that characterize neutrons entering the object V, were selected.

The shape and dimensions of the object V were determined in accordance with the following requirements:

• effects of individual differences in the geometry and the material composition of fuel rods on the neutron flux at the surface of the object V should be negligible;

• dimensions of the object V should ensure the maximum reduction of the calculation result variance.

The practical implementation of these requirements allowed to obtain the following geometric characteristics of the object V:

- the shape of the object is cylinder;

- the radius of the object is 39.5 mm;

- the height of the object is 170 mm.

The assessment of the effects of IGR reactor model on the calculation accuracy was carried out on the basis of comparing neutron spectra at the surface of the capsule, obtained within the framework of the solution of the stationary problem, with the reference spectrum calculated by solving the non-stationary problem.

The analysis of the effects of the material composition and the geometry of fuel rods on neutron flux parameters at the surface of the object V demonstrates that individual features of fuel rods have practically no effects on surface neutron fluxes (for this particular calculation model of the reactor). This circumstance was used to develop the scheme of performing variant calculations of fuel rods.

Scheme of variant calculations and calculation results

In accordance with optimization calculation results, the following two criticality calculations of IGR reactor were carried out within the framework of the first stage of ALIGR algorithm implementation:

• reactor calculations for the version of water filling of the capsule with fuel rods;

• reactor calculations for the version of air filling of the capsule with fuel rods.

Calculations resulted in values of surface fluxes of neutrons entering the object V.

23 calculations of IGR reactor with 23 variants of geometric dimensions and material compositions of capsules with fuel rods of C, D, F types were performed for the second stage of ALIGR algorithm. In this case two sets of values of surface fluxes of neutrons entering the object V, that were obtained at the first stage of implementing the algorithm, were used as the input data.

Calculations results, presented in the table form of integral number of fissions in tally regions for each of the main fissile isotopes, were the input data for procedures to determine energy deposition fields in each C, D, E fuel rods, described on section 4.8. The calculations were performed for the following scheme of dividing fuel rods into tally regions:

4.24

- number of regions along the radius - 5 (5th region corresponds to rim layer);
- number of regions along the height - 15-20.

In addition to tables of integral number of fissions in tally regions, the integral number of fissions in the volume of the fuel rod, the integral number of fissions in the special fuel sample and the ratio between the number of fissions in the central fuel pellet of E-type fuel rod and in the special fuel sample were calculated for each fuel rod. These results were also used as input data for the procedure described in section 4.8.

Calculation error

The basic error of the method is the methodological one, related to the error of assigning the neutron flux distribution at the surface of the volume V. This error is due to the fact that the neutron flux was calculated within the framework of the above approximation on the possibility of switching from the solution of the non-stationary problem to the solution of the stationary criticality problem. According to calculations, this error is about 3 %.

The systematic error related to the data base on constants is 0.5 % – 1 %. The statistical error of calculating the number of fissions in fuel rods and in special fuel samples does not exceed 2 % (one standard deviation). The statistical error of calculating the ratio between the number of fissions in the central fuel pellet of E-type fuel rods and the number of fissions in special fuel samples is about 2.2 %.

Verification procedures

As it has already been noted, MCU code was reliably verified on the basis of various experiments including assemblies of different geometry and material composition. Within the framework of this work, the following additional verification procedures were implemented:

a) The comparison of calculated and experimental values of coefficients, that connect the integral (over the duration of the tests) number of fissions in central fuel pellets of E-type fuel rods and in special fuel samples, was carried out.

b) The comparison of calculated and experimental number of fissions distributions in C-type fuel rods was carried out using results of special experiments at MIR research reactor.

Verification procedure using measured number of fissions in central fuel pellet of E-type fuel rods

According to the analysis of results of comparing calculation and experimental ratios of number of fissions in fuel rods of type E and fuel rods of type C, the average relative deviation of these values is about 4 %.

Verification procedure using MIR reactor experiment

The purpose of this work was to conduct a special experiment with fuel rods of C and E types at MIR research reactor, to perform the calculation simulation of fission densities in fuel rods using MCU code and to compare calculation and experimental results.

MIR reactor is a channel-type research thermal neutron reactor intended for lifetime testing of fuel assemblies and individual fuel rods of various reactors [30, 31].

MIR reactor core is located in the water pool and consists of hexagonal beryllium blocks. Blocks are arranged with a gap to ensure the cooling with the pool water. There are holes along the axis of the central block and of blocks of the first four rows of the reactor core to position reactor fuel assemblies and loop experimental channels.

Experimental channels are located in the second and the third rows of the reactor stack to ensure the arrangement when each of them is surrounded by 6 channels with reactor fuel assemblies. The reactor fuel assembly consists of co-axial annular fuel rods (2 mm thick, 2.5 mm space between fuel rods). The height of the fuel rod core in the reactor fuel assembly is 1000 mm. The fuel is uranium-aluminum alloy with 90 % enrichment in U^{235}; fuel cladding is made of aluminum alloy. The maximum reactor power is 3.6 MW. The power is controlled using control rods. The cartogram of MIR reactor core is presented in Fig. 4.13.

The scheme of the special verification experiment conducted at MIR reactor was as follows [32]:

1. Three C-type fuel rods and three E-type fuel rods were manufactured. C-type fuel rods were fabricated from commercial fuel elements ## 316, 23 and 166 of fuel assembly # 1114 of NV NPP-5. The average

   fuel burnup in refabricated fuel rods was 49.2, 44.4, 43.2 MWd/kg U. γ-spectrometric measurements of fuel rod activity were performed.

4.25

2. Six fuel rods of C and E types were irradiated in the experimental channel # 3-7 of MIR reactor. In addition to fuel rods of C and D types, six fuel rod simulators (rods with steel cladding, filled with water) were installed in the channel. Fuel rod simulators were used as activation detectors to determine the distribution of the thermal neutron flux in the channel. The arrangement of fuel rods in the channel is presented in Fig. 4.14.

Reactivity shim fuel assembly;

Operating channel with MIR fuel assembly;

Experimental loop channel;

Special channel;

Compensator rod;

Control rod.
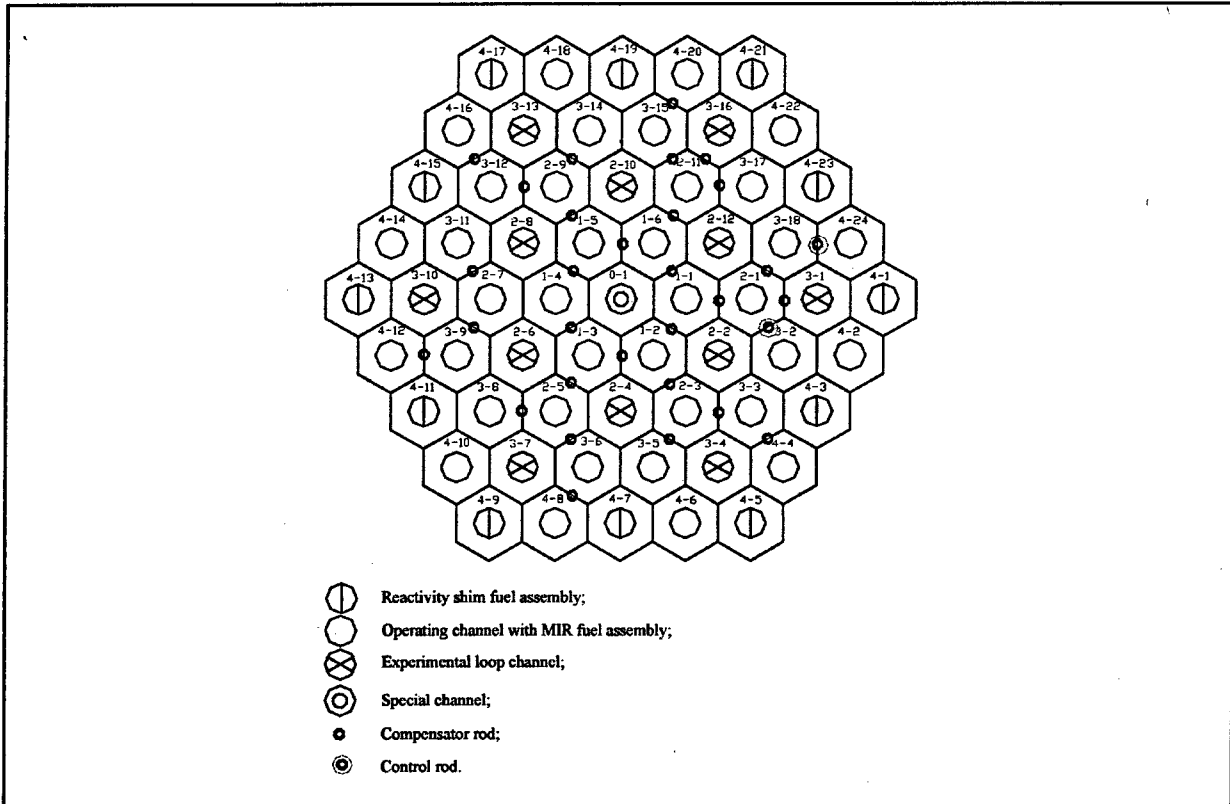
Fig. 4.13. The cartogram of MIR reactor core

H   High burnup fuel rods
S   Simulator of fuel rods
F   Fresh fuel rods
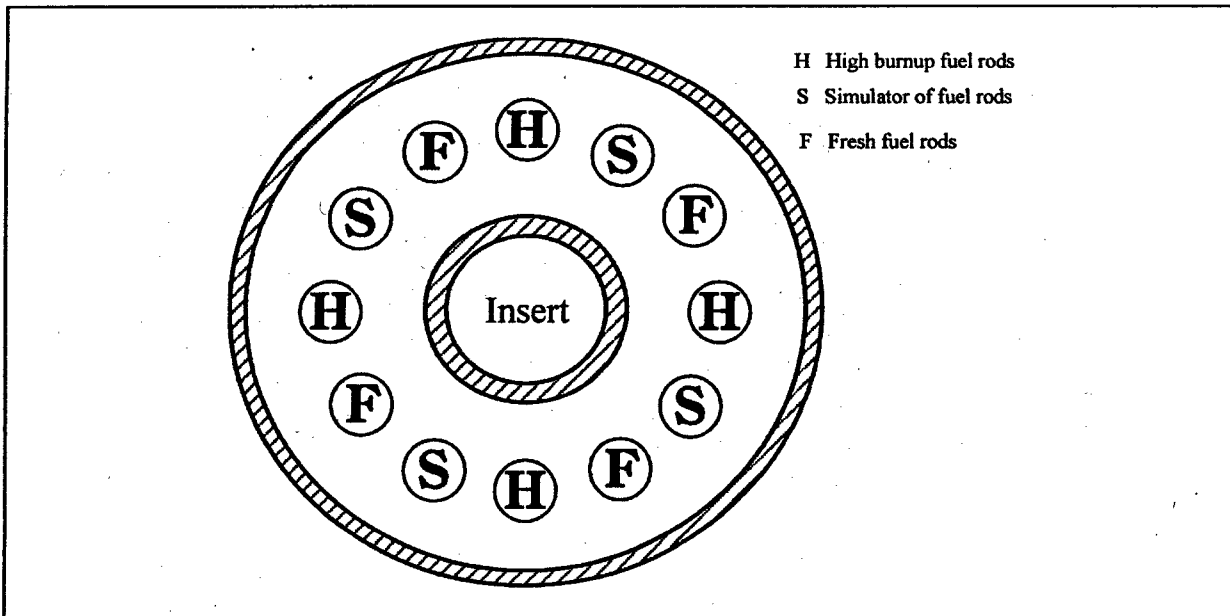
Fig. 4.14. The arrangement of fuel rods in the loop channel at MIR reactor

3. Fuel rod irradiation conditions were as follows:

- coolant temperature at the channel inlet   182°C
- coolant temperature at the channel outlet   186°C
- coolant flow rate   5000 kg/hour
- coolant type   water
- irradiation time   5 days
- MIR reactor fuel assembly power   about 500 kW

4. γ-spectrometric measurements were performed after fuel rods were removed from MIR reactor, and the axial distribution of Zr^{95} was obtained for fuel rods of C- and E- type. Each measurement was repeated 10 times.

5. Zr^{95} isotope concentration ratios in central fuel pellets of C- and E-type fuel rods were determined in accordance with measurement results under item 4 taking into account corrections related to the non-uniformity of the neutron flux in fuel rod locations and differences in coefficients of gamma quanta self absorption in fuel rods with the fresh and burnt-out fuel.

The random error in determining the concentration ratios is ~ 3.5% (2σ).

The computer modeling of this experiment was performed using MCU code. The reactor cell containing a loop channel surrounded with six fuel assemblies of the reactor core was used as the calculation model (Fig. 4.15).

Input data for calculations were taken from [32].

The verification procedure covered the comparison of the calculation and experimental ratio K, where K characterizes the ratio between the fission density in the central fuel pellet of C-type fuel rod and the fission density in the central fuel pellet of E-type fuel rod. Results of this procedure are presented in Table 4.5.
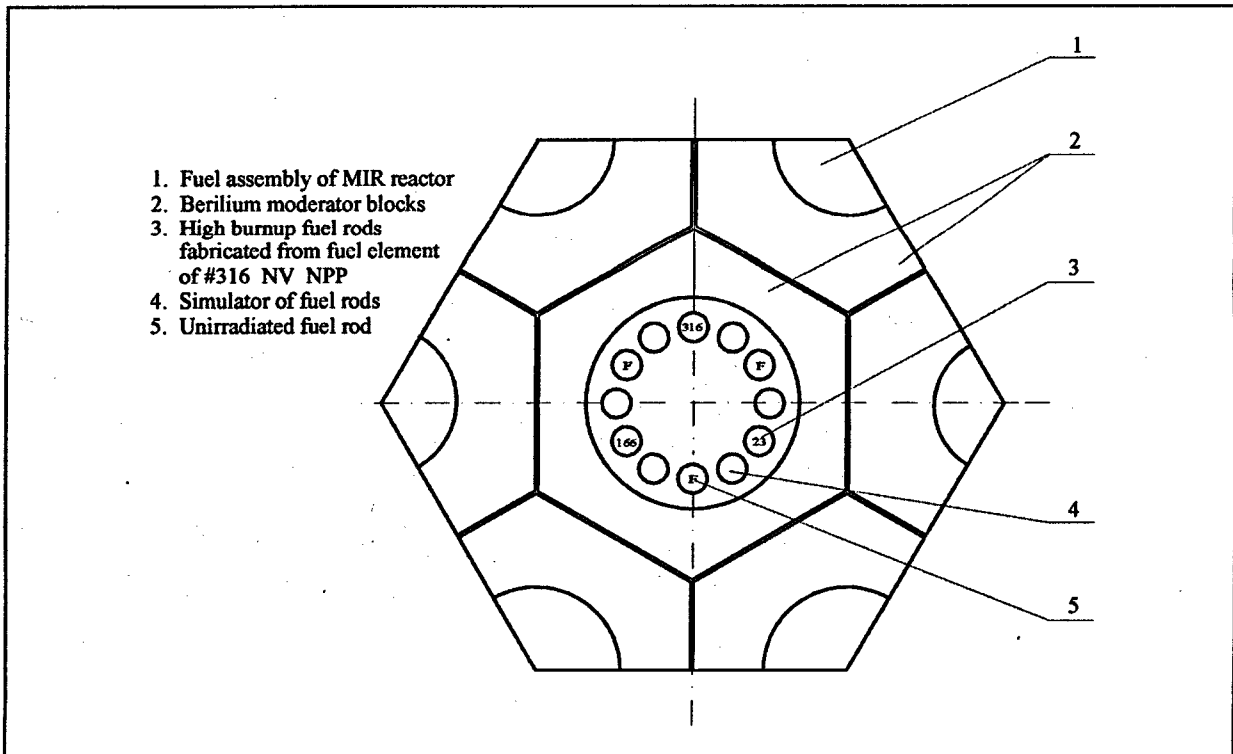
Fig. 4.15. The calculation cell for MCU code

Table 4.5. Verification results of MCU code based on MIR reactor experiment

Number of fuel rod tested at MIR reactor	Fuel burnup (MWd/kg U)	K_m as measured (per-unit)	K_c as calculated (per-unit)	$\dfrac{K_m - K_c}{K_m}100\,(\%)$
1	49.2	0.358	0.365	-2
2	44.4	0.388	0.392	-1
3	43.2	0.388	0.417	-7

According to verification results, the average difference between experimental and calculation results does not exceed the statistical measurement error. Thus, the verification confirmed a high quality of the procedure developed to determine the energy deposition in fuel rods of C-, D-, E- types.

4.8. r, z, t distribution of the energy deposition and power of fuel rods

A special algorithm was developed to determine the energy deposition distribution in fuel rods of C-, D-, E-types as a function of time and r, z coordinates [32]. The main components of the algorithm are presented below.

Input data

The following was used as the input data:

- sets of fission values in tally regions of fuel rods of C-, D-, E- types, obtained as a result of the procedure described in section 4.7;

- sets of integral number of fissions values in the fuel volume of fuel rods of C-, D-, E- types and in special fuel samples, obtained according to the procedure described in section 4.7;

- values of coefficients connecting the number of fissions in central fuel pellets of E-type fuel rods and the number of fissions in special fuel samples, that were calculated on the basis of the procedure in section 4.7;

- experimental values of number of fissions in central fuel pellets of E-type fuel rods and in special fuel samples, experimental values of coefficients connecting the number of fissions in central fuel pellets of E-type fuel rods and the number of fissions in special fuel samples, that were obtained on the basis of procedures described in sections 4.3, 4.4;

- adjusted profiles of power and energy deposition in IGR reactor versus time, obtained within the framework of procedures in section 4.6;

- geometry and material composition of fuel rods of C-, D-, E- types and of the capsule in accordance with the data base in Appendixes C, D, E, F, Volume 3 of the present Report;

- geometry and material composition of special fuel samples in accordance with the data in chapter 2 of the present volume.

Norming the set of calculated fission densities

The set of integral values of fission densities in tally regions of fuel rods of C-, D-, E- types, calculated using MCU code, was obtained within the framework of solving the stationary criticality problem. In this case the integral number of fissions characterizes the number of fissions caused by one neutron entering the volume V (capsule with fuel rods). The procedure of switching to the set of real integral fission densities in tally regions of fuel rods of C-, D-, E- types over the entire time of the tests was implemented using the following ratios:

$$n_{im} = n_{ic}\,k_m f_{fr} \tag{1}$$

$$k_{1m} = \frac{n_{sm}}{n_{sc} f_{frs}} \qquad\qquad k_{2m} = \frac{n_{Em}}{n_{Ec} f_{frE}}$$

$$k_m = \frac{k_{1m} + k_{2m}}{2} \qquad \text{\textit{for two fuel rods in the capsule,}}$$

$$k_m = k_{1m} \qquad \text{\textit{for one fuel rod in the capsule,}}$$

where n_{im} = the calculated (on the basis of experimental data) fission density in a given elementary volume of the fuel rod for the ith fissile isotope at the mth test (fiss./cm³);

n_{ic} = the fission density in a given elementary volume for the ith fissile isotope at the mth test (fiss./cm³), that was calculated based on the procedure in section 4.7;

k_m = the norming coefficient (per-unit);

f_{fr} = the temperature correction which depends on the fuel rod of type C, D, E (see section 4.9) (per-unit);

k_{1m} = the norming coefficient for the number of fissions in the special fuel sample (per-unit);

k_{2m} = the norming coefficient for the number of fissions in the central fuel pellet of E-type fuel rod;

n_{sm} = the measured number of fissions in the special fuel sample (fiss./g U²³⁵);

n_{sc} = the calculated number of fissions in the special fuel sample (fiss./g U²³⁵);

n_{Em} = the measured number of fissions in the central fuel pellet of E-type fuel rod (fiss./gU²³⁵);

n_{Ec} = the calculated number of fissions in the central fuel pellet of E-type fuel rod (fiss./gU²³⁵);

f_{frS} = the temperature correction for special fuel sample (per-unit);

f_{frE} = the temperature correction for fuel rods of E-type (per-unit).

Determination of the spatial distribution of the fission rate for fuel rods of C-, D-, E- types versus time

The fission rate of each fissile isotope in a given elementary volume of a specific fuel rod as a function of time was determined using the following formula:

$$R_i(r,z,t_k) = \frac{P(t_k)n_{im}}{E_r},$$

where $R_i(r,z,t_k)$ = the fission rate for the ith isotope at t time moment (fiss./cm³s);

$P(t_k)$ = the reactor power in the ionization chamber measurement units at t_k time moment (μA);

n_{im} = the number of fissions for the ith isotope over the entire test, adjusted based on formula (1) (fiss./cm³);

E_r = the energy deposition in IGR reactor over the entire time of the test in the ionization chamber measurement units (μAs).

The integral fission density for the ith isotope in a given elementary volume of the fuel rod at time moment t_k is determined on the basis of the formula:

$$n_i(t_k) = \frac{n_{im}\sum_{k=1}^{k} P(t_k)\Delta t_k}{E_r},$$

where $n_i(t_k)$ = the integral fission density for the ith isotope in the time interval 0-t_k (fiss./cm³);

n_{im} = the integral fission density for the ith isotope over the entire test (fiss./cm³);

$P(t_k)$ = the reactor power at time moment t_k in the ionization chamber measurement units (μA);

Δt_k = the time step in the numeric scheme (s);

E_r = the reactor energy deposition over the entire test in the ionization chamber measurement units (μAs).

<u>Calculation procedure to determine the energy deposition in fuel rods of C-, D-, E-types</u>

In the general case, the balance of the volume energy density in the elementary fuel volume at time moment t can be written in the following form:

$$E_{fr}(t) = E_{ff}(t) + E_{pr}(t) + E_{\beta}(t),$$

where $E_{fr}(t)$ = the integral energy deposition in the elementary volume of the fuel rod (C, D, E) at time t (J/cm^3);

$E_{ff}(t)$ = the energy deposition due to fission fragments of all fissile isotopes (J/cm^3);

$E_{pr}(t)$ = the energy deposition in the fuel due to prompt neutron and gamma radiation (J/cm^3);

$E_{\beta}(t)$ = the energy deposition in the fuel due to delayed beta and gamma radiation (J/cm^3).

The energy deposition due to fission fragments in the elementary volume of the fuel rod was calculated on the basis of the formula:

$$E_{ff}(t_k) = \sum_{i=1}^{n} E_i n_i(t_k),$$

where $E_{ff}(t_k)$ = the integral energy deposition due to fission fragments by the time moment t_k (J/cm^3);

E_i = the kinetic energy of fragments in case of fission of the ith isotope [34] (J/fiss.);

$n_i(t_k)$ = the integral fission density for the ith isotope in the time interval 0-t_k (fiss./cm^3);

i = the number of the isotope: for C-type fuel rod $n=4$ (U^{235}, U^{238}, Pu^{239}, Pu^{241}), for fuel rods of D and E types $n=2$ (U^{235}, U^{238}).

Values of the kinetic energy of fragments, which were used to determine energy deposition, are presented in Table 4.6.

Table 4.6. Kinetic energy of fragments

Energy (MeV/fiss.)	Isotope			
	U^{235}	U^{238}	Pu^{239}	Pu^{241}
	172.7	170.3	178.6	175.1

The energy deposition due to the prompt neutron and gamma radiation was calculated according to the formula:

$$E_{pr}(t_k) = E_{pr,fr} \sum_{i=1}^{n} n_i(t_k),$$

where $E_{pr}(t_k)$ = the integral energy deposition in the elementary volume of the fuel rod due to the prompt radiation by the time moment t_k (J/cm^3);

$E_{pr,fr}$ = the energy deposition due to the prompt radiation absorbed in the volume of the fuel rod of C-, D-, E- types and normalized per the number of fissions in the fuel rod volume (J/fiss.);

$n_i(t_k)$ = the integral fission density for the ith isotope in time interval 0-t_k (fiss./cm^3).

Energy deposition values due to the prompt radiation in the entire fuel volume $E_{pr,fr}$ were calculated using ANISN computer code with CASK system of constants [35]. The radial distribution of the neutron density in IGR reactor was calculated with CITATION code [36]. The obtained radial distribution of the neutron density was used as the input data for ANISN code. The neutron radiation contribution to the energy deposition was assessed using kerma-factors from the library of BLANC code [37]. The neutron sources ratio in IGR reactor and in fuel rods was determined using experimental data obtained in IGR reactor. Table 4.7 presents values of $E_{pr,fr}$ and of their components.

Table 4.7. Energy deposition due to the prompt radiation in fuel rods of C-, D-, E- types

Type of radiation	Energy deposition (MeV/fiss.)					
	E, D type of fuel rod		C type of fuel rod			
			fuel rod refabricated from #22 fuel element		fuel rod refabricated from #317 fuel element	
	water coolant	air coolant	water coolant	air coolant	water coolant	air coolant
Neutrons from reactor	0.007	0.02	0.01	0.04	0.02	0.06
Neutrons from fuel rod	0.025	0.02	0.03	0.02	0.03	0.03
Gamma quanta	6.1	9.1	8.0	12.7	8.3	14.3
Total	**6.2**	**9.2**	**8.0**	**12.7**	**8.4**	**14.4**

The power due to the delayed beta and gamma radiation was calculated as a function of time using the following formula [38]:

$$P_\beta(t_k) = \sum_{i=1}^{n} \int_0^{t_k} R_i(t')[\beta_i(t_k - t') + C\gamma_i(t_k - t')]dt',$$

Where $P_\beta(t_k)$ = power deposited in the fuel rod due to delayed radiation at time moment t_k (MeV/s);

t' = time moment when the neutron, that caused the fission, was absorbed (s);

$R_i(t')$ = fission rate at the time moment t' (fiss./s);

$\beta_i(t_k-t')$ = power deposited in the fuel rod after the fission of the ith isotope due to delayed β radiation during the time interval t_k-t' [38] (MeV/s·fiss.);

$\gamma_i(t_k-t')$ = power deposited in the fuel rod after the fission of the ith isotope due to delayed γ radiation during the time interval t_k-t' [38] (MeV/s·fiss.);

C = fraction of γ radiation absorbed energy in the fuel rod (per-unit);

i = number of fissile isotope.

Calculations of fuel rod power due to the delayed radiation were performed taking into account the assumption that all the energy of beta particles is deposited in the fuel rod.

Coefficient C in the formula to determine the power deposited in the fuel rod due to the delayed radiation was determined as a result of calculations with ANISN code in accordance with the procedure used to calculate $E_{pr}(t_k)$. Values of this coefficient are presented in Table 4.8. To determine the contribution of delayed radiation the data characterizing $E_\beta(t)$ are presented in the Fig. 4.16 for one of high burnup fuel rods tested at IGR reactor.

Table 4.8. Energy fraction of the delayed gamma radiation absorbed in fuel rods of C-, D-, E- types vs. time

Coolant type	Value of C coefficient (per-unit)		
	E-, D- types of fuel rod	fuel rod refabricated from #22 fuel element	fuel rod refabricated from #317 fuel element
Water	0.29	0.34	0.33
Air	0.36	0.42	0.44
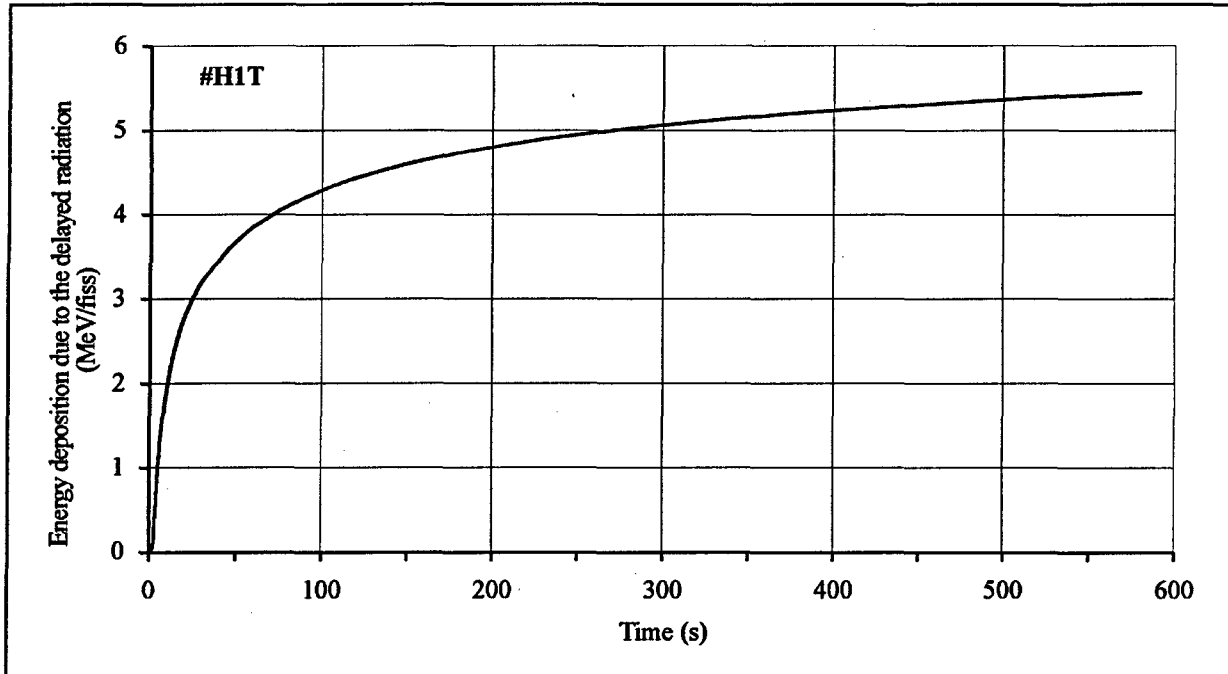
Fig. 4.16. $E_\beta(t)$ normalized on the one fission vs. time for fuel rod #H1T

The energy deposition in fuel rods of C-, D-, E- types due to the delayed radiation $E_\beta(t_k)$ was determined using the procedure of integrating the sets of $P_\beta(t_k)$ values. In the final form, the set of energy deposition values in fuel rods of C-, D-, E- types is presented in tables of Appendixes G, H, I, Volume 3, as energy per fuel unit mass. A corresponding set of power values was determined due to the procedure of differentiating the corresponding values of energy deposition using reactor power profile versus time.

4.9. Dependence of the number of fissions in fuel rods on the temperature

As it has been noted in section 4.7, calculations of the spatial distribution of the number of fissions in fuel rods of C-, D-, E- types with MCU code were carried out without considering the temperature changes of the reactor core, the coolant in the capsule and fuel rods, i.e. at the initial conditions.

From the physical point of view the thermal neutron spectrum is a function of the temperature. In its turn, the thermal neutron spectrum determines the ratio of fission densities for various fissile isotopes. It is special importance for C-type fuel rods, i.e. for fuel rods containing isotopes of Pu^{239} and Pu^{241} since there are clearly expressed resonances for these isotopes in the energy region of 0.3 - 0.5 eV. This factor results in changes of the fission density ratio for all main fissile isotopes U^{235}, Pu^{239}, Pu^{241} depending on the neutron gas temperature in the capsule with fuel rods; moreover, the neutron gas temperature affects the block-effect in fuel rods.

According to a preliminary analysis, the maximum differences in the number of fissions density in C-type fuel rod taking into account temperature change effects does not exceed 4 % of the initial values of the fission density obtained for the value of $T_0=17°C$. Thus, in the final form the temperature correction was introduced as an average in time and fuel isotopic composition. To determine it the following function was used:

$$f_{fr} = \frac{1}{E_r} \int_0^\infty \varphi(t) P(t) dt,$$

where f_{fr} = the temperature coefficient in formula (1) in section 4.8;

4.32

$\varphi(t) =$ the functional reflecting the ratio of fission densities in the fuel rod for the initial and current temperature values (at time moment t) (per-unit);

$P(t) =$ IGR reactor power in the ionization chamber measurement units (μA);

$E_r =$ the integral energy deposition in the reactor in the ionization chamber measurement units (μAs).

Calculations of the functional $\varphi(t)$ were performed using the following formulas:

$$\varphi(t) = \frac{k_T(t)}{k_{To}},$$

$$k_T(t) = \frac{\sum_{i=1}^{n} n_{fr}(t)}{\sum_{i=1}^{n} n_s(t)}, \quad k_{T_o} = \frac{\sum_{i=1}^{n} n_{To,fr}}{\sum_{i=1}^{n} n_{To,s}},$$

where $\varphi(t) =$ the functional which takes into account the ratio of fission densities in the fuel rod for the initial temperature and the temperature at the time moment t (per-unit);

$k_{To}, k_T(t) =$ coefficients characterizing the ratios of the section-average fission density in the central fuel pellet of the fuel rod and the fission density in the special fuel sample for the initial temperature T_o and temperature T, respectively (per-unit);

$n_{To,fr}, n_{fr}(t) =$ fission densities in the central fuel pellet for the ith isotope for the initial temperature T_o and temperature T, respectively (fiss./cm^3);

$n_{To,s}, n_s(t) =$ fission densities in the special fuel sample for the ith isotope for the initial temperature T_o and temperature T, respectively (fiss./cm^3);

$i =$ the number of the fissile isotope.

This approach to the determination of temperature corrections was implemented within the framework of the following procedure:

1. The determination of the radial distribution of the energy deposition in IGR reactor, the fuel rod and the coolant for critical reactor conditions (i.e. at temperature T_o). Calculations of the energy deposition from fission sources were carried out using CITATION code [36].

2. The differentiation of the absolute value of the energy deposition in the reactor according to the reactor power as a function of time. The absolute value of the energy deposition in IGR reactor (J) was determined experimentally at the end of each test.

3. The formation of the set of energy deposition radial distributions in the reactor as a function of time, using calculation results under item 1 and the set of integral values of the power deposition in the reactor as a function of time obtained under item 2.

4. Calculations of the radial temperature distribution in the reactor as a function of time using the set of energy deposition radial distributions as a function of time and the set of values of the material heat capacity of the reactor core and the capsule as a function of time.

5. The formation of the set of temperature distribution of the fuel in the fuel rod as a function of time by using results of the computer simulation of thermo-mechanical fuel rod behavior with FRAP-T6 code according to the procedure described in section 4.11.

6. Determination of the set of fission densities in fuel rods of C-, D-, E- types and in special fuel samples as a function of time (i.e. as a function of temperature) by carrying out the computer simulation of IGR reactor, in each of the time moments t under consideration, using WIMS-4D code [39]. Sets of z,t temperature values obtained in accordance with procedures in items 4 and 5 were used as the input data for WIMS code.

Results of calculating temperature coefficients f are presented in Table 4.9 for C-type fuel rods. This set of values was used in the procedure in section 4.8 during the stage of using the formula (1). Results of

calculating temperature coefficients for fuel rods of D-, E- types demonstrate that, since the main contribution to the fission process in these fuel rods is made by isotope U^{235}, the value of coefficient f does not exceed 1.005. Therefore, the temperature coefficient in fuel rods of D-, E- types was not considered.

Table 4.9. Values of the temperature coefficient f for C-type fuel rods

Para-meter	Number of fuel rod												
	H1T	H2T	H3T	H4T	H5T	H6T	H7T	H8T	B9T	B10T	B11T	B12T	B13T
f (per-unit)	1.018	1.02	1.02	1.014	1.017	1.01	1.017	1.005	1.02	1.015	1.03	1.025	1.03

4.10. Uncertainty analysis

This chapter covers the analysis of uncertainties related to the determination of the fuel rod energy deposition and the power.

Errors in other characteristics used as incoming data to calculate the fuel rod energy deposition and the power are presented in corresponding sections of Chapter 4.

The algorithm of the uncertainty analysis in energy deposition units contains the following sequential stages:

- determination of the random and systematic errors in the integral energy deposition in the elementary volume of each fuel rod type (here, the term "elementary volume" is equivalent to the one in sections 4.7, 4.8);

- determination of the random and systematic errors in all types of r, z, t distributions of the energy deposition in fuel rods.

The error assessment was performed for each fuel rod type on the basis of their specific set according to the following scheme:

- H7T for high burnup fuel rods cooled by water;

- B9T, B13T for high burnup fuel rods cooled by air (fuel of B9T rod had the burnup of 42 MWd/kg U, fuel of B13T rod had the burnup of 49 MWd/kg U);

- H16T for fuel rods of D, E types cooled by water;

- B20T for fuel rods of D, E types cooled by air.

The error assessment of the energy deposition in high burnup fuel rods was performed only for undamaged sections (see Table C.2.1-C.2.3 Appendix C, Volume 3 of the Report).

4.10.1. Methodological aspects of the procedure

The analysis was based on the determination of the following characteristics of the error for an arbitrary parameter X.

- standard deviation S_x for the assessment of the random error in determining parameter X;

- boundary of the non-eliminated remainder θ_x for the assessment of the systematic error in determining parameter X;

- total error Δ_x for the assessment of the accumulated error in determining parameter X.

Values S_x and θ_x were assessed with 95 % confidence level. The total error was calculated using the following formula (with the same confidence level):

$$\Delta_x = S_x + \theta_x$$

4.34

Regarding the distribution laws of assessed values, standard assumptions were made:

- all reference random values, which determine the set of values S_{xi}, have Gaussian distribution;
- all reference random values, which determine the set of values θ_{xi}, have equipartition distribution.

Since the main set of reference data characterizing errors in measured parameters was presented in the form of the relative error expressed in percentage, this procedure also uses values δ_x, S_x and θ_x, presented in the relative form:

$$\delta_x = \frac{\Delta_x}{\overline{X}}100; \quad \delta_{Sx} = \frac{S_x}{\overline{X}}100; \quad \delta_{\theta x} = \frac{\theta_x}{\overline{X}}100;$$

where $\delta_x, \delta_{Sx}, \delta_{\theta x}$ = relative total error, relative standard deviation, relative systematic error, respectively (%);

$\overline{X}$ = the sample mean of value X.

The assessment of the error in determining the value $y=f(X_1,X_2...X_k...X_m)$ was performed using the following approach [40, 41]:

$$\delta_{Sy} = \sqrt{\sum_{k=1}^{m} \delta_{Sy}^2(X_k)},$$

$$\delta_{Sy}(X_k) = \frac{\overline{X}}{y}\frac{\partial f}{\partial X_k}\,\delta_S(X_k),$$

$$\delta_{\theta y} = 1.1\sqrt{\sum_{k=1}^{m} \delta_{\theta y}^2(X_k)},$$

$$\delta_{\theta y}(X_k) = \frac{\overline{X}}{y}\frac{\partial f}{\partial X_k}\delta_\theta(X_k),$$

$$\delta_y = \delta_{Sy} + \delta_{\theta y},$$

where y = the complex parameter which is a function of f type of values $X_1...X_k...X_m$;

$\delta_{Sy}(X_k), \delta_{\theta y}(X_k)$ = random and systematic relative errors in determining parameter y due to the presence of random and systematic errors in determining the reference value X_k (%);

$\delta_y, \delta_{Sy}, \delta_{\theta y}$ = total, random, systematic relative errors in parameter y, respectively, (%).

4.10.2. Energy deposition error in the elementary volume of fuel rods

Type of the functional dependence to determine the energy deposition in the elementary volume of fuel rods of C-, D-, E- types.

As it was indicated in section 4.10.1, the error calculation for the complex parameter y (which, in this case, is the energy deposition in the fuel rod elementary volume) is based on the differentiation on partial derivatives of function $y = f(X_1...X_m)$. Thus, combining the individual stages of the complex procedure to determine the energy deposition (see sections 4.8, 4.9) into a single functional dependence is a necessary step in order to analyze the energy deposition determination error. The result of such operations can be presented in the form of the following formula:

$$E_{fr}(t) = k_m f_{fr}\left[\sum_{i=1}^{n} E_i n_i(t_k) + (E_{pr,fr} + E_\beta)\sum_{i=1}^{n} n_i(t_k)\right],$$

where $E_{fr}(t)$ = the integral energy deposition in the fuel rod elementary volume at time t (J/cm^3);

k_m = the norming coefficient (per-unit);

4.35

f_{fr} = the temperature correction (per-unit);

E_i = the kinetic energy of fission fragments per one fission event of the ith isotope (J/fiss.);

$n_i(t_k)$ = the integral calculated fission density for the ith isotope in the time interval $0\text{-}t_k$ (fiss./cm^3);

$E_{pr,fr}$ = the energy of prompt neutron and gamma radiation deposited in the fuel per one fission event (J/fiss.);

E_β = the energy deposited in the fuel due to delayed beta and gamma radiation per one fission event (J/fiss.).

Procedure to determine errors in parameters determining the type of the functional dependence for the energy deposition in the elementary volume of fuel rods of C-, D-, E- types

A detailed description of this rather complex procedure is outside the scope of the Report, thus, only its main principles are presented here.

The basic provisions of this procedure are as follows:

- passport data for sensors or results of metrological qualification of the method are used as random and systematic components of the error for all measured parameters;

- random and systematic errors of computer codes are presented in the form of results of their qualification, verification or results of implementing special standard procedures to assess the computer code errors;

- errors in parameters which are functions of a known type of measured characteristics are determined in accordance with the requirements of the procedure in section 4.10.1;

- errors in parameters which practically cannot be presented in the form of a strict functional dependence are assessed using the sensitivity method of calculation results to incoming parameters.

To analyze the sensitivity of calculation results to incoming parameters, a method was selected which is based on the perturbation theory [42, 43].

In this method the sensitivity coefficient of the functional to the incoming parameter is presented in the following form [42]:

$$P_{Rn}(X_1, X_2 ... X_N) = \lim_{\Delta X_n / X_n \to 0} \frac{\Delta R / R}{\Delta X_n / X_n},$$

where P_{Rn} = the sensitivity coefficient of the outgoing parameter R, that characterizes changes in parameter R in percentage in case of changing the incoming parameter X_n by 1%;

$X_1, X_2 ... X_N$ = incoming parameters;

$\Delta X_n, \Delta R$ = increments in parameters X_n and R;

n = 1, 2, ... N.

The final purpose of this method is to determine the relative error in the outgoing parameter $\delta_R = \Delta R / R$ using the dependence which, for the case of the linear relation between δ_R and δ_{Xn}, is as follows:

$$\delta_R = \sum_{n=1}^{N} P_{Rn} \, \delta_{Xn} \, ,$$

where δ_R = the relative error in the outgoing parameter R;

δ_{Xn} = the relative error in the incoming parameter $X_n (\delta_{Xn} = \Delta X_n / X_n)$;

P_{Rn} = the sensitivity coefficient.

The functional to determine δ_R for the case of non-linear relation between the incoming and outgoing parameter is much more complex and is not presented here.

In practice, procedures of the sensitivity analysis of outgoing parameters (such as fission densities, etc.) to incoming parameters (such as fuel mass in the elementary volume, burnup, nuclide composition, etc.) were applied using computer code WIMS-4D [39] or the same computer codes used within the framework of procedures to calculate outgoing parameters (see sections 4.7, 4.8, 4.9).

To illustrate results of practical application of this method in the procedure of analyzing the energy deposition determination error in the fuel rod elementary volume, Table 4.10 contains sensitivity coefficients of fission density for different isotopes.

Table 4.10. Sensitivity coefficient of the fission density in the elementary volume of fuel rod #H7T to incoming parameters

Incoming parameters	Sensitivity coefficients of fission density for different isotopes (%)			
	U^{235}	U^{238}	Pu^{239}	Pu^{241}
Burnup	-2.5	-0.54	-0.42	0.19
Fuel mass	-0.21	0.5	-0.19	-0.19
U^{235} concentration	0.99	0.07	-0.004	-0.005
U^{238} concentration	-0.1	1.13	-0.08	-0.09
Pu^{239} concentration	-0.12	0.42	0.88	-0.12
Pu^{241} concentration	-0.01	0.06	-0.01	0.99

Results obtained using the procedure of determining energy deposition errors in the elementary volume of fuel rods of C-, D-, E- types

Errors of determining the energy deposition in elementary volumes of fuel rods of C-, D-, E- types are presented in Table 4.11 - Table 4.14.

In addition to final error values, Tables contain data on errors in all main parameters, which determine the error in the energy deposition.

Table 4.11. Energy deposition error in elementary volume of fuel rod #H7T

Incoming parameters	Random error		Systematic error	
	δ_{S_x} (%)	δ_{S_y} (X_k) (%)	δ_{θ_x} (%)	δ_{θ_y} (X_k) (%)
1.The kinetic energy of fragments (J/fiss.)	0	0	1.0	0.56
2.The energy deposition due to prompt radiation per the number of fissions (J/fiss.)	0	0	20.0	0.86
3.The energy deposition due to delay radiation per the number of fissions (J/fiss.)	0	0	20.0	0.86
4.The fission density in the central fuel pellet of the E-type fuel rod as measured (fiss./g·fuel)	4.4	4.4	2.1	2.1
5.The fission density in the central fuel pellet of the E-type fuel rod as calculated by MCU code (fiss./cm^3)	2.0	1.4	1.0	0.7
6.Burnup (MWd/kg U)	5.0	4.9	3.5	3.4
7.Fuel mass (g)	4.8	0.92	1.3	0.25
8.The concentration of U^{235} in the fuel as calculated by TRIFOB code (1/cm^3)	2.0	0.64	2.0	0.64
9.The concentration of U^{238} in the fuel as calculated by TRIFOB code (1/cm^3)	2.0	0.16	2.0	0.16
10.The concentration of Pu^{239} in the fuel as calculated by TRIFOB code (1/cm^3)	2.0	0.72	2.0	0.72
11.The concentration of Pu^{241} in the fuel as calculated by TRIFOB code (1/cm^3)	2.0	0.36	2.0	0.36
12.The fission density of U^{235} in the fuel as calculated by MCU code (fiss./cm^3)	2.0	0.65	0	0
13.The fission density of U^{238} in the fuel as calculated by MCU code (fiss./cm^3)	2.0	0.015	0	0
14.The fission density of Pu^{239} in the fuel as calculated by MCU code (fiss./cm^3)	2.0	0.95	0	0
15.The fission density of Pu^{241} in the fuel as calculated by MCU code (fiss./cm^3)	2.0	0.38	0	0
16.The thermal fission cross-section of U^{235} (cm^2)	0	0	0.5	0.34
17.The thermal fission cross-section of Pu^{239} (cm^2)	0	0	0.5	0.24
18.The thermal fission cross-section of Pu^{241} (cm^2)	0	0	0.5	0.09
19.The temperature correction coefficient (per-unit)	0	0	3.0	0.30

Total error of energy deposition is 12%.

Table 4.12. Energy deposition error in elementary volume of fuel rod #B9T

Incoming parameters	Random error		Systematic error	
	δ_{s_x} (%)	δ_{s_y} (X_k) (%)	δ_{θ_x} (%)	δ_{θ_y} (X_k) (%)
1.The kinetic energy of fragments (J/fiss.)	0	0	1.0	0.56
2.The energy deposition due to prompt radiation per the number of fissions (J/fiss.)	0	0	20.0	0.86
3.The energy deposition due to delay radiation per the number of fissions (J/fiss.)	0	0	20.0	0.86
4.The fission density in the central fuel pellet of the E-type fuel rod as measured (fiss./g·fuel)	4.4	4.40	2.1	2.10
5.The fission density in the central fuel pellet of the E-type fuel rod as calculated by MCU code (fiss./cm³)	2.0	1.64	1.0	0.82
6.Burnup (MWd/kg U)	5.0	4.5	3.5	3.1
7.Fuel mass (g)	4.8	0.53	1.3	0.14
8.The concentration of U^{235} in the fuel as calculated by TRIFOB code (1/cm³)	2.0	0.52	2.0	0.52
9.The concentration of U^{238} in the fuel as calculated by TRIFOB code (1/cm³)	2.0	0.095	2.0	0.095
10.The concentration of Pu^{239} in the fuel as calculated by TRIFOB code (1/cm³)	2.0	0.92	2.0	0.92
11.The concentration of Pu^{241} in the fuel as calculated by TRIFOB code (1/cm³)	2.0	0.36	2.0	0.36
12.The fission density of U^{235} in the fuel as calculated by MCU code (fiss./cm³)	2.0	0.54	0	0
13.The fission density of U^{238} in the fuel as calculated by MCU code (fiss./cm³)	2.0	0.026	0	0
14.The fission density of Pu^{239} in the fuel as calculated by MCU code (fiss./cm³)	2.0	1.03	0	0
15.The fission density of Pu^{241} in the fuel as calculated by MCU code (fiss./cm³)	2.0	0.40	0	0
16.The thermal fission cross-section of U^{235} (cm²)	0	0	0.5	0.36
17.The thermal fission cross-section of Pu^{239} (cm²)	0	0	0.5	0.26
18.The thermal fission cross-section of Pu^{241} (cm²)	0	0	0.5	0.1
19.The temperature correction coefficient (per-unit)	0	0	3.0	0.30

Total error of energy deposition is 11%.

Table 4.13. Energy deposition error in elementary volume of fuel rod #H16T

Incoming parameters	Random error		Systematic error	
	δ_{s_x} (%)	δ_{s_y} (X_k) (%)	δ_{θ_x} (%)	δ_{θ_y} (X_k) (%)
1. The kinetic energy of fragments (J/fiss.)	0	0	1.0	0.91
2. The energy deposition due to prompt radiation per the number of fissions (J/fiss.)	0	0	20.0	0.88
3. The energy deposition due to delay radiation per the number of fissions (J/fiss.)	0	0	20.0	0.88
4. The fission density in the central fuel pellet of the E-type fuel rod as measured (fiss./g·fuel)	4.4	4.4	2.1	2.10
5. The fission density in the central fuel pellet of the E-type fuel rod as calculated by MCU code (fiss./cm³)	2.0	1.44	1.0	0.72
6. Fuel mass (g)	0	0	0.5	0.36
7. The concentration of U^{235} in the fuel as calculated by TRIFOB code (1/cm³)	0	0	0.5	0.49
8. The concentration of U^{238} in the fuel as calculated by TRIFOB code (1/cm³)	0	0	0.5	0.048
9. The fission density of U^{235} in the fuel as calculated by MCU code (fiss./cm³)	2.0	2.0	0	0
10. The fission density of U^{238} in the fuel as calculated by MCU code (fiss./cm³)	2.0	0.007	0	0
11. The thermal fission cross-section of U^{235} (cm²)	0	0	0.5	0.002

Total error of energy deposition is 8%.

4.10.3. Errors for the fuel rod power and t distribution of the energy deposition

The following functional dependencies were used to determine the power and the energy deposition of fuel rods as a function of time (see section 4.8):

$$P(t_k) = \frac{E\, i(t_k)\, m}{\int\limits_0^\infty i(t)dt},$$

$$E(t_k) = \frac{E \int\limits_0^{t_k} i(t)dt}{\int\limits_0^\infty i(t)dt},$$

where $P(t_k)$ = the fuel rod power at the time t_k (W);

E = the integral energy deposition in the fuel rod at the time t=∞ (J/g fuel);

$E(t_k)$ = the energy deposition in the fuel rod at the time t_k (J/g fuel);

$i(t_k)$ = the ionization chamber current at the time t_k (µA);

$i(t)$ = the ionization chamber current at the time t (µA);

m = the fuel rod mass (g).

4.40

Table 4.14. Energy deposition error in elementary volume of fuel rod #B20T

Incoming parameters	Random error		Systematic error	
	δ_{S_x} (%)	δ_{S_y} (X_k) (%)	δ_{θ_x} (%)	δ_{θ_y} (X_k) (%)
1.The kinetic energy of fragments (J/fiss.)	0	0	1.0	0.91
2.The energy deposition due to prompt radiation per the number of fissions (J/fiss.)	0	0	20.0	0.88
3.The energy deposition due to delay radiation per the number of fissions (J/fiss.)	0	0	20.0	0.88
4.The fission density in the central fuel pellet of the E-type fuel rod as measured (fiss./g·fuel)	4.4	4.4	2.1	2.1
5.The fission density in the central fuel pellet of the E-type fuel rod as calculated by MCU code (fiss./cm^3)	2.0	1.6	1.0	0.82
6.Fuel mass (g)	0	0	0.5	0.40
7.The concentration of U^{235} in the fuel as calculated by TRIFOB code (1/cm^3)	0	0	0.5	0.49
8.The concentration of U^{238} in the fuel as calculated by TRIFOB code (1/cm^3)	0	0	0.5	0.047
9.The fission density of U^{235} in the fuel as calculated by MCU code (fiss./cm^3)	2.0	2.0	0	0
10.The fission density of U^{238} in the fuel as calculated by MCU code (fiss./cm^3)	2.0	0.011	0	0
11.The thermal fission cross-section of U^{235} (cm^2)	0	0	0.5	0.3

Total error of energy deposition is 8%.

4.10.4. Errors in z distributions of the energy deposition

This procedure is based on the following principles:

- the random error in the energy deposition for any axial section of the rod fuel stack is equal to the random error in the energy deposition in the fuel rod elementary volume if the length of this axial section is equal to the length of the axial section which forms the fuel rod elementary volume;

- the systematic error in the energy deposition in the axial section, determined by a corresponding dimension in the fuel rod elementary volume, includes (in addition to the systematic error in the energy deposition in the elementary volume) an additional error related to the MCU code error in calculating the axial distribution of the neutron flux in the capsule.

According to calculations, when the additional systematic error is taken into account, the total energy deposition error is increased not more than by 0.5 %.

4.10.5. Errors in r distributions of the energy deposition

According to the analysis, in comparison with the energy deposition error in the elementary volume, the total error in r distributions of the energy deposition must take into account two additional factors:

- error reduction due to the averaging procedure of the energy deposition values in elementary volumes in the volume of the radial zone;

- error increase due to the presence of an additional systematic error related to calculations of r distribution of nuclide concentrations.

According to calculation results, both these factors practically compensate one the other, and the final errors in r distributions agree within the accuracy of 0.2 % with the errors in the energy deposition in the elementary volume of fuel rods of C-, D-, E- types.

Errors in parameters $P(t_k)$ and $E(t_k)$ were calculated in accordance with the procedure described in section 4.10.1, calculation results are presented in Table 4.15, Table 4.16.

Table 4.15. Power error and energy deposition error vs. time for fuel rod #H7T

Time (s)	Power (per-unit)	Power error		Energy deposition	
		Systematic error (%)	Total error (%)	Systematic error (%)	Total error (%)
0.60	0.01	5.1	12.6	4.5	12
1.90	0.05	5.1	12.6	4.4	12
2.45	0.10	5.1	12.6	4.4	12
3.10	0.50	5.1	12.6	4.5	12
3.40	1.00	5.0	12.5	4.4	12
3.70	0.50	5.1	12.6	4.4	12
4.00	0.10	5.1	12.6	4.5	12
4.15	0.05	5.1	12.6	4.4	12
5.50	0.01	15.6	24.2	4.4	12

Table 4.16. Power error and energy deposition error vs. time for fuel rod #B16T

Time (s)	Power (per-unit)	Power error		Energy deposition	
		Systematic error (%)	Total error (%)	Systematic error (%)	Total error (%)
0.85	0.01	3.7	9.1	2.7	8
3.85	0.05	3.7	9.1	2.7	8
4.35	0.10	3.7	9.1	2.7	8
4.95	0.50	3.7	9.0	2.7	8
5.35	1.00	3.6	9.0	2.7	8
5.80	0.50	3.7	9.0	2.7	8
6.45	0.10	3.7	9.1	2.7	8
7.00	0.05	3.7	9.1	2.7	8
10.00	0.01	15.2	21.8	2.7	8

4.10.6. Summation of errors

According to the analysis of results obtained, the main contribution to the final error in determining the energy deposition is made by experimental data (error in number of fissions measurements in central fuel pellets of E-type fuel rods, error in the isotopic composition determination in high burnup fuel which, in its turn, largely depends on the error in determining the burnup, etc.).

It should also be noted that errors related to the system of assumptions for the error assessment procedure were not analyzed. This can only be carried out on the basis of special reference experiments with the aim of qualifying this procedure.

4.11. Fuel enthalpy

Purpose and tasks of the procedure

Fuel rods of C-, D-, E- types were tested in IGR reactor under conditions when the power pulse was rather wide (half pulse width about 700 ms). Therefore, only a part of the energy deposition was spent to increase the fuel enthalpy, some heat was absorbed by the coolant due to the heat exchange between fuel rods and the surrounding water. However, it is the enthalpy which is the licensing criterion determining the possibility of fuel element damage in case of reactivity initiated accident.

Thus, the main purpose of this procedure was to determine the value set of peak fuel enthalpies for each fuel rod of C-, D-, E- types by computer simulation of the thermo-mechanical fuel rod behavior under conditions of capsule tests at IGR reactor. Detail analysis of this procedure, description of the computer codes used to determine the fuel enthalpy are presented in Chapter 5.

4.12. References

[1] A.Bortash et.al "Measurements of Specific Energy Deposition in Fuel Rods during Capsule Tests at GIDRA Reactor", Rus., IAE "Kurchatov Institute", Report, No. 37/860688, 1988.

[2] "Data on Gamma-Rays of Radioactive Decay of Atomic Nuclei. Recommended Information", Log. No 21028, Data status in State Standard 8.310-78, 1992, Database is repaired on the basis of the assessed data file ENSDF from the National Centre of Nuclear Data, USA.

[3] M.Berger and J.Hubball. "XCOM: Photon Cross Sections on a Personal Computer", NBSIR 87-3597, U.S. Department of Commerce National Bureau of Standards, Gaithersburg, MD 20899, July 1987.

[4] "Passport for Special Fuel Samples", Rus., Scientific and Industrial Association "LUCH", Passport No. 837.5.02.00.03ET, Podolsk, 1990.

[5] T.England, B.Rider. "Evaluation and Compilation of Fission Product Yields", Los Alamos National Laboratory Report LA-UR-94-3106, Oct., 1994.

[6] V.Chesanov, M.Pozdeev. "Determination of Specific Energy Deposition in the Fresh Fuel of Mock-Up Fuel Rods of VVER-1000 Type during Capsule Tests at IGR Reactor", Rus., Report No. 0-4276, Research Institute of Atomic Reactors, Dimitrovgrad, 1993.

[7] B.Galperin et.al "Study of IGR Reactor Parameters after Its Reconstruction", Rus., Report No. 36/622, IAE "Kurchatov Institute", Moscow, 1968.

[8] B.Galperin et.al "Reconstruction of IGR Reactor", Rus., Report No. 36/598, IAE "Kurchatov Institute", Moscow, 1967.

[9] "Experimental Study of the Residual Energy Deposition in IGR Reactor. Test series No. 132F", Act, IAE National Nuclear Centre of Kazakhstan, Semipalatinsk, 1995.

[10] A.Avvakumov, V.Malofeev. "Simulation of Regulating Pulse Dynamics in IGR Reactor", Rus., Report No. 90/1-17-95, Nuclear Safety Institute of Russian Research Centre "Kurchatov Institute", 1995.

[11] A.Avvakumov, V.Malofeev. "3-D Simulation of Delayed Neutron Transients in Heterogeneous Reactor", Rus., At.Energia, Vol.70(1), 1991.

[12] A.Galanin. "Heterogeneous Reactor Theory", Rus., Moscow, Atomizdat, 1971.

[13] A.Kvaratshely, B.Kochurov. "Calculation of Neutron Parameters of Heterogeneous Reactor Cell", Rus., At.Energia, Vol.58(2), 1985.

[14] V.Malofeev. "TREC-the Code for Calculation of a Large Heterogeneous Reactor", Rus., VANT, Ser. Nuclear Reactor Physics and Engineering, Vol.4, pp.29-32, 1985.

[15] B.Kochurov, V.Malofeev. "Difference Approach to the Solution of Heterogeneous Reactor Equations", Rus., Annals of Nuclear Energy, Vol.4, p.21, 1977.

[16] G.Liman, L.Maiorov, M.Yudkevich. "MCU Monte Carlo Code for Neutron Transport Calculations", Rus., Voprosy Atomnoy Nauki i Tekhniki", Ser. Fizika i Tekhnika Yadernykh Reaktorov, Vol.7, p.27, Moscow, 1985.

[17] E.Gomin, L.Maiorov, M.Yudkevich. "Some Aspects of Monte Carlo Method Application to Nuclear Reactor Analysis", Progress in Nuclear Energy, Vol.24, p.211, 1990.

[18] E.Gomin, L.Maiorov. "The MCU-RFFI Monte Carlo Code for Reactor Design Applications", Report at the International Conference on the Mathematics and Computations, Reactor Physics and Environmental Analyses, April 30 - May 4, USA, 1995.

[19] L.Abagyan, E.Gomin, M.Gurevich, L.Maiorov et.al "MCU-3 Code for Calculations by Monte Carlo Method of Neutron and Physical Characteristics of Nuclear Reactors", Rus., Vol.1,2,3,5, Reports No. IAE-5772/5, IAE-5777/5, IAE-5736/5, IAE-5739/5, Russian Research Centre "Kurchatov Institute", Moscow, 1994.

[20] L.Abagyan, N.Bazaziants, M.Nickolayev, A.Tsybulia. "Group Constants for Calculating Reactors and Protection", Rus., Moscow, Energoizdat, 1981.

[21] L.Abagyan. "LIPAR-5 - Resonances Parameters Library, Part 1", Rus., Report IAE-5688/4, Russian Research Centre "Kurchatov Institute", Moscow, 1993.

[22] Y.Glushkov, N.Ponomarev-Stepnoy, E.Gomin, J.Sapir et.al "Comparison of Codes and Neutronic Data Used in the United States and Russia for the TOPAZ-2 Nuclear Safety Assessment", Proceedings of 11 Symp. Space Nucl. Power and Propulsion, Albuquerque NM, Part 1, pp.137-141, 1994.

[23] L.Abagyan, E.Gomin, M.Yudkevich. "Evaluation of Constants of Isotopes Pu^{239} - Pu^{242} and Their Verification Conformably to the Calculations of Thermal Reactors", Proceedings of the Topical Meeting on the Advances in Reactor Physics, March 8-11, Charleston, USA, 1992.

[24] L.Abagyan, N.Alexeyev, V.Bryzgalov et. al. "MCU Monte Carlo Code. Verification", Rus., Report IAE-5751/5, Russian Research Centre "Kurchatov Institute", Moscow, 1994.

[25] L. Abagyan et.al "MCU-3 Code for Calculations by Monte Carlo Method of Neutron and Physical Characteristics of Nuclear Reactors. Volume 4. Verification", Rus., Report IAE-5741/5, Russian Research Centre "Kurchatov Institute", Moscow, 1994.

[26] "Theoretical Investigation of the Physical Properties of VVER-Type Uranium-Water Lattices", Edited by L.Maiorov, Academia "Kurchatov Institute" ado, Budapest, 1994.

[27] L.Maiorov. "Verification of Design Codes for Analysis of Hexagonal Lattices", Proceedings Transactions of ANS Winter Meeting, 13-17 Nov., 1994.

[28] M.Kalugin, L.Maiorov. "Algorithms of the Monte Carlo Method for Analyzing the Reactivity Initiated Accidents", Proceedings of RPSD Topical Meeting: Advancements and Applications in Radiation Protection and Shielding (published), No.Falmouth, Massachusetts, April 21-25, 1996.

[29] M.Kalugin, L.Maiorov "Application of the Monte Carlo Method to Determine the Distribution of Number of Fissions in Fuel Rods of VVER-1000 Type under RIA Conditions", Report IAE-6037/5, 1997.

[30] G.Bat et.al. "Research Nuclear Reactors", Rus., Moscow, Energoatomizdat, 1985.

[31] V.Tsyckanov et.al. "Research Reactors of the Institute and Methods of the In-Core Investigations", Rus., Research Institute of Atomic Reactors, Report No. NIIAR-1 (682), CNIIatominform, 1986.

[32] V.Smirnov et.al. "Determination of the Energy Deposition Ratio in the Fresh and High Burnup VVER Fuel after Irradiation in the Research Reactor", Rus., Research Institute of Atomic Reactors, Report No. O-4421, Dimitrovgrad, 1995.

[33] A.Bortash, L.Yegorova, A.Zvjageen, V.Palvanov "The determination of the r, z, t distributions of the energy deposition in the VVER fuel rods under RIA test conditions at the IGR and GIDRA reactors", Report IAE-6088/3, 1998.

[34] "Basic Physics of the Fission Process. Nuclear Fission Cross Section", Ed. by A.Michaudion, Oxford, Pergamon Press, 1981.

[35] W.Engle. "A Users Manual for ANISN", Union Carbide Corporation, K-1693, 1967.

[36] T.Fowler, D.Vondy and G.Cunningham. "Nuclear Reactor Core Analysis Code: CITATION", USAEC REPORT ORNL-TM-2496, Revision-2, ORNL, 1971.

[37] S.Marin, D.Markovsky, G.Shatalov. "Code for Calculations of Spatial Energy Distribution of Neutrons in 1-Dimentional Geometry (BLANK)", Rus., IAE "Kurchatov Institute", Report No. 2832, Moscow, 1977.

[38] K.Tasaka et.al "JNDS Nuclear Data Library of Fission Products", JAERI-1287, 1983.

[39] J.Askew et.al "A General Description of the Lattice Code WIMS", J. of the Brit. Nucl. Energy Soc., Vol.5, p.564, 1966.

[40] Under the editing of R.Vasiliev. "Metrology of Neutron Measurements at Nuclear Facilities (Recommended information and measurement procedures) ", Vol.2, Central Scientific Research Institute of Information and Feasibility Studies in the Field of Nuclear Science and Technology, Moscow, 1976.

[41] Himmelblau. "Process Analysis by Statistical Methods", J.Wiley and Sons, ING, New York, London, Sydney, Toronto, 1970.

[42] V.Boliatko et.al "Errors in Calculations of Protection Versus Irradiation", Rus., Moscow, Energoatomizdat, 1983.

[43] L.Usachev. "Disturbances Theory for Reproduction Coefficient and Other Ratio of Numbers for Reactor Processes", Rus., At. Energia, Vol.15, Iss.6, 1963.

5. COMPUTATIONAL ANALYSIS OF FUEL ROD BEHAVIOR AT IGR/RIA TESTS

5.1. Formulation of a problem

Technical requirements to the list of parameters required for the development of the data base within the framework of the computational analysis are presented in Chapter 1 of this Volume together with a brief characteristic of FRAP-T6 [1] and SCANAIR [2] codes that were selected as instruments for the computational analysis.

The next stage of studies covered the applicability assessment of these codes to achieve this goal. The consolidated list of main physical phenomena that determine the behavior of high burnup fuel rods in IGR tests and code capabilities in describing these processes are contained in Table 5.1. According to the analysis, none of the codes has a complete set of models required for the description of IGR test results.

Table 5.1 Physical phenomena and capabilities of codes

	Physical phenomenon	Code possibility to model a physical phenomenon	
		FRAP-T6	SCANAIR
1.	Parameters of high burnup fuel before IGR tests (at the end of fuel cycle)	No	No
2.	Geometry of VVER fuel rod	No	Yes
3.	Heat transfer in fuel rod with account for heat conductance through fuel-clad gap	Yes	Yes
4.	Clad-to-coolant heat transfer for the following coolants:		
	• water	Yes	Yes
	• air	No	No
5.	Behavior of gas inside a fuel rod	Yes	Yes
6.	Cladding oxidation	Yes	No
7.	Cladding and fuel melting, chemical interaction and relocation	No[1]	No
8.	Fission product release	Yes	Yes
9.	Fuel hoop strain due to:		
	• swelling	No	Yes
	• thermal expansion	Yes	Yes
	• plasticity	No	Yes
10.	Plastic cladding hoop strain due to:		
	• pellet/cladding mechanical interaction (PCMI)	Yes	Yes
	• gas pressure inside a fuel rod	Yes	No
11.	Cladding failure due to:		
	• PCMI	No	No
	• ballooning	Yes	No
	• melting	No[1]	No

[1] Code allows to predict initiation of these processes, but does not contain models, describing their evolution.

Therefore, a series of special code modifications was performed during the studies to adapt the codes to IGR test conditions. The main attention was paid to the development of a modified data base that characterizes material properties of VVER fuel rods. This work required the conduct of new additional experimental studies to get original mechanical properties of unirradiated and irradiated claddings. The validation of codes was the final stage of studies. This procedure was implemented in two stages. The first stage included the verification of intermediate code versions. Results of the second stage allowed to finally determine the region of the applicability of each code and to develop the procedure of their practical use within the framework of results presented in Volume 3 of the Report.

5.2. Assessment of required input data on VVER material properties to calculate IGR tests with FRAP-T6 and SCANAIR codes

A specific problem of these studies was related to the fact that MATPRO-V11 [3] library of properties is used in FRAP-T6 code and the original input data base is used in SCANAIR code to describe material properties of the cladding and of the fuel. At present, MATPRO-V11 is probably the most complete data base characterizing physical and mechanical properties of fuel claddings made of Zircaloy 2, 4 alloys and UO_2 fuel of PWR type. SCANAIR code library of properties combines the data base that is partially based on MATPRO library and partially - on packages of properties developed for earlier French codes ; moreover it includes results of special experiments conducted in France. SCANAIR library, as well as MATPRO, is intended to describe properties of PWR fuel rods.

This is why two problems arose within the framework of the task of describing the behavior of high burnup fuel rods during the IGR tests. The first one was the modification of libraries as applied to properties of VVER materials. The second problem was related to the fact that the practical study of characteristics of commercial high burnup fuel elements and their testing under RIA conditions have started simultaneously only recently. Therefore, results of studies intended to investigate corresponding material properties have not yet been included into the above libraries.

Thus, the validation of the approach to develop the data base with material properties for IGR tests was conducted taking into account both problems. It should be noted that the development of a full-scale specialized data base with VVER material properties is far beyond the scope of the present study. Therefore, the approach based on an integrated use of the following procedure was applied:

- expert judgments of the necessity of using VVER original properties in each considered case;

- preliminary sensitivity analysis of codes to properties selected on the basis of expert judgments;

- modification of code libraries by introducing VVER original properties that have been obtained earlier and been published;

- development and implementation of special studies to get missing data on properties.

Results of the first stage of this procedure are schematically presented in Table 5.2. It is important to underline that the following considerations formed the basis of the obtained expert judgments. As for fuel, it is obvious that differences in technological processes of manufacturing PWR and VVER fuel pellets result in certain differences in their initial characteristics. Particular features of power operating cycles can cause additional differences. However, it should be noted that quantitative differences in properties of fresh fuel are small, and a modern data base for high burnup fuel still does not exist. Moreover, it was taken into account that the accurate knowledge of fuel characteristics is of a principle importance during the interpretation of RIA tests scenarios for the stage of the mechanical fuel – cladding interactions. However, a particular feature of IGR/RIA tests is the cladding rupture of ballooning type. In other words, the failure of cladding occurs due to gas pressure effects on the fuel cladding. In this case a significant effect from the fuel side is the heat flux to the cladding. This is why at the stage of the expert judgment, it was decided to introduce, into libraries, the models which characterize the thermal conductivity and specific heat of the high burnup fuel. Regarding cladding properties, differences in the composition of Zircaloy and Zr-1%Nb alloys can result in more significant differences in properties. Therefore it was decided to get additional information on the relevance of the problem by conducting the sensitivity analysis of codes to material properties of the fuel and the cladding. The sensitivity analysis was performed for the following set of material properties:

Cladding	Fuel
• specific heat;	• specific heat;
• specific enthalpy;	• specific enthalpy;
• thermal conductivity;	• thermal conductivity;
• thermal expansion;	• thermal expansion;
• Young's modulus;	• Young's modulus;
• Poisson's ratio;	• Poisson's ratio;
• and other parameters of stress-strain diagrams.	• yield stress.

Table 5.2. Material properties required to calculate fuel rod behavior in IGR test with computer codes

Material properties	Expert estimation to correct data base for VVER cladding and fuel
1. Cladding	
1.1. Thermal physical constants	Yes
1.2. Specific heat	Yes
1.3. Thermal conductivity	Yes
1.4. Density	No
1.5. Specific enthalpy	Yes
1.6. Oxidation	Yes
1.7. Emissivity	No
1.8. Mechanical properties	Yes
1.9. Thermal expansion	Yes
2. Fuel	
2.1. Thermal physical constants	No
2.2. Specific heat	Yes
2.3. Thermal conductivity	Yes
2.4. Density	No
2.5. Specific enthalpy	Yes
2.6. Emissivity	No
2.7. Thermal expansion	Yes

The objective of the first stage of research of the sensitivity analysis was comparison of the data base characterizing the above VVER material properties with the similar data bases presented in MATPRO and SCANAIR codes. Results of this comparison are presented in Fig. 5.1-Fig. 5.5.
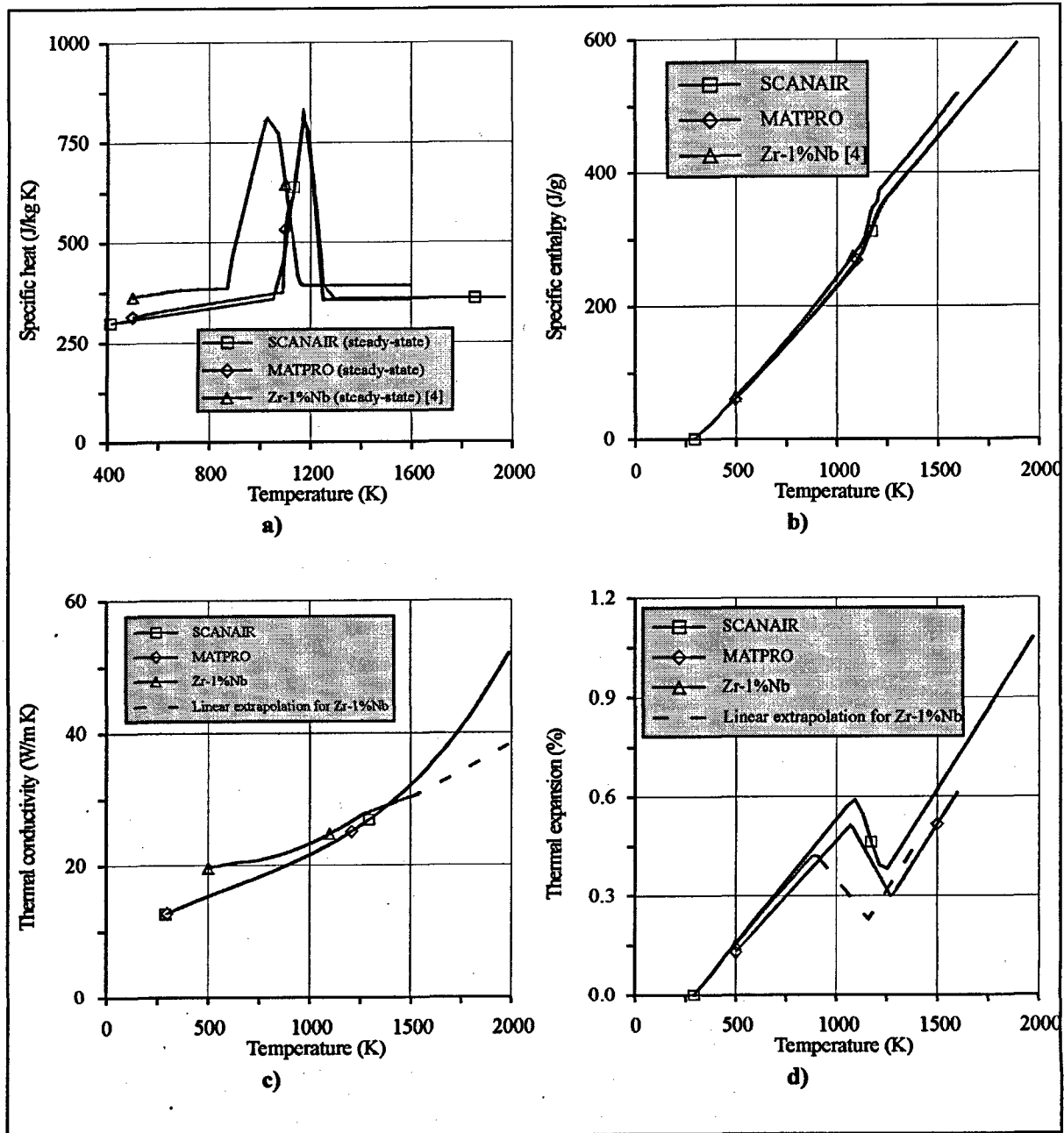
Fig. 5.1. Specific heat (a), specific enthalpy (b), thermal conductivity (c), thermal expansion (d) vs. temperature for unirradiated Zry and Zr-1%Nb
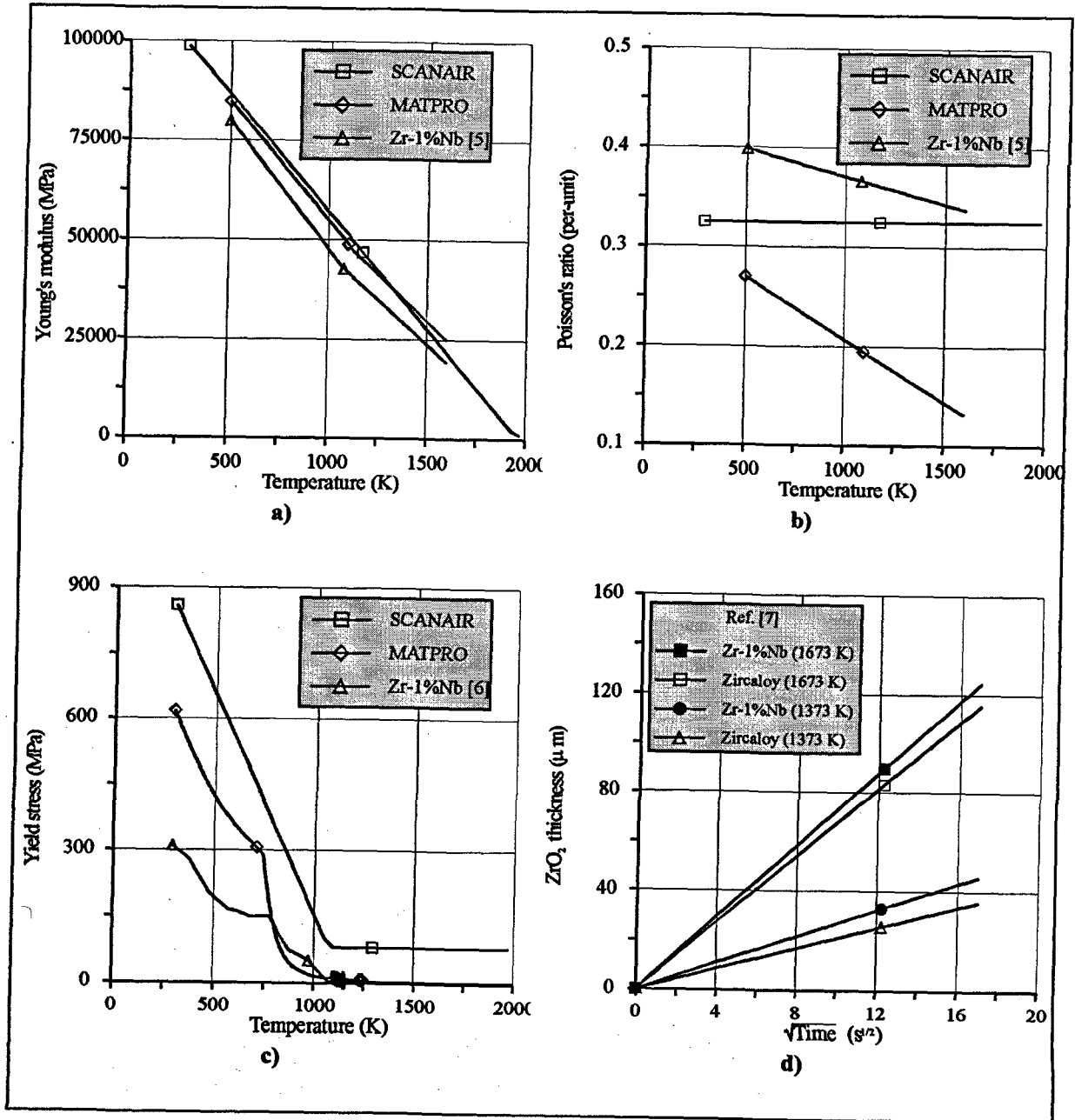
Fig. 5.2. Young's modulus (a), Poisson's ratio (b), yield stress (c) vs. temperature and ZrO₂ thickness (d) vs. time for unirradiated Zry and Zr-1%Nb
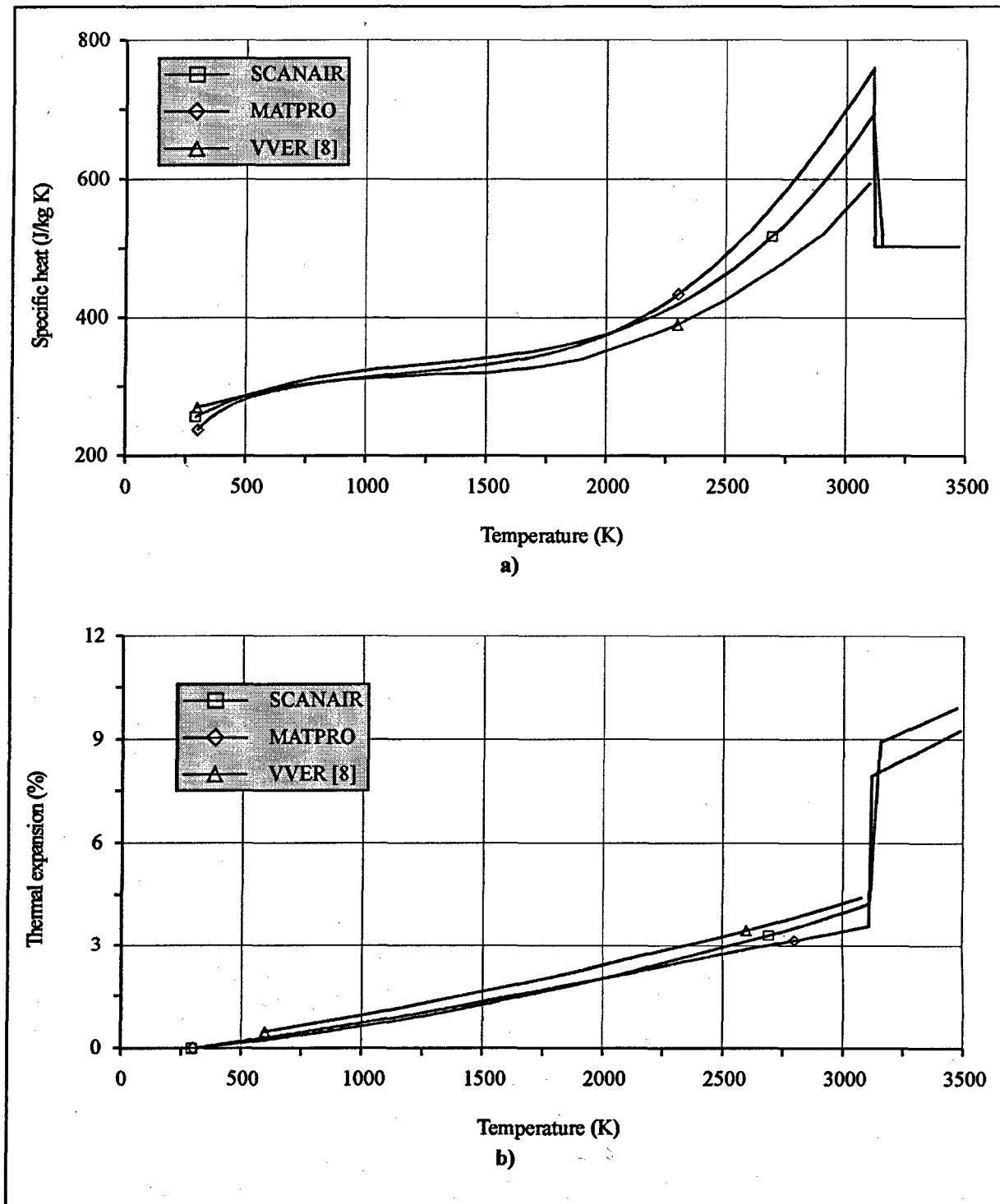
Fig. 5.3. Specific heat (a) and thermal expansion (b) for unirradiated fuel of PWR and VVER type
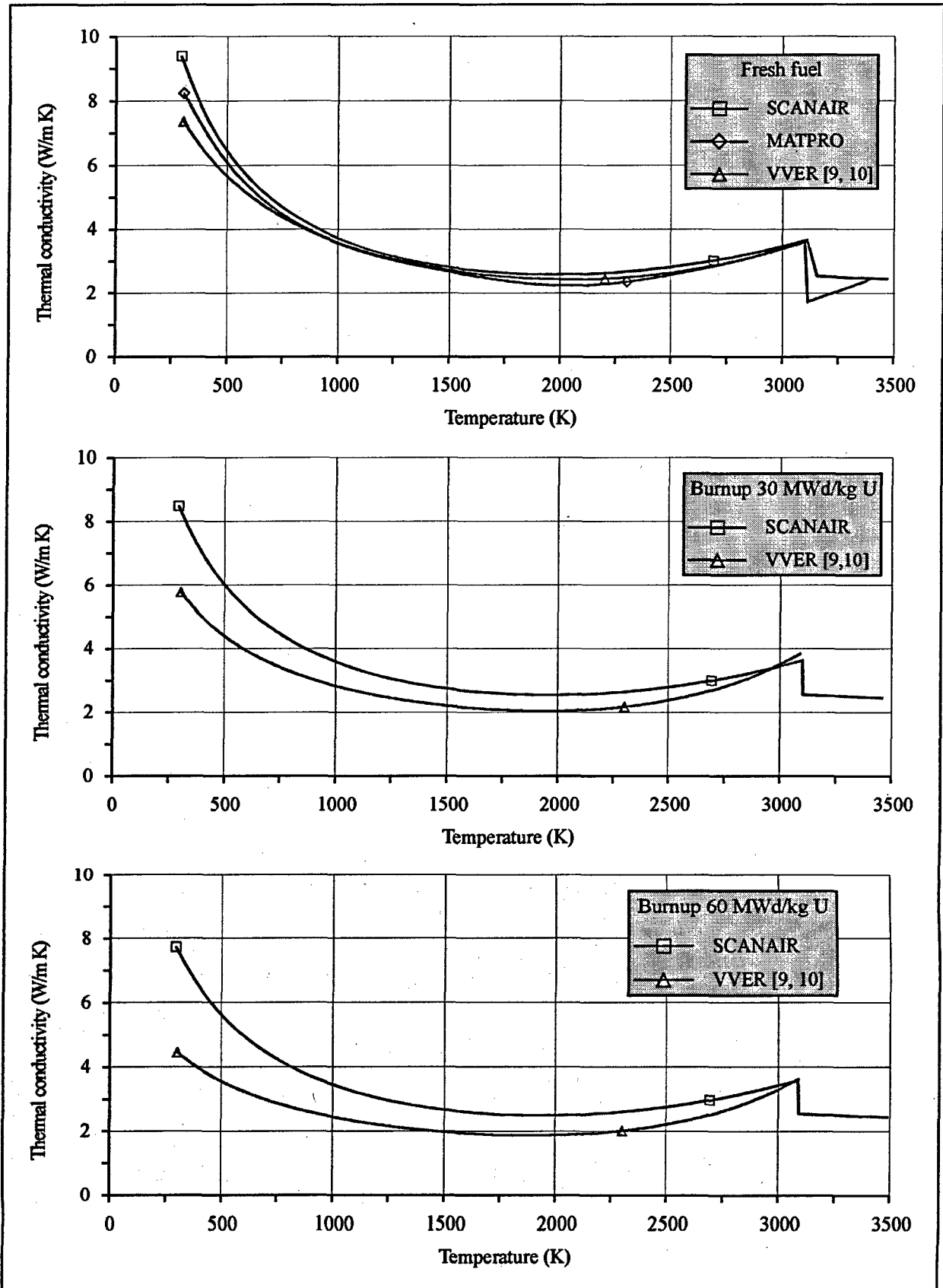
Fig. 5.4. Thermal conductivity of uranium dioxide fuel vs. temperature and burnup
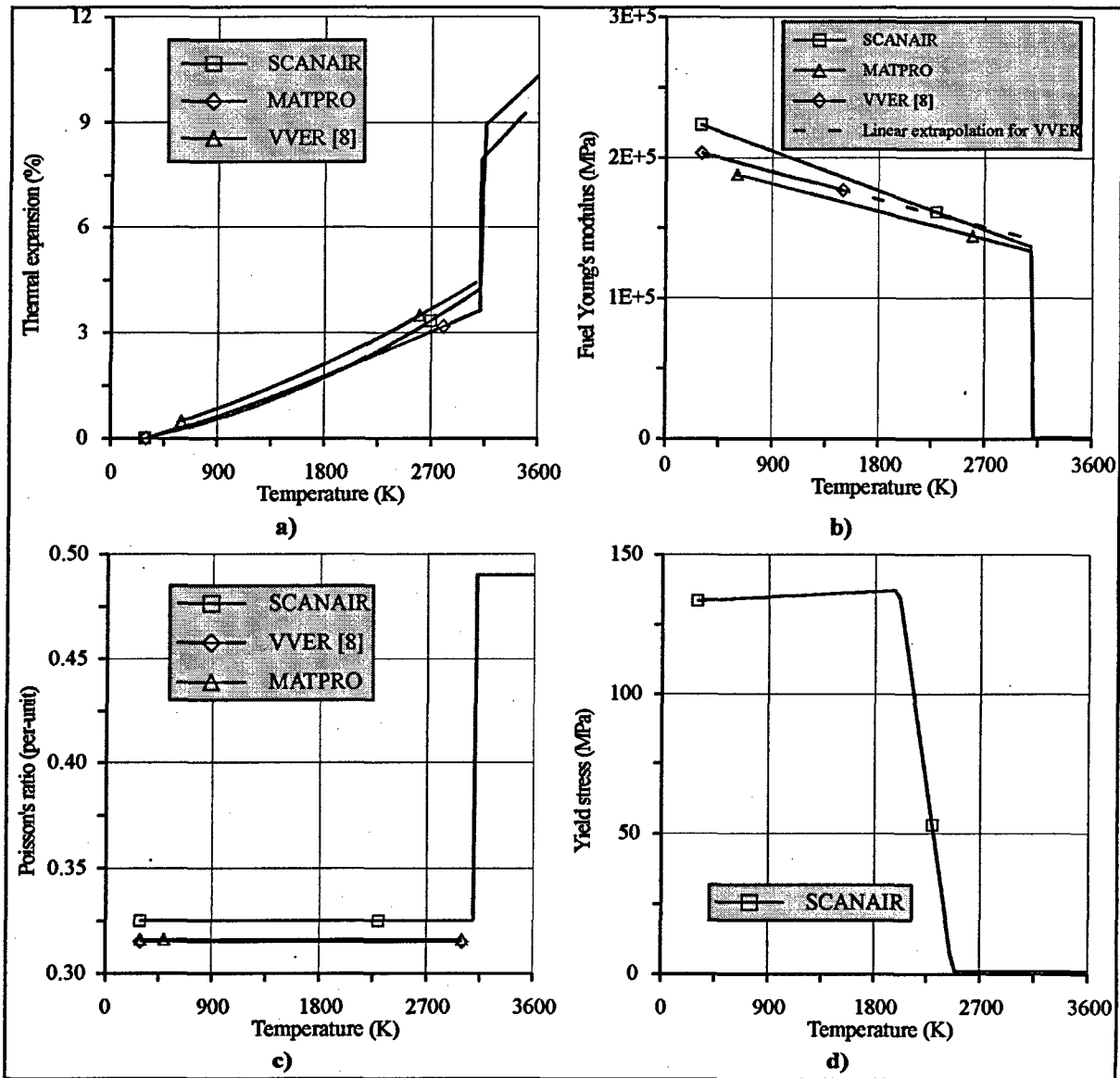
Fig. 5.5. Thermal expansion (a), Young's modulus (b), Poisson's ratio (c), and yield stress (d) vs. temperature for unirradiated fuel of PWR and VVER type

Comparative analysis of the whole batch of material properties necessary for the IGR test simulation indicated that:

- in some cases there exist significant discrepancies in the three data bases (MATPRO-V11, SCANAIR, VVER);

- MATPRO and VVER databases have not been renewed for a long time;

- there exists the deficiency of the data characterizing the properties of irradiated claddings and high burnup fuel;

- there exists the lack of the necessary scope of data characterizing material properties under fast transient conditions;

- some of the data are missing in the data bases.

With consideration of these remarks the program for the second stage of the work on sensitivity analysis was targeted at assessing the scope of consequences which can be caused by uncertainties of the input data on material properties.

Sensitivity analysis was done in the framework of a very simple procedure; hence the obtained results are a very preliminary nature.

This procedure was based on the standard perturbation by ±20% deviation in all values of each property under consideration. The procedure was sequentially applied to each property; then the code response was observed in accordance with the selected list of output parameters.

The set of the main output parameters included fuel enthalpy, clad temperature, clad stress. #H1T high burnup fuel rod was selected for the study in order to perform the sensitivity analysis procedure. Evaluation of the results obtained with the help of this procedure is presented in the report for two groups of material properties:

- basic group includes thermal-physical properties, Young's modulus, Poisson's ratio for cladding and fuel, yield stress for fuel;

- mechanical group includes the cladding mechanical properties to describe the stress-strain diagrams.

<u>Results of sensitivity analysis of FRAP-T6 and SCANAIR codes to the basic group of material properties</u>

It is important to note that the presented evaluation of the results of sensitivity analysis of FRAP-T6 and SCANAIR codes to the basic group of material properties, obtained for # H1T fuel rod are of great value. This fuel rod was tested under the conditions close to the failure threshold, but the threshold was not reached. That is why, theoretically even the slight change of the input data can result in the qualitatively and quantitatively different output parameters.

Summarizing of the results obtained by the basic group of material properties allowed to make the following conclusions:

- Two parameters of this group are the decisive ones from the standpoint of their influence onto the output parameters. These are: fuel specific heat, and fuel thermal conductivity.

- Response of output parameters to 20% disturbance of the other basic properties has the following values:

	SCANAIR	FRAP-T6
⇒ peak fuel enthalpy not more than	±1.2%	±1.3%;
⇒ cladding temperature not more than	±3.2%	±2.0%;
⇒ cladding stress not more than	±3.4%	±2.6%.

Table 5.3 contains some results characterizing response of some output parameters to the disturbances introduced as the input for fuel specific heat and fuel thermal conductivity.

These results are graphically presented in Fig. 5.6 for specific heat of fuel.

Table 5.3. Response of output parameters of codes to the disturbance of some input parameters

Input parameters		Response of output parameters[1] (%)					
		Peak fuel enthalpy (%)		Peak clad temperature (%)		Peak clad hoop stress (%)	
		FRAP-T6	SCANAIR	FRAP-T6	SCANAIR	FRAP-T6	SCANAIR
1. Fuel specific heat	+20%	+2.4	+4.5	-6.2	-6.9	+8.5	+5.0
	-20%	-4.5	-5.8	+5.2	+7.7	-1.4	-3.7
2. Fuel thermal conductivity	+20%	-1.1	-1.3	+1.3	+3.8	+10.6	+8.2
	-20%	~0	+1.7	-2.1	-5.5	-4.2	-12.0

[1] Response was determined as relative deviation from normal value of parameter
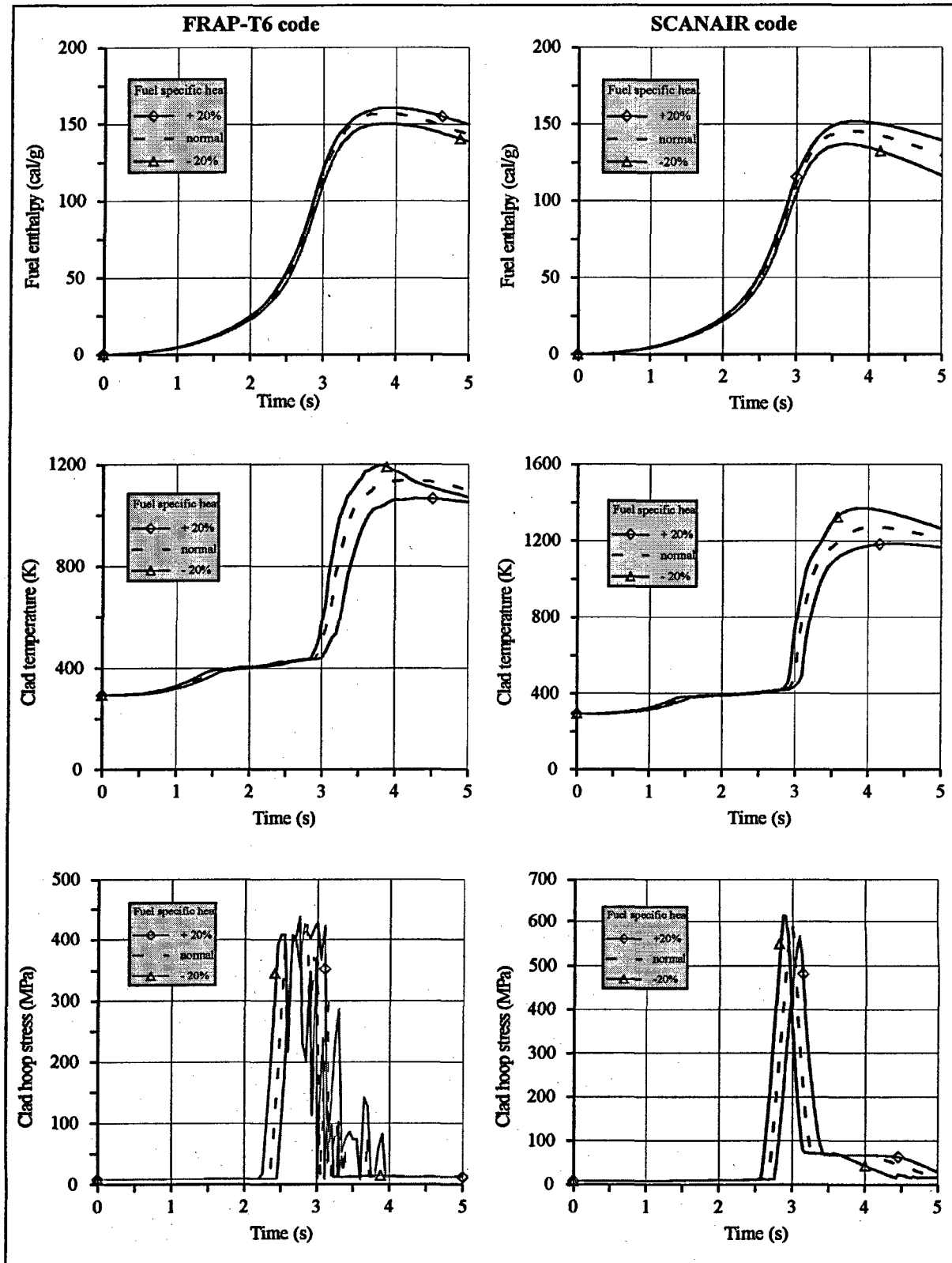
Fig. 5.6. Response of fuel enthalpy, clad temperature and hoop stress to 20% disturbance of the fuel specific heat

On the whole analysis of results obtained for the basic group of material properties allowed to work out the following recommendations:

- specific heat and thermal conductivity of the VVER fuel are to be certainly included into the MATPRO package and SCANAIR input block;

- adding of the rest of VVER properties to the MATPRO package and SCANAIR input block is a desirable but not compulsory procedure;

- peak fuel enthalpy is the least sensitive output parameter; in the some cases cladding temperature and cladding hoop stress can be sensitive enough to the uncertainties in material properties, that is why the results of computer simulation of VVER fuel rod performance are to be analyzed with consideration of the material properties problem.

Results of sensitivity analysis of FRAP-T6 and SCANAIR codes to the mechanical group of material properties of the cladding

The problem of sensitivity analysis of the code output parameters in respect to the set of the cladding mechanical properties is far beyond the framework of this report because those properties depend in their turn on a great number of factors characterizing not only the cladding composition, but also the technology of its manufacture, irradiation conditions, loading conditions, etc. That is why only some preliminary assessments were made during this stage.

It is also necessary to remember that this group of properties is presented in the SCANAIR input block and in MATPRO-V11 package differently. Hence, the sensitivity analysis procedure was developed for each code independently.

Input block for SCANAIR code contains three parameters characterizing mechanical properties of the cladding. There are Young's modulus, Poisson's coefficient and yield stress. The only difference from previous analysis was that the 30% initial disturbance was specified. Response of output parameters to 30% disturbance of Young's modulus and Poisson's ratio does not exceed 1%. Fig. 5.7 presents the responses of output parameters to clad yield stress disturbance.

Data presented in Fig. 5.7 indicate that sensitivity assessment of the code to the cladding mechanical properties is not unique and universal, i.e. thermal characteristic of fuel rods reacts weakly onto the uncertainty specified by the cladding mechanical properties. Still peak cladding hoop stress changes by (+6; -14) % in case of 30% disturbance of the yield stress. That means that the issue is of principal importance when prediction of parameters characterizing fuel rod failure is a part of the tasks to be solved by this computer code. It should be additionally noted that in this case we analyzed the situation when the cladding failure can be only due to PCMI mechanism. Physical phenomena following cladding failure of ballooning type can be analyzed by FRAP-T6 code.

MATPRO-V11 code which is used by FRAP-T6 code as the input data package does not contain mechanical properties as functional dependencies for the yield stress, ultimate strength, uniform elongation, etc.

This code operates with a number of K, n, m functionals characterizing relationship between stress and strain not only as the function of temperature, but also with consideration of the cladding cold work, burnup, oxidation, strain rate, fast flux. Strength coefficient K, and strain hardening exponent n allow to describe stress-strain power law for the basic cladding strain rate, and strain rate sensitivity exponent m allows to consider the influence of the loading conditions for different cladding strain rate. Detailed description of the MATPRO approach in order to characterize cladding mechanical properties is presented in Chapter 6, section 6.4.

With consideration of the above mentioned 30 % disturbance of K, n, and m functionals was performed with the already described procedure and responses of output parameters for the fuel rod #H1T were found. These responses are presented in Fig. 5.8–Fig. 5.10.
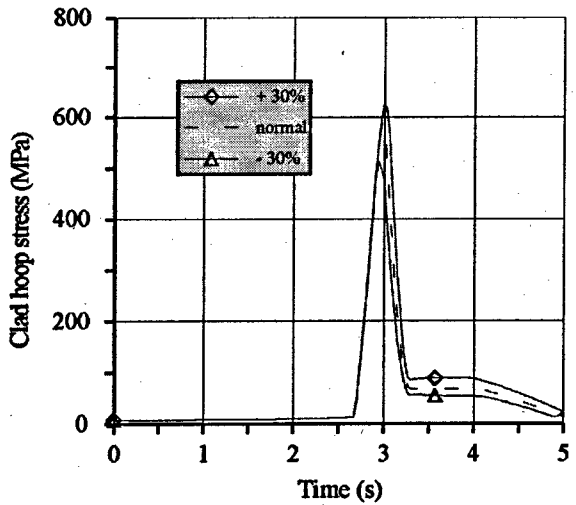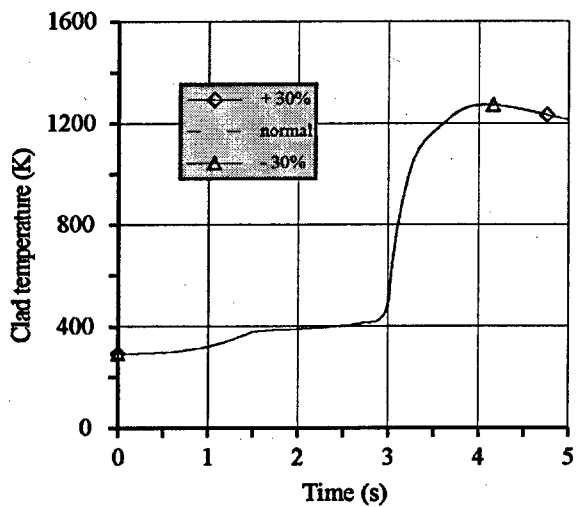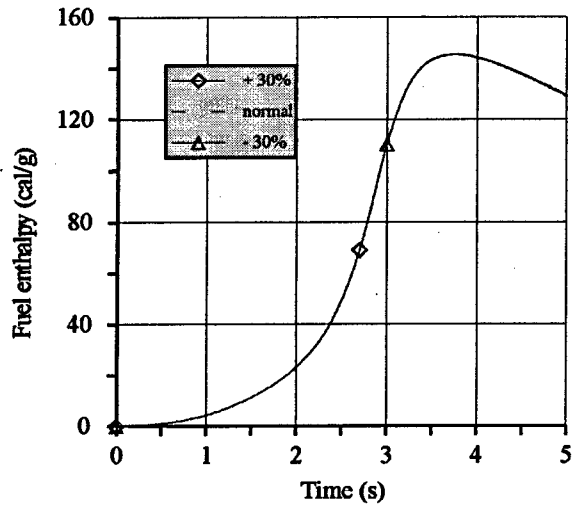
Fig. 5.7. Response of fuel enthalpy, clad tempera-
ture and clad hoop stress calculated by
SCANAIR code to the 30% disturbance
of clad yield stress
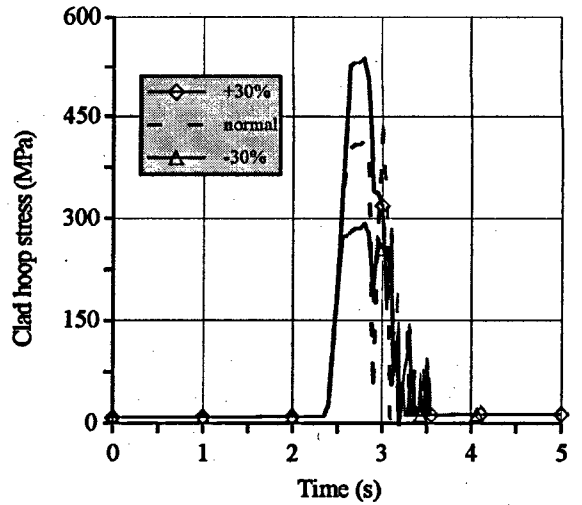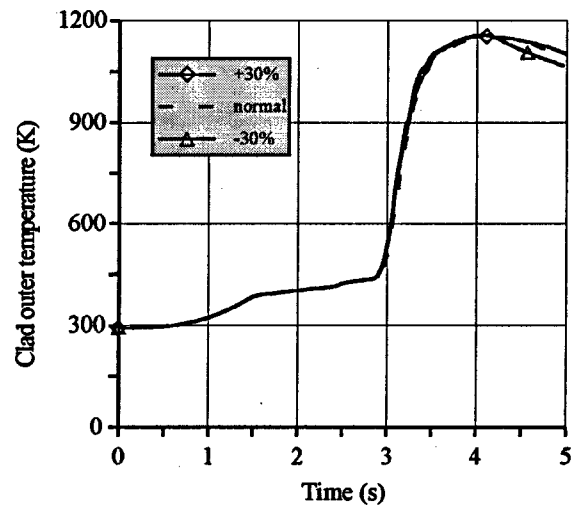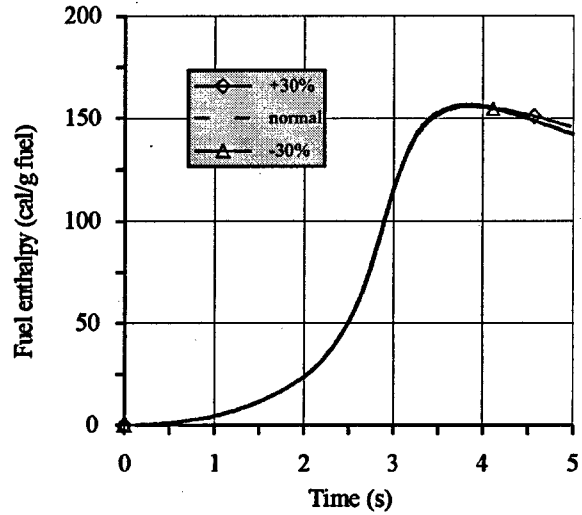
Fig. 5.8. Response of fuel enthalpy, clad tem-
perature, clad hoop stress calculated by
FRAP-T6 code on 30% disturbance of
strength coefficient K

5.12
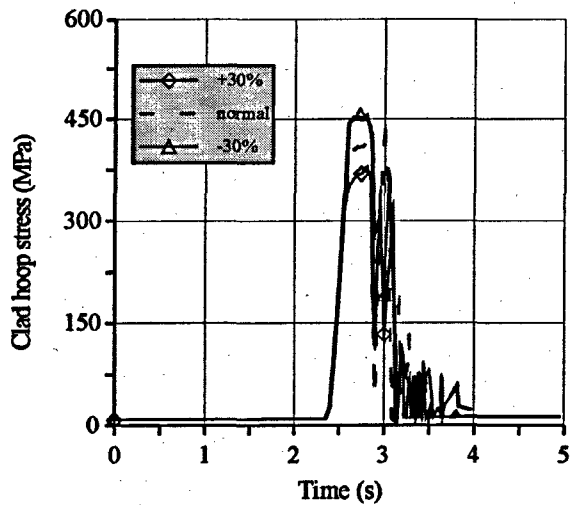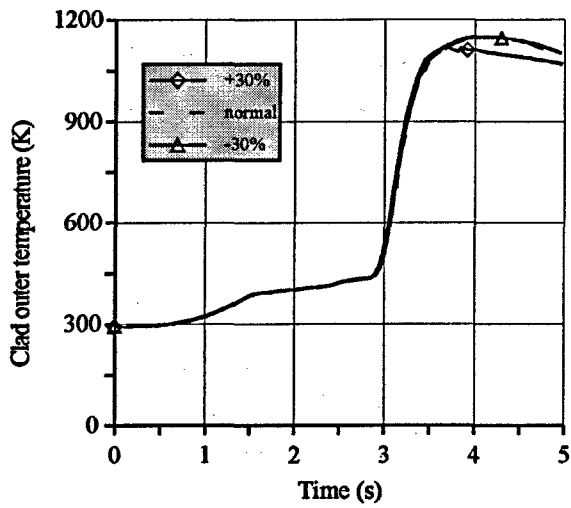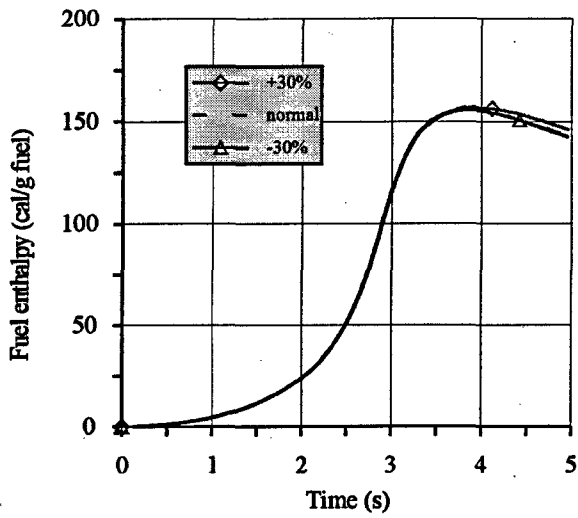
Fig. 5.9. Response of fuel enthalpy, clad tempera-
ture, clad hoop stress calculated by
FRAP-T6 code on 30% disturbance of
strain hardening exponent n
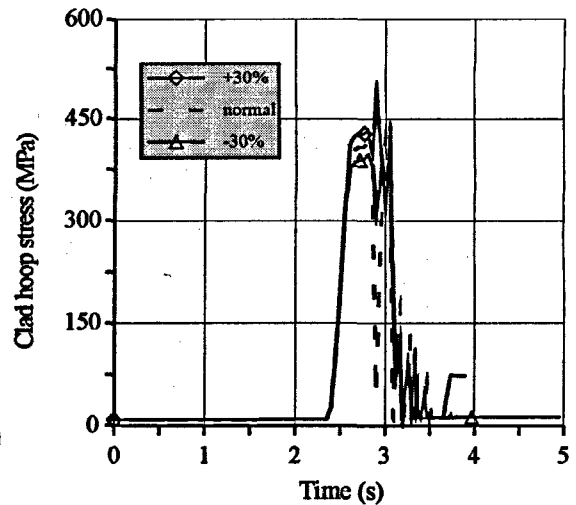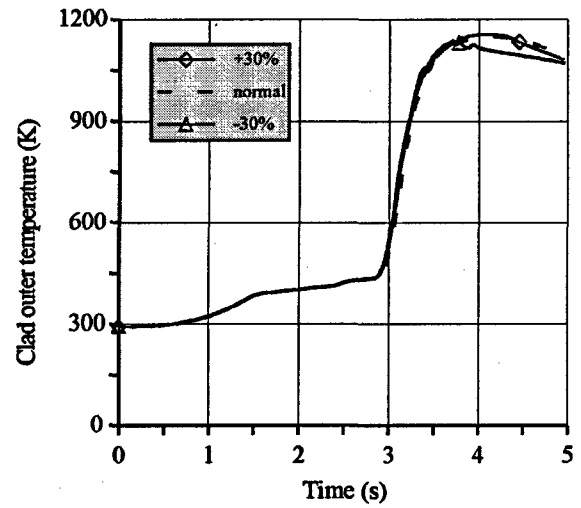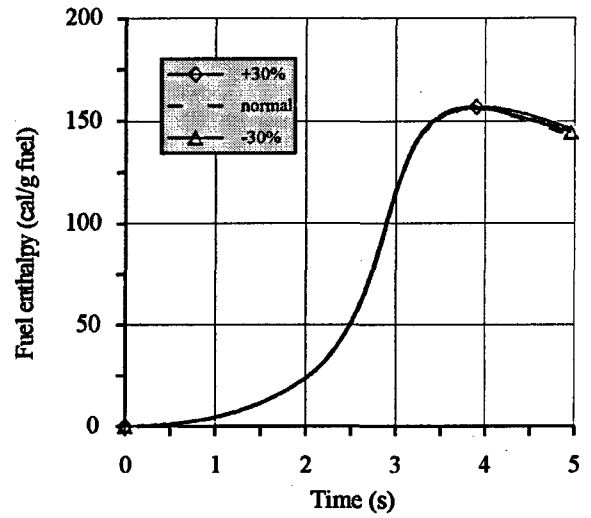
Fig. 5.10. Response of fuel enthalpy, clad tempe-
rature, clad hoop stress calculated by
FRAP-T6 code on 30% disturbance of
strain rate sensitivity exponent m

Analysis of the obtained data shows that just like in the SCANAIR code the highest sensitivity to the uncertainty of the input data is demonstrated by the cladding hoop stress, its peaking response to the 30% disturbance being:

47% for strength coefficient;

13% for strain hardening exponent;

10% for strain rate sensitivity exponent.

That is why the following final conclusion can be made based on the results of this type of research: correct prediction of the deformation behavior of the high burnup fuel rod under the conditions of the pellet-cladding mechanical interaction can be assured in case we know the cladding mechanical properties very accurately.

But the codes sensitivity analysis to the cladding mechanical properties performed on the basis of the fuel rod #H1T can not be considered sufficient because the issues connected with the cladding failure of ballooning type were not reviewed in this case. The following procedure was developed in order to evaluate this effect:

1. Energy deposition was artificially increased in H1T fuel rod up to the value when FRAP-T6 code predicted cladding failure due to ballooning.

2. 30% disturbance was specified sequentially for the K, n, m functionals. The value of energy deposition resulting in the cladding failure due to ballooning was selected for each six variants of the input data.

3. Additive effect of the cladding hardening influencing the peak fuel enthalpy was also reviewed by the simultaneous increase of K and n by 30%.

4. Peak fuel enthalpies characterizing fuel rod failure were identified for each case.

5. Relative deviations of peak fuel enthalpies from the value reached according to item 1 were identified and presented in Table 5.4.

Table 5.4. Response of peak fuel enthalpy in case failure due to ballooning onto disturbances of the cladding mechanical properties

Response of output parameter	Input parameter disturbance (%)						
	K		n		m		K, n
	+30	-30	+30	-30	+30	-30	+30
Relative deviation of peak fuel enthalpy (%)	+9	-22	+7	-5.5	+5.6	-6	+21

One of the variants of this procedure is graphically presented in Fig. 5.11.

Analysis of results obtained in the framework of the developed procedure leads to the conclusion that reliability of the computational data base characterizing VVER fuel rod performance can be ensured only in case original properties of the VVER cladding are used. That is why we worked out and performed the special cycle of the studies aimed at getting the data base with mechanical properties of unirradiated and irradiated VVER cladding versus temperature and strain rate. Results of this work are discussed in detail in Chapter 6.
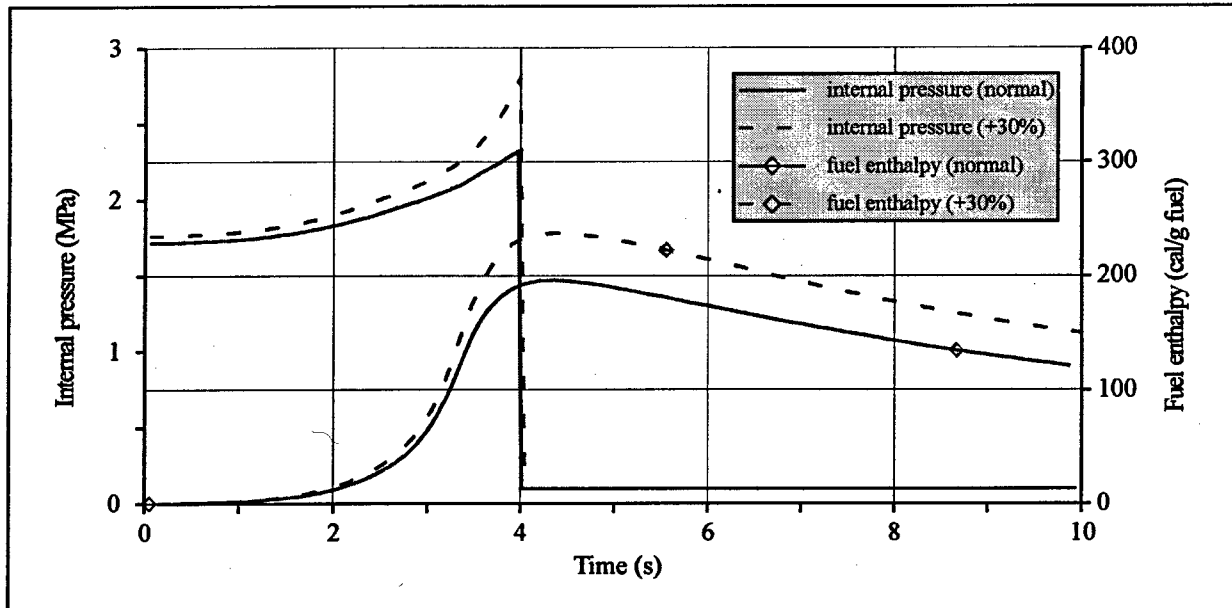
Fig. 5.11. Response of fuel enthalpy and internal gas pressure on 30% disturbance of K and n

5.3. Specific requirements for computer codes to simulate geometry of VVER fuel rods and IGR test conditions

The central hole in fuel pellets of VVER fuel rods is the specific feature that makes its geometry different from PWR fuel rods. According to the computer code analysis, it is possible to simulate this type of fuel rods in SCANAIR code and FRAP-T6 codes.

The next problem was related to the fact that VVER fuel rods tested in IGR reactor had an extended upper gas plenum that is not provided for in SCANAIR code. The neglect of this feature resulted in a principally incorrect description of gas parameters inside the fuel rod. Thus, it will be necessary to develop special procedures to eliminate this shortcoming.

A non-standard requirement was set for codes regarding those IGR tests when the air was used as the coolant. Special modules were developed for both codes to calculate the fuel rod behavior in these tests.

And finally, a serious problem was related to the fact that the usual set of input data that characterizes the fuel geometry and the material composition is not sufficient for the simulation of the behavior of high burnup fuel under power pulse conditions. In this case it is necessary to know not only the r, z distribution of fissile isotopes, but also the spatial distribution of fission products in the fuel after the base irradiation. The preparation of corresponding input data for SCANAIR code was conducted using TOSUREP code [11] that is intended for these purposes and has the coupling with SCANAIR code. FRAPCON-2 code [12] is usually used to prepare similar data for FRAP-T6 code. Unfortunately this code was not available to the authors of the Report. However it is known that some researches expanded the application range of FRAP-T6 code to include calculations of fuel rod characteristics at NPP base-irradiation modes [13, 14]. Therefore, a similar approach was used within the framework of the present work. In this case a special attention was paid to the verification of calculational results obtained at the first stage. Verification procedures consisted of several stages including the comparison of calculated results with both, experimental data and results of calculations using TOSUREP, TRIFOB [15] codes. Detailed description of corresponding procedures and obtained results are contained in subsequent sections of this Chapter.

5.4. Development of IGR/VVER version of FRAP-T6 code

5.4.1. Description of FRAP-T6 code

FRAP-T6 code was developed to calculate the behavior of LWR fuel rods during reactor transients and accidents such as loss-of-coolant and reactivity initiated accidents [1]. The code allows to predict the fuel rod behavior as a function of the fuel rod power, coolant boundary conditions, burnup and to simulate the following main physical phenomena:

- heat conduction;
- heat transfer from cladding to coolant;
- elastic fuel deformation;
- elastic-plastic cladding deformation;
- creep of cladding;
- fission gas release;
- fuel rod pressure;
- cladding failure due to stress corrosion cracking, cladding-pellet mechanical interaction, ballooning.

Fig. 5.12 shows the order of the general models in FRAP-T6 code. The calculation cycle starts with the determination of the temperature of the fuel and cladding in each calculation node of the fuel rod.

Then, the following parameters are sequentially calculated:

- gas temperature in the gas plenum;
- the stresses and strains in the fuel and cladding;
- the gas pressure inside fuel rod.

The entire calculation cycle is repeated until conditions, set in the numerical scheme, are satisfied. After that, calculations of the cladding oxidation, cladding ballooning and fission gas release are conducted. Iterative procedures allow to take into account the influence of calculation results in each model on other models.

In a general case the calculation of the fuel pin performance under NPP transient conditions is conducted by coupling FRAP-T6 code with FRAPCON-2 and SCDAP/RELAP5/MOD3 (or TRAC-F1) codes [12, 16, 17]. This procedure is schematically presented in Fig. 5.13. In this case FRAPCON-2 code provides the calculation of initial conditions for the fuel pin as a function of the burnup; SCDAP/RELAP5/ MOD3 or TRAC-PF1 codes calculate thermal-hydraulic boundary conditions. However the structure of FRAP-T6 code allows to set thermal-hydraulic boundary conditions independently using corresponding options of the code. In this case there is no need in using SCDAP/RELAP5/MOD3 or TRAC-PF1 codes.

It should be noted that FRAP-T6 code does not have an original data base to describe fuel rod material properties. For this purpose MATPRO-V11 is used [3]. The MATPRO-V11 material properties package allows to calculate thermal and mechanical properties of uranium oxide fuel and Zircaloy-4 cladding up to the melting temperature.

Properties of helium and fission gases are also calculated using the same code package. FRAP-T6 code has a direct interface with MATPRO-V11 package.

Regarding the FRAP-T6 code application region, the analysis shows that FRAP-T6 code and MATPRO-V11 codes are well adapted and verified for steady-state and slow transient conditions. The set of material properties and other physical correlations that take into account fast transient conditions is significantly less complete. Thus, the analysis of fuel rod behavior by FRAP-T6 code under RIA conditions requires a special attention and must be accompanied by special verification procedures. These comments are relevant also to tasks related to calculations of high burnup fuel rods. Since the last version of MATPRO package was developed in 1981, it does not contain many material properties that characterize conditions of commercial fuel rods at burnups of 50 MWd/kg U and higher obtained in more recent years.

5.16

```
                    ┌─────────────────────┐
              ┌────▷│   Fuel and cladding  │
              │     │  temperature model   │
              │     └──────────┬──────────┘
              │                ▽
              │     ┌─────────────────────┐
              │     │  Plenum temperature  │
              │     │        model         │
              │     └──────────┬──────────┘
              │                ▽
              │     ┌─────────────────────┐
              │  ┌─▷│   Fuel and cladding  │
              │  │  │  deformation model   │
              │  │  └──────────┬──────────┘
              │  │             ▽
              │  │  ┌─────────────────────┐
              │  │  │  Failure probability │
              │  │  │        model         │
              │  │  └──────────┬──────────┘
              │  │             ▽
              │  │  ┌─────────────────────┐
              │  └──│  Internal gas pressure│
              │     │        model         │
              └─────└──────────┬──────────┘
                               ▽
                    ┌─────────────────────┐
                    │  Cladding oxidation  │
                    │        model         │
                    └──────────┬──────────┘
                               ▽
                    ┌─────────────────────┐
                    │  Cladding ballooning │
                    │        model         │
                    └──────────┬──────────┘
                               ▽
                    ┌─────────────────────┐
                    │     Fission gas      │
                    │    release model     │
                    └──────────┬──────────┘
                               ▽
                         New time step
```
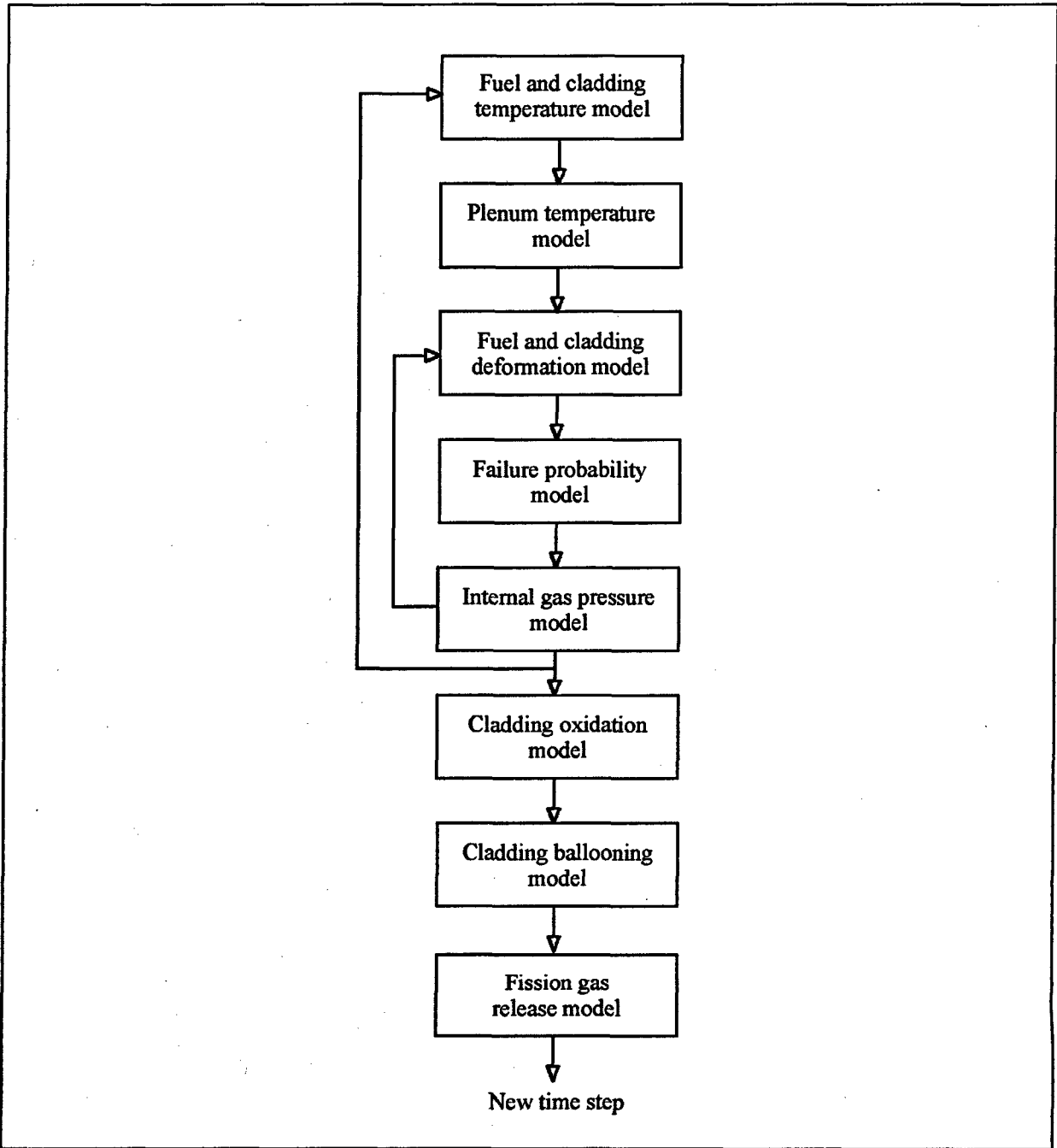
Fig. 5.12. Order of general models [1]

5.17

```
┌─────────────────────────────────────────────────────────────────────────┐
│                        ┌──────────────────────────┐                       │
│                        │        FRAPCON-2         │                       │
│                        │  Calculated burnup-dependent │                   │
│                        │   fuel pin initial conditions │                  │
│                        └──────────────────────────┘                       │
│                                     │                                     │
│                                     ▽                                     │
│                        Initial values of:                                 │
│                         • released fission gas inventory                  │
│                         • retained fission gas inventory                  │
│                         • permanent cladding strains                      │
│                         • cladding oxide thickness                        │
│                         • amount of open fuel porosity                    │
│                                     ▽                                     │
│       ┌──────────────────────────┐      ┌──────────────────────────┐      │
│       │  SCDAP/RELAP5 or TRAC-PF1 │      │        FRAP-T6           │      │
│       │ Calculates primary system thermal- │  │ Steady - state case run to provide │ │
│       │ hydraulic response, including: │   │ initial steady - state conditions │  │
│       │  • primary system pressures, tem- │ │ for SCDAP components │          │
│       │    peratures, void distributions │ └──────────────────────────┘      │
│       │  • break flow              │                                       │
│       │  • core thermal-hydraulics │         • Initial gap conductance      │
│       │  • containment isolation signal │    • Initial gap gas pressure      │
│       │    timings                 │         • Radial temperature profile   │
│       │  • fuel pin ballooning and rupture │                                │
│       └──────────────────────────┘                                        │
│                                     ▽                                     │
│                        Time-dependent tables of:                          │
│                         • bulk thermal-hydraulic conditions in            │
│                           core nodes and core inlet and outlet            │
│                           volumes                                         │
│                         • coolant mass flux in core nodes                 │
│                         • fuel pin power distribution                     │
│                                     ▽                                     │
│                        ┌──────────────────────────┐                       │
│                        │        FRAP-T6           │                       │
│                        │   Calculated transient    │                       │
│                        │    fuel performance       │                       │
│                        └──────────────────────────┘                       │
│                                     ▽                                     │
│                        Fuel pin failure timing                            │
└─────────────────────────────────────────────────────────────────────────┘
```

Fig. 5.13. Flow chart of methodology using FRAP-T6

5.4.2. Preliminary adaptation of FRAP-T6 code to analysis IGR/RIA tests

Formulation of the problem to adapt the FRAP-T6 code to IGR/RIA tests included the following working areas:

1. Account of design features of the fuel rod and the test capsule that were not provided for in the specification of input data, and the optimization of the calculational scheme.

2. Outline of FRAP-T6 models to calculate VVER fuel rods performance under IGR test conditions.

3. Development of new models and modification of FRAP-T6 models.

4. Outline of MATPRO-V11 code models required to calculate PWR fuel rod performance under IGR test conditions.

5. Modification of MATPRO-V11 models taking into account original material properties for VVER fuel rods.

6. Verification of FRAP-T6 version adapted for VVER fuel rods and IGR test conditions.

In accordance with these items, the first stage of the work was implemented to adapt FRAP-T6 code and MATPRO-V11 package for VVER fuel rods tested in IGR reactor. The schematic list of these activities is presented in Table 5.5.

Table 5.5. List of codes modifications

Research position	Set of actions
1. Adaptation of calculational scheme for fuel rod	• Account of central hole in fuel pellet • Account of material mass in upper gas plenum • Optimization of axial meshing in calculational scheme
2. Modification of FRAP-T6 models	• Heat transfer from cladding to air • Oxidation of Zr-1%Nb cladding • Correction of axial length of ballooning region in correspondent model
3. Modification of MATPRO-V11 package	• Thermal physical constants for unirradiated Zr-1%Nb • Thermal conductivity, specific heat, enthalpy of unirradiated Zr-1%Nb • Poisson's ratio, Young's modulus, thermal expansion of unirradiated Zr-1%Nb • thermal conductivity of VVER high burnup fuel • specific heat of VVER fuel

The analysis of presented data shows that at the first stage of FRAP-T6 adaptation it was impossible to solve one of the most important problems listed in Table 5.5 related to the modification of the data base on material properties of Zr-1%Nb. This is the problem of replacing Zry mechanical properties by corresponding properties of Zr-1%Nb, including properties of irradiated Zr-1%Nb claddings as a function of not only the temperature, but also of the strain rate, which is important for the interpretation of IGR/RIA tests. It was impossible to solve this problem because there is no corresponding data base available for Zr-1%Nb claddings. Thus, a decision was made to conduct a special cycle of experimental studies to obtain the required data. A detailed discussion of these studies is presented in Chapter 6 of this Volume. The obtained data base formed the basis for the modification of FRAP-T6 and MATPRO at the stage of the final adaptation of FRAP-T6 code for VVER fuel rods.

The final stage of the work cycle on the preliminary FRAP-T6 adaptation was the verification of the code version obtained. The characteristic of the experimental data base used for the verification is presented in section 5.9 of this Volume. Verification procedures were primarily focused on checking the correctness of rod cladding temperature calculations. The analysis of first verification calculations demonstrated that Bromley-Pomerantz model [18], recommended in FRAP-T6 code for the description of the heat transfer in post-critical heat flux (post-CHF) region, lead to unacceptable results (see Fig. 5.14). This conclusion forced us to look for an alternative model that takes into account the subcooling effect. Modified Labuntzov model was selected as the alternative model [19, 20]. This model takes into account the subcooling effect [21] and is intended for the simulation of the heat transfer under film boiling conditions. The use of this model allowed to get rather good results for the simulation of all heat transfer modes up to rewetting phase (see Fig. 5.15). The comparison of experimental and calculated results shows that Labuntzov model overestimates the duration of the film boiling and, consequently, overestimates the cladding temperature. The rewetting phase begins significantly earlier in the experiment.
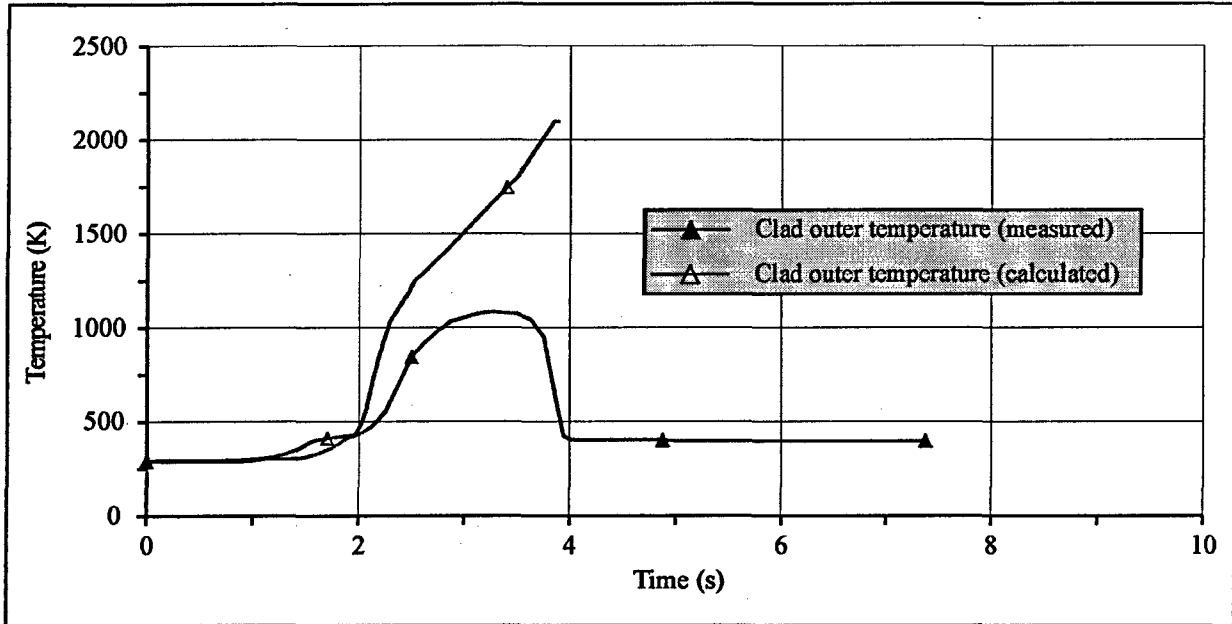
Fig. 5.14. Comparison of the measured clad outer temperature and calculated by FRAP-T6 with Bromley-Pomerantz model
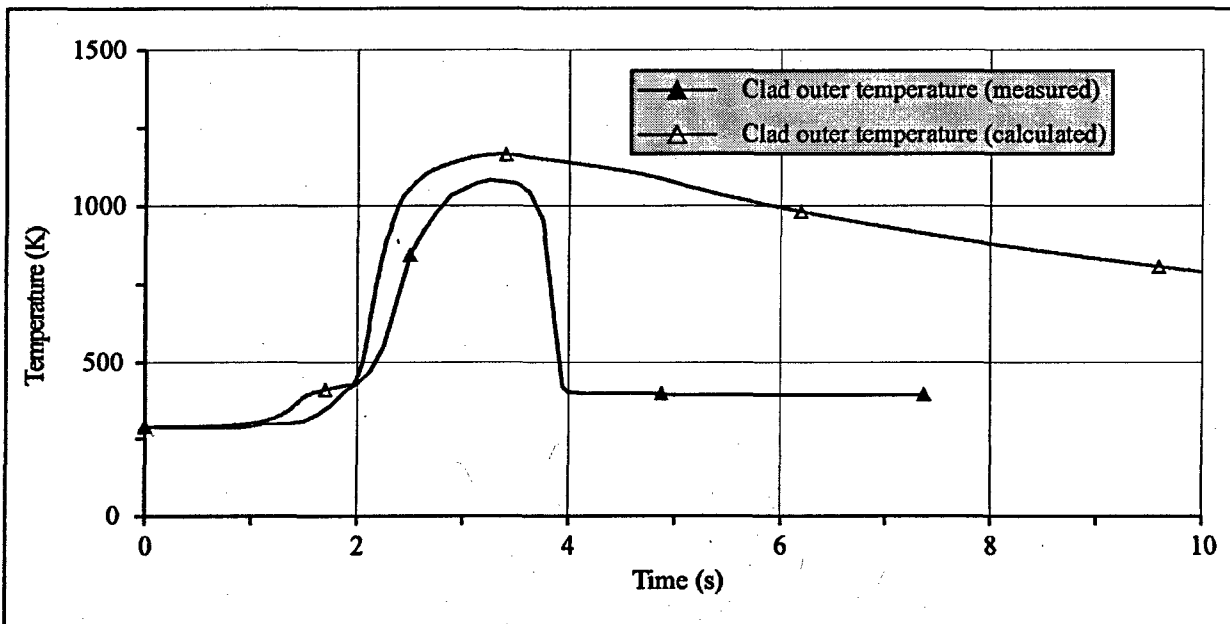
Fig. 5.15. Comparison of the measured clad outer temperature and calculated by FRAP-T6 with Labuntzov model

The next verification stage was the comparison of measured and calculated values of the cladding temperature for tests with the air coolant. Promising results were obtained for this case. The outcome of the preliminary adaptation of FRAP-T6 code for the behavior analysis of VVER fuel rods under IGR test conditions was the understanding that, in order to consider the FRAP-T6 adaptation to be successful, it is necessary to perform a serious modification of the model of the post-CHF heat transfer and to obtain mechanical properties of Zr-1%Nb claddings. During subsequent studies these two problems were solved to a significant extent and the original version of FRAP-T6 code was developed to simulate IGR tests.

5.20

5.4.3. Description of FRAP-T6 version to predict VVER fuel rod performance under IGR test conditions

5.4.3.1. Calculational scheme

As it was noted in Section 2.1 three types of fuel rods were tested in IGR reactor:

- fuel rods with high burnup fuel and irradiated cladding (C-type);

- fuel rods with fresh fuel and irradiated cladding (D-type);

- fuel rods with fresh fuel and unirradiated cladding (E-type).

From the point of view of the geometry, the design of all three types of fuel rods was similar. Thus, a common approach was developed for all types of fuel rods. The following assumptions formed the basis of the calculational scheme of VVER fuel rod:

- fuel and cladding are of cylindrical form and are arranged axisymmetrically;

- initial fuel diameter, cladding thickness and gap width are constant on the axial coordinate;

- there are no changes in the fuel density and composition along the fuel rod height and radius;

- only the active part of the fuel rod is simulated.

The geometrical scheme of VVER fuel rod including the meshing scheme is presented in Fig. 5.16. The calculational scheme of the fuel rod consists of the fuel stack with the central hole, cladding, fuel-cladding gap, lower and upper plenums and pseudo spring. The meshing scheme determines axial and radial calculational nodes.
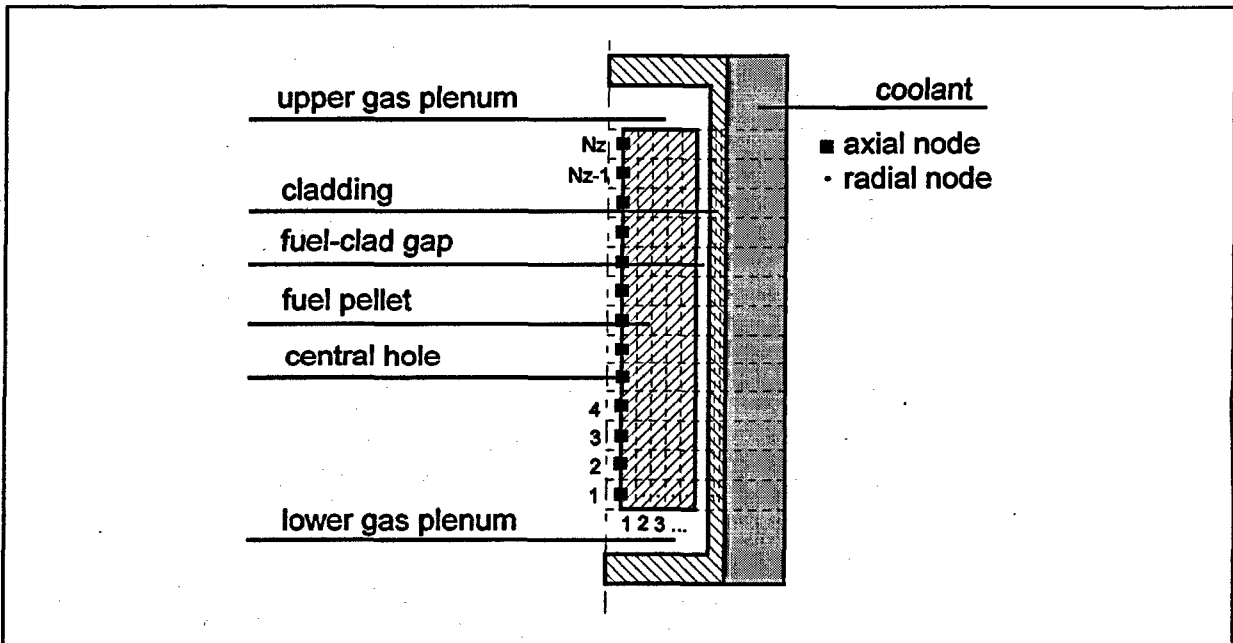
Fig. 5.16. Calculational scheme of fuel rod

The optimization procedure was used to determine meshing parameters for VVER fuel rod.

The sensitivity of calculated parameters to meshing conditions was used as the optimization criterion. As a result, the following characteristics of the calculational scheme were obtained:

- axial nodes: 10

- radial nodes: 31, including

fuel:	25
cladding:	6
• time step during fast transient:	$1 - 5 \ 10^{-3}$ s
• time step during slow transient:	$5 \ 10^{-3} - 1.0$ s
• accuracy parameters of the numerical solution:	
fuel temperature	±1 K
number of iterations in calculations of the gas pressure and radial temperature distribution	200
relative difference between two iterations (criterion to stop the calculation)	0.1%

The design of the test capsule, in which the VVER fuel rod was placed during tests in IGR reactor, was not simulated by FRAP-T6 code. All calculations were performed under the assumption that the fuel rod is surrounded either by an infinite volume of stagnant water under normal initial conditions, or by an infinite volume of air under the same conditions.

5.4.3.2. Input data to characterize the geometry of VVER fuel rods and IGR test conditions

VVER fuel rods

The set of characteristics that were used to form the input data in FRAP-T6 code is presented in Table 5.6. The table contains also a brief description of methods that were used to get individual input data for each VVER fuel rod. Measured parameters for each fuel rod were taken from Appendix C, D and E of Volume 3.

Regarding the material composition of fuel rods, it was assumed that the uranium dioxide is the material of the fuel pellet, and Zr-1%Nb alloy is the material of the cladding, and He is the gas inside fuel rod.

Other components of the high burnup fuel (fission products) were taken into account, if necessary, by using material properties for high burnup fuel. Special input data were developed for the calculation module that describes the fission product release. These issues are discussed in more detail in the following Section of the Report.

IGR test conditions

In addition to initial data for the coolant, parameters that characterize the power of each fuel rod were used as input data. These parameters allow to describe r, z, t distributions of the fuel rod power using the following data base presented in Appendixes G, H, I of Volume 3 of the Report:

- power time history;
- axial power profile;
- radial power profile.

As it has been noted earlier, the adjustment of FRAP-T6 module that describes the radial power profile was performed to take into account the central hole in the fuel pellet.

Table 5.6. Set of input data on fuel rod design

Parameters of fuel rod		Method to determine the parameters for VVER fuel rods
1.	**Fuel rod data**	
1.1.	Fuel stack cold length	as measured
1.2.	Cold fuel rod outer diameter	as measured
1.3.	Cold state fuel rod temperature	293 K
1.4.	Gas gap radial thickness	as measured and estimated
2.	**Pellet data**	
2.1.	Cold state pellet height	It was calculated in the assumption that fuel stack consists of 10 pellets
2.2.	Cold state pellet dish volume	It was calculated taking into account the pellet geometry
2.3.	Pellet outer diameter	as measured
2.4.	Pellet inner diameter	as measured
2.5.	Pellet surface roughness	estimated according to [32]
2.6.	Fraction of theoretical density	It was calculated taking into account the data on 2.7
2.7.	Fuel density	as measured
3.	**Cladding data**	
3.1.	Inner surface roughness	estimated according to [32]
3.2.	Cladding thickness	It was calculated taking into account the cladding outer diameter, pellet outer diameter, gas gap thickness
4.	**Plenum data**	
4.1.	Upper plenum volume	as measured
4.2.	Lower plenum volume	as measured
4.3.	Initial gas composition	He
4.4.	Initial gas pressure	as measured

In the current version of FRAP-T6 code, the integral of the relative power in the pellet area is calculated as follows:

$$\frac{\int_{0}^{2\pi}\int_{r_1}^{r_2} P(r,\theta)r\,dr\,d\theta}{\pi(r_2^2 - r_1^2)} = 1 \pm 0.01,$$

where $P(r,\theta)$ = normalized radial power factor at r, θ,

r = current pellet radius;

θ = azimuthal angle;

r_1 = pellet inner radius;

r_2 = pellet outer radius.

Materials properties

MATPRO-V11 package was used to form input data required for the calculation of VVER fuel rod behavior under IGR test conditions. As it has already been noted, additional original material properties of VVER fuel rods and air coolant were developed and included into the package according to the procedures, described in Section 5.6.

5.4.3.3. Output data

The data base that characterizes the behavior of VVER fuel rods under IGR test conditions was obtained using the following set of output parameters of FRAP-T6 MOD1 code:

- time history of energy deposition, power of fuel rod, specific energy of metal-water reaction, specific leakage of energy, fuel enthalpy;

- time–axial–radial distributions of the temperature for fuel and cladding;

- time history of heat transfer coefficient and heat flux on the cladding surface;

- time history of fuel rod pressure, gas gap thickness, ZrO_2 thickness on the cladding;

- time history of cladding hoop stress;

- time history of fuel swelling, fuel hoop strain, fission gas release;

- special set of peak- and failure parameters characterizing fuel rod performance under the test condition.

5.4.3.4. Selection of FRAP-T6 models to calculate VVER fuel rod performance

FRAP-T6 MOD1 code contains a lot of models for predicting the fuel rod behavior under accident conditions [1]. However the purpose of this Section is to present the list of FRAP-T6 code models from which the user must select the required model out of several alternatives. The list of models that were modified for VVER fuel rod is presented in the next Section of the Report.

FRAP-T6 code provides model selection for the following options:

- internal gas pressure;

- metal-water reaction;

- deformation;

- failure;

- heat conduction.

Suboption of "plenum temp" was selected to calculate the internal gas pressure in VVER fuel rod, since this model is recommended as a preferable one in FRAP-T6 Model Selection Data Block. The option "Metal-Water Reaction" in FRAP-T6/VVER code version was described using the model presented in Section 5.4.3.6. This is why none of FRAP-T6 suboptions was used. In accordance with IGR test conditions and FRAP-T6 recommendations, suboptions named "FRACAS-I", "General" and "CENTRAL VOID" were selected for options "Deformation", "Failure" and "Heat Conduction", respectively.

5.4.3.5. Approach to determine the input data characterizing fission product distribution in the high burnup VVER fuel before IGR tests

In order to calculate fission gas release (FGR) and fuel swelling for VVER high burnup fuel under RIA test conditions, initial distribution of fission gas products is to be known for each of high burnup fuel rods. As was stated earlier standard procedure of calculating FGR by FRAPCON-2 code is usually performed for such cases [12]. The final result of these calculations is spatial distribution of Kr and Xe isotopes. As the authors of this report had no possibility to use FRAPCON-2 code, Kr and Xe spatial distribution at the end of fuel cycle for Unit 5 NV NPP was identified by FASTGRASS model of FRAP-T6 code. Specifics of the obtained data were confirmed later by a number of verification procedures, described in section 5.7.

5.24

Input data from Appendixes A, B of Volume 3 of the report were used to calculate performance of commercial fuel elements during fuel cycle. Heat transfer from fuel elements to coolant was calculated with the help of standard FRAP-T6 code models for the water coolant with the given parameters, characterizing flow rate, inlet temperatures, outlet pressure, hydraulic diameter of the channel, etc. Real geometry of the VVER fuel element was taken as the basis for the development of the nodalization scheme. Power history was calculated without consideration of the transients connected with the shut downs of the reactor. The procedure of special axial meshing of fuel elements was performed after the calculation results of the fuel cycle were obtained. The objective of this procedure was to find the sections within the length of commercial fuel element for which the average value of burnup is corresponded to the average value of burnup for each of re-fabricated high burnup fuel rods within the heated length. The number of the respective fuel rod was given to each of these sections, and FGR radial distribution within these sections was assumed as the input data characterizing FGR in 13 high burnup fuel rods prior to IGR tests.

It is important to note that a number of modifications was made in order to get final calculational results including:

- FSWELL model from MATPRO library was introduced to calculate the steady-state fuel swelling;
- fuel densification model from PIN-04M code [22] library was used to consider fuel radiation densification, besides we also considered a number of original VVER characteristics;
- dependence of fuel thermal conductivity vs. burnup was considered;
- RIM effect was considered by introducing the radial coefficient of the energy density non-uniformity vs. time.

The final set of FGR distribution contains the following data base for Kr and Xe in each of fuel rods:

- radial distribution of intragranular bubbles concentration;
- radial distribution of bubbles on grain face;
- radial distribution of bubbles on grain edges.

5.4.3.6. Modified models in FRAP-T6 code

The list of modified models in FRAP-T6 code includes the following items:

- metal-water reaction;
- heat transfer to air coolant;
- DEFORM subroutine;
- film boiling correlations;
- BALON2 subroutine.

Metal-water reaction

Parameters that characterize the oxidation kinetics of Zr-1%Nb were obtained on the basis of experiments conducted with samples of unirradiated claddings [7]. Tests were performed in the water steam at the atmospheric pressure under isothermal and quasi-isothermal conditions. To describe the cladding oxidation, the classical parabolic dependence was proposed:

$$W^2 = A\exp(-B/T)\tau,$$

where $W =$ ZrO_2 or $\alpha Zr(O)$ thickness (m);

$\quad\quad T =$ temperature (K);

$\quad\quad \tau =$ time (s);

$\quad\quad A, B =$ coefficients.

Experimentally determined coefficients A and B allow to use the equation for the calculation of the thickness of ZrO_2 layer and of alpha zirconium layer stabilized by oxygen.

Values of A and B coefficients are presented in Table 5.7.

Table 5.7. A, B coefficients for Zr-1%Nb oxidation

Temperature. (K)	ZrO$_2$		αZr(O)	
	A	B	A	B
<1773	5.19 10^{-7}	15355	1.44 10^{-6}	14088
1773 - 1873	17.72 10^{-7}	14680	5.16 10^{-5}	19520
>1873 up to melting	17.72 10^{-7}	14680	1.5142 10^{-7}	24230

Model of heat transfer to air coolant

For the above conditions heat transfer coefficient can be presented as follows:

$$h = h_{con} + h_{rad},$$

where h_{con} = heat transfer coefficient due to convection;

h_{rad} = heat transfer coefficient due to radiation (the code already has this model).

Heat transfer coefficient due to convection can be determined by the system of the following equations [20]:

$$Nu = CRa^n, \quad Ra = GrPr,$$

$$Gr = \frac{g\beta(t_W - t_f)z^3}{v \cdot a},$$

$$h_{con} = \frac{\lambda Nu}{z},$$

where Nu, Ra, Gr, Pr = Nusselt number, Rayleigh number, Grashof number, Prandtl number, respectively;

g = acceleration due to gravity (m/s^2);

β = thermal expansion volumetric coefficient (1/K);

z = heating length (m);

t_W = wall temperature (K);

t_f = fluid temperature (K);

C, n = coefficients;

λ = thermal conductivity (W/m K);

h_{con} = heat transfer coefficient due to convection;

v = kinematic viscosity (m^2/s);

a = temperature conductivity (m^2/s).

Nu, Ra, Gr, Pr are calculated at the temperature:

$$t_m = \frac{(t_W + t_f)}{2},$$

C, n coefficients are identified according to the data of Table 5.8.

Table 5.8. C, n coefficients vs. Ra, Pr

Ra	Pr	C	n
$10^3 - 10^9$	0.1	0.32	0.25
	1.0	0.54	0.25
	10	0.62	0.25
	100	0.66	0.25
$10^9 - 10^{13}$		0.15	0.333

DEFORM subroutine

DEFORM subroutine calculates the gap between the fuel and cladding. Despite the fact that FRAP-T6 declares the capability to account for fuel strain by swelling when calculating pellet/cladding gap, this procedure is not performed automatically. That is why this effect was additionally taken into account by DEFORM subroutine.

BALON2 subroutine

Correction of the axial length of ballooning region was made by BALON2 subroutine in order to consider specific features of VVER fuel rods. Original version of BALON2 subroutine suggests to consider that axial length is equal to 8 cm. But the heated length of VVER fuel rods is equal to 15 cm only. Use of the axial length of ballooning, which exceeds the half of the fuel rod length, makes it much more difficult to interpret the calculation results. Moreover, the results of post-test examinations of the VVER fuel rod indicated that the actual axial length was 2-4 cm. That is why axial length in the BALON2 was decreased to 3 cm.

Heat transfer models for water coolant

FRAP-T6 code has multiple correlations to calculate the heat transfer from the fuel rod to the coolant. For IGR test conditions, the following set of correlations was selected, that sequentially describes the change of heat exchange regimes on the fuel rod surface in the straight and reverse directions: convection, nucleate boiling, transition boiling, film boiling. The nature of the change of the heat flux from cladding to the coolant for these regimes is presented in the linearized form in Fig. 5.17.
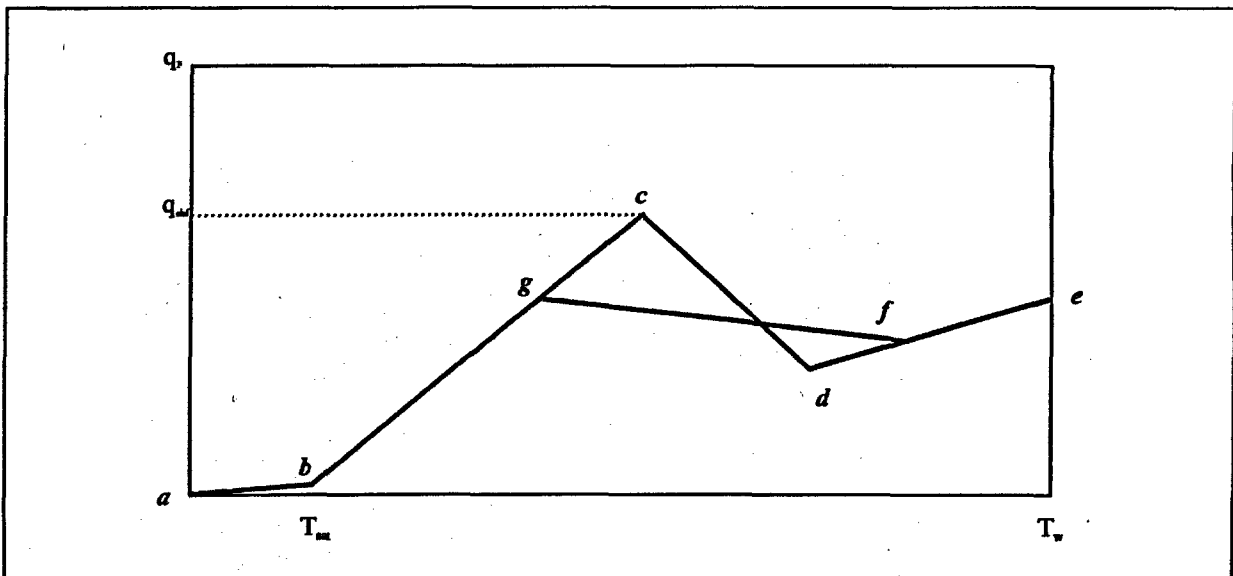
Fig. 5.17. Heat flux from cladding to coolant vs. wall temperature used in FRAP-T6 code for IGR tests

The convection regime (section a-b) was described by Dittus-Boelter correlation [23]. When the wall temperature reaches the saturation temperature T_{sat} the transition to the nucleate boiling takes place. Chen correlation [24] was used for the nucleate boiling regime (section b-c). The transition from the nucleate

5.27

boiling regime to the transition boiling regime takes place when the heat flux reaches the critical heat flux value (q_{chf}). McDonough correlation was provided to describe the transition boiling regime (section c-d). Calculations of heat transfer coefficients in section c-d are performed in parallel with calculations of heat transfer coefficients using film boiling correlations. As soon as the comparison of two coefficients shows that heat transfer coefficients for film boiling are higher than the heat transfer coefficient for transient boiling, the transition to the film boiling regime takes place (point d). As it was noted in section 5.4.2, results of the preliminary verification of FRAP-T6 code shows that the use of Bromley-Pomerantz model [18] to describe the film boiling regime (section d-e) leads to a significant overestimation of the cladding temperature. The search for an alternative model allowed to propose Labuntzov model [19] with a subcooling factor, that takes into account particular features of the heat exchange at subcooling of water. As it was shown in section 5.4.2, the use of this model allows to predict the cladding temperature with a good accuracy till the rewetting phase (point f). The rewetting phase begins in IGR tests much earlier in comparison with predictions by the original model of FRAP-T6 code. Therefore, a special model was developed for this phenomenon and the criterial rewetting temperature T_{wet} was proposed in order to find point f that characterizes the reverse transition from the film boiling to the nucleate boiling regime (section d-g). The heat flux for this section was calculated using heat transfer coefficients for which the linear interpolation law was specified.

Thus, two additional models were introduced in FRAP-T6 code to calculate parameters of the film boiling regime.

The first one - Labuntzov model - is described by the following expression:

$$\alpha_{FB} = 0.25(\lambda_g^2 c_{pg}(\rho_f - \rho_g)\frac{g}{v_g})^{1/3},$$

where α_{FB} = heat transfer coefficient (W/m²K);

λ_g = steam thermal conductivity (W/m K);

c_{pg} = steam specific heat (J/kg K);

ρ_f = fluid density (kg/m³);

ρ_g = steam density (kg/m³);

g = gravity acceleration (m/s²);

v_g = steam kinematic viscosity (m²/s).

To take into account the initial subcooling of water, the correction factor is introduced [21]:

$$\alpha_{FB}^{\bullet} = \alpha_{FB}(1 + 0.1(\frac{\rho_f}{\rho_g})^{0.75}\frac{\Delta i}{h_{fg}}),$$

where $\alpha_{FB}^{\bullet}$ = corrected heat transfer coefficient (W/m²K);

Δi = enthalpy of fluid at saturation minus enthalpy at fluid bulk temperature (J/kg).

The second developed model - Rewetting model - is based on the hypothesis of the associative similarity of the rewetting and reflooding regimes. The main idea of the proposed method is as follows [25]:

• the wetting rate does not depend on the rate of the fluid supplied from the outside; it depends only on the rate of the steam bubble generation, since under these conditions a free access of the fluid to the steam film is provided;

• the presence of axial – radial heat leakages through cold end elements of the fuel rod leads to the generation of wetting waves at the top and bottom boundaries of the heated section of the fuel rod; and boundaries of wetting waves gradually move to the fuel rod center.

5.28

In other words, axial heat leakages into unheated parts of the fuel rod lead to a decrease in the cladding temperature in axial segments near unheated parts of the fuel rod. Thus, rewetting fronts occur and move from upper and lower parts of the fuel rod to the center of the heated length.

To model processes of this type, a large number of models was developed [26-28]. In this case the original rewetting model that takes into account specific features of IGR tests was developed. Approximate analytical dependencies were obtained to calculate the rewetting front velocity and the time history for the temperature distribution in the multi-layer system of the fuel rod [25].

The solution of the two-dimensional non-stationary equation of the heat conductivity in the solid with internal heat sources formed the basis of the method:

$$\rho c_p \frac{\partial T}{\partial t} = \frac{\partial}{\partial z}\left(\lambda \frac{\partial T}{\partial z}\right) + \frac{1}{r}\frac{\partial}{\partial r}\left(r\lambda \frac{\partial T}{\partial r}\right) + q_v,$$

where ρ = clad density (kg/m^3);

c_p = clad specific heat (J/kg K);

T = temperature (K);

λ = clad thermal conductivity (W/m K);

q_v = volume internal heat source (W/m^3).

In this case, ρ, c_p, λ_z, λ_r are functions of the temperature. Additionally, an axial profile of cladding temperature is specified in the region of the rewetting front by the corresponding equations. This profile depends on the velocity of the rewetting front. At the rewetting front the cladding temperature is equal to the minimum stable film boiling temperature.

The solution of this equation is reduced to the solution of a system of algebraic equations with respect to the dislocation velocity of the rewetting front.

The values obtained for the velocities of the rewetting fronts, moving upward and downward, are used to obtain the moment of rewetting for each axial slice. Distances, covered by each of the rewetting fronts by the time t, are found by integration:

$$L_U(t) = \int_{t_o^U}^{t} u_U(\tau)d\tau, L_D(t) = \int_{t_o^D}^{t} u_D(\tau)d\tau,$$

where t = current time (s);

$L_U(t)$ = distance covered by the rewetting front, moving upward (m);

$L_D(t)$ = distance covered by the rewetting front, moving downward (m);

t_o^D = time at which rewetting of the lower heated part of the fuel rod starts (s);

t_o^U = time at which rewetting of the upper heated part of the fuel rod starts (s);

$u_U(\tau)$ = velocity of the rewetting front, moving upward (m/s);

$u_D(\tau)$ = velocity of the rewetting front, moving downward (m/s).

To apply the obtained model, the following logical approach was developed for FRAP-T6 code:

- till $T_{clad} \approx 740$ K, calculation are performed in accordance with the procedure sequence described for Fig. 5.17;

- then, in parallel, calculations of parameters of the film boiling regime and parameters characterizing the rewetting front movement are conducted;

- transition from the film boiling to the transition boiling occurs simultaneously for all axial slices when rewetting front reaches the axial slice of the fuel rod with maximum power.

5.5. Development of IGR/VVER version of the SCANAIR code

5.5.1. Description of the SCANAIR code

SCANAIR computer code is designed to model thermal mechanical behavior of LWR fuel rods under reactivity initiated accident conditions [2]. Version 2.2 used by us was developed in the Institute for Protection and Nuclear Safety (IPSN, France) in order to model the first stage of the accident. The models describing cladding failure, cladding oxidation, etc. are still being developed, and thus are not present in this code version.

The following physical processes are modeled by the SCANAIR code in order to describe fuel rod behavior under RIA conditions:

- heat transfer in fuel, clad and in pellet-cladding gap;
- heat transfer from cladding to coolant, and from coolant to the channel wall;
- gas pressure inside fuel rod;
- fuel and cladding mechanical behavior;
- fission gas transient behavior.

Fig. 5.18 presents the logical scheme used by SCANAIR code to calculate fuel rod performance.
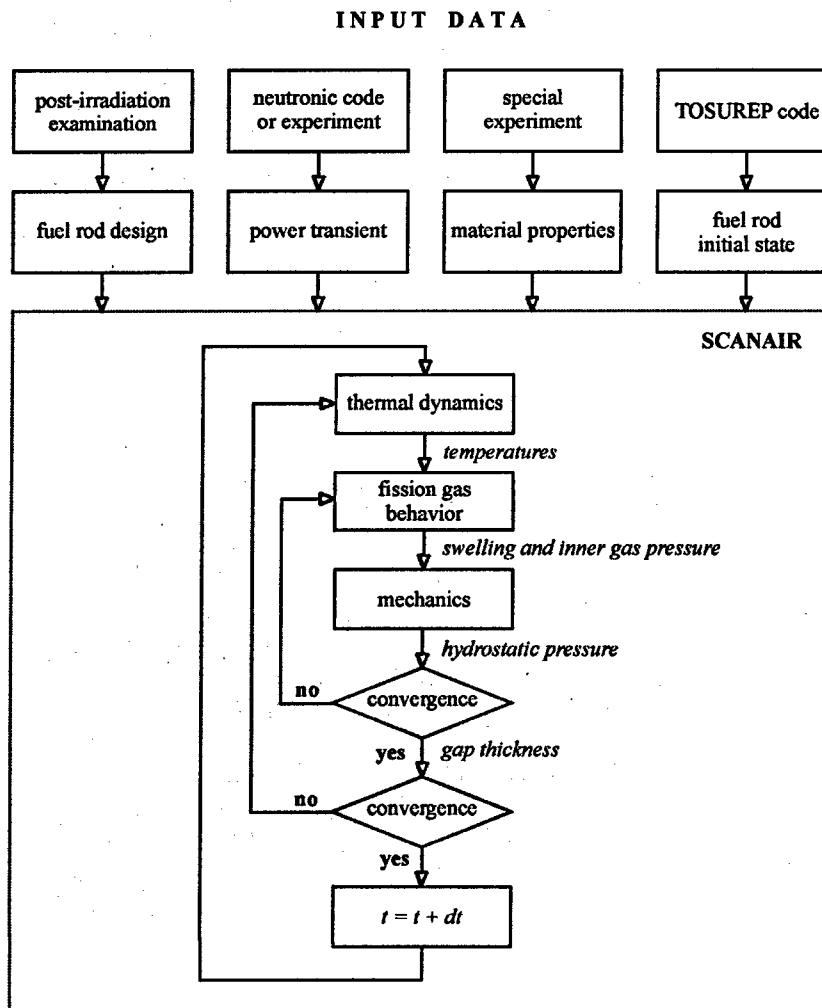
Fig. 5.18. Principal scheme of SCANAIR code

5.30

Temperature distribution within the fuel, cladding and coolant is calculated by the thermal dynamics model, then the results are transferred to the model of fission gas behavior. Fission gas behavior model calculates composition and spatial distribution of the fission gas products, and transfers the current data on the swelling and inner gas pressure to the mechanics model. Stress-strain conditions in the fuel and cladding are calculated by the mechanics model. Fuel hydrostatic pressure data are transferred to the model of fission gas behavior and used to calculate gas pressure in the porous area. The whole computation cycle in the fission gas behavior and mechanics models is iteratively repeated up to convergence in hydrostatic pressure in the fuel. After that the value characterizing pellet–cladding gap is transferred to the thermodynamic model, and the whole computation process is repeated up to convergence in the pellet-clad gap. Then the whole procedure is repeated within the new integration stage.

SCANAIR can use the following set of input data in order to model an irradiated fuel rod:

- measured geometrical fuel rod parameters;

- measured or calculated power history;

- thermal-physical and mechanical properties of materials;

- parameters characterizing initial state of a fuel rod (prior to RIA).

It is important to note that the initial state of a fuel rod is characterized by geometric parameters, as well as by composition and spatial distribution of fission gas products. Special TOSUREP code is used to calculate this set of parameters for the required moment of a fuel cycle at the NPP [11]. Hence, all the initial geometric parameters of fuel rods can be either measured or calculated the complex approach can also be applied.

Brief description of each of the major SCANAIR models is presented below.

Thermal-dynamics model

This model describes heat transfer in the fuel rod, thermal-hydraulic behavior of coolant and heat transfer between fuel rod and coolant.

These are the major peculiarities of the heat transfer module:

- heat transfer in fuel rod is calculated in the radial direction only;

- radial coordinates of calculational nodes are the function of time;

- axial coordinates of calculational nodes are not the function of time;

- gas temperature in the gas plenum is equal to the gas temperature in the adjacent gas gap;

- heat transfer model for the pellet-cladding gap considers conductive and radiation components only, heat transfer due to natural convection and the contact component are not considered.

The coolant is modeled as a single-phase flow and by one-dimensional equations of conservation of the mass and energy. Boundary conditions are specified as the mass flow rate and the inlet temperature. Coolant material properties and heat transfer coefficients at the cladding surface and channel wall are used as the closure relations.

SCANAIR code assumes modeling of three typical modes of heat transfer between cladding and coolant:

- heat transfer due to convection;

- heat transfer due to nucleate boiling;

- heat transfer due to film boiling.

Two options exist for heat transfer due to convection. In the first option Dittus-Boelter law [23] is used for forced convection. In the second option it is considered that heat transfer coefficient is equal to 100 W/m²K. The code automatically selects for the calculations the option, which predicts the higher value of the heat transfer coefficient. If the cladding temperature reaches the saturation temperature the change takes place for heat transfer due to nucleate boiling which is described by the Chen model [24]. Criterion for the departure from nucleate boiling is based on the temperature of the minimum stable film boiling. This temperature is calculated in accordance with the Groenveld-Stewart law [29]. Bromley law is used to calculate heat transfer due to nucleate boiling [18].

Mechanics model

Mechanics model is based on the assumption that the fuel column and the cladding are long axial asymmetric cylinders. Total fuel strain includes the following components: elastic strain, plastic strain, thermal expansion, cracking strain, strain due to swelling. Cladding strain is calculated with consideration of elastic strain, plastic strain, and thermal expansion.

Mechanics model calculates fuel and cladding displacement in the axial and radial directions, cladding anisotropy is not considered. Elastic strain and plastic strain of the cladding is calculated on the basis of the assumption on isotropic mechanical properties. Calculation of the stress – strain state for the cladding is done on the basis of the assumption on the ideal elastic plastic material. I.e. elastic region is calculated by the Hooke's law with the specified Young's modules. Hypothesis of the ideal plastic body with no strain hardening is used to calculate simultaneous plastic strain of the cladding, flow of materials is described according to the Prandtl-Reuss rule. Plastic strain increments are calculated for the effective stress equal to the yield stress. Finite element technique is used to solve equilibrium equations.

It is important to note that calculation of the fuel clad local plastic strain of the ballooning type is not possible by the mechanics model of the SCANAIR code. Neither does the code have the models for cladding failure.

It is important that elastic and plastic strain in the fuel is not modeled if the initial fuel cracking is specified.

Model of fission gas behavior

This model describes fission gas release, fuel swelling and redistribution of the fission gas within the fuel between three types of populations: intragranular bubbles, intergranular bubbles, porosity gas. It is assumed that intragranular bubbles move to the grain boundary due to the temperature gradient and Brownian motion. Temperature increase and coalescence of the intragranular bubbles lead to the growth of the gas pressure in the bubbles and to the increase of their radius. These two effects result in their turn in the intragranular fuel swelling. Intergranular bubbles are located at the boundaries of fuel grains. Temperature growth leads to the intergranular fuel swelling. Besides, migration of the intragranular bubbles to the grain boundaries results in the intergranular swelling as well. It is assumed that if gas pressure inside intergranular bubbles leads to the pressures exceeding fuel fracture stress, this gas volume goes to the porous area.

Initial concentration of porosity gases is calculated by the TOSUREP code. Current values characterizing porosity gases are calculated on the basis of the balance correlations between initial porosity gases, additional porosity gases due to intergranular gas flow, and porosity gases migrating in the free gas volume of the fuel rod according to the Darcy law.

5.5.2. Preliminary adaptation of the SCANAIR code to analysis of IGR/RIA tests

At this stage the major effort was directed to solving a number of standard and specific tasks. By the standard problem we mean development and optimization of the nodalization scheme, preparation of individual input data for 25 VVER fuel rods, etc. The set of specific tasks included the following issues:

- analysis of the SCANAIR code representativity to calculate VVER fuel rod behavior under RIA test conditions, and modification of some code models;
- development of an approach to consider VVER original material properties;
- development of the preliminary SCANAIR version to analyze IGR tests;
- preliminary verification of the SCANAIR/VVER code version;
- working out of recommendations to develop the final version of the SCANAIR code for VVER fuel rods.

As for the code representativity the major problem is that SCANAIR code does not allow to predict cladding failure, besides it is not designed to calculate great values of clad hoop plastic strain typical for the pressurized VVER fuel rods tested at the level equal to or higher the failure threshold value. Considering the fact that a significant group of fuel rods was tested below the failure threshold value, use of the SCANAIR code to analyze such fuel rods can be justified under condition that we review special aspects connected with the original material properties of the VVER fuel rods, and some other specific features of the fuel rod design and conditions of testing.

In accordance with the recommendations of sections 5.1, 5.2 preliminary package of the VVER material properties was developed, and other input data and nodalization scheme were prepared. Then preliminary stage of the verification procedure with the use of specific test data base was completed. Verification results allowed us to find two serious problems at this stage of the study:

- non-adequacy of the SCANAIR heat transfer models for the IGR test conditions;
- necessity to correct gas pressure model.

Modification of heat transfer models

Verification procedures have indicated that the use of original Chen model to calculate heat transfer from the fuel rod to the coolant under nucleate boiling conditions leads to the unacceptable overestimation of the cladding temperature (Fig. 5.19).
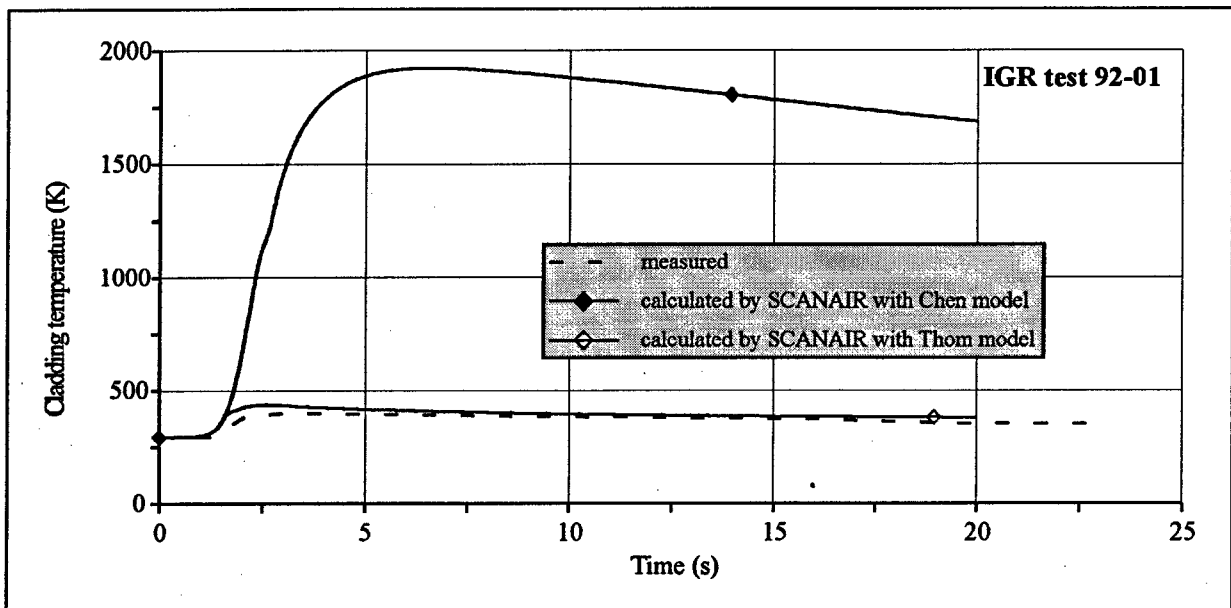
Fig. 5.19. Cladding temperature vs. time

In order to comprehend the reasons for this overestimation it is necessary to review the Chen model in more details. Chen correlation is presented as:

$$\alpha = F\alpha_{con} + S\alpha_{nb},$$

where α = total heat transfer coefficient;

α_{con} = macroscopic heat transfer coefficient due to turbulent convective flow;

α_{nb} = microscopic heat transfer coefficient due to nucleate boiling;

F = intensification factor of convective heat transfer;

S = factor of boiling suppression.

Analysis of this correlation indicates that consideration of pool-boiling conditions typical for IGR tests leads to very small values of α_{con} coefficient. Besides, it was found out that suppression factor S is equal to zero, and F factor - to 1 for the single phase flow model which is used in the SCANAIR code. In the frames of the Chen model both of these reasons lead to a very fast departure from nucleate boiling (DNB), and as the consequence - to overestimation of the cladding temperature. That is why the attempt was made to use Thom correlation to calculate cladding temperature [30]. This correlation developed specifically for the sub-cooling boiling conditions is described by the following expression:

$$q_F = 2000\Delta T^2 \exp(\frac{P}{4.34}),$$

$$\Delta T = T_W - T_S,$$

where q = heat flux (W/m²);

ΔT = superheating of the wall (K);

T_W = wall temperature (K);

T_S = saturation temperature (K);

P = coolant pressure (MPa).

Introducing of this correlation into SCANAIR code allowed us to obtain good agreement between the measured and calculated temperatures for nucleate boiling (see Fig. 5.19). But the next stage of verification procedures to test SCANAIR code under post-CHF conditions revealed a new problem. The problem is that the transfer from the nucleate boiling to the film boiling is done by the SCANAIR code with the help of the temperature criterion described by the following expression [29]:

$$T_{MFB} = 284.7 + 4.4110^{-5}P - 0.037210^{-10}P^2,$$

where T_{MFB} = minimum temperature of the stable film boiling (°C);

P = coolant pressure (Pa).

Application of this criterion for the IGR test conditions leads to the fact that heat transfer crisis does not occur because the cladding temperature happens to be always less than T_{MFB} (Fig. 5.20).
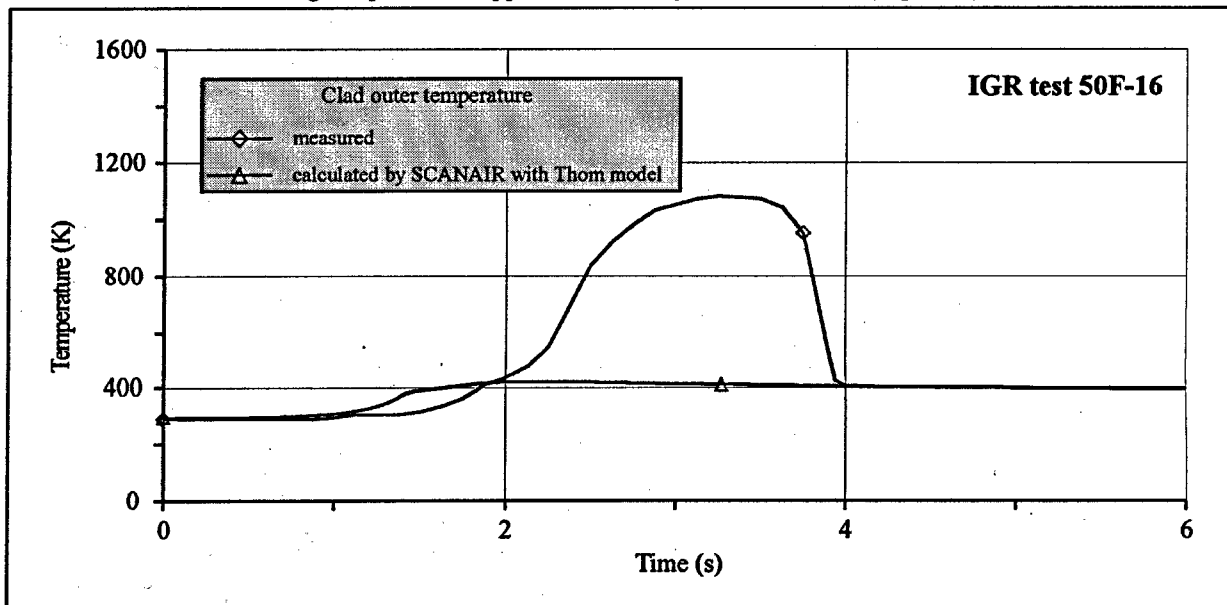
Fig. 5.20. Verification of SCANAIR code with Thom model for nucleate boiling and original SCANAIR DNB criterion

That is why the above set of correlations can not be used to predict cladding temperature under post-CHF conditions for IGR tests. So the third step in this direction was made to improve the criterion for DNB. The selected Kutateladze model is based on the correlation for critical heat flux under pool boiling conditions [21]:

$$q_{CHF} = 0.23h_{fg}\sqrt{\rho_g}\sqrt[4]{\sigma g(\rho_f - \rho_g)},$$

where q_{CHF} = critical heat flux (W/m²);

$$h_{fg} = \text{latent heat (J/kg);}$$

$$\rho_f = \text{fluid density (kg/m}^3\text{);}$$

$$\rho_g = \text{steam density (kg/m}^3\text{);}$$

$$\sigma = \text{surface tension (J/m}^2\text{);}$$

$$g = \text{gravity acceleration (m/s}^2\text{).}$$

IGR tests are characterized by the high water sub-cooling. In this case it is recommended to increase q_{CHF} by the value necessary to support saturation temperature at the boundary between the nucleate boiling region and the sub-cooled water region [21]. Account for this correction leads to the modified expression for the critical heat flux:

$$q_{CHF}^* = q_{CHF}(1 + 0.1(\frac{\rho_f}{\rho_g})^{0.75}\frac{\Delta i}{h_{fg}}),$$

where q_{CHF}^* = modified critical heat flux (W/m^2);

Δi = difference between the water enthalpy at the saturation level and enthalpy of the sub-cooled water (J/kg).

Verification of the SCANAIR code with the modified correlations for nucleate boiling and CHF criterion, and Bromley correlation for heat transfer in the post CHF region indicated that the Bromley correlation overestimated the fuel cladding temperature (Fig. 5.21).
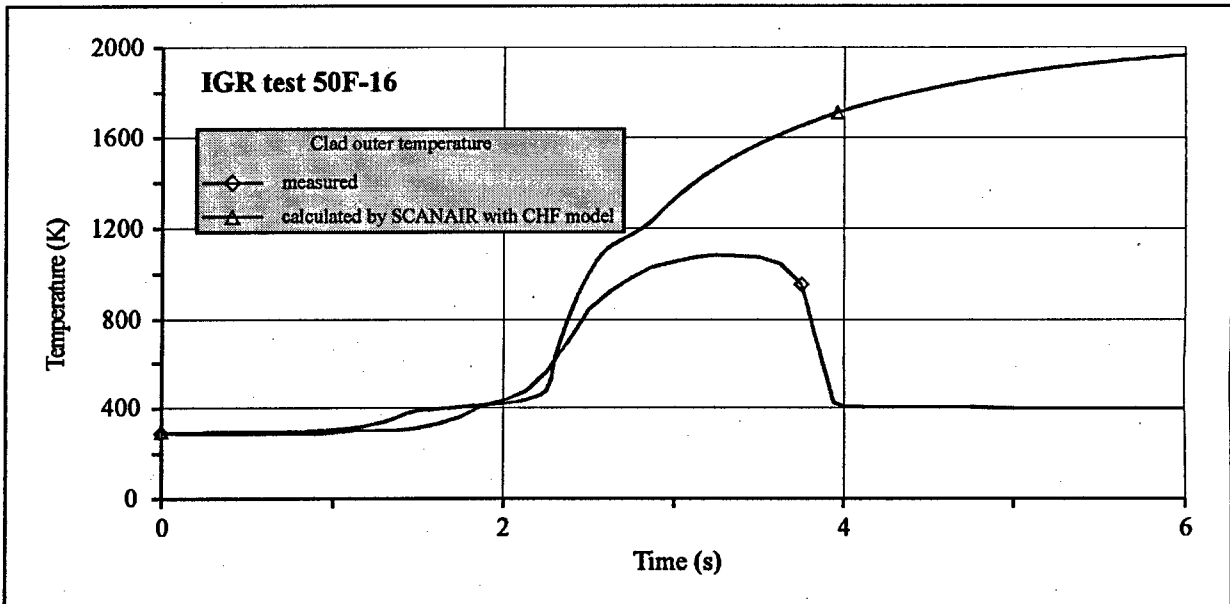
Fig. 5.21. Verification of SCANAIR code with CHF model

Therefore, the next step was made to adapt SCANAIR code to IGR test conditions.

Bromley correlation uses the equation for the heat transfer coefficient that was obtained in experiments with horizontal tubes cooled by stagnant water under conditions of the film boiling and laminar state of the steam film. However in IGR tests, the fuel rod was positioned vertically. Moreover, the non-stationary energy deposition mode is a characteristic feature of these tests. Taking into account these two factors, it can be assumed that the steam film on the fuel rod surface is in the turbulent mode already at an early boiling stage.

Thus, a decision was made to replace Bromley correlation by Labuntzov model that was developed for turbulent film boiling modes [19]. This model is described by the following expression:

$$\alpha_{FB} = 0.25(\lambda_g^2 c_{pg}(\rho_f - \rho_g)\frac{g}{v_g})^{1/3},$$

where α_{FB} = heat transfer coefficient for film boiling (W/m^{2}K);

λ_g = thermal conductivity of steam (W/m K);

c_{pg} = specific heat of steam (J/kg K);

ρ = fluid density (kg/m^3);

ρ_g = steam density (kg/m^3);

g = gravity acceleration (m/s^2);

v_g = steam kinematic viscosity (m^2/s).

Moreover, the effect of the water subcooling should be taken into account for this case, since it can affect significantly the cladding temperature. This correction was introduced similarly to the correction for q_{CHF} [21]:

$$\alpha_{FB}^* = \alpha_{FB}(1+0.1(\frac{\rho_f}{\rho_g})^{0.75}\frac{\Delta i}{h_{fg}}),$$

A corresponding adjustment of SCANAIR models allowed to obtain results presented in Fig. 5.22.
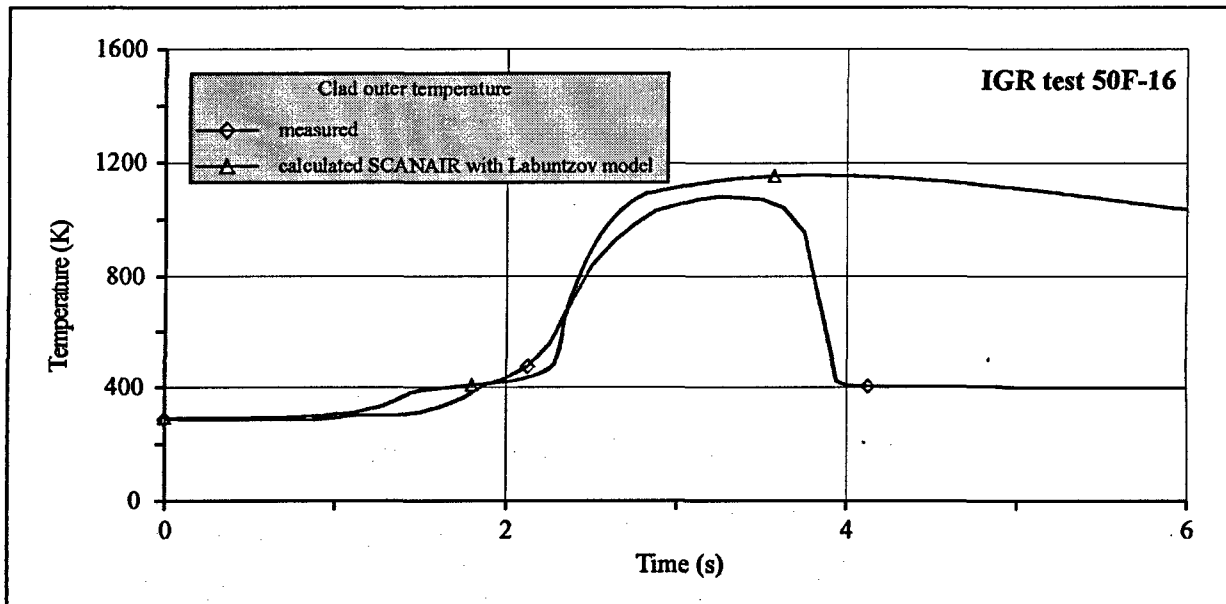
Fig. 5.22. Verification of SCANAIR code with Labuntzov model

The analysis of the results obtained shows that another problem remained unresolved at this stage. In the experiment, the rewetting stage begins much earlier than the modified model of SCANAIR code predicts. This results in an overestimation of the film boiling duration, and, thus, in an overestimation of the cladding temperature at this stage of the scenario. However this problem can be a study topic within the framework of the development of the final version of SCANAIR code for IGR tests analysis.

5.36

Modification of gas pressure model

It is obvious that the gas pressure model that calculates the gas pressure inside the fuel rod is very important for pressurized VVER fuel rods. Thus, the verification of this model in SCANAIR code was performed on the basis of the test data base obtained using fresh pressurized fuel rods, tested in the air coolant. According to verification results, SCANAIR model significantly overestimates the gas pressure (see Fig. 5.23).
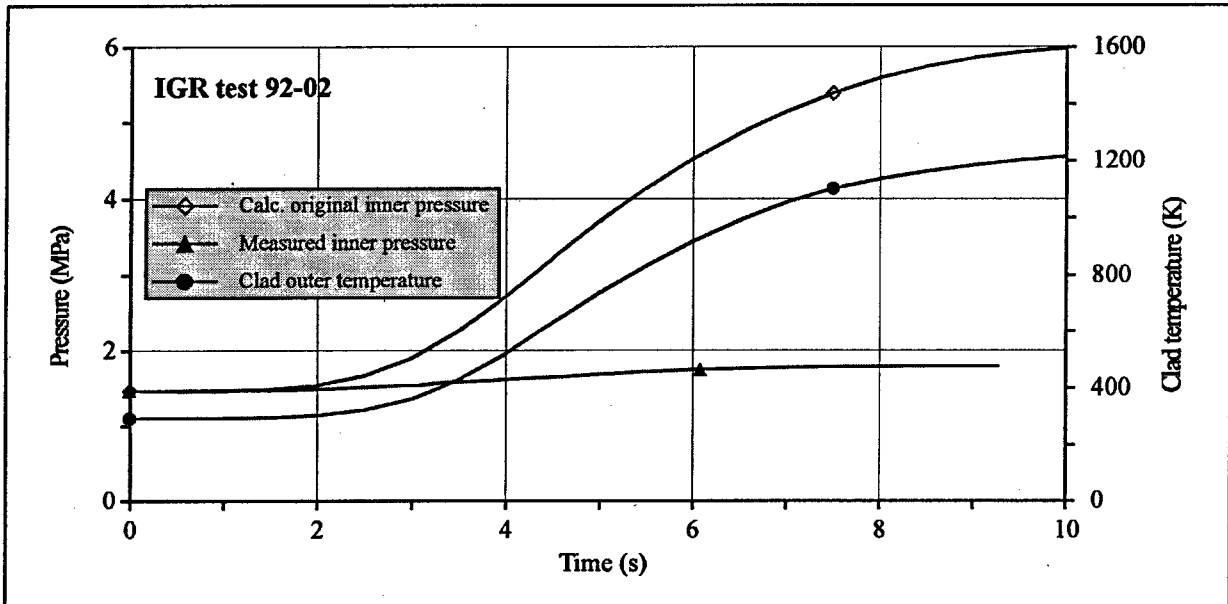
Fig. 5.23. Verification of original gas pressure model in SCANAIR code

The analysis of causes of the discrepancy between measured and calculated gas pressures shows that SCANAIR original model calculates the pressure in gas plenum in accordance with the assumption that the gas temperature in the plenum is equal to the gas temperature in the fuel-cladding gap (adjacent to the gas plenum). SCANAIR code uses the following equation to calculate the temperature in the gas plenum:

$$T_{PL} = \frac{T_{if} + T_{ic}}{2},$$

Where T_{PL} = temperature of gas plenum;

T_f = fuel outer temperature;

T_c = cladding inner temperature;

i = index of first or last axial node.

In other words, this model does not take into account the heat exchange between the fuel rod (at the length of the gas plenum) and the coolant in the gas plenum region. Such an assumption can be true for fuel rods with small volumes of gas plenums and low values of the initial gas pressure. However, another model must be used for fuel rods of VVER type tested in IGR reactor. A corresponding model was developed, and verification procedures show that it can be used for SCANAIR/VVER version (see Fig. 5.24). This model is described in section 5.5.3.

5.37
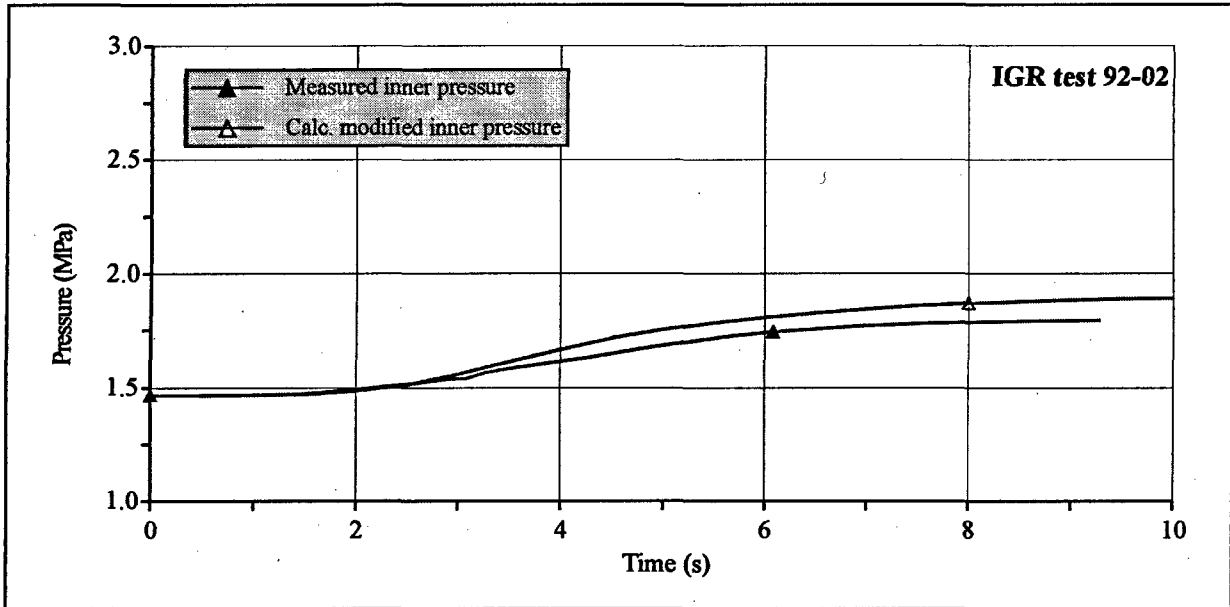
Fig. 5.24. Verification of modified gas pressure model in SCANAIR code

5.5.3. Description of SCANAIR code version to predict VVER fuel rod performance under IGR test conditions

5.5.3.1. Calculational scheme

As in the case of FRAP-T6 code, a unified calculational scheme was developed to model VVER fuel rods of three types. The geometric calculational scheme of the fuel rod, presented in Fig. 5.25, consists of fuel pellets, cladding, fuel-pellet gap, low and upper gas plenums and coolant. Axial and radial meshings define the coordinates of calculation nodes where the temperature, pressure, strain, stress etc. are determined.
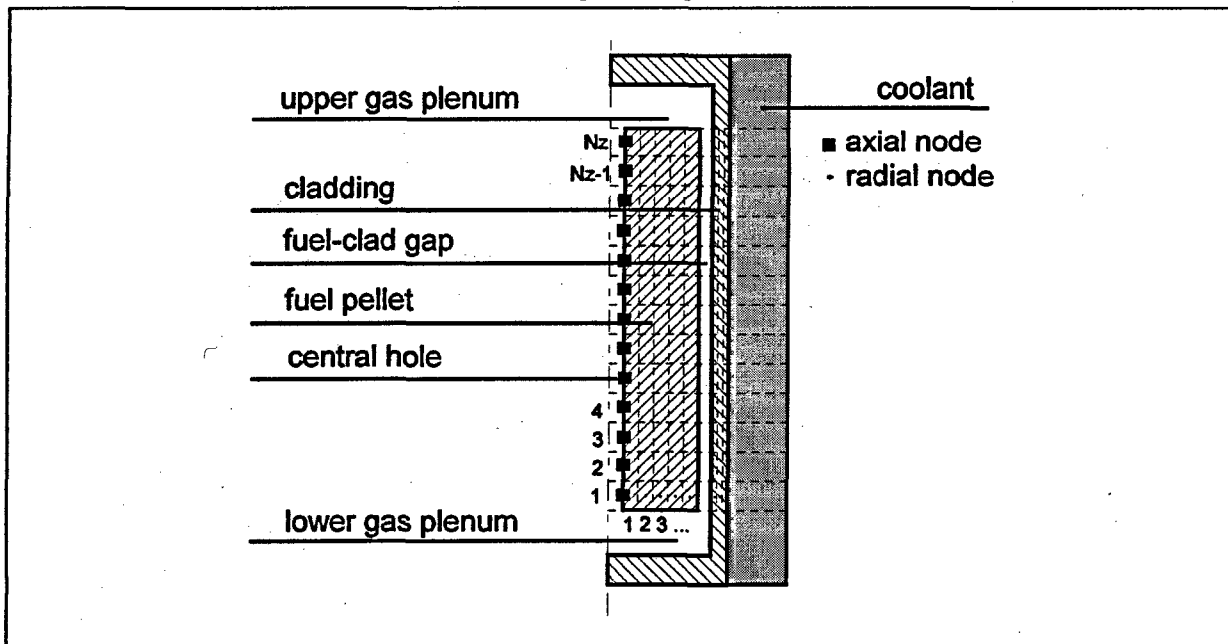
Fig. 5.25. Calculational scheme of VVER fuel rod SCANAIR code

5.38

The modeling of VVER fuel rods with SCANAIR code was performed using the following set of assumptions:

- the fuel and cladding are of regular cylindrical form and are arranged axisymmetrically;
- there are no changes in initial dimensions of fuel pellets, cladding and gap along the fuel rod height;
- there are no changes in the fuel density along the fuel rod height;
- there are no changes in the fuel composition along the fuel rod height;
- the axial meshing is applied only at the heated length of the fuel rod.

The calculation experience obtained at the stage of the preliminary adaptation of SCANAIR code allowed to get the following optimum parameters for the calculational scheme:

- axial nodes: 10
- radial nodes: 31, including
  - fuel: 25
  - cladding: 6
- time step during fast transient: $1 - 5 \cdot 10^{-3}$ s
- time step during slow transient: $5 \cdot 10^{-3} - 1.0$ s

All calculations were performed taking into account the assumption that the fuel rod is surrounded by an infinite volume of stagnant coolant under normal initial conditions.

5.5.3.2. SCANAIR input data to characterize the VVER fuel rods and IGR test conditions

The main set of input data, that characterize VVER fuel rods, was specified using the data base, presented in Appendixes C, D, E of Volume 3. This set includes parameters listed in Table 5.9.

Additional parameters were required to calculate the behavior of high burnup fuel rods with the help of the fission gas release model. These parameters were obtained using TOSUREP code within the framework of the procedure described in the following section of the Report. As it has already been noted, initial parameters of the coolant were characterized by the zero flow rate and atmospheric pressure. The initial coolant temperature was assumed to be 293 K, the coolant volume was equal to the infinity. Test conditions in IGR reactor were described by the following set of input data:

- power history of fuel rod;
- axial power profile;
- radial power profile.

These input data were prepared individually for each fuel rod in accordance with the data base, presented in Appendixes G, H, I of Volume 3.

Account of original material properties of VVER fuel rods was a separate study area in the development of input data for SCANAIR code. These studies were applied simultaneously for SCANAIR and FRAP-T6, and their results are presented in section 5.6 taking into account particular features of each code.

5.5.3.3. Input data to calculate fission gas release from high burnup fuel

In order to calculate fission gas release and fuel swelling for the VVER high burnup fuel under IGR test conditions initial distribution of fission gas products is to be assigned for each fuel rod. It has been already noted that SCANAIR code can not model basic irradiation conditions, that is why we used TOSUREP code [11].

Table 5.9. Set of input data on fuel rod design

Parameters of fuel rod	Method to determine the design parameters
1. Fuel rod data	
1.1. Fuel stack cold length	as measured
1.2. Cold state fuel rod temperature	293 K
1.3. Gas gap radial dimension	as measured and estimated
2. Pellet data	
2.1. Fuel material	UO_2
2.2. Pellet outer diameter	as measured
2.3. Pellet inner diameter	as measured
2.4. Pellet surface roughness	estimated according to [31]
2.5. Fuel density	as measured
3. Cladding data	
3.1. Cladding material	Zr-1%Nb
3.2. Cladding outer diameter	as measured
3.3. Cladding inner diameter	It was calculated, taking into account the cladding outer diameter, pellet outer diameter, gas gap thickness
4. Plenum data	
4.1. Upper plenum volume	as measured
4.2. Lower plenum volume	as measured
4.3. Initial gas composition	He
4.4. Initial gas pressure	as measured

TOSUREP code can model behavior of LWR fuel elements over fuel cycles at NPP. The code calculates heat transfer in the fuel element and in the coolant, pellet-cladding mechanical behavior, fission gas products behavior. TOSUREP considers the following main physical phenomena:

- thermal mechanical pellet-clad behavior;
- in-pile densification;
- fuel swelling due to fission products;
- clad creep down;
- clad growth;
- gap closure;
- clad strain by PCMI after gap closure;
- fission gas generation and release;
- evolution of pressure in the free volume and plenum;
- evolution of radial power profile.

TOSCAN code [2] is used to arrange the interface between the TOSUREP and SCANAIR codes. TOSCAN code reads the output files with the results calculated by TOSUREP code, processes this information and prepares the input data deck for SCANAIR code.

In general, TOSUREP code calculates r, z and t distribution of the following output parameters:

- axial height (cm);
- radius of the central hole (cm);

- external fuel radius (cm);
- diametric gap size (μm);
- columnar radius (cm);
- equiaxis radius (cm);
- total pin power (W);
- linear power rating (W/cm);
- burnup (at %);
- plenum gas pressure (bars);
- fission gas release (%);
- gas retention (cm^3);
- gap conductance ($W/cm^2/K$);
- fuel temperature (C);
- cladding temperature (C);
- cladding deformation (%);
- cladding hoop strain due to irradiation creep (%);
- cladding axial growth due to irradiation (%);
- residual clad strain (%);
- contact pressure between fuel and cladding (Pa).

In order to determine initial characteristics of the fission gas products in VVER fuel elements before IGR tests TOSUREP code calculated behavior of the VVER commercial fuel element # 317 over the fuel cycles of Unit 5 NV NPP.

Initial data characterizing VVER commercial fuel element, coolant parameters and power history were taken from Appendixes A, B of Volume 3. General approach to the development of the nodalization scheme and calculations by TOSUREP was the same as for FRAP-T6 code (section 5.4.3).

The procedure for axial meshing of commercial fuel elements was performed after completion of calculations by the TOSUREP code. Meshing of fuel elements into the parts was performed so that the set of average burnups for 13 selected parts corresponded to the set of average burnups for 13 refabricated high burnup fuel rods tested in IGR reactor.

In this case the final set of input data for SCANAIR code obtained by TOSUREP code contained the following information for each of high burnup fuel rods:

- radial distribution of fission gas products;
- radial distribution of fuel porosity;
- radial distribution of fuel burnup.

5.5.3.4. Output data of SCANAIR code

To get the set of parameters presented in Appendixes G, H, I of Volume 3, the following output parameters were prepared by SCANAIR code as the data base that characterizes the VVER fuel rod behavior:

- time history of energy deposition, power of fuel rod, specific leakage of energy, fuel enthalpy;
- time – axial – radial distributions of temperature for fuel and cladding;
- time history of heat transfer coefficient on the cladding surface;
- time history of fuel rod pressure, gas gap thickness;
- time history of cladding hoop stress;

- time history of fuel swelling, fuel hoop strain, fission gas release;
- special set of peak parameters, characterizing fuel rod performance under the test condition.

5.5.3.5. Selection of SCANAIR models to calculate VVER fuel rod performance

Similar to the corresponding section for FRAP-T6 code, this section will present only those models that were either modified or added to SCANAIR code, or selected by the user out of several options provided for in the code.

Selection of original models of SCANAIR code

TM-COUPLING option provides for the selection of the numerical method of the coupling between the heat transfer and mechanic models in the fuel rod. Two suboptions are intended for this purpose. Suboption "implicit" is recommended for slow power ramps. Suboption "explicit" that provides calculations of the heat transfer for the explicit geometry is recommended for RIA conditions. The latter suboption was used for VVER calculations. CRACKS option has two alternative models to calculate the mechanical behavior of the fuel pellet. Both these models were used for this series of calculations. The behavior of high burnup fuel was calculated using the model that assumes that fuel pellets had cracks before IGR tests, and therefore, the calculation of elastic-plastic strain was not performed for them. The alternative model was used for the fresh fuel. In this case the elastic-plastic strain was calculated by SCANAIR code.

The next STICKING option allows to take or not to take into account the sticking effect between the fuel and the cladding under PCMI conditions. In accordance with the code developers recommendations, calculations were conducted based on the assumption that there is no sticking.

PORO-EQ option is used to calculate the fuel swelling. The option allows to change the fuel porosity during the calculation in order to take into account effects of the grain boundary saturation or grain boundary failure. However, in a general case it is recommended to calculate the fuel swelling at constant porosity of the fuel, thus, this variant was used for VVER calculations.

FLUID-CALC option provides for the selection of method to simulate the coolant behavior. Suboption "no" was used to calculate parameters of stagnant and high subcooled water.

Additional and modified models for SCANAIR code

To predict the behavior of VVER fuel rods tested in the air coolant, a special program module was added to the thermal dynamics model of SCANAIR code.

Correlation ratios that were used in this module are in full agreement with correlations described in section 5.4.3.6 for FRAP-T6 code.

In accordance with results of the preliminary adaptation, the calculation of the temperature in the gas plenum was modified in the gas pressure option according to the following expression:

$$T_{PL} = \frac{T_{co}S_{co} + T_f S_f}{S_{co} + S_f},$$

where T_{PL} =   temperature of gas in gas plenum;

T_{co} =   coolant temperature;

T_f =   average temperature of fuel pellet, adjacent to the gas plenum;

S_{co} =   area of gas plenum surface in contact with coolant;

S_f =   area of fuel pellet, adjacent to the gas plenum.

As it has already been noted, the preliminary adaptation of SCANAIR code shows that heat transfer models must be seriously modernized to be able to describe IGR tests. The final stage of this cycle of the work covered the development of an original heat transfer model to calculate the transition from the film boiling on the cladding surface to the rewetting phase of the fuel rod (see Fig. 5.26). A special rewetting model was developed within the framework of unified requirements for FRAP-T6 and SCANAIR codes. A detailed description of this model is presented in section 5.4.3.6.

In general, the entire complex of the work in this area can be summarized in the form of idealized schematic diagram that characterizes the logical sequence of using individual heat transfer modules and criteria to calculate the heat flux from the cladding to the coolant (see Fig. 5.26).
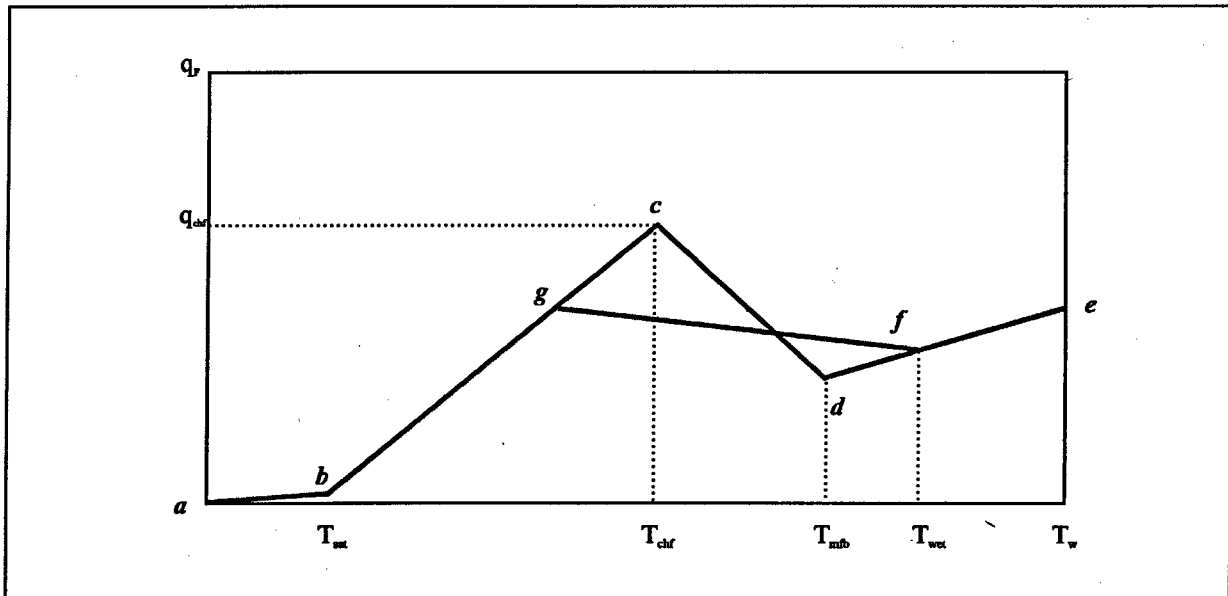
Fig. 5.26. Wall to coolant heat flux vs. wall temperature used in VVER/IGR version of SCANAIR code

The calculation starts with the section a-b of diagrams. Dittus-Boelter correlation [23] is used to calculate the heat flux for the convection regime. The transition from the convection to the nucleate boiling regime takes place when the wall temperature reaches the saturation temperature T_{sat}. Thom correlation [30] is used for the nucleate boiling regime (section b-c). Point "c" is the point of the departure from nucleate boiling. Critical heat flux (q_{chf}), that is calculated using Kutateladze correlation [21], defines the coordinates of this point.

Section d-e of the diagram characterizes the turbulent film boiling regime. Labuntzov correlation [31] with subcooling factor [21] is used for this regime.

The heat flux for point "d" is determined using Labuntzov correlation at the wall temperature T_{mfb}, that is equal to the minimum stable film boiling temperature calculated using Groenveld-Stewart correlation [29]. Section c-d characterizes the transient boiling regime. The heat flux for this regime is calculated using the linear interpolation for heat transfer coefficients in points "c" and "d". The reverse transition from the film boiling to the nucleate boiling takes place when the wall temperature becomes equal to the rewetting temperature T_{wet}. The heat flux at the transition section from the film boiling to the nucleate boiling (section f-g) is calculated using the linear interpolation for the heat transfer coefficient.

It is necessary to note that one more problem was met after implementation of mechanical properties of Zr-1%Nb in the SCANAIR code. This problem is that the SCANAIR code does not have a model to calculate cladding plastic deformation induced by inner gas pressure. When the clad temperature reaches the value at which inner gas pressure causes cladding plastic deformation, disconvergence of inner mechanical iterations occurs in the SCANAIR code. That is why the moment of initiation of cladding plastic deformation induced by inner gas pressure was chosen as a criterion to stop calculations by the SCANAIR code. By this reason only initial stage of fuel rod behavior can be simulated with the SCANAIR code for large group of tested fuel rods. To extend the possibilities of the SCANAIR code a model was proposed in which calculation of the cladding mechanical behavior was stopped after the above-mentioned criterion was reached. It is done by making inner gas pressure equal to coolant pressure, stresses in the cladding become equal zero. At the same time, thermal dynamics model, fission gas behavior model and fuel mechanics model continue to work. The calculational analysis has shown that this model is valid for fuel rods not failed in the tests (for example, #H1T, #50F-16).

Besides, a model allowing to account for influence of clad strain rate on clad yield stress was included in the mechanics model of the SCANAIR code (for more details see section 6.4.2 in Chapter 6).

5.6. Input data on material properties of fuel rods and coolants

The integrated list of material properties included into MATPRO package contains the following items:

- thermal conductivity, specific heat, temperature conductivity, dynamic viscosity, density for air;
- thermal physical constants of Zr-1%Nb alloy;
- specific heat of Zr-1%Nb and VVER fuel;
- specific enthalpy of Zr-1%Nb and VVER fuel;
- thermal conductivity of Zr-1%Nb cladding and VVER fuel;
- thermal expansion of Zr-1%Nb alloy and VVER fuel;
- mechanical properties for Zr-1%Nb cladding:
    ⇒ Young's modulus and Poisson's ratio;
    ⇒ stress-strain diagrams;
    ⇒ anisotropy coefficients for strains and stresses;
    ⇒ mechanical limits and failure criteria;
- mechanical properties for VVER fuel:
    ⇒ Young's modulus;
    ⇒ Poisson's ratio;
    ⇒ yield stress.

The analysis of the representativity and sufficiency of the existing data base on material properties is contained in section 5.2. The following paragraphs of this Section describe specific correlation dependencies that were added to MATPRO and SCANAIR package to characterize conditions of IGR/RIA tests.

Thermal properties for air coolant

Thermal physical properties of the air coolant are proposed to be calculated using the following correlation set [32]:

$$\lambda = 24.407 + 7.978 \cdot 10^{-2} \cdot t - 3.154 \cdot 10^{-5} \cdot t^2 + 0.802 \cdot 10^{-8} \cdot t^3,$$

$$c_p = 1004.16 - 9.761 \cdot 10^{-3} \cdot t + 55.229 \cdot 10^{-5} \cdot t^2 - 36.275 \cdot 10^{-8} \cdot t^3,$$

$$a = 10^{-6} \cdot (18.788 + 13.484 \cdot 10^{-2} \cdot t + 13.959 \cdot 10^{-5} \cdot t^2 - 4.654 \cdot 10^{-8} \cdot t^3),$$

$$\mu = 10^{-6} \cdot (17.162 + 49.894 \cdot 10^{-3} \cdot t - 2.935 \cdot 10^{-5} \cdot t^2 + 1.133 \cdot 10^{-8} \cdot t^3),$$

$$\rho = -2.883 \cdot 10^{-3} + 355.06/(t + 273) + 353.527/(t + 273)^2,$$

where $\lambda =$ thermal conductivity (W/m K);
     $c_p =$ specific heat (J/kg K);
     $a =$ temperature conductivity (m^2/s);
     $\mu =$ dynamic viscosity (Pa/s);
     $\rho =$ density (kg/m^3);
     $t =$ temperature (°C).

Thermal physical constants of Zr-1%Nb

Thermal physical constants for unirradiated material of VVER cladding are presented in Table 5.10 [5].

Table 5.10. Thermal physical constants of Zr-1%Nb

Parameter	Unit	Value
Melting temperature	K	2133
Specific temperature	J/g K	210
Temperature of the beginning of α–β phase transition	K	883
Temperature of the end of α–β phase transition	K	1153
Density	kg/m^3	6550

Thermal physical properties of the Zr-1%Nb alloy

The set of Thermal physical properties of the Zr-1%Nb alloy is characterized by the specific heat, specific enthalpy, thermal conductivity and thermal expansion. At present all the data base on these parameters is available only for unirradiated material. However it should be assumed that, for all cases when an additional oxidation and hydration of the fuel rod cladding during the power operating cycle is small, this data base certainly can also be used for irradiated material.

It should also be noted that the specific heat and specific enthalpy for Zr alloys suffer a perturbation in the region of α–β transition (see Fig. 5.1 of section 5.2). In this case the perturbation scale depends on the cladding temperature increase rate. However, taking into account results of the sensitivity analysis of fuel rod parameters to these properties, this effect was ignored. Thus, in this case the correlation is of the following form [4]:

for temperature region up to 1050 K:

$$c_p = 2.375 \cdot 10^{-1} + 15.91 \cdot 10^{-5} \cdot T,$$

$$H_T - H_{293K} = -74.53 + 2.375 \cdot 10^{-1} \cdot T + 7.955 \cdot 10^{-5} \cdot T^2,$$

for temperature region from 1200 K to 1600 K:

$$c_p = 1.997 \cdot 10^{-1} + 12.364 \cdot 10^{-5} \cdot T,$$

$$H_T - H_{293K} = 4.125 \cdot 10^{-1} + 1.997 \cdot 10^{-1} \cdot T + 6.182 \cdot 10^{-5} \cdot T^2,$$

where c_p = specific heat (J/kg K);

H = specific enthalpy (J/g);

T = temperature (K).

Experimental data obtained in [4] for 1100-1200K were processed and presented in the form of interpolation Table 5.11.

Table 5.11. Specific heat and specific enthalpy for temperature region 1100 - 1200 K

T (K)	C_p (J/g·K)	T(K)	H_T (J/g)
1100	412	1000	242.5
1110	420	1050	262.5
1120	480	1113	307.6
1134	600	1133	322.0
1142	1000	1153	336.3
1150	1400	1173	350.6
1155	1600	1200	370.0
1161	1400		
1168	1000		
1177	600		
1180	400		
1190	360		
1200	348		

The thermal effect of α–β phase transition for Zr-1%Nb alloy is about 48 J/g [4].

The following data set [5] was used to describe the thermal conductivity of Zr-1%Nb alloy:

273 K < $T \leq$ 373 K $\qquad \lambda = 9.5 \cdot 10^{-3} \cdot (T - 273) + 17.01$,

373 K < $T \leq$ 673 K $\qquad \lambda = 10.3848 \cdot (T - 273)^{0.117} \cdot \exp(-0.115 \cdot 10^{-3} \cdot (T - 273))$,

673 K < $T \leq$ 1273 K $\qquad \lambda = 167.88 \cdot (T - 273)^{-0.429} \cdot \exp(1.169 \cdot 10^{-3} \cdot (T - 273))$,

T = 1273 K $\qquad \lambda = 27.8$,

T = 1473 K $\qquad \lambda = 30.1$,

T = 1573 K $\qquad \lambda = 31.0$,

where λ = thermal conductivity (W/m K);

$\qquad T$ = temperature (K).

The thermal conductivity of Zr-1%Nb at temperature above 1773 K was described by the extrapolation dependence:

$\lambda = 15.0636 \cdot \exp(0.4618 \cdot 10^{-3} \cdot T)$.

The thermal expansion of the LWR cladding is usually characterized by a system of two coefficients for axial and circumferential directions since zirconium alloys have obvious anisotropy of properties. The existing data base for unirradiated Zr-1%Nb was obtained for temperature up to 923 K, inclusively, and is presented in Table 5.12.

Table 5.12. Thermal expansion coefficients for Zr-1%Nb cladding in axial and radial directions [5]

Parameter	Unit	Value			
Temperature	K	293-393	393-573	573-773	773-923
$\alpha_z \cdot 10^6$	1/K	5.3	5.4	5.5	5.6
$\alpha_\theta \cdot 10^6$	1/K	5.7	5.9	6.3	6.8

Taking into account the fact that the thermal expansion of Zircaloy in α–β region have a step-like changes, the following approach was used to get Zr-1%Nb data base for the temperature above 923 K. The temperature region was divided into two sections:

5.46

923 - 1153 K (α–β region)

above 1153 K (β region).

The linear interpolation was applied to each section. The slope of curves at each section in "temperature – thermal expansion" coordinates corresponded to the slope of curves for Zircaloy taken from MATPRO package. The obtained set of correlation dependencies is presented in Table 5.13.

Table 5.13. Thermal expansion for Zr-1%Nb alloy for temperature region above 923 K

Temperature (K)	Thermal expansion (%)
923 – 1153	$\varepsilon_\theta = -17.95 + 0.0549\ T - 5.4\ 10^{-5}\ T^2 + 1.74\ 10^{-8}\ T^3$ $\varepsilon_z = -17.28 + 0.0533\ T - 5.3\ 10^{-5}\ T^2 + 1.72\ 10^{-8}\ T^3$
above 1153	$\varepsilon_\theta = -0.886 + 9.7\ 10^{-4}\ T$ $\varepsilon_z = -1.038 + 9.7\ 10^{-4}\ T$

Mechanical properties of Zr-1%Nb cladding

To describe the cladding deformation, two main models are used in FRAP-T6 and SCANAIR codes:

1. Hooke's model for the region with elastic strain.

2. Model of elastic – plastic body for strain region above the yield point.

The first method requires the data base that characterize Young's modulus and Poisson's ratio. Therefore the following correlation dependencies were added to MATPRO package and SCANAIR code for unirradiated Zr-1%Nb alloy [5]:

$$E = 1.121 \cdot 10^{11} - 6.438 \cdot 10^{7} \cdot T, \quad for\ 273 < T < 1073K,$$

$$E = 9.129 \cdot 10^{10} - 4.500 \cdot 10^{7} \cdot T, \quad for\ T > 1073K,$$

$$\mu = 0.42628 - 5.556 \cdot 10^{-5} \cdot T,$$

where E = Young's modulus (Pa);

μ = Poisson's ratio (per-unit);

T = temperature (K).

A corresponding data base for irradiated Zr-1%Nb does not exist, however results of the sensitivity analysis of FRAP-T6 and SCANAIR codes to these parameters show that even a high level of their uncertainty affects little the calculation results obtained using FRAP-T6 and SCANAIR codes.

The second model of the FRAP-T6 code is based on the approximation of real stress – strain curves by power law of the following form:

$$\sigma = K\varepsilon^n \left(\frac{\dot{\varepsilon}}{\dot{\varepsilon}_o}\right)^m,$$

where σ = true effective stress (Pa);

ε = true effective plastic strain (per-unit);

$\dot{\varepsilon}$ = strain rate (1/s);

$\dot{\varepsilon}_o$ = basic strain rate (1/s);

K = strength coefficient (Pa);

n = strain hardening exponent (per-unit);

m = strain rate sensitivity exponent (per-unit).

Thus, the set of coefficients (K, n, m) is the actual data base for MATPRO package. In their turn, these coefficients are determined using the data base that characterizes the yield stress, ultimate strength and

5.47

uniform elongation. The preliminary experience of applying FRAP-T6 and SCANAIR codes and the sensitivity analysis of the codes show that original properties of Zr-1%Nb cladding are a necessary condition to get acceptable calculation results for VVER fuel rods under IGR test conditions. Thus, a special research program was implemented to develop a corresponding data base for unirradiated and irradiated claddings. A detailed description of this research cycle is presented in Chapter 6. It contains also final results that characterize K, n, m coefficients as a function of the burnup, temperature, strain rate etc.

Fuel properties

As it has been noted earlier, the thermal conductivity for fresh and high burnup VVER fuel was additionally introduced into MATPRO-V11. To determine the thermal conductivity of VVER fuel, the ratio of the following type was proposed [10]:

$$\lambda_B = \lambda_o K_1 K_2,$$

where λ_B = thermal conductivity of fuel for current burnup (W/m K);

λ_o = thermal conductivity of fresh fuel (W/m K) [9];

K_1 = coefficient accounting for dependence of thermal conductivity on fuel composition;

K_2 = coefficient accounting for dependence of thermal conductivity on fuel porosity.

In its turn, the thermal conductivity of the fresh fuel with a given density ρ is determined using the following correlations:

$$\lambda_o = 2.158 \lambda_{0.95} \frac{\rho}{32.91 - \rho},$$

$$\lambda_{0.95} = \frac{100}{0.0258T + 3.77} + 1.1 \cdot 10^{-4} T + 1.01 \cdot 10^{-11} \cdot T^3 \cdot \exp(7.2 \cdot 10^{-4} \cdot T),$$

where $\lambda_{0.95}$ = thermal conductivity (W/m K) for fuel with relative density = 0.95;

ρ = density of fresh fuel (g/cm^3);

T = temperature (K).

Coefficients K_1, K_2 are determined on the base of SIMFUEL thermal conductivity [33, 34]:

$$K_1 = \frac{0.053 + 2.2 \, 10^{-4} T}{0.053 + 1.71 10^{-3} b + (2.2 - 5.33 10^{-4} b) 10^{-4} T}, \quad K_2 = 1 - 0.001 cb,$$

$$c = 5.31 - 3.42 \, 10^{-3} T + 4 \, 10^{-7} T^2 \, for T \leq 1773K,$$

$$c = 0.5 \, for T > 1773K,$$

where K_1, K_2, c = coefficients (per-unit);

b= burnup (MWday/kgU);

T = temperature (K).

Regarding the specific heat for VVER fuel, results presented in section 5.2 show that, firstly, output parameters of FRAP-T6 code are rather sensitive to this parameter, and, secondly, the initial data base characterizing the specific heat of VVER fresh fuel is very different from corresponding data for PWR fuel. Therefore, an original data base with specific heat for VVER fuel was prepared in accordance with data in Table 5.14 [8].

Table 5.14. Specific heat of VVER fresh fuel vs. temperature [8]

Parame-ter	Temperature (K)														
	300	500	700	900	1100	1300	1500	1700	1900	2100	2300	2500	2700	2900	3100
Specific heat (J/kg K)	270	287	302	310	314	319	320	328	340	364	390	426	470	520	594

5.7. Validation of IGR/VVER versions of FRAP-T6 and SCANAIR codes

5.7.1. General principles of validation

Verification procedures were the main basis to test and validate these versions of codes. The complex of original in-pile and out of pile tests and research was performed in order to get the data base for verification. But the obtained results were not enough to check the quality of modeling of each physical phenomena presented in Table 5.1 (section 5.1). Besides, at this stage this was not the main objective of the code validation.

The main objective was to verify reliability in predicting of as much as possible of the calculated parameters presented in Appendixes G, H, I of Volume 3 as the integral elements of the data base on the behavior of the VVER fuel rods under IGR/RIA test conditions.

That is why the specific approach was developed to verify FRAP-T6 and SCANAIR codes in the framework of this task. The approach schematically described in Fig. 5.27 consists of several stages of verification of the calculated results. Each of the stages contains the integral check procedure and the procedures to check the separate physical phenomena. Cladding temperature versus time is the basic verification criterion for the integral check procedure. Practical experience indicates that the cladding temperature is very sensitive to the quality of the models used in the codes. That is why the adequacy of the calculated and measured cladding temperature is a reliable guarantee that the main set of other output parameters characterizing fuel rod behavior will be determined correctly. Still, it is important to note that the model of heat transfer from cladding to coolant is often the main reason of discrepancies between the predicted and actually measured cladding temperature.
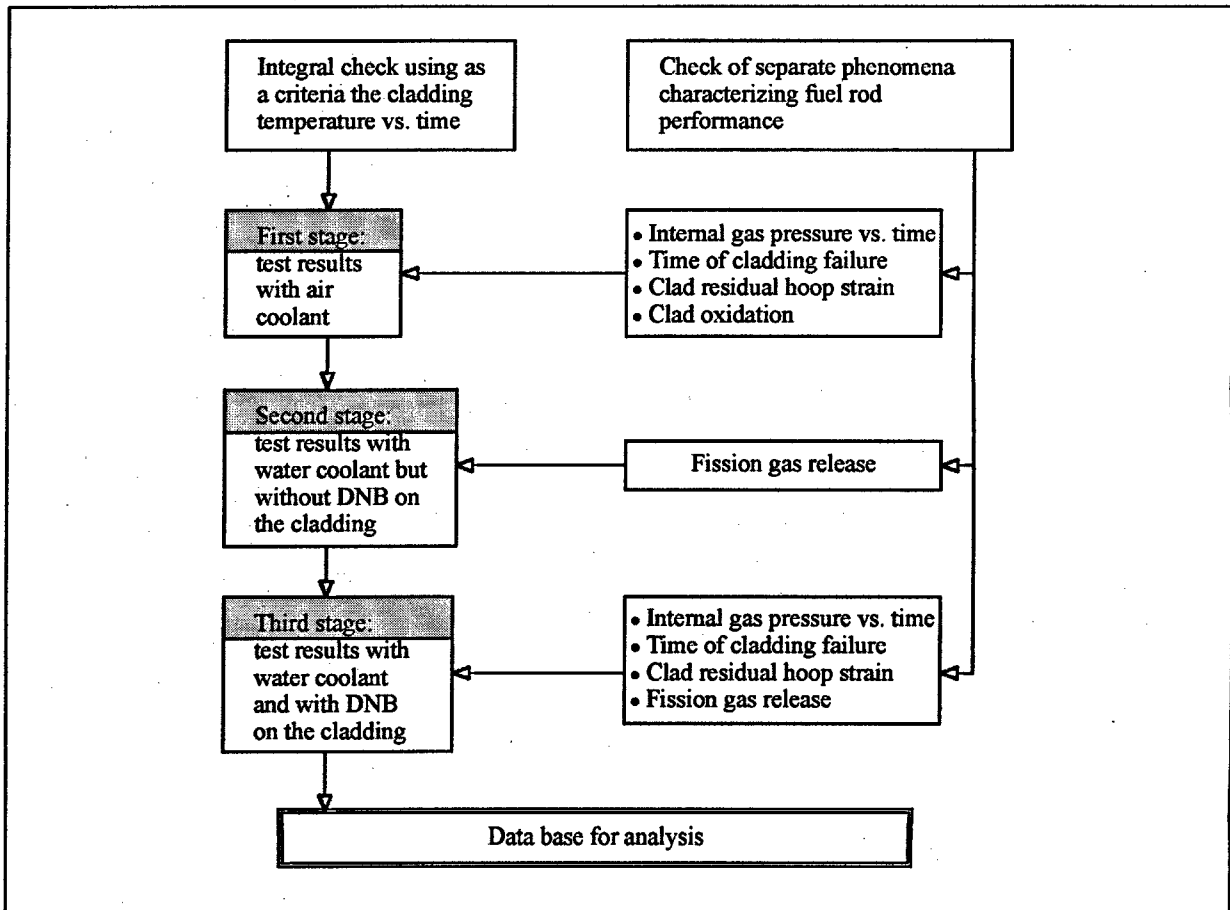
Fig. 5.27. Scheme of verification for FRAP-T6 and SCANAIR

So three sequential stages of verification procedures were planned:

1. Code validation for simple boundary conditions of heat transfer at the cladding surface (heat transfer to air coolant).

2. Code validation for test conditions with the water coolant and test modes before departure from nuclear boiling (DNB).

3. Code verification for test conditions with the water coolant and test modes after departure from nuclear boiling.

It is important to note that serious complications arose during the analysis of representativity of the test data base for the integral check of codes. The main problem was that this test data base was obtained for the fresh VVER fuel rods tested at IGR reactor.

That is why we also performed the procedures to check the specific phenomena for high burnup fuel rods. These procedures intended to compare the calculated and measured parameters characterizing the following processes:

- fission gas release;

- clad hoop strain;

- clad failure.

Besides checking of the separate phenomena was done to validate the code models used for prediction of the ballooning type cladding rupture and cladding oxidation.

5.7.2. Assessment of verification results

5.7.2.1. Assessment of integral check results

As it has already been noted, the first stage of the verification was carried out using fresh fuel rods tested in the air coolant. The verification base consisted of five fuel rods. Calculated and measured time history of the cladding temperature for one of fuel rods is presented in Fig. 5.28. In general, obtained results demonstrate that both computer codes predict rather adequately the cladding temperature. In its turn, this allows to conclude that both codes describe correctly the set of all physical phenomena that influence the fuel rod cladding temperature.
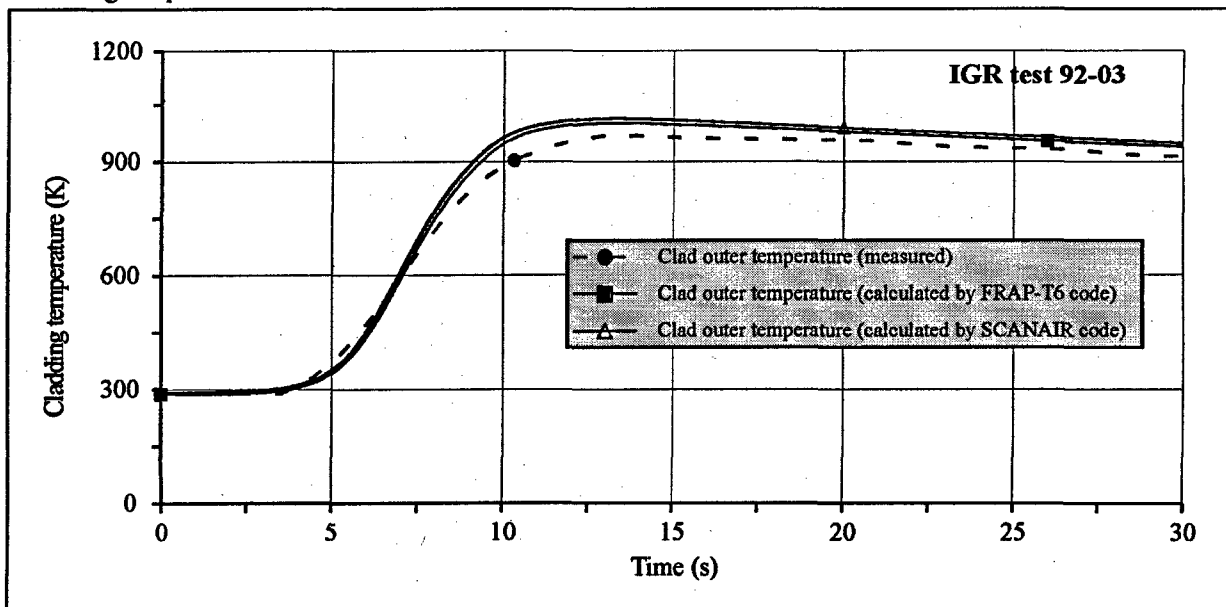
Fig. 5.28. Measured and calculated cladding temperature for air coolant

The following verification stages were intended to assess the quality of both codes for water-cooled fuel rods.

These procedures were provided for two characteristic modes of the heat exchange on the fuel rod surface. In the first case the heat flux from the fuel rod to the coolant did not exceed the critical heat flux. In the second case the verification was performed for fuel rods in which modes of the transient and film boiling were reached. It was difficult to select representative fuel rods for these procedures, since the analysis of many results of the fuel rod temperature measurements for modes with the surface boiling shows that the temperature distribution in the axial and azimuthal directions is largely non-uniform. This non-uniformity is of a random nature caused, probably, by the formation of the socalled hot spots on the cladding surface. Naturally, methodological errors of thermocouples that were used for temperature measurements also affected the final measurement results. Taking into account above mentioned factors, the following approach was developed to select representative measurements:

- comparative analysis of temperature measurement results for a group of fuel rods that were rather similar in test conditions;

- selection of measurements that demonstrate the maximum values of temperature vs. time for this group of fuel rods.

Thus, a possible measurement error due to the thermocouple installation method, thermocouple dimensions and its position was minimized.

Verification results of FRAP-T6 and SCANAIR codes for the nucleate boiling regime and film boiling regime are presented in Fig. 5.29, Fig. 5.30.

The analysis of verification results of FRAP-T6 and SCANAIR codes in these regimes shows that certain issues remain unresolved. In all cases under consideration, both codes predict an earlier beginning of the nucleate boiling in comparison with the experiment. Moreover, both codes provide some overestimation of the maximum cladding temperature for the film boiling and the cladding temperature for the transition from the film boiling to the nucleate boiling.

However, in general it is possible to conclude that for this type of fuel rod cooling modes, results of integral checks demonstrate a good agreement between measured and calculated temperatures. This allowed to begin the following stage of the code validation with the aim of checking separate effects.
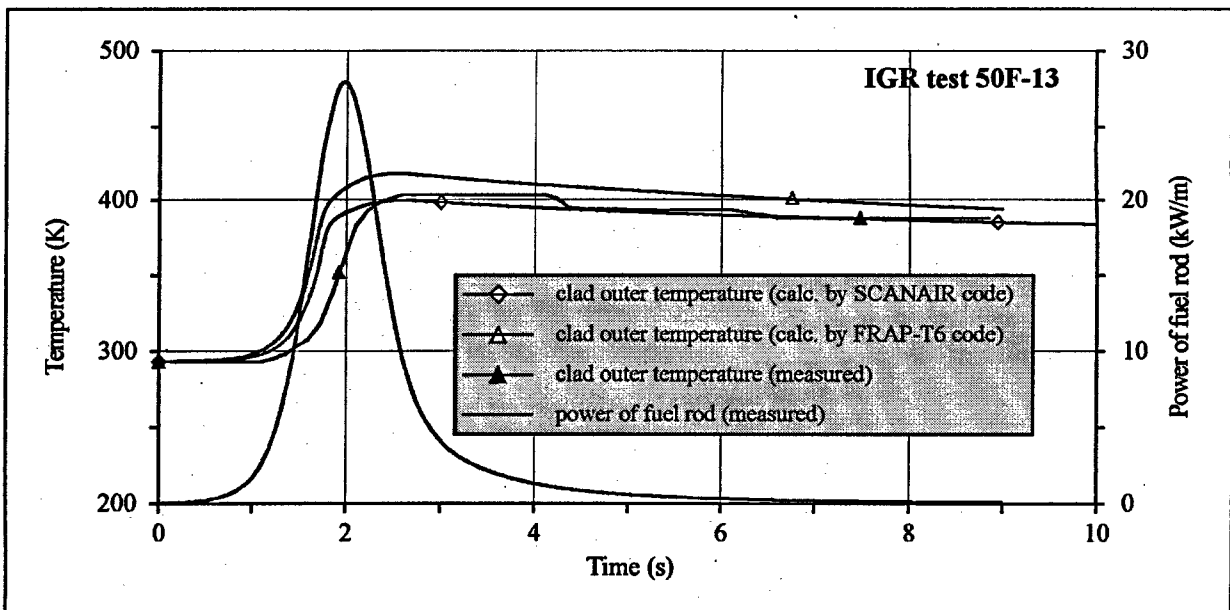
Fig. 5.29. Measured and calculated cladding temperature for nucleate boiling regime

5.51
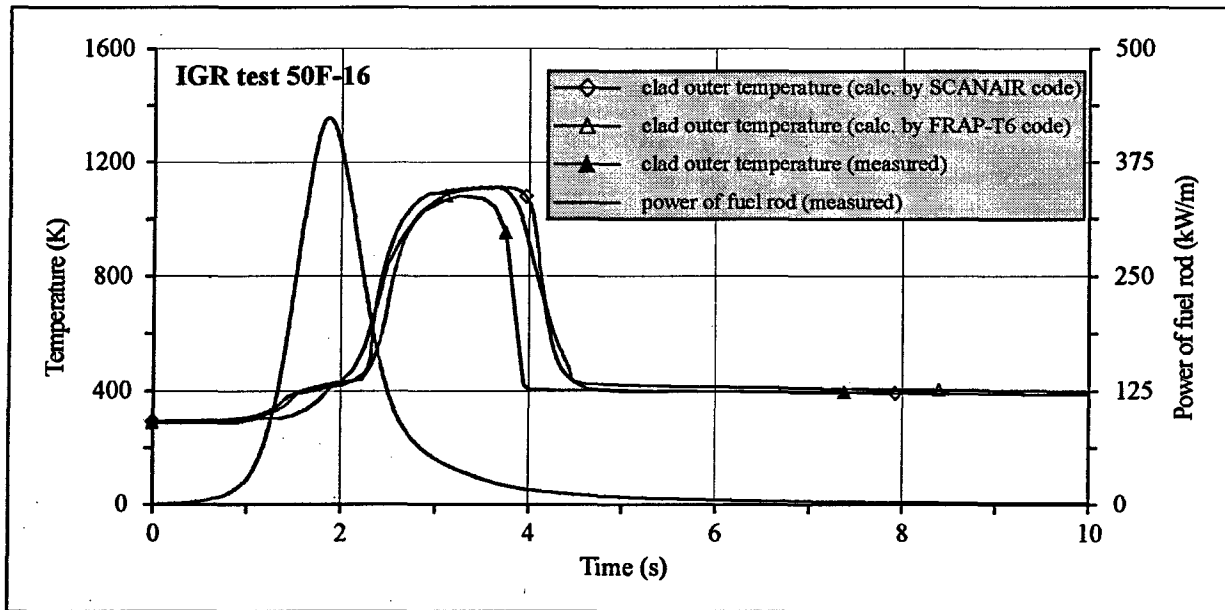
Fig. 5.30. Measured and calculated cladding temperature including post-CHF regimes

5.7.2.2. Assessment of results of separate phenomena check

Various test data bases were used to verify separate phenomena at each stage shown in Fig. 5.27. Summarized results of these studies were grouped individually for each of the phenomena and are presented in this section.

Fission gas release

From the point of view of code verification, this physical phenomenon is of a principal value only for the high burnup fuel. In this case the optimum verification variant must include two levels:

- verification of calculation methods for the fission gas release during the base irradiation of VVER commercial fuel elements;

- verification of results of fission gas release calculations during the IGR transient tests.

The first verification level allows to obtain results characterizing the quality of the preparation of input data on fission gas distribution in VVER fuel rods before IGR tests. As it has already been noted, this type of calculations was performed using FRAP-T6 and TOSUREP codes. In this case the fuel cycle of one of fuel elements of 5th unit NV NPP was modeled by each code. Within the framework of the verification procedure, the same calculation was performed using TRIFOB code [15], that is described in detail in Chapter 4. For this case, TRIFOB code calculated 8 main fission products (Xe^{135}, Rh^{105}, Sm^{149}, Sm^{151}, Pm^{149}, Pm^{151}, Cd^{113}, Cd^{157}), 4 effective fission products for U^{235}, Pu^{239}, Pu^{241} with their precursors and 8 isotopes Kr and Xe (Kr^{83}, Kr^{84}, Kr^{85}, Kr^{86}, Xe^{131}, Xe^{132}, Xe^{134}, Xe^{136}). TRIFOB code took into account an additional release of nuclides Kr and Xe through the following channels: $Kr^{83}(n,\gamma)Kr^{84}$, $Xe^{131}(n,\gamma)Xe^{132}$, $Xe^{135}(n,\gamma)Xe^{136}$. The radioactive decay of Kr^{85} was also taken into account.

As a result of the verification procedure, results obtained using three independent codes were compared. Comparative results presented in Fig. 5.31 demonstrate a good agreement in fission gas generation predicted by the codes. Although results are somewhat different from each other, nevertheless this difference is not of a principle nature for parameters such as the fission gas release. The verification of the radial distributions of fission gases was performed in a similar procedure scheme; it is results are presented in Fig. 5.32.
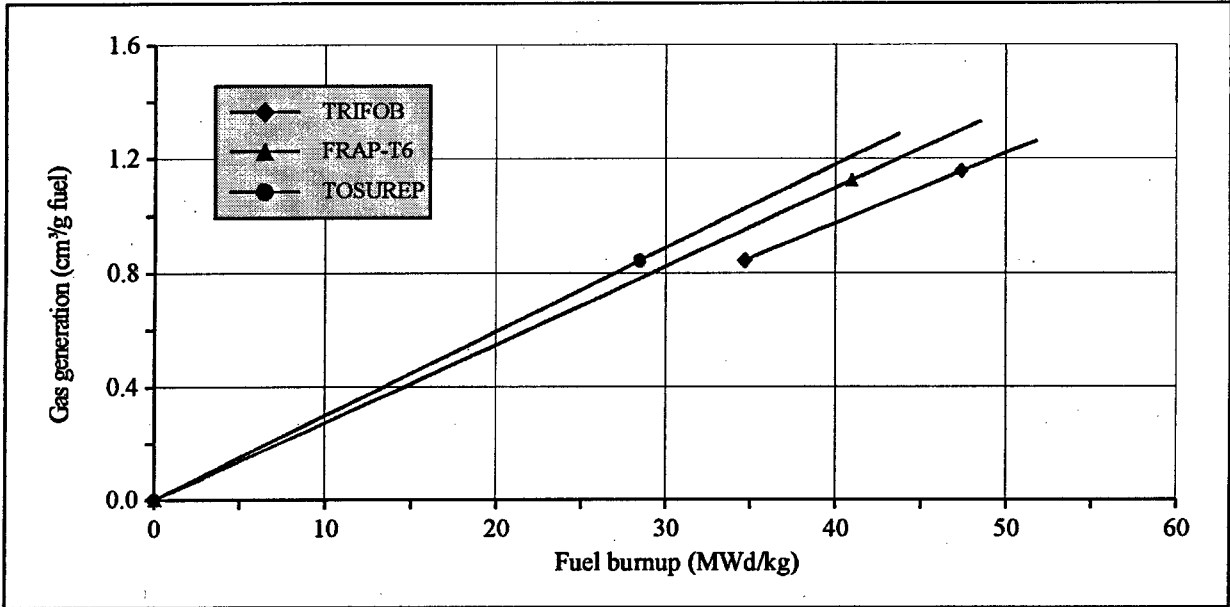
Fig. 5.31. Specific fission gas generation vs. burnup calculated by FRAP-T6, TOSUREP, TRIFOB computer codes for fuel elements #317 during the fuel cycles of NV NPP
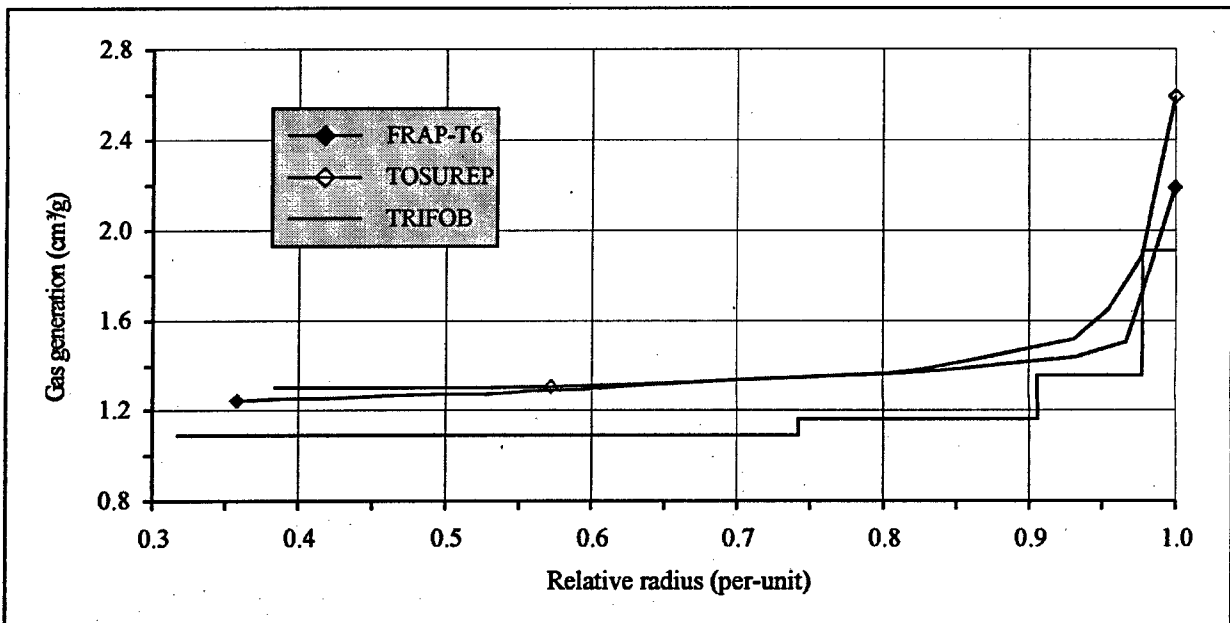
Fig. 5.32. Radial distributions of fission gas generated in fuel calculated by FRAP-T6, TOSUREP, TRIFOB computer codes for fuel element #317 at burnup 48 MWd/kg U

Unfortunately, this stage of the codes validation was not confirmed by a corresponding test data base. However the next verification level has a test data base that is sufficient for the assessment of not only results of the fission gas release during the IGR transient tests, but also calculational results of this phenomenon as a whole.

The data base described in Appendix G of Volume 3 characterizes the fission gas release and Kr concentration in the fuel grains after the IGR tests for four VVER fuel rods. Corresponding calculations using FRAP-T6 and SCANAIR codes were conducted for these four fuel rods and summarized results are presented in Table 5.15. TRIFOB code was used to calculate Xe-to-Kr connection ratio.

The analysis of results in Table 5.15 allows to make the following conclusions:

- FRAP-T6 and SCANAIR codes predict correctly Kr concentration in the fuel after IGR test. This confirms the fact that the entire scenario of Kr formation (during base irradiation and during IGR irradiation) is calculated by these codes with a good accuracy;

- the fission gas release is predicted by both codes with a satisfactory accuracy for this class of physical phenomena; however a tendency to underestimate the fission gas release for modes with relatively low fuel temperatures is obvious.

In general verification results demonstrate that both codes can be used for the development of the data base on fission gas release.

Table 5.15. Comparison of measured and calculated parameters of fission gases

Parameter	Number of fuel rod			
	H1T	H4T	H6T	H8T
Calculated peak fuel temperature (K):				
• FRAP-T6	2681	2313	1920	1489
• SCANAIR	2593	2229	1813	1386
Kr concentration in fuel (cm³/g fuel):				
• measured	0.13	0.13	0.14	0.16
• calculated by FRAP-T6 code	0.15	0.15	0.15	0.13
• calculated by SCANAIR code	0.17	0.19	0.20	0.20
Kr concentration in free gas volume of fuel rod (% by volume):				
• measured	1.39	1.01	0.59	0.49
• calculated by FRAP-T6 code	2.26	1.34	0.65	0.10
• calculated by SCANAIR code	2.48	0.59	0.31	0.36
Xe concentration in free gas volume of fuel rod (% by volume):				
• measured	13.02	9.71	5.4	4.05
• calculated by FRAP-T6 code	13.53	8.06	3.29	0.80
• calculated by SCANAIR code	14.89	3.51	1.86	2.16

Cladding oxidation

Unfortunately, SCANAIR code contains no model to calculate cladding oxidation. As for FRAP-T6 code, original correlations for Zr-1%Nb alloy were used to describe the phenomenon of cladding oxidation with water coolant under IGR test conditions. Special measurements of the oxidation thickness were performed with the cross-sections of VVER fuel rods tested in IGR reactor. Results of these measurements are presented in Appendixes G, H, I of Volume 3. Description of the measurement procedure is presented in section 3.4 of Volume 2. This data base was used to verify the respective model of FRAP-T6 code.

Results of comparison of the tested and predicted values for ZrO_2 thickness are listed in Table 5.16.

Table 5.16. Measured and calculated ZrO₂ thickness for VVER fuel rods with water coolant

Parameter	Number of fuel rods												
	H1T	H2T	H4T	H5T	H6T	H7T	H8T	H14T	H15T	H16T	H17T	H18T	H6C
State of cladding before IGR tests:													
• irradiated	+	+	+	+	+	+	+	+	+	+	+	+	−
• unirradiated	−	−	−	−	−	−	−	−	−	−	−	−	+
Calculated peak cladding outer temperature (K)	1149	1231	437	1212	432	1221	426	417	1301	433	428	425	1415
Region of measured ZrO₂ thickness (μm)	5	8-18	5	10-17	5	5	5	5	5	5	5	5	5
Calculated peak value of ZrO₂ thickness (μm)	5.29	5.5	5	5.31	5	5.32	5	5	5.73	5	5	5	7.07

Fuel rod #H3T was excluded take into account melting of fuel and cladding

Analysis of the results presented in Table 5.16 indicates that there exists underestimation of ZrO₂ thickness for fuel rods ## H2T and H5T, and some overestimation of ZrO₂ thickness for fuel rods ## H1T, H7T, H15T, H6C. That is why the question arises whether the calculation of the time history for the cladding temperature was accurate enough, and as the consequence, whether the initial data characterizing energy deposition in fuel rods were accurate. Detailed review of these issues will be done in section 5.8. As for the verification problems, the main issue is the analysis of the consequences of the cladding oxidation underestimation with the help of the used oxidation correlation (see the results for fuel rods ## H2T, H5T). Consequences of the possible overestimation of the cladding oxidation (fuel rods ## H1T, H7T, H15T, H6C) will in any case be disappearingly small, and besides, it is possible to state with great confidence that overestimation of ZrO₂ layer thickness (up to 14 %) in this case is caused by high level of uncertainty of the initial value of ZrO₂ thickness before IGR tests and by insufficient representativity of the measured ZrO₂ thickness (one cross-section for each fuel rod of this group).

Analysis of the consequences of the underestimation of the cladding oxidation was done by artificial 15 time increase of the oxidation rate in the used kinetic correlation. This new correlation was used to calculate fuel rod #H2T with the same initial energy deposition. The calculations indicated that thickness of ZrO₂ layer for this specific case will be 19 μm, i.e. it will be approximately equal to the maximum measured value of ZrO₂ thickness for the fuel rod #H2T. In this case the peak cladding temperature increases by 25 K and peak fuel enthalpy increases by 4 cal/g fuel. The obtained results indicate that the impact of the error (because of underestimation of the cladding oxidation) onto the other parameters is insignificant. The other problem connected with the use of this version of FRAP-T6 code to calculate fuel rods cooled with air was: on the one hand it is known that the oxidation rate of Zr alloys in the air exceeds several times their oxidation rate in the steam, on the other hand, the data characterizing oxidation kinetics of Zr-1%Nb in the air were never published. Hence, calculations of oxidation were not performed for those fuel rods by FRAP-T6 code. Evaluation of potential errors in predicting cladding temperature and fuel enthalpy in the framework of this approach leads to approximately the same results as for the fuel rods cooled with water.

Thus the verification has indicated that:

• understanding of the oxidation kinetics for Zr-1%Nb claddings for transients should be improved in the future;

• majority of the predicted results characterizing oxidation of fuel rods cooled with water is in good agreement with the test data base;

• lack of oxidation models in the SCANAIR code and oxidation model for the cladding cooled with air in FRAP-T6 code do not practically influence the other calculation results.

Mechanical behavior of fuel rods

Test data base characterizing internal gas pressure vs. time, time of cladding failure and cladding residual hoop strain was used to verify mechanical behavior of VVER fuel rods under IGR test conditions.

Internal gas pressure vs. time is an important parameter influencing the deformation behavior of the cladding of the VVER pressurized fuel rods. Verification of the respective models was done with fresh fuel rods equipped with pressure transducers (Chapter 4 of this Volume). Verification results for two fuel rods characterizing time history of the pressure for the failed fuel rod with the air coolant and time history of the pressure for the failed fuel rod with water coolant are presented in Fig. 5.33 and Fig. 5.34. Calculation of internal gas pressure by SCANAIR code are presented up to ballooning initiation, because SCANAIR code does not predict the fuel rod behavior under these conditions and does not calculate the time of the cladding rupture.
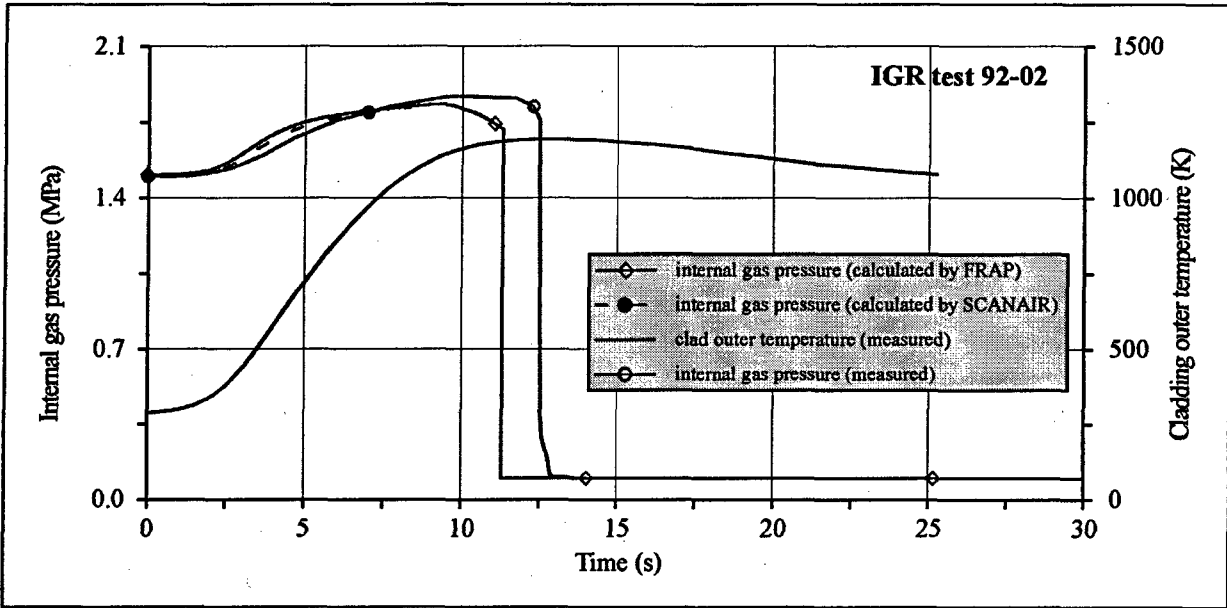
Fig. 5.33. Calculated and measured internal gas pressure vs. time for failed fuel rod cooled with air
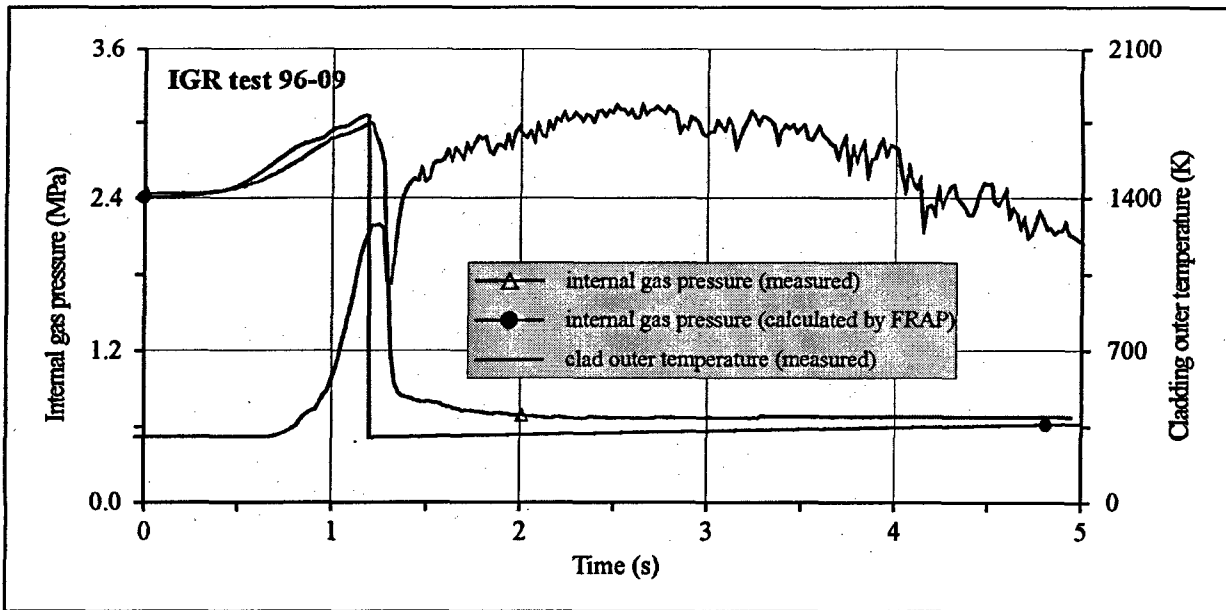
Fig. 5.34. Calculated and measured internal gas pressure vs. time for failed fuel rod cooled with water

5.56

Analysis of the presented results confirms the fact that calculation of internal gas pressure by this version of FRAP-T6 code is done correctly enough. Results obtained by SCANAIR code demonstrate good agreement with the test up to the ballooning stage. Still evident problems arise if we try to use SCANAIR code to calculate internal gas pressure under ballooning conditions, because the fuel rod geometry changes greatly in this case, and the cladding rupture occurs. That is why the decision was made not to use SCANAIR code to calculate this parameter for the respective test conditions in the framework of the computational data base development.

The next item in the verification procedure for mechanical behavior of VVER fuel rods was the failure conditions of the cladding. This verification stage was done for FRAP-T6 code only. In fact BALON2 subroutine with the original VVER mechanical properties was subject to verification.

Detailed checking of BALON2 subroutine was done with the help of the test data base obtained for fresh fuel rods equipped with the cladding thermocouples and pressure transducers (see Fig. 5.33 and Fig. 5.34). The checking has indicated that the predicted and measured failure parameters were in good agreement.

Results presented in Fig. 5.33 indicate that there exist a discrepancy between the calculated and measured failure time equal to 1.4 s. But this does not practically influence any of the other output parameters, because all of these parameters are the quasi steady-state ones in this time interval. The indirect confirmation to the fact that the developed version of FRAP-T6 code predicts failure conditions adequately enough is the comparison of the actual and predicted cladding rupture for all the 25 fuel rods presented in the data base of Volume 3. This comparison indicates that FRAP-T6 code was always correct in predicting the presence or absence of the fuel rod failure.

The last stage in the verification procedure for mechanical behavior of fuel rods was checking of the cladding hoop strain calculations. The checking was performed for two different end states of the fuel rods:

- unfailed fuel rod;

- failed fuel rods due to ballooning.

Thus, the first group of fuel rods allowed to check the quality of predicting the cladding hoop strain before ballooning phenomenon. The second group ensured checking of the prediction of the limiting values of the cladding hoop strain typical for the cladding failure of the ballooning type. It is obvious that SCANAIR code was checked for the first group of fuel rods only. Though the fuel rods of the first group are characterized by insignificant residual strains, analysis of their behavior is very useful to understand the initial stage of the cladding plastic deformation. Wide verification data base characterizing these processes exists for fresh and high burnup fuel rods. But the most useful are the comparative results of the profilometry before and after IGR tests for high burnup fuel rods. Such results exist for four fuel rods ## H1T, H4T, H6T, H8T. Still in the three of them measured residual hoop strain is equal to zero, that is why fuel rod H1T was used to check the measured and calculated residual hoop strain of the cladding vs. axial coordinate. Results presented in Fig. 5.35 demonstrate the real and predicted cladding residual hoop strain obtained mainly at the stage of the pellet-cladding mechanical interaction (PCMI). Comparative analysis indicates that both codes predict average strain along the length of the fuel rod well enough, though FRAP-T6 code has some tendency to overestimation of the clad strain. Besides, the obtained results illustrate that deformation of the cladding of the standard fuel element is determined by the effects, which are not considered in the existing code models. Hence this stage of verification allows to make a conclusion that it is expedient to calculate weighted mean values of the cladding hoop strain only.

The focus of the next verification stage was targeted at checking of the quality of the peak clad hoop strain calculations for the fuel rods that had failed due to ballooning. This type of the cladding deformation is modeled by BALON2 subroutine driven by FRAP-T6 code.
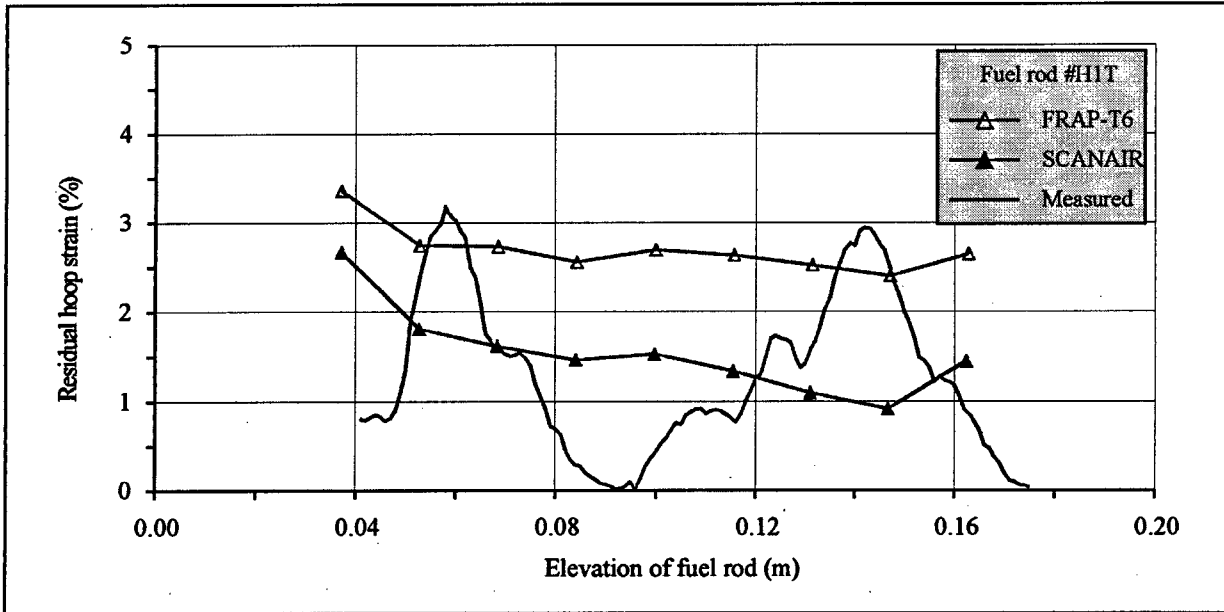
Fig. 5.35 Calculated and measured cladding residual hoop strain vs. axial coordinate for fuel rod #H1T

It is important to note that the special cycle of experimental research necessary to adapt BALON2 subroutine for the VVER cladding was performed in 1997. The major part of results of this research, which are described in details in Chapter 6 is already included into the input data for BALON2, but the final analysis and generalization of the data were done after completion of verification procedures. Hence it was assumed that some certain additional modification of BALON2 subroutine could be done in the future.

Verification data base necessary to check the peak clad hoop strain predicted by BALON2 subroutine was developed on the basis of both the results of testing VVER fuel rods presented in this report, and on the results of earlier IGR tests. Comparative data characterizing the measured and predicted hoop strain are presented in Fig. 5.36.
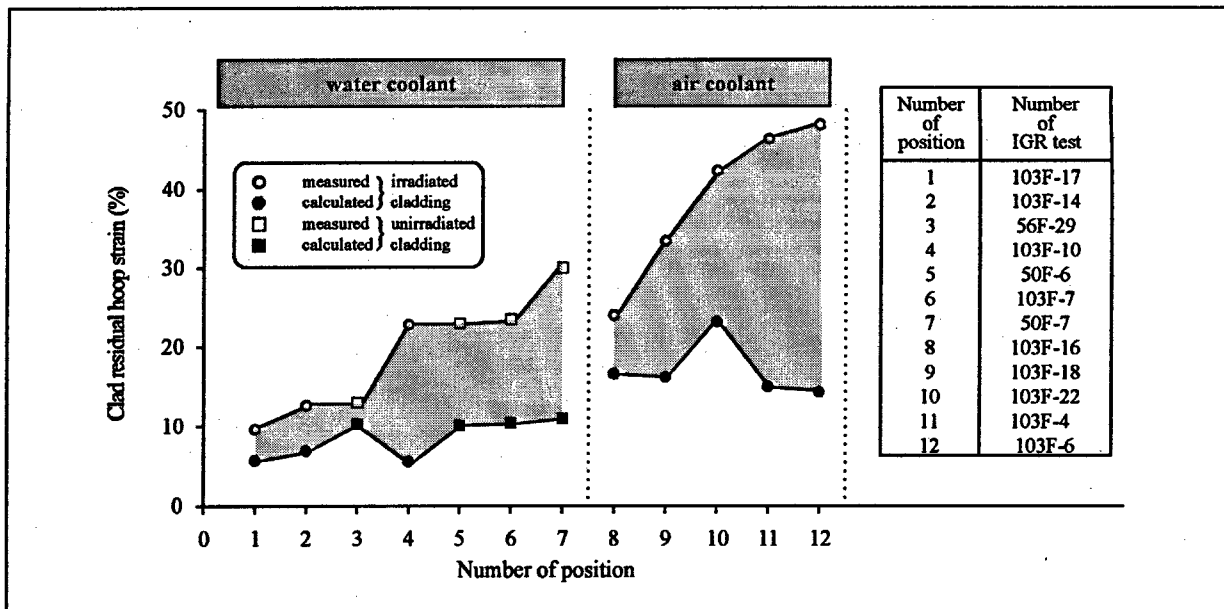
Fig. 5.36. Measured and calculated peak clad residual hoop strain for ballooning area (original approach)

Obtained results indicate that FRAP-T6 code systematically underestimates peak clad residual hoop strain for the ballooning area. It is even more evident for the fuel rods cooled with air when the values of clad hoop strain are of 20 % and higher. An analysis of models used in the BALON2 program was performed to understand causes of a considerable difference between experimental and calculated data.

BALON2 belongs to a group of codes that allow to calculate the asymmetric cladding deformation in time. For this purpose the assumption on the azimuth non-uniformity of the cladding temperature is used during the initialization of the BALON2 program. In this case, temperature variations significantly affect the value of the circumferential elongation. The effect of the elongation decrease with the increase in the temperature non-uniformity was intensively studied in experiments that simulate LOCA [35, 36]. According to experiments, this effect is a key factor that influence the cladding elongation. Parametric calculations using the FRAP-T6/BALON2 code also demonstrated a significant sensitivity of the circumferential elongation at burst to the azimuth variation of the cladding temperature (Fig. 5.37).
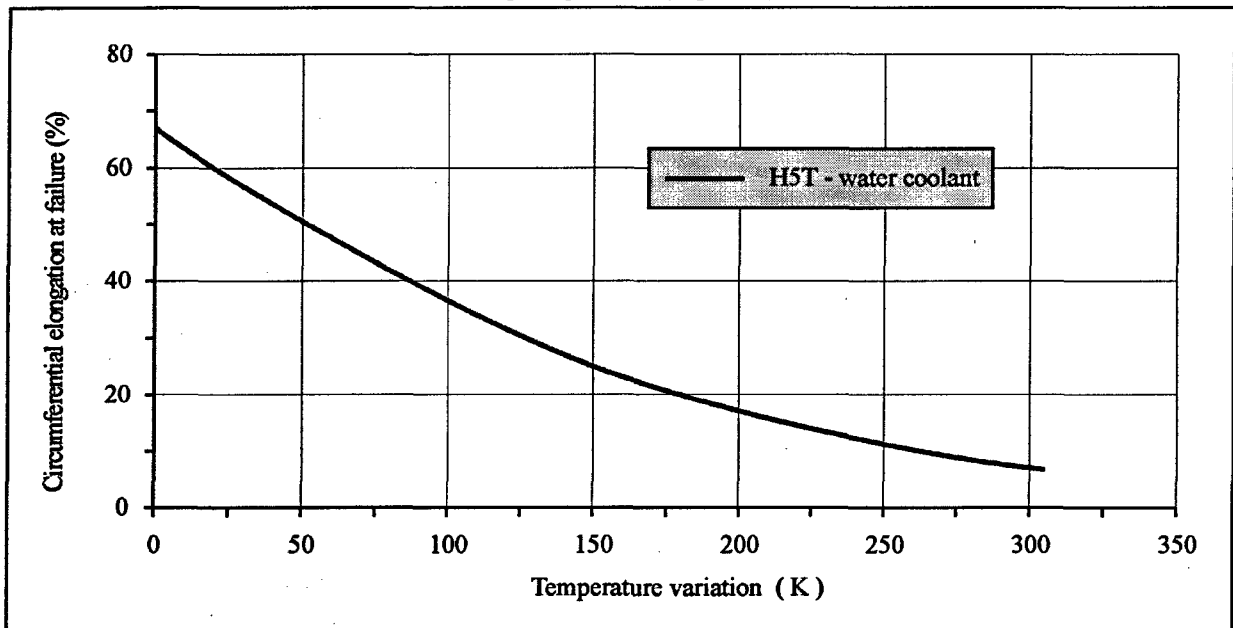
Fig. 5.37. Calculated cladding circumferential elongation at burst vs. azimuth variation of temperature

IGR test results do not allow to quantitatively estimate the azimuth variation of the cladding temperature and, thus, to verify the calculation model of the asymmetric temperature field in the fuel rod. Nevertheless, it is possible to make important qualitative conclusions based on post-test studies:

- fuel rods tested in the water coolant are characterized by a considerable temperature non-uniformity along the azimuth. This is confirmed by a low level of the circumferential elongation at burst and the local necking of the cladding in the area of the burst tear;

- in case of the air coolant, the azimuth non-uniformity of the temperature field in the fuel rod is considerably lower. As a consequence, the uniform deformation of the entire middle line of the cladding takes place, that leads to much larger circumferential elongations at burst in comparison with water-cooled fuel rods.

This is why two different approaches were used to describe the fuel rod behavior in the air and water coolant. An original approach of the BALON2 to simulate the asymmetric temperature field in air-cooled fuel rods resulted in unrealistic predictions of the cladding deformation at burst. To solve this problem, the BALON2 program was modified as follows. For the determination of cladding dimensions during the ballooning, the assumption on the cladding bending in the axial plane is used, that leads to a relative offset of the fuel pellet and the cladding till the time of the contact. At the time of the contact of the fuel and the cladding a sharp surge of the cladding temperature is predicted in the contact zone. The use of the bending model for fuel rods under consideration would be unjustified. Therefore, this model was disabled during calculations of air-cooled fuel rods.

On the other hand, the bending model was used in BALON2 calculations for water-cooled fuel rods. It should be noted once more that it was difficult to verify the model since there were no data on the azimuth variation of the temperature. However taking into account the statistic nature of the film boiling and the presence of the geometric eccentricity in the real fuel rod, the prediction of the fuel and cladding contact during the ballooning can be considered as a simplified approach to the simulation of the "hot spot" on the cladding under DNB conditions.

Calculation results of the peak deformation of failed fuel rod claddings were in a satisfactory agreement with experimental data (see. Fig. 5.38).

Number of position	Number of IGR fuel rod
1	H5T
2	H15T
3	H2T
4	H7T
5	H6C
6	B10T
7	B9T
8	B22T
9	B21T
10	B20C
11	B20T
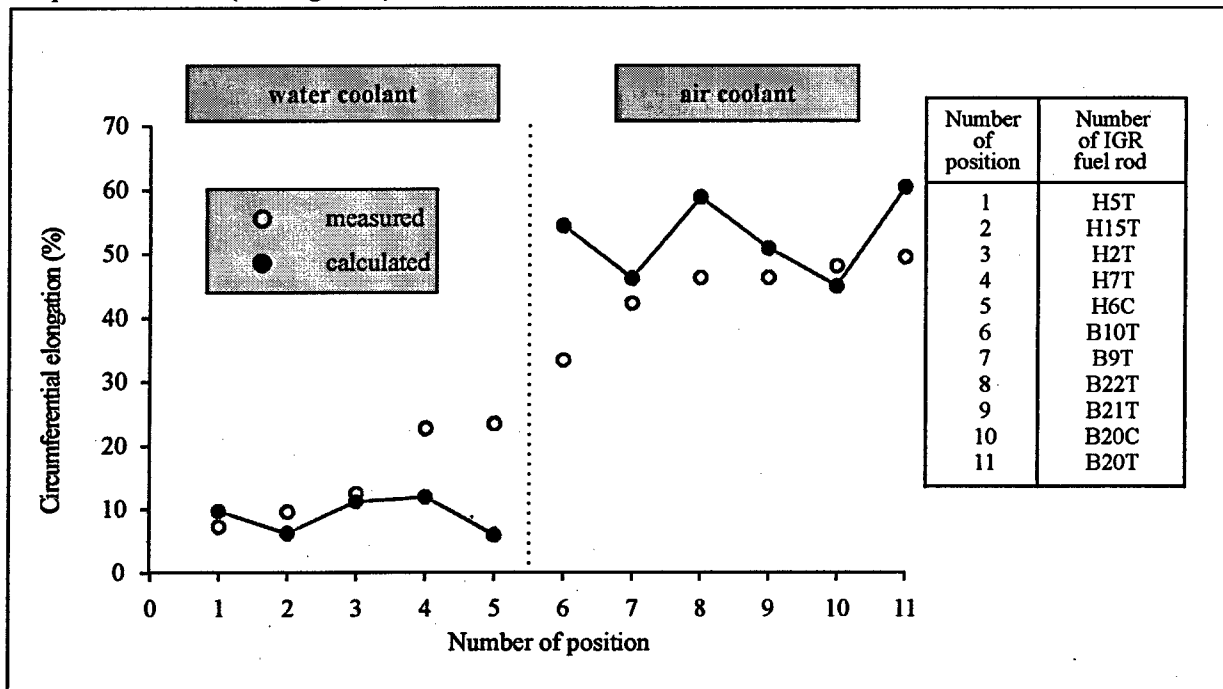
Fig. 5.38. Measured and calculated cladding residual hoop strain for ballooning area (modified approach)

At the same time the calculation experience using the BALON2 subroutine demonstrated that for more adequate deformation calculations during the ballooning under RIA conditions, it is necessary to develop more accurate fuel rod thermal models that allow to reduce uncertainties and get adequate estimates of the mechanical behavior of fuel rod claddings.

5.8. Main provisions of the procedure to obtain calculation results by FRAP-T6 and SCANAIR codes

The developed versions of FRAP-T6 [37] and SCANAIR codes [38] were used to calculate the behavior of 25 VVER fuel rods tested in IGR reactor under RIA conditions. These calculation results are presented in Appendixes G, H, I of Volume 3. Taking into consideration specific features of the codes, as well as specific features of three different types of fuel rods, the following approach was developed to get the computational data base done:

- main set of parameters characterizing fuel rod behavior was calculated for axial coordinate corresponding to the peak axial power in each fuel rod;

- SCANAIR code was not used to calculate cladding oxidation parameters of the fuel rods, and FRAP-T6 code was not used to calculate cladding oxidation parameters for the fuel rods cooled with air;

- calculations characterizing fission gas behavior in the fresh fuel were excluded out of the data base, as they represent no practical interest;

- taking into consideration that in SCANAIR code there is no model characterizing cladding deformation of the ballooning type, and the models predicting failure of fuel rods, calculation results obtained by SCANAIR code are to be presented in the data base up to the fixed time of initiation of clad plastic deformation due to inner gas pressure. As described in section 5.5.3.5 thermal dynamic calculations for H1T fuel rod were obtained and presented for the whole time period:

⇒ pellet-cladding gap reopened;

⇒ cladding stress achieved yield stress;

- calculations are completed and calculation results are not to be presented into the data base starting with the fixed time moment for which the condition of the peak fuel temperature reaching the fuel melting temperature is observed.

Detailed description of the specific features characterizing computational data base presented in Volume 3 is given in Chapter 1 of Volume 3.

5.9. Data base to verify FRAP-T6 and SCANAIR codes with respect to thermal parameters

Special instrumented fuel rods were used to verify computer codes. Fig. 5.39 presents the view of such a fuel rod.
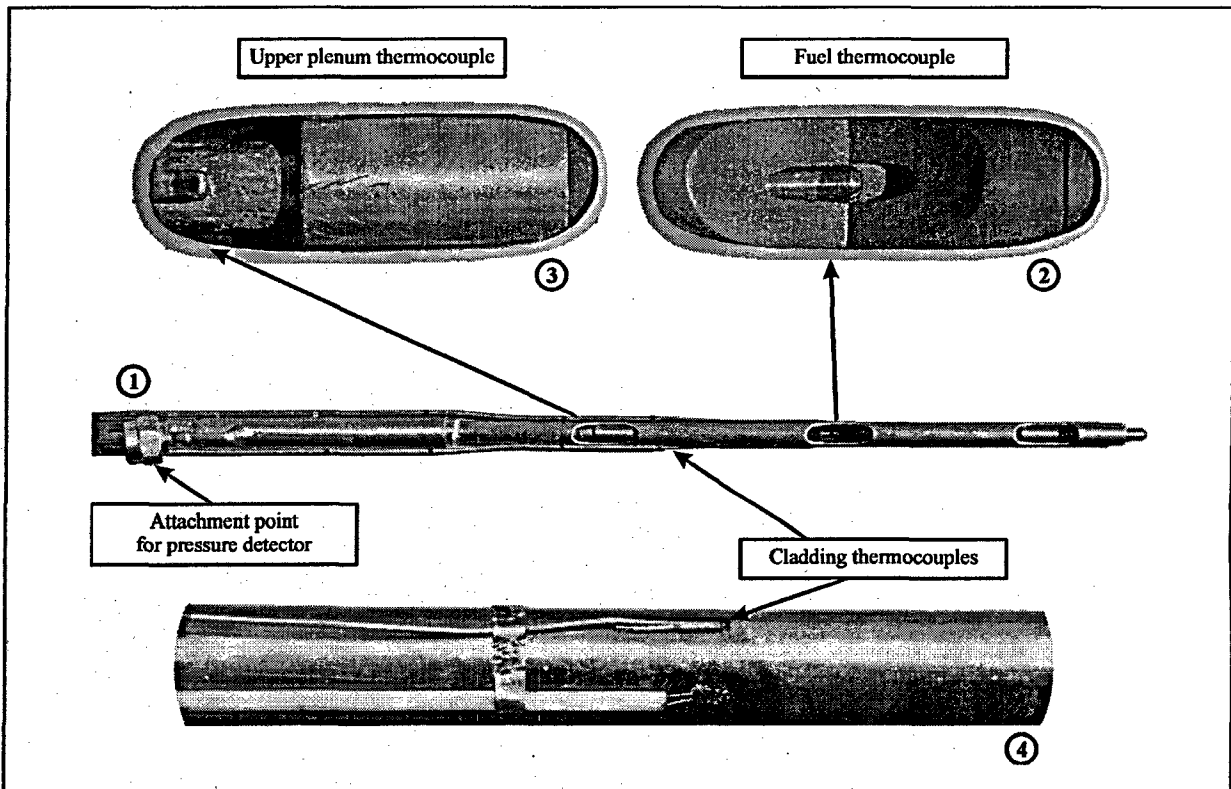
Fig. 5.39. View of the instrumented VVER fuel rod

Generally, it was possible to measure the following parameters with the help of instrumented fuel rods:

- gas pressure inside the fuel rod;
- gas temperature in the upper plenum;
- fuel temperature;
- cladding temperature.

All instrumented fuel rods were fabricated of unirradiated materials so that the active part of the instrumented fuel rods was the same as of the traditional unirradiated fuel rods. The only difference was that from two to six thermocouples were located on the cladding surface.

It was noted earlier that two measured parameters were used to verify FRAP-T6 and SCANAIR codes:

- gas pressure inside the fuel rod;
- cladding temperature.

It was not an easy task to develop instrumentation methods to measure these parameters under IGR/RIA test conditions. For example, two contradicting requirements were drawn to the gas pressure detector:

- high quality of the transfer function for the system consisting of the pulse tube, pressure detector, amplifier, etc.;
- low sensitivity to irradiation taking into consideration that during these tests neutron flux density in IGR reactor reached $1.0 \cdot 10^{16}$ n/cm^{2}s.

Therefore the special detector was designed on the basis of the inductive type pressure detector. The time constant of the pneumatic line of this detector was 0.01 s, and the measurement error – 7 % in the dynamic mode if the pressure shock duration was 0.01 s. There were many problems connected with designing of detectors to measure cladding temperature under RIA conditions. In this case it was necessary to satisfy the following main requirements:

- to ensure that the temperature measured by thermocouple is the temperature of the cladding, and not something intermediate of the cladding and coolant temperatures;
- to have the minimum possible dimensions of the thermocouple hot junction, so that the dynamic measurement error under transient temperature mode is acceptable;
- to locate thermocouples on the cladding in such a way that the azimuth temperature distribution can be controlled.

The main effort of the final cycle of the research was focused to these issues. Description of the research work and its results is beyond the frames of this Report. It is necessary to state, though, that two main types of thermocouples were chosen to measure cladding temperature:

- W/Re or chromee-alumee thermocouples in the protective shroud with the typical dimension of about 0.4 mm, located in the grooves made on the cladding, fixed by welding;
- W/Re thermocouples with the open hot junction welded to the cladding surface.

RRC "KI" was the program manager of the investigations targeted at the designing of the instrumented fuel rods. Different Russian Institutes participated in the designing of these fuel rods at different stages of the program. Initial stage of the work is described in [39]. Results of the other stages of work have not been published. The greatest contribution to the development of the instrumented fuel rods was made by Dr. V. Nalivayev, and the experts of the "Technoluch" Division headed by him of the Scientific Industrial Association "Luch" (Podolsk, Russia).

Measurement results of the gas pressure inside fuel rods used as the data base to verify FRAP-T6 and SCANAIR codes were obtained by the pressure detectors developed at the same organization. Some part of the used temperature measurements was also obtained owing to the efforts of the same team of experts. Still, the measurement results based on the procedures described in [39] were also used for the verification. Selection of the verification test data base was performed very carefully. The main problems were connected with the choice of the representative measurements of the cladding temperature for the test modes, when departure from the nucleate boiling took place. Two circumstances could significantly influence the measured history of the cladding temperature:

- systematic measurement errors (bad contact of the thermocouple and the cladding, imperfection of the thermocouple design, etc.);
- high degree of non-uniformity of the r, θ, z temperature distributions under crisis of the boiling conditions.

We believe, there is no need to describe the importance of the first issue in detail. The data presented in Fig. 5.40 will allow to understand the degree of importance of the second issue.
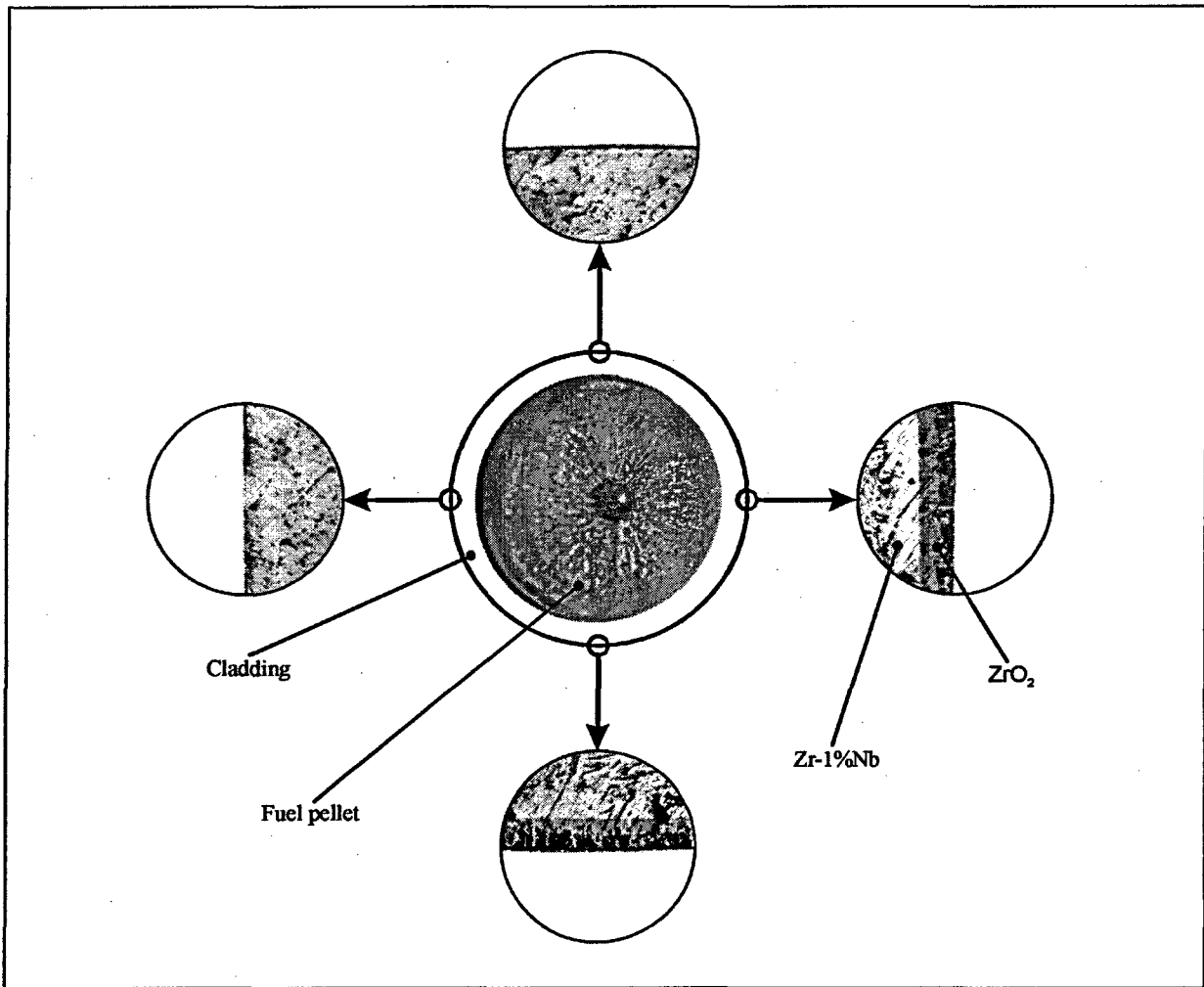
Fig. 5.40. Cross-section of the VVER fuel rod after IGR test

We selected the fuel rod that was tested under peak fuel enthalpy higher than the failure threshold, because in this case oxidation of the cladding during film boiling reaches clearly expressed values. Cross-section of this fuel rod was made, and the photograph of the cladding microstructure was made for four azimuth angles. The data presented in Fig. 5.40 state that there was significant temperature non-uniformity in this cross-section, because in the two cross-sections significant ZrO_2 layer and the layer of α-Zr stabilized by oxygen were formed, but those effects were completely absent in the other two cross-sections. That is why even if the cladding temperature would have been measured with the absolute accuracy in each of those positions, the measurement results would still have been different by no less than 200-250 K in the point of the temperature maximum. If we analyze both of the above problems, we can notice that:

1. any systematic measurement error leads to underestimation of the cladding temperature;

2. if the cladding temperature is measured in several points, then it is always possible to chose such a measurement (out of the series of the similar type measurements), which most accurately reflects the temperature scenario for the hottest part of the cladding.

Therefore, if for the given level of the peak fuel enthalpy we select (of the measured mass of temperature histories) the history with the maximum temperature, and perform verification of the computer code just for the cross-section with the peak enthalpy, we can assume with good confidence that the used test data base is representative. This was the approach used to prepare the data base for verification of FRAP-T6 and SCANAIR codes.

5.63

5.10. Analysis of the computational data base to characterize VVER fuel rod performance under IGR test conditions

The main objective of this analysis was directed to:

- reveal such specific differences in the calculated parameters of fuel rods which are caused by the corresponding differences in the mathematical models used by FRAP-T6 and SCANAIR codes;

- compare calculated and measured results, and to assess reliability of the obtained computational data base.

Decomposition of the tested scenario can be done in the framework of the following approach in order to review the complex of physical phenomena which determined VVER fuel rod performance under IGR test conditions:

1. The stage when there exists the open gap between the fuel and cladding.

2. The stage when the gap disappears, and mechanical interaction between fuel and cladding takes place.

3. The stage when the gap reopens, and the cladding is loaded with the gas internal pressure.

Specific features of the change of parameters of all types of fuel rods for each of these stages of scenarios are reviewed later, and analysis of the data base for peak fuel enthalpy and the data base for cladding failure was emphasized as a separate issue.

5.10.1. Analysis of the scenario first stage

Some group of representative parameters was selected to analyze the calculated behavior of the three typical fuel rods (Fig. 5.41):

- high burnup fuel rod tested in the water coolant (#H1T);

- high burnup fuel rod tested in the air coolant (#B9T);

- fuel rod with fresh fuel and irradiated cladding tested in the water coolant (#H16T).

Analysis of the data presented in the figure demonstrates that both of the codes predict practically identical thermal parameters of different types of fuel rods, tested in different coolants. The main problem that was revealed during this type of scenario was caused by the fact that FRAP-T6 and SCANAIR codes predicted different time histories for the gas gap in high burnup fuel rods. If we take into consideration the fact that there are no differences in the prediction of time histories for the cladding temperature and cladding hoop strain, then it becomes evident that the discrepancy between time histories for the fuel total hoop strain can be the reason caused the discrepancy between time histories for the gas gap. The data presented in Fig. 5.41 confirmed to this conclusion. Still, total hoop strain of high burnup fuel includes two components:

- hoop strain due to thermal expansion;

- hoop strain due to fuel swelling.

In order to check the adequacy of calculations of the first component calculated results of the total hoop strain were compared for fuel rod #H16T. This fuel rod had the fresh fuel, and thus it was possible to assume that the swelling component was equal to zero. It is demonstrated in Fig. 5.41 both codes calculated fuel hoop strain caused by thermal expansion completely adequately. It is evident that the models describing fuel swelling were the source of discrepancy between the codes. Analysis of the respective results has demonstrated that FRAP-T6 code predicted much higher values for fuel swelling than the SCANAIR code. Unfortunately, it is impossible to verify these code models using VVER/IGR test data base. Therefore, additional effort will be made to assess reliability of each of these results during the stage of preparation of the Final Report.
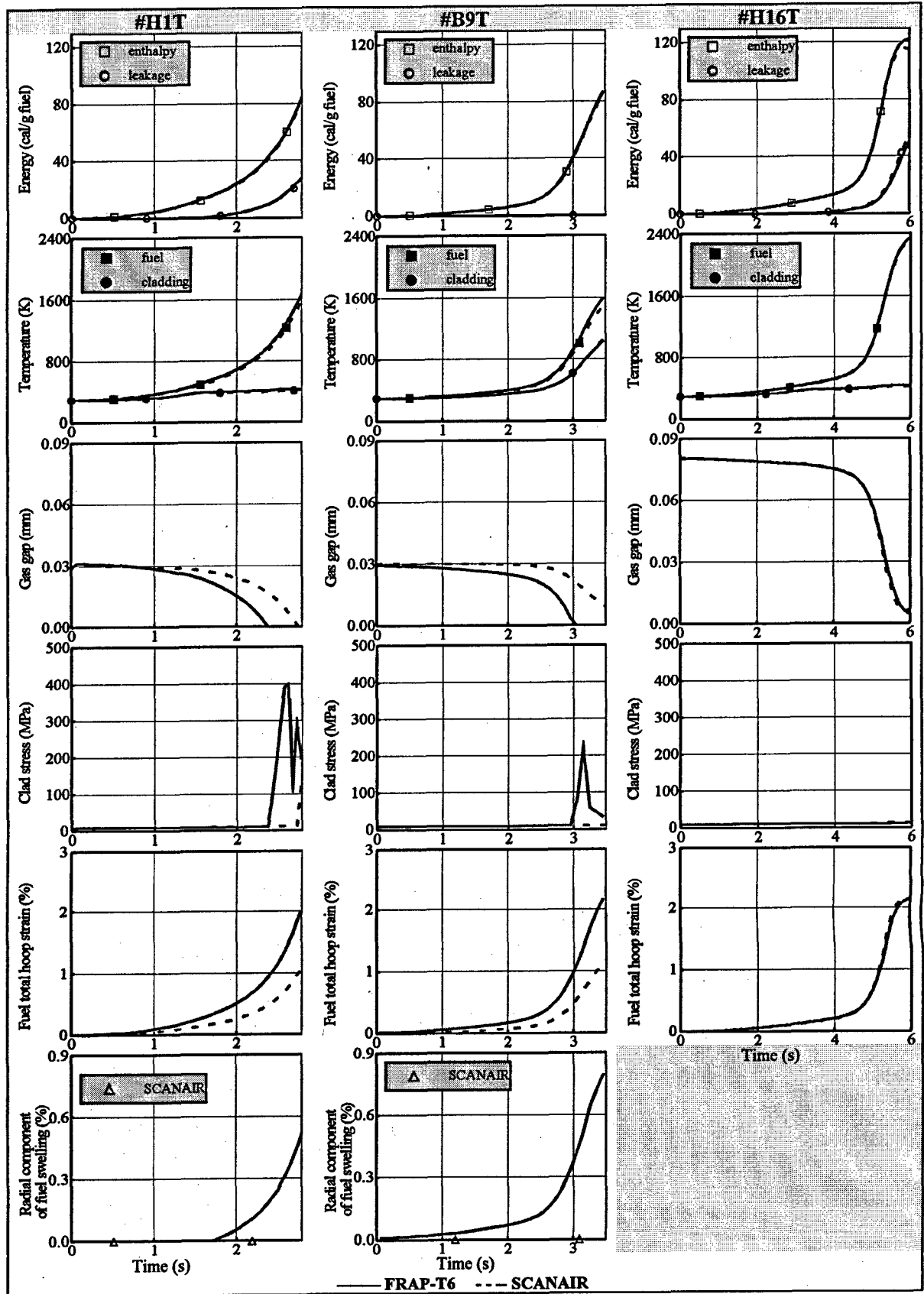
Fig. 5.41. Parameters of some fuel rods for the first stage of IGR tests

5.10.2. Analysis of the scenario second stage

Three fuel rods were also selected to assess the results of this stage of scenario (Fig. 5.42):

- high burnup fuel rod tested in the water coolant (#H4T);
- high burnup fuel rod tested in the air coolant (#B9T);
- fuel rod with fresh fuel and irradiated cladding tested in the water coolant (#H16T).

This stage of scenario is characterized by the situation when the PCMI occurs after the gas gap is closed, and high cladding hoop stresses can occur due to PCMI effect. Cladding failure can occur during this stage of the scenario, therefore it is extremely important to assess the calculated results for the group of representative parameters.

It has already been noted that different calculated time histories for the radial component of fuel swelling, and accordingly for the fuel total hoop strain resulted in the situation that FRAP-T6 code predicted earlier gas gap closure, than SCANAIR code for two high burnup fuel rods. This leads to the situation that the typical process of the abrupt increase of the cladding stress started according to the FRAP-T6 scenario by 0.5 s earlier than according to SCANAIR scenario (for the high burnup fuel rod cooled with water). Besides, FRAP-T6 code predicted a little higher level for the maximum cladding hoop strain during PCMI stage. Still, taking into account complexity of physical phenomena, determining the dynamics of the process, it is possible to consider that agreement of the results, predicted for the cladding hoop stress in the high burnup fuel rod cooled with water, is satisfactory. Calculated results for the cladding hoop stress in the high burnup fuel rod cooled with air differ much more, because this fuel rod has demonstrated the case when FRAP-T6 had predicted gap closure and PCMI stage, and SCANAIR code had predicted that the gap would not be closed, and no PCMI stage would take place. That is why time histories for the cladding hoop stress predicted by two codes differ in principal. This also confirms to the earlier made conclusion that in the future special attention is to be paid to the problem of fuel swelling. As for the fuel rod with fresh fuel, this stage of the scenario is not important to analyze reliability of predicting cladding hoop stress, as the gas gap remains open, and the PCMI effect does not take place in this type of fuel rods.

One more issue was revealed during the comparative analysis of the results obtained over this phase by two codes. Significant discrepancies were revealed between time histories predicted by the codes for the following thermal parameters in the fuel rods cooled with water:

- fuel temperature;
- fuel enthalpy;
- leakage of energy.

It is evident that two main reasons can lead to these discrepancies:

- different models are used in SCANAIR and FRAP-T6 codes to describe heat transfer from the fuel rod to the coolant;
- SCANAIR and FRAP-T6 codes predict time histories of the gas gap width differently, and assess gas heat conductance through the gas gap differently.

Theoretically both reasons can take place. Therefore, the first one was analyzed at first. During the first stage we assessed behavior of the fuel rod #B22T cooled with air. This fuel rod was chosen as the referenced one, because it had the minimum peak fuel enthalpy of the group of air cooled fuel rods, and therefore, SCANAIR code ensured its analysis up to the maximum parameters. Besides, completely the same models were developed for SCANAIR and FRAP-T6 codes to calculate heat transfer to the air coolant. Results of calculations for the fuel rod #B22T are presented in Fig. 5.43.

The obtained results demonstrate that despite the fact that the same models were used to describe heat transfer from the fuel rod to the air coolant, FRAP-T6 code predicted a little higher values for the temperature of the fuel central line. Discrepancies between FRAP-T6 and SCANAIR codes obtained for this fuel rod and other fuel rods cooled with air are not of the principal value, but those discrepancies indicate that the heat flux from fuel to cladding is the reason for disagreement of the results. In order to review individual aspects of this problem for the fuel rods cooled with water in more details, it is useful to analyze the stage of the gas gap reopening as well.
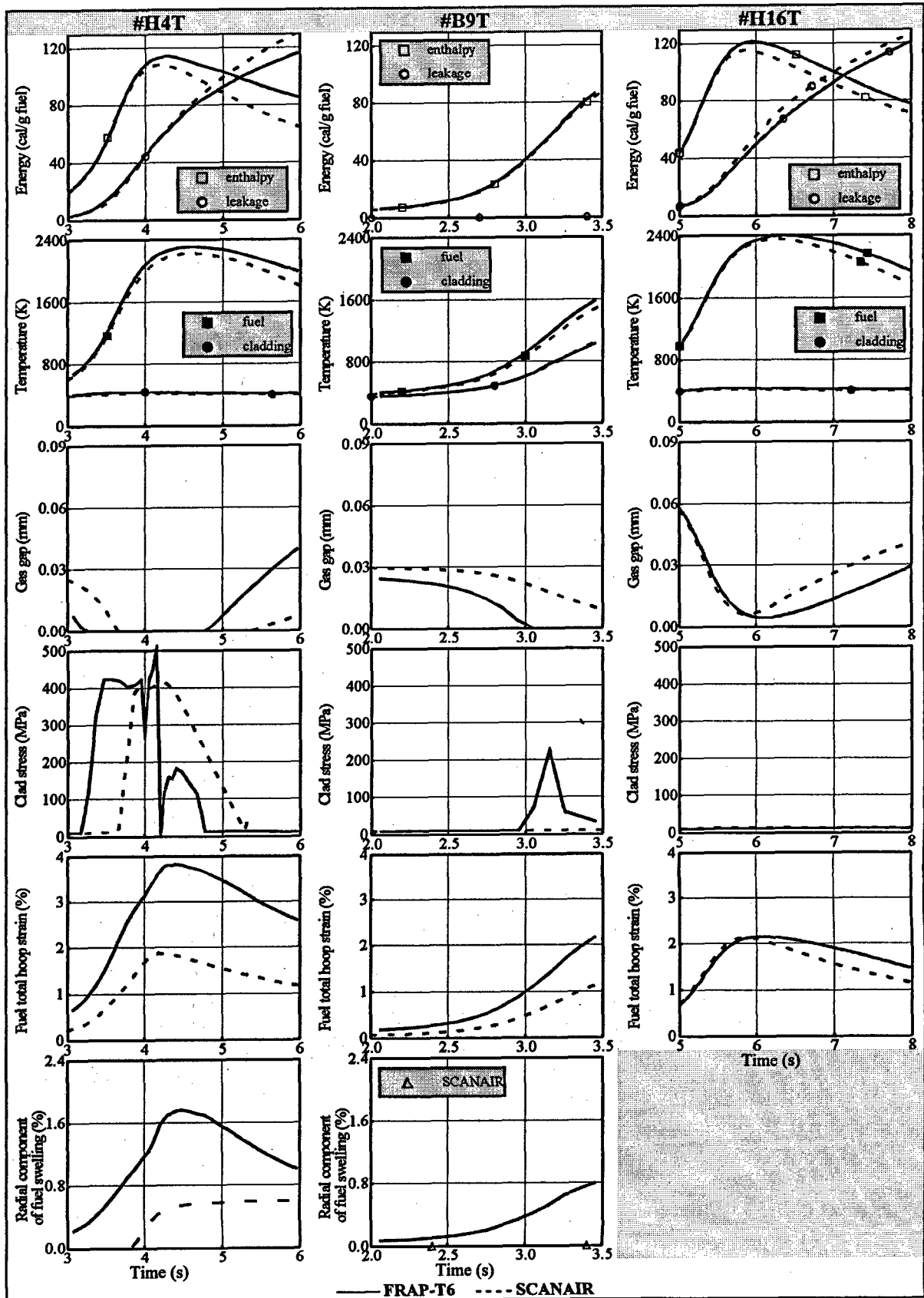
Fig. 5.42. Parameters of some fuel rods for the second stage of IGR tests
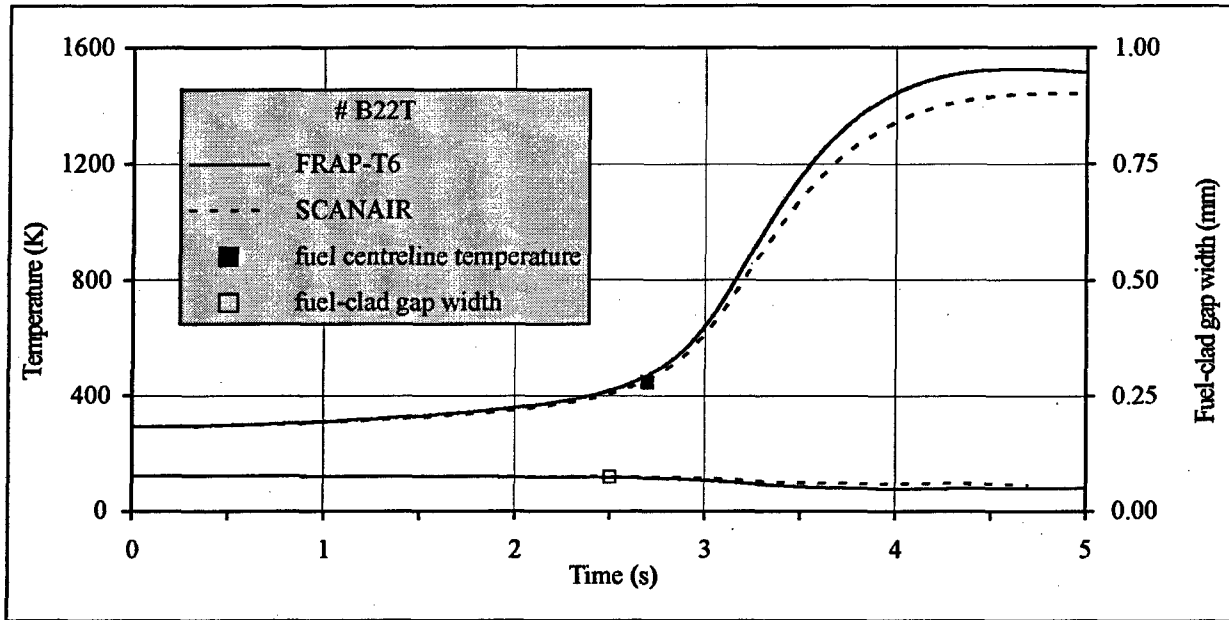
Fig. 5.43. Time histories of some parameters for the fuel rod #B22T

5.10.3. Joint analysis of the second and third stages of scenario for unfailed fuel rods cooled with water

Results obtained for #H4T and H16T fuel rods were used as the basis for the analysis (Fig. 5.44).

This analysis has started with fuel rod #H16T with fresh fuel. It is also important to note that the discrepancy between the predictions by FRAP-T6 and SCANAIR codes for time histories of thermal parameters for this one and other fuel rods of the similar type is insignificant. Therefore, it is possible to consider that both codes predict the behavior of this group of fuel rods well. Still, this is just the fuel rod that allows to clearly illustrate the influence of the gas gap parameter onto the main tendencies determining time histories of thermal parameters. Besides, it is important that gas gap size can decrease up to zero (just as presented in Fig. 5.41, Fig. 5.42, Fig. 5.44) only in the frames of mechanical models of both codes. As for the thermal models, then both codes assume that even in case of fuel-cladding mechanical contact some effective thermal gas gap, which is due to roughness of the fuel and cladding surfaces, still remains. Moreover at the same input data on the surface roughness (fuel roughness is 2 μm, and cladding roughness is 2 μm) FRAP-T6 code predicts that the effective gas gap width will be 0.012 mm, at the same time SCANAIR code assesses this value as 0.004 mm. In order to understand how it influences the fuel rod thermal parameters, it is expedient to review the data presented in Fig. 5.45.

These data demonstrate that thermal parameters predicted by FRAP-T6 and SCANAIR codes start to vary from t_1 time point. This time point characterizes such a state of the fuel rod after which the gap starts to decrease, and then increases in the time range $t_1 - t_2$ according to the logic of SCANAIR code, while FRAP-T6 code assumes that the gap remains constant in the $t_1 - t_2$ time range. The size of this gap is equal to the effective width of 0.012 mm. The data presented in Fig. 5.45 indicate that the gas heat conductance calculated by SCANAIR code exceeds significantly the corresponding heat conductance calculated by FRAP-T6 code due to the difference in the sizes of gas gap. This in its turn, leads to the fact that energy leakage from the fuel to cladding and from the cladding to water takes place more intensively than for SCANAIR option. Starting with the time point t_2 agreement of results in prediction of thermal and mechanical behavior of fuel rods by both codes is good. Some small discrepancy that exists is caused by the fact that the fuel rod cooling process occurs starting with different initial fuel temperatures, registered by both codes in the time point t_2. At first sight it is not very clear, why approximately the same case leads to more serious discrepancies of the fuel parameters in fuel rod #H4T at the stage of the open gap (Fig. 5.44).
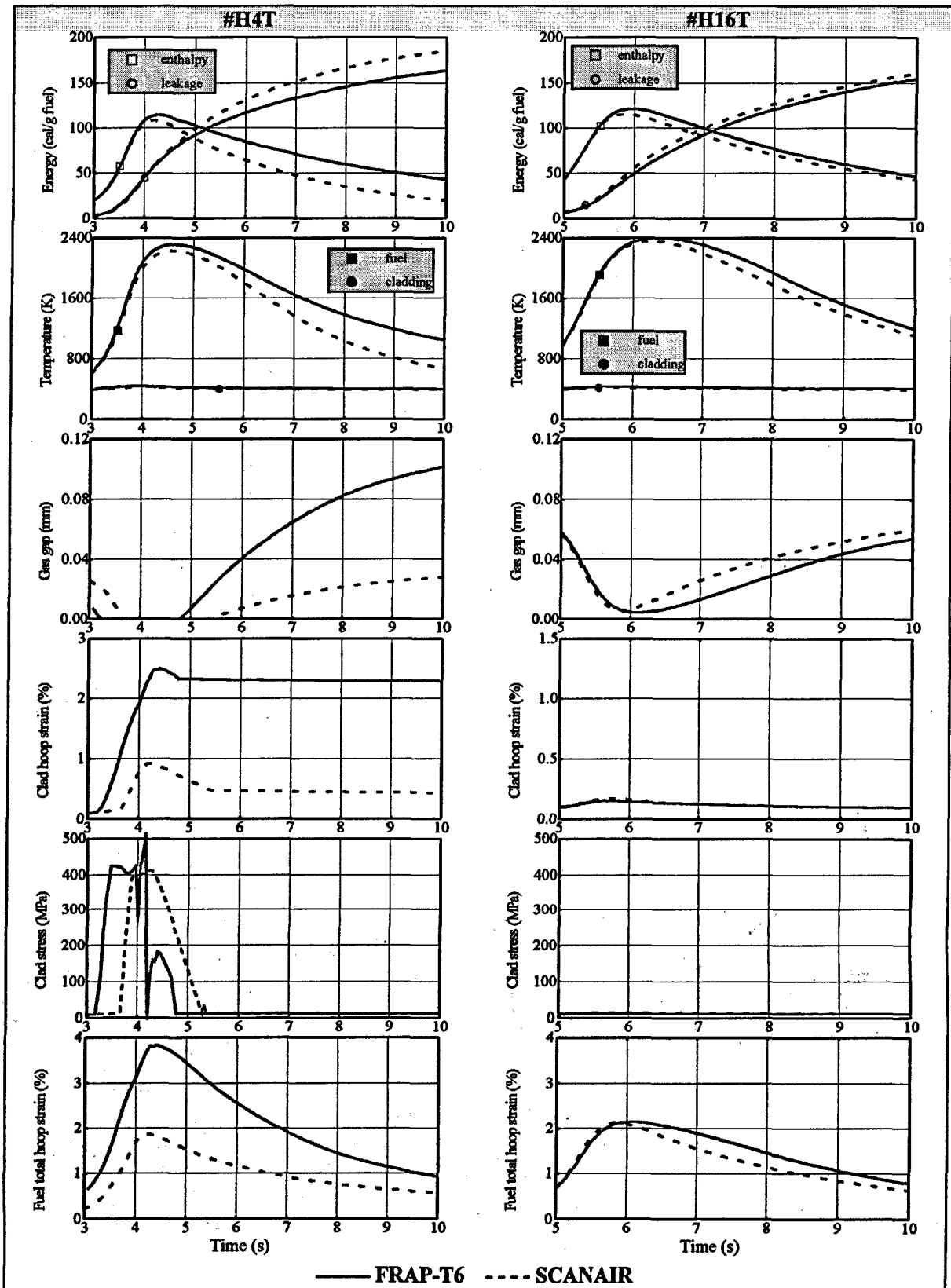
Fig. 5.44. Calculated parameters of some fuel rods for the second and third stages of IGR tests

5.69
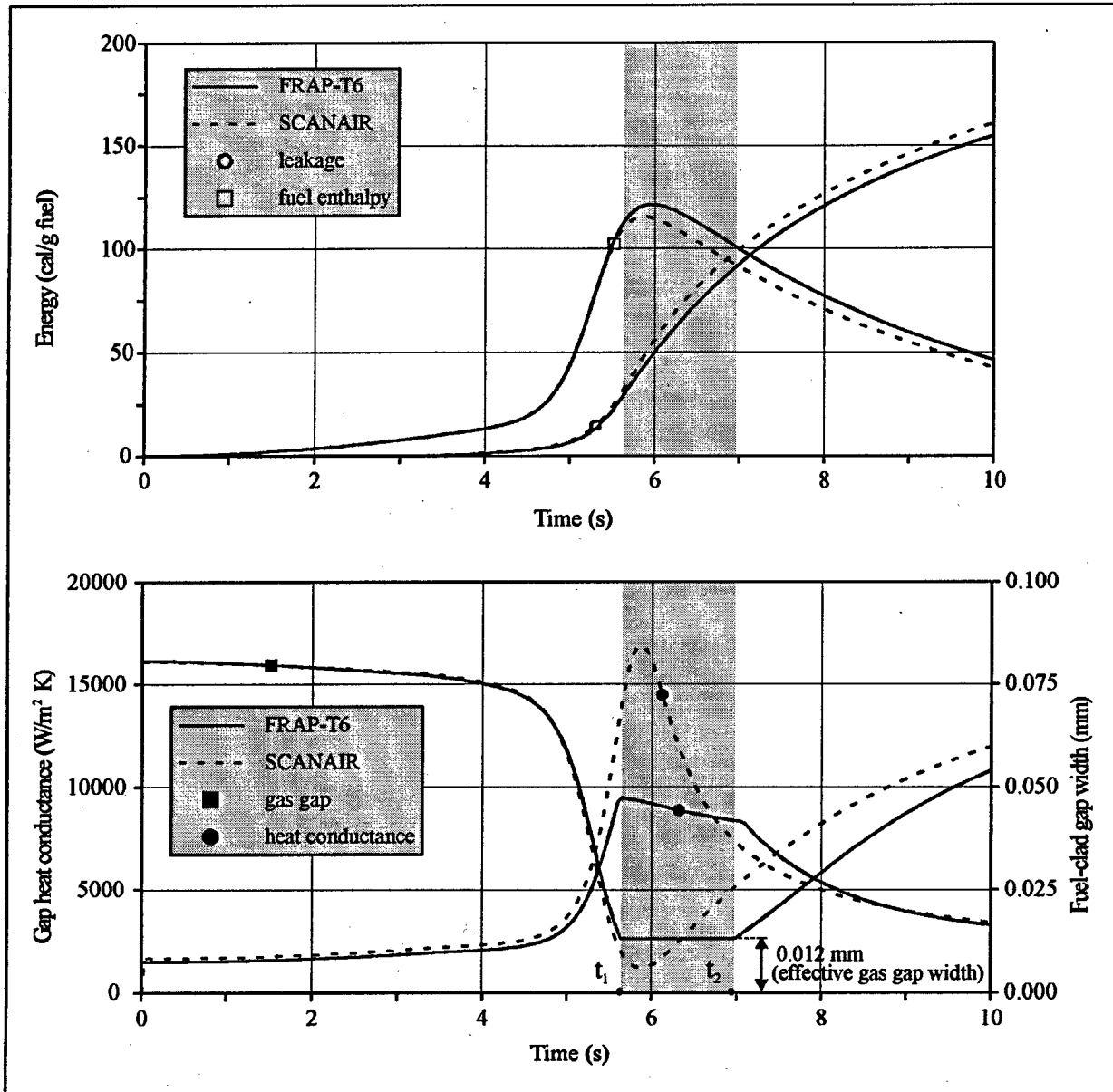
Fig. 5.45. Time history of fuel enthalpy, leakage of energy from fuel rod, gap heat transfer coefficient vs. gas gap width

In order to understand it we should first pay attention to the fact that FRAP-T6 code predicts significantly larger size of the gas gap for the stage of the gap opening (5 – 10 s). As the consequence this code predicts low energy leakage, higher fuel enthalpy, and higher fuel temperature. In order to understand the reason of the great discrepancy between the codes in predicting the gas gap width it is expedient to compare time histories of the cladding hoop strain presented in Fig. 5.44. Comparative analysis of the two curves obtained by FRAP-T6 and SCANAIR codes indicates that FRAP-T6 code predicted not only much higher level of the cladding hoop strain, but it also predicted cladding plastic deformation. It means that as soon as the fuel starts to cool down, the gap size is determined not only by the decrease of the radial dimensions of the fuel, but also by the residual hoop strain of the cladding. On the whole it is probable that these are the consequences of discrepancies in the fuel swelling models revealed by the analysis of the first stage of scenario. Still in this case, there was the possibility to check the values at the cladding hoop strain predicted by FRAP-T6 and SCANAIR codes using the respective test data base. Outer diameter of the cladding versus

5.70

fuel rod length was measured for fuel rod #H4T using profilometry before and after IGR tests. Results of these measurements were processed in accordance with the following procedure:

- average outer diameter of the cladding versus fuel rod length was determined by the results of profilometry for the states both before and after test;

- the difference of the average diameter versus axial coordinate was determined by deduction of the file of the average diameters before test out of the file of average diameters after test.

The sign of the obtained difference characterizes presence and absence of the cladding residual hoop strain for the fuel rod #H4T. Results of this procedure are presented in Fig. 5.46.
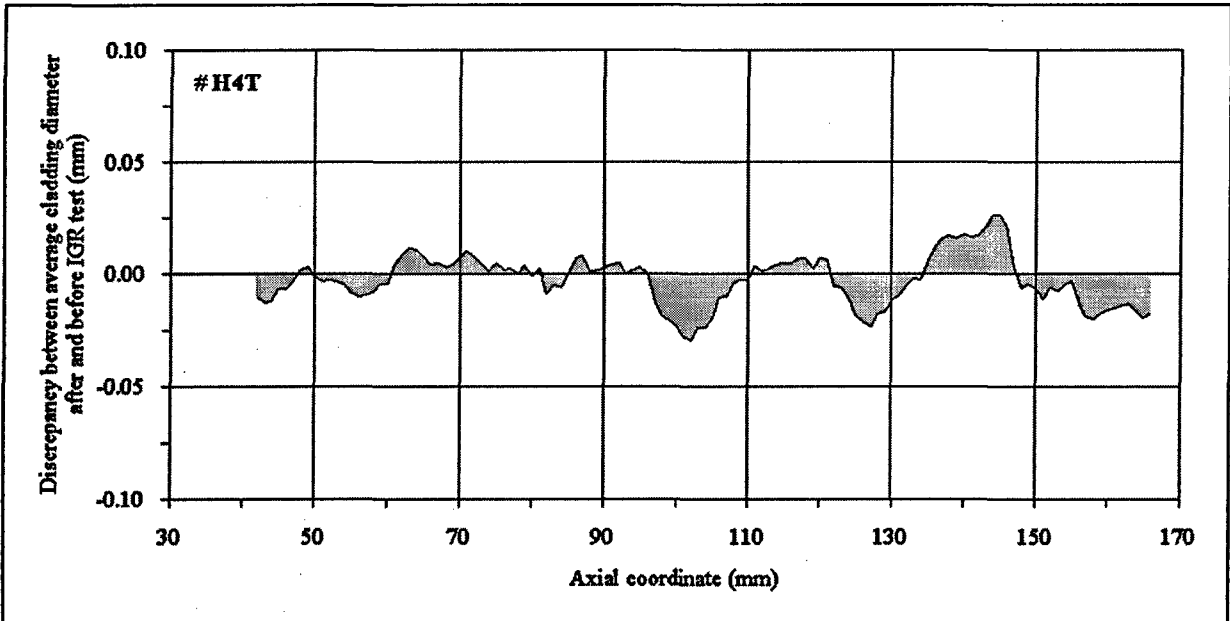
Fig. 5.46. Measured results to estimate cladding residual hoop strain for fuel rod #H4T

These results clearly demonstrate the random spread of the measurement results around zero. I.e this conforms to the fact that residual hoop strain is absent for the fuel rod H4T. Comparative data for the cladding residual hoop strain are also listed in Table 5.17.

Table 5.17. Data base to characterize cladding residual hoop strain for fuel rod #H4T

Parameter	Calculated and measured results		
	Experiment	SCANAIR code	FRAP-T6 code
Cladding residual hoop strain (%)	0	0	1.7

Thus, the presented data indicate that SCANAIR code predicts cladding strain for this fuel rod reasonably, while FRAP-T6 code overestimates this parameter. Similar results were also obtained for the fuel rod #H1T (Fig. 5.35).

Summarizing results of the analysis it is possible to conclude with the delicate confidence that FRAP-T6 code overestimates fuel swelling for high burnup fuel rods, and that leads to overestimation of the fuel hoop strain and cladding hoop strain, and finally results in overestimation of the fuel enthalpy and fuel temperature at the stage of cooling down of the fuel rod.

5.10.4. Analysis of the third stage of scenario for the failed fuel rods

This stage of analysis was performed for FRAP-T6 code only, because SCANAIR code does not contain any models to predict fuel rod failure. Typical options of the scenario, that lead to the cladding failure of the ballooning type are presented in Fig. 5.47 for two types of fuel rods:

* high burnup fuel rod #H5T cooled with water;

* high burnup fuel rod #B22T cooled with air.

Fig 5.47 shows time dependencies of key parameters at the failure stage for fuel rods H5T, B22T.

A key feature of this stage is the transition to the estimates of the local plastic deformation according to the ballooning mechanism. As it has already been noted, during the PCMI the cladding temperature increases to the level of 1100 – 1200 K. In this case its strength is reduced to the degree when its further deformation takes place as a result of the internal pressure. When the plastic deformation reaches the value of the uniform elongation, the calculation of the asymmetric deformation using the BALON2 subroutine is initiated in a corresponding axial cross section. The subroutine uses the nodalization scheme that is independent from the FRAP-T6 and consists of 16 azimuth and 16 axial partitions. The BALON2 predicts the cladding failure when in any element the circumferential stress reaches the local burst stress. It should be noted that both the uniform elongation, and the failure criterion for unirradiated and irradiated Zr-1%Nb claddings were obtained on the basis of experimental studies described in Chapter 6. In this case the local burst stress criterion is not a result of direct measurements, and was obtained under a number of assumptions (the procedure to obtain this criterion is presented in section 6.4.1). After the failure the internal pressure is set equal to the coolant pressure, and further changes in the cladding geometry (and fuel geometry) depend only on the temperature expansion.

From the practical standpoint it is necessary to review two main issues while analyzing this stage of the scenario:

* to estimate reliability of the peak cladding hoop strain prediction;

* to check reliability of the burst temperature and burst pressure prediction.

The first of these issues was actually reviewed in Chapter 5 during the stage dedicated to verification of the FRAP-T6 code. Special burst tests were performed to verify the prediction validity of burst temperatures and pressures. The comparison of experimental and calculated basic parameters of the failure (pressure and temperature) is of interest from the point of view the integral verification of the analytical calculation model and a corresponding failure criterion. Fig. 5.47 shows pressures and temperatures of IGR fuel rod failure, that were predicted by the FRAP-T6, and results of burst tests (see. Chapter 6). For a more adequate comparison, results of burst tests are presented in the form of a region that covers the range of pressure increase rates 0.1 – 1.0 MPa/s. In accordance with calculation estimates, this range of pressurization rates is characteristic for fuel rods tested under IGR/RIA conditions. Moreover, temperatures at the failure time predicted by the main thermal model of the FRAP-T6, that uses the assumption of the axisymmetric temperature field in the fuel rod, were considered as calculated failure temperatures. In this case such an approach to the interpretation of calculation results seems to be justified since conditions of burst tests assumed the azimuth uniformity of the specimen temperature. Therefore, a direct comparison of burst tests results with BALON2 predictions, that are based on the assumption of the cladding failure in the "hot spot", might be not quite adequate.

Thus, as it can be seen in Fig. 5.48, calculated burst pressures are in a good agreement with burst tests results. The chart also shows the predicted peak pressure and temperature of the intact H1T fuel rod cladding, that are below the threshold region. Other intact fuel rods, according to calculations, did not reach the DNB, and corresponding peak parameters are below the failure region obtained in burst tests. The comparative analysis allows to make conclusions on a good reliability of predicting fuel rod cladding failures under IGR/RIA conditions.
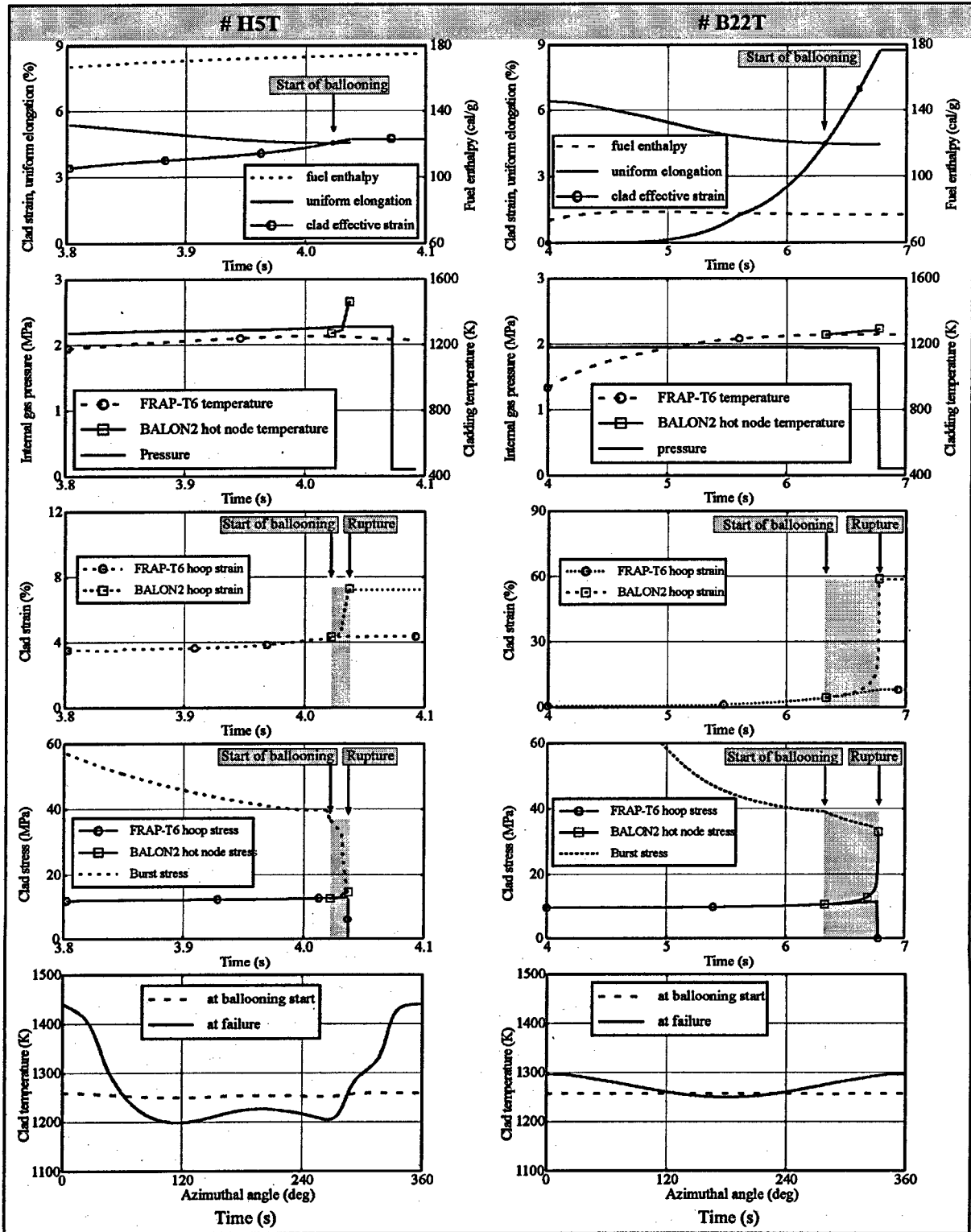
Fig. 5.47. Parameters calculated by FRAP-T6 code for fuel rods ##H5T, B22T vs. time

5.73
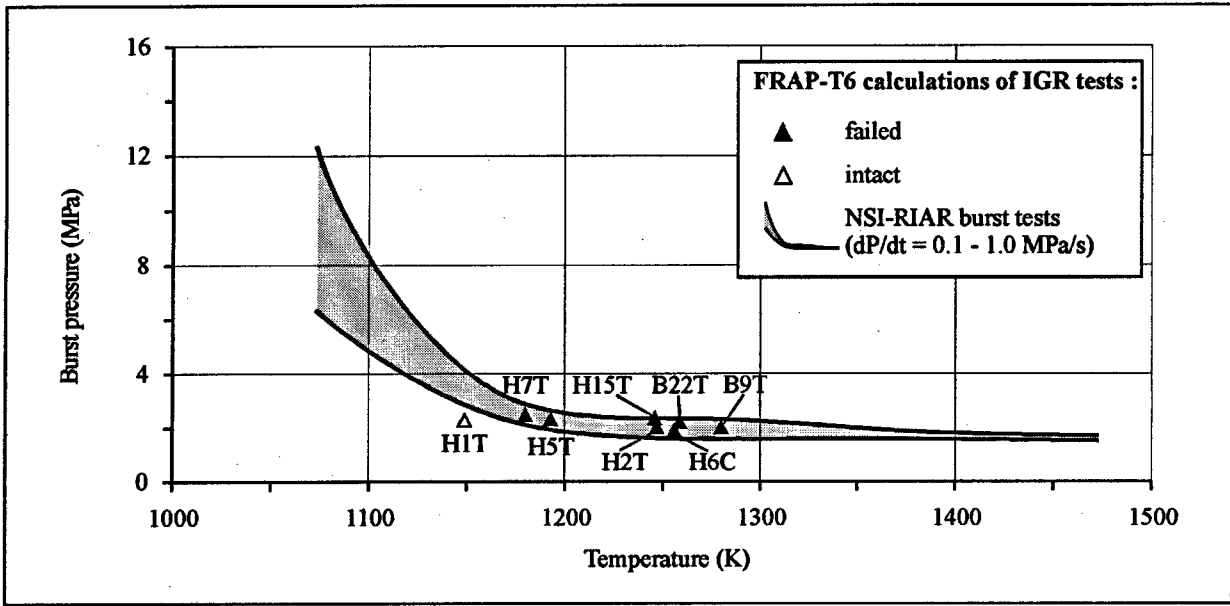
Fig. 5.48. Comparison of FRAP-T6 results with burst test data

5.10.5. Analysis of peak fuel enthalpies at the cladding failure

It is the peak fuel enthalpy that is currently used as the criterion determining failure threshold of fuel rods under RIA conditions. This is the reason why assessment of reliability of this parameter calculation is very important. From the practical standpoint the most important group of the tested VVER fuel rods is the group with the peak fuel enthalpy close to the failure threshold or less than the failure threshold. In this case comparison of the calculated results of the peak fuel enthalpy by the two preliminary verified codes was used as the initial data base for the analysis (Fig. 5.49).

It has already been noted in section 5.10.3 that the differences in some of the models used by FRAP-T6 and SCANAIR codes lead to the situation when FRAP-T6 code somehow overestimates the value of peak fuel enthalpy in comparison with SCANAIR code. Average relative deviation of peak fuel enthalpies calculated by these codes is about 3 %. Further attempts will be made to adjust the code models and to diminish the deviations.
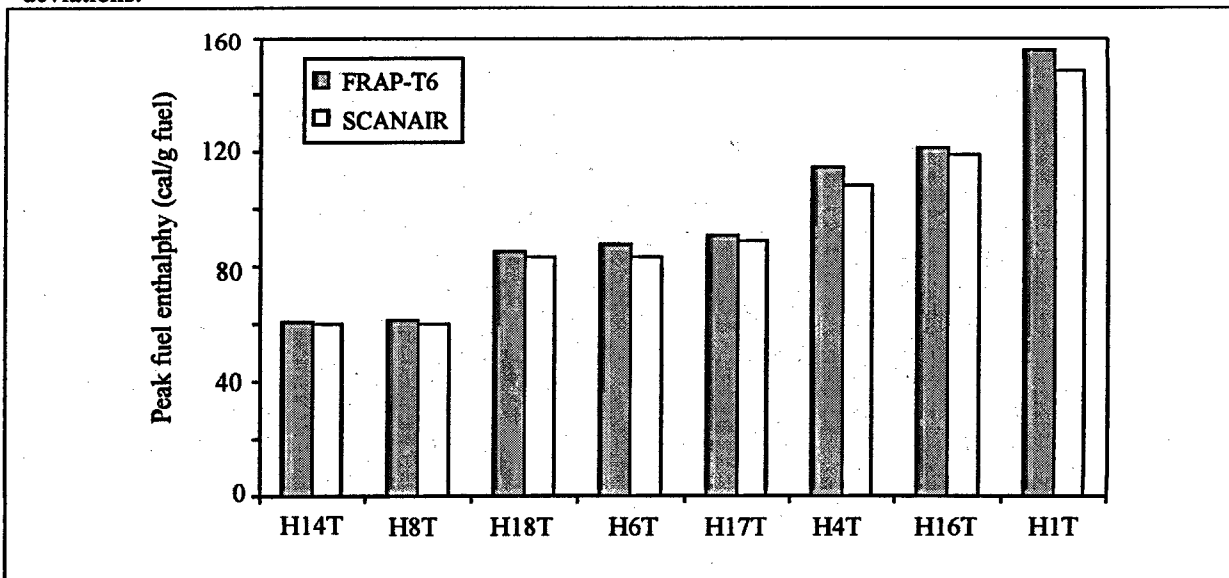
Fig. 5.49. Comparison of peak fuel enthalpies calculated by FRAP-T6 and SCANAIR codes

5.10.6. Analysis of fission gas release calculated by FRAP-T6 and SCANAIR codes.

In the chapter describing verification procedures it is shown that satisfactory agreement of calculated and experimental data on the integral release out of fuel and relative concentration of Xe and Kr in the free volume of the fuel rod, as well as on the pressure inside the fuel rod after irradiation in the cold state was obtained in the regime of pulse heating of fuel. To analyze dependence of Xe and Kr release out of fuel versus temperature on the basis on the results of gas composition inside the cladding, it is necessary to take into account the volume of gas mixture in the fuel rods. For instance, gas volume for fuel rods H8T, H6T, H4T, H1T under normal conditions is 97, 123, 106, 107 cm^3 (Table 5.15). Hence, for interpretation of the calculated and experimental results of fission gas release we will use the absolute and not the relative volume of the released fission gas, considering that experimental fuel rods have reached approximately the same burnup (46 - 49 MW day/kg U).

Fig. 5.50 presents dependencies of calculated and experimental summarized release of Xe and Kr stable isotopes out of fuel into the fuel rod free volume versus the peak enthalpy of fuel rods of 103F series. Experimental data on the fission gas volume converted into normal conditions were obtained due to processing of experimental data listed in Table 5.15. Calculated data were also converted into normal conditions. Analysis has indicated that calculated results are very sensitive to the grain size. Hence, Fig. 5.50 presents the correlations corresponding to the average fuel grain size (6 μm), which was determined in the course of pre-test examination, it also presents the region boundaries for the whole range of the average grain size (4 – 8 μm). It is important to note that distribution of the initial grain size in the fuel is of a bimodal character. Still, FRAP-T6 and SCANAIR codes use the averaged parameters of the grain size. Hence, the range of experimental data on the average initial grain size listed in Table A.1 (Volume 3) was used to calculate sensitivity.

Calculation results indicate that fission gas release in the course of the pulse heating greatly depend on the fuel peak enthalpy (temperature). Peculiar feature in modeling behavior of gas phase in the fuel during its fast heating (up to the melting temperature) is that fission gas release out of fuel is mainly determined by the amount of gas located along the grain boundaries and in the intergranular space. Gas release due to the mechanism of thermo-activation diffusion out of the grain is insignificant. Hence, to calculate fission gas release in the pulse regime it is necessary to know gas distribution in the fuel grains and in the intergranular space by the end of the basic irradiation mode. TOSUREP [11] and FRAP-T6 codes were used to calculate fission gas distribution over the basic irradiation mode. According to calculations by FRAP-T6 and TOSUREP codes some 15 – 20 % of atoms and gas bubbles are localized in the intergranular space by the end of the quasi-state mode of operation of fuel rods.

As it was expected the greatest discrepancy of calculated and experimental results was obtained for the relatively low fuel temperatures, and low values of fission gas release. Along with the growth of the fuel temperature agreement of calculated and experimental results on the fission gas release becomes better. Taking into account complicated mechanism of the described processes, agreement of the calculated and experimental results can be considered satisfactory. Still, it is necessary to note that both FRAP-T6 and SCANAIR codes underestimate fission gas release for IGR pulse mode in the enthalpy range up to 120 cal/g. Similar data were obtained in [13], where experimental data on fission gas release in the fuel rods of TS series (NSRR reactor) were studied. Experimental data were compared with the calculated ones by FRAP-T6 code in the range of fuel peak enthalpy from 60 to 180 cal/g.

Calculated results indicate clear dependence of fission gas release versus fuel temperature. Still, the curve of fission gas release versus peak enthalpy calculated by FRAP-T6 code has more clear dependence versus temperature, than the similar curve obtained by SCANAIR code for low fuel temperatures. This is due to difference in the models of gas release. The model in SCANAIR code predicts fission gas release for lower fuel temperatures than FRAP-T6 model, because it takes into account additional flow of intergranular gas inside the net of interconnected channels due to the temperature drop along the fuel radius. In the future it will be necessary to correct the models of fission gas release to be able to get higher values of integral fission gas release out of the fuel typical for IGR tests.
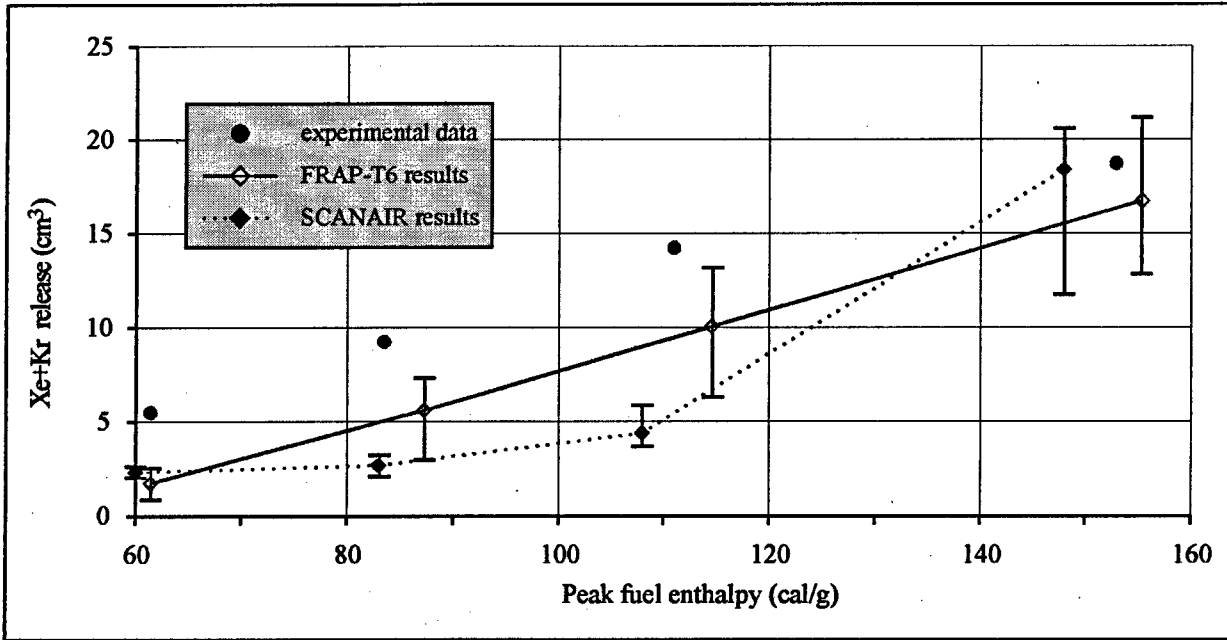
Fig. 5.50. Calculated and measured Xe and Kr volume inside the fuel rod free volume vs. peak fuel enthalpy

Fig. 5.51 presents the results of comparative analysis of fission gas release obtained by FRAP-T6 and SCANAIR codes. Fission gas release is represented as the relative fraction of the volume of the fission gas released out of the fuel to the amount of fission gas generated in the fuel over the basic irradiation mode. Deviations of the calculated data obtained with the change of initial grain size – 4-8 μm are also presented there. SCANAIR calculation results were obtained for the tight fuel rods only (H1T, H4T, H6T, H8T), because calculation of behavior of fuel rods with higher peak enthalpies is beyond the capabilities of the code.
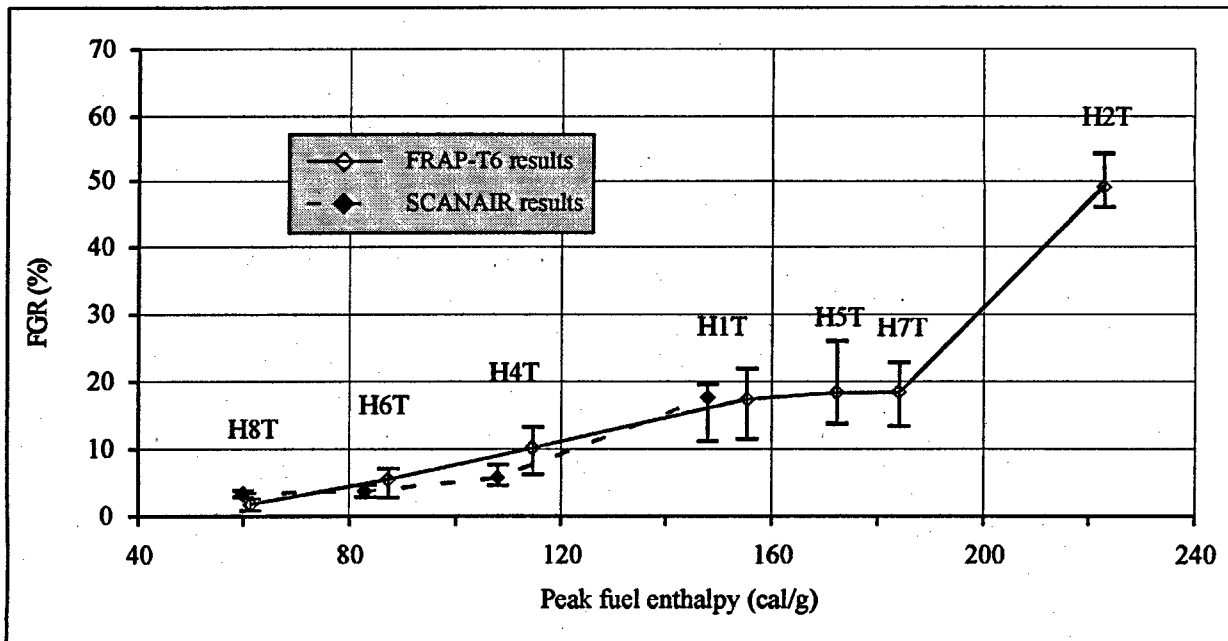
Fig. 5.51. Comparison of the FRAP-T6 and SCANAIR results on FGR for IGR fuel rods

A little lower gas release was predicted for H7T fuel rod than for the H5T one despite the higher peak enthalpy. This in particular can be explained by the higher burnup of the fuel of H5T fuel rod (49 MW d/kg U) if compared to H7T fuel rod (47 MW d/kg U). Still, the difference in the calculated data is sufficiently small, and is within the corridor of deviations caused by the difference in the technological parameter. Abrupt increase of the fission gas release in H2T fuel rod is caused by the fact that the fuel temperature has reached the melting point; for this situation 7 % of the pellet's melted area was predicted.

It should be noted that description of the main mechanisms of fission product behavior in fuel, implemented in the above models, indicated that it is necessary to know physical and technological parameters of fuel, micro constants of the irradiated grain, diffusion parameters of gas bubbles, etc. in order to determine fission gas release. This set of parameters is not usually clearly determined and has a significant spread. That is why calculation of behavior of the gas phase in the fuel is based on some effective (averaged) value of this or that parameter, which does not necessarily lead to the adequate description of the gas circulation and release. Besides, this can introduce uncertainty into the calculated value of fission gas release. Hence, analysis of sensitivity of the data on fission gas release to the initial grain size of the fuel matrix was performed to demonstrate potential uncertainty of the calculated data.

Sensitivity analysis of the calculated fission gas release versus grain size indicated that the value of the calculated fission gas release could change up to 1.5 times in the range of the specified grain diameters – 4-8 μm. This testifies to great uncertainty in predicting gas release out of fuel, and to the influence of the fuel technological parameters onto calculated results. While reviewing the behavior of the full-scale burnt fuel element, it is necessary to note that even in case of low values of the fission gas release (~10 %) its contribution into the pressure under the cladding can be very sufficient. In case of the maximum burnup of ~50 MW d/kg U, approximately 1800 cm^3 if converted to normal conditions are generated in the fuel element of the VVER reactor. Initial concentration of the technological gas (He) is approximately 640 cm^3 (n.c.). If over the period of an accident some ~10 % of the fission gas is released (180 cm^3), then the pressure inside the fuel element will increase by the following value: $180/640 \approx 0.3$ (~ 30 %).

Hence, analysis of the calculated results allowed to make the following conclusions:

- Both codes underestimate fission gas release in the range of fuel peak enthalpies up to 120 cal/g. In the future it is necessary to correct the models of fission gas release in order to get higher values for the integral fission gas release out of the fuel in this range of peak enthalpies;

- Experimental results indicate practically linear increase of the fission gas release versus fuel enthalpy. Calculated results obtained by FRAP-T6 code have the similar trend. Calculated curve obtained by SCANAIR code shows exponential dependence versus temperature. The greatest discrepancy of the calculated and experimental results is in the range of the fuel peak enthalpies up to 120 cal/g;

- Sensitivity analysis has indicated significant uncertainty in predicting gas release out of the fuel depending on the initial grain size.

5.11. References

[1] L. Siefken, Ch. Allison, M. Bohn, S. Peck "FRAP-T6: Computer Code for the Transient Analysis of Oxide Fuel Rods" *NUREG/CR-2148 EGG-2104, May 1981.*

[2] F. Lamare, J.C. Latche, "SCANAIR. A Computer Code for Reactivity Initiated Accidents in LWRs", *Rapport Technique SEMAR 95/01*

[3] D.L. Hagrman, G. A. Reymann, R.E. Mason "MATPRO-Version II (revision 1): A Handbook of Material Properties for Use in the Analysis of Light Water Reactor Fuel Rod Behavior", *NUREG/CR-0497 TREE-1280, Rev I, February 1980.*

[4] V.E. Ljusternik, V.E. Peletski, I.I Petrova. "Experimental research of zirconium reactor materials thermal properties. E-IIO alloy" *M., J. High Temperature Thermal Physics. v. 31, N4, 1993.*

[5] B.Yu.Volkov et. al. Material property library for H-1 alloy cladding, Report IAE-4941/11, 1989 (rus).

[6] G.P.Kobyliansky, A.N.Novoselov, "Behavior of Zirconium and Its Alloys under irradiation. Guide Book on Reactor Materials". Edited by V.A.Tsycanov. GNC RF NIIAR, Dimitrovgrad, 1996 (rus).

[7] N.B. Sokolov et. al. "Kinetics of interaction between VVER core materials" (Recommendations for application in the frame of International Standard Problem on CORA-W2 experiment), *Report ASRIIM. N8068. October 1993* (rus).

[8] Material properties of VVER-1000 fuel rod clad and pellet. State Committee on Atomic Energy, *1983* (rus).

[9] V.I. Kolyadin et. al. Heat conductance of uranium dioxide. *Journal Atomnaya energiya, 1974, v. 36(3), p. 59* (rus).

[10] A.S. Scheglov et. al. Simulation of VVER-440 high burnup fuel rod behavior (on example of the 3-th unit of Cola NPP), *Journal Atomnaya energiya, 1996, v. 81(4), p. 254-261* (rus).

[11] F. Lemoine, TOSUREP Documentation, *Note Technique SEMAR 97/43, May 1997.*

[12] G.A. Berna, M.P. Bohn, W.N. Rausch, R.W. Williford, and D.D. Lanning. "FRAPCON-2: A Computer Code for the Calculation of Steady State Thermal-Mechanical Behavior of Oxide Fuel Rods". *NUREG/CR-1845 (January 1981).*

[13] T. Nakamura, M. Yoshinaga, Boiling Water reactor fuel behavior at burnup of 26 GWd/tonne U under reactivity-initiated accident conditions. *J. Nuclear Technology v.108(1), 1994.*

[14] T. Fujishiro, K. Ishijima, NSRR experiments to study the effects of burnup on the fuel behavior under reactivity-initiated accident conditions, *Trans. of 22-nd Water Reactor Safety Information Meeting, Bethesda, Maryland, USA, October 24-26.1994.*

[15] M.A.Vostrikov, B.P.Kochurov. "TRIFOB - The Code for Calculation of Isotopic Composition Changes in a Cylindrical Reactor Cell Taking into Account Neutron Spatial-Energy Distribution", *Report, ITEP-106, Moscow, 1981.*

[16] SCDAP/RELAP5/MOD3.1 Code Manual. *NUREG/CR-6150 EGG-2720, 1993.*

[17] *"GE SBWR Preliminary stability analysis using TRAC-BFI time domain code" ANS transaction. New Orlean. June 19-23, 1994.*

[18] A. Bromley, "Heat Transfer in Stable Film Boiling" *Chemical Engineering Progress. 46. (1950) pp. 221-227.*

[19] A. Labuntzov. *Teploenergetika. 12 (1959). pp. 19-26* (rus).

[20] V.P. Isachenko, V.A. Osipova, A.S. Sukomel Heat Transfer. - *M. Energoizdat, 1981* (rus).

[21] S.S. Kutateladze. Fundamentals of Heat Transfer Theory, *M., Atomizdat, 1979* (rus).

[22] PIN-micro: User's Guide for the Computer Code, *1991, Rez UIV-9515-T.*

[23] F.W. Dittus, L.M.K. Boelter, "Heat Transfer in Automobile Radiators of the Tubular Type", *University of California Publications, 2 (1930) pp. 443-461.*

[24] C. Chen, "A Correlation for Boiling Heat Transfer to Saturated Fluids in Convective Flow", *Process Design Development. 5. (1966) pp 322-327*

[25] G.N. Poletaev "Analytical equations for approximate analysis of fuel rod rewetting in reactivity initiated accidents", *Report IAE-6090/5, 1998.*

[26] C.L.Tien and L.S.Yao, Analysis of conduction-controlled rewetting of a vertical surface, *J. Heat Transfer 97, 161-165 (1975).*

[27] J.G.M.Andersen and P.Hansen, Two dimensional heat conduction in rewetting phenomenon. Report No NORHAV-D-6. *Danish Atomic Energy Comission Research Establishment, Riso, Denmark, (1974).*

[28] S.S.Dua and C.L.Tien. A generalized two-parameter relation for conduction-controlled rewetting of a hot vertical surface, Int.J. Heat Mass Transfer, vol.20, pp. 174-176.

[29] D.C. Groenveld, J.C. Stewart, "The Minimum Film Boiling Temperature for Water During Film Boiling Collapse", *Proc. VII Internat. Heat Transfer Conf. Munich. 1982. Vol. 5 (1982). p. 393*

[30] J.R.S. Thom et. al. "Boiling in Subcooled Water During Flow Up Heated Tubes or Annuli" *Proceedings Instrumentation of Mechanical Engineers. (London). 180 (Part 30 (1966) pp. 226-246.*

[31] K. Lassmann, et. al., "Transuranus Calculation on Experimental VVER Fuel Rod", *Proceedings of the Second Int. Seminar VVER Reactor Fuel Performance Modeling and Experimental Support, pp. 156-161, April 1997, Bulgaria.*

[32] P.L. Kirillov, Yu.S. Yuryev, V.P. Bobkov. Thermohydraulic Analysis Handbook (Nuclear Reactors, Heat Exchangers, Steam Generators). *-M., Energoatomizdat, 1990* (rus).

[33] P.G. Lucuta, H. Matzke, R.A. Verrall, H.A. Tasman Thermal conductivity of SIMFUEL. *J. Nucl. Mater., v. 188, p. 198-204. 1992.*

[34] P.G. Lucuta, H. Matzke, R.A. Verrall Modelling of UO_2 based SIMFUEL thermal conductivity. The effect of the burnup. *J. Nucl. Mater. v.217, p.279-286. 1994.*

[35] H.M. Chung and T.F. Kassner, *Deformation Characteristics of Zircaloy Cladding in Vacuum and Steam Under Transient-Heating Conditions: Summary Report,* NUREG/CR-0344, ANL-77-31, July 1978.

[36] K.Wiehr, F.J. Erbacher and H.J. Neitzel, *Influence of Thermohydraulics on Fuel Rod Behavior in a LOCA,* Proceedings of the CSNI Specialist Meeting on Safety Aspects of Fuel Behavior in Off-normal and Accident Conditions, Helsinki, Finland (1980) 59-73.

[37] A.Shestopalov, K.Lioutov, L.Yegorova, G.Abyshov, K.Mikitiouk, *Modification of US NRC's FRAP-T6 Fuel Rod Transient Code for High Burnup VVER Fuel,* Report of RRC "KI", RRC KI 2180, 1999.

[38] K.Mikitiouk, A.Shestopalov, K.Lioutov, L.Yegorova, G.Abyshov, *Modification of IPSN's SCANAIR Fuel Rod Transient Code for High Burnup VVER Fuel,* Report of RRC "KI", RRC KI 2181, 1999.

[39] L. Yegorova et. al. "Analysis of capsule dynamic tests with VVER fuel rods at IGR and GIDRA reactors", *Report of RRC "Kurchatov Institute", N 30/694186, Moscow, 1986* (rus.).

6. TEST PROCEDURES TO OBTAIN THE MECHANICAL PROPERTIES OF ZR-1%NB CLADDING AND DEVELOPMENT OF THE ORIGINAL INPUT DATA FOR MATPRO-V11 AND SCANAIR CODES

6.1. Formulation of the problem

It is important to stress that in the framework of the research work presented in this report there was never an objective to get the universal data base characterizing mechanical properties of the VVER cladding as the function of the manufacture technology, basic irradiation conditions, and accident conditions. Development of this program in order to study mechanical properties of the VVER cladding is based on the approach, which can be characterized by the following provisions:

1. Analysis of specific features of unirradiated and irradiated Zr-1%Nb cladding is to be preliminary performed and the results of this analysis are to be considered in the course of the program development in order to measure mechanical properties of Zr-1%Nb cladding.

2. Assessment of MATPRO and SCANAIR data bases with mechanical properties of PWR claddings is to be done and used in order to define the set of requirements to the data base with the original mechanical properties of Zr-1%Nb cladding.

3. There should be enough measured mechanical properties of Zr-1%Nb cladding in order to be able to use FRAP-T6 and SCANAIR codes for the development of computational data base characterizing VVER fuel rod behavior under IGR test conditions.

The complex of research was performed for each of above items. Results of the work are presented in succession in the respective sections.

6.1.1. Peculiarity analysis of unirradiated VVER claddings

Zr-1%Nb alloy is used for the claddings of fuel elements of the VVER reactor type. The data listed in Table 6.1 allow to compare chemical compositions of VVER and PWR zirconium alloys [1].

Table 6.1. Concentration of doping elements in zirconium alloys

Doping element (% by weight)	Type of alloy		
	Zr-1%Nb	Zry-2	Zry-4
Nb	0.9–1.1	–	–
Sn	–	1.5	1.5
Fe	0.05	0.15	0.2
Cr	0.02	0.1	0.1
Ni	0.05	0.007	0.007
Fe+Cr+Ni	0.12	up to 0.3	up to 0.3
O_2	0.11	0.1–0.14	0.1–0.14

Comparative analysis of those compositions allows to see that the difference of two types of the claddings from the standpoint of their chemical compositions is that niobium was chosen as the basic element for doping of zirconium in the alloy for VVER reactors, and tin was the element used for the same purpose in PWR reactors. The purpose of doping in both cases was the desire to improve strength and corrosion parameters of the fuel element claddings. The choice of Zr-1%Nb alloy as the cladding material for VVER reactors was caused by the fact that Zr-1%Nb alloy just slightly yields to Zry-2 alloy in the sense of corrosion when oxidized in the pure water and steam, but in this case Zr-1%Nb alloy absorbs 5-10 times less hydrogen generated when the cladding is oxidized by water [1].

Currently the tubes manufactured of zirconium fabricated by the electrolysis method are used for the VVER claddings. Cladding tubes are manufactured by the rolling method, after that they are subject to thermal processing. Annealing of the VVER tubes is done under the temperature of 580°C within 3 hours. This process leads to complete recrystallization of the tube material. At the same time cladding tubes of the PWR reactors are annealed till the state of partial recrystallization.

Procedure of the chemical etching and anodizing of the fuel claddings is the last stage of the technological cycle for the VVER fuel elements. The objective of this procedure is to remove the impurities and to make the protective 1-3 μm thick ZrO_2 layer.

The whole complex of differences in the chemical composition and in manufacture of VVER and PWR claddings results in the differences of the initial mechanical properties of fresh claddings. It is necessary to note that both here and after only short-term mechanical properties are considered, because these are the properties important to interpret IGR/RIA tests. Fig. 6.1 illustrates the difference of properties of unirradiated Zr-1%Nb and Zry as the function of temperature.
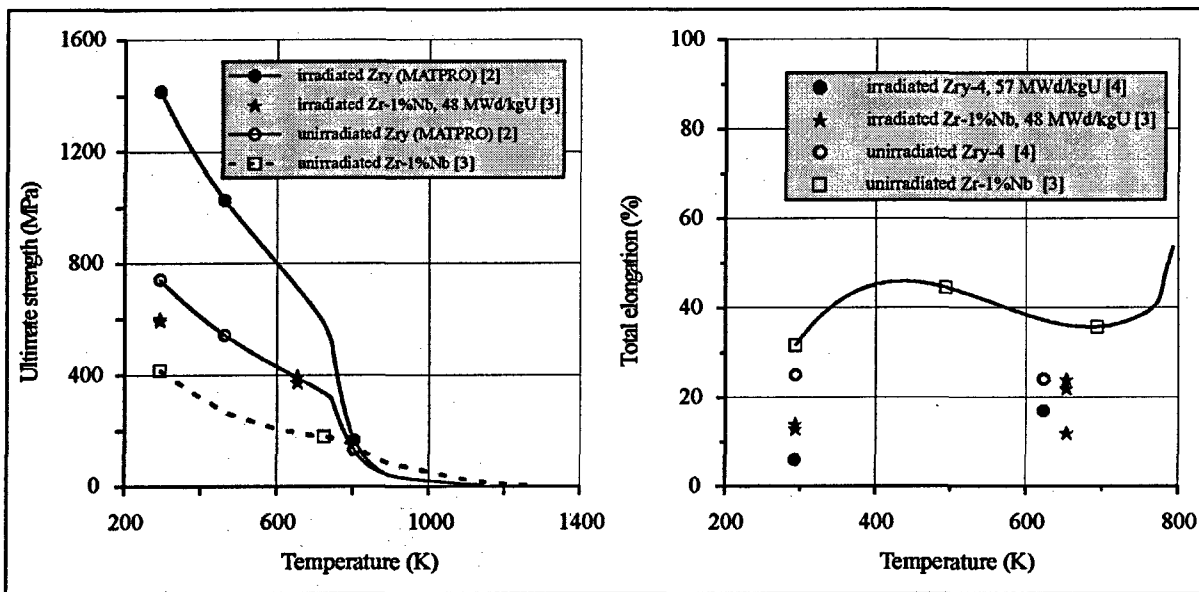
Fig. 6.1. Mechanical properties of Zry-4 and Zr-1%Nb vs. temperature

Analysis of the data presented in Fig. 6.1 allows to make the following conclusions:

- difference between the absolute values of mechanical properties of these alloys decreases along with the temperature growth;

- both alloys have similar tendencies of the change of properties as the function of temperature.

In other words, general character of dependencies of mechanical properties versus temperature is determined by zirconium properties. Doping elements and manufacture technologies influence the absolute values and define the bending points of the presented curves. Analysis of the total influence of the physical phenomena, which cause similarity and difference in mechanical properties of two types of the claddings, leads to the necessity of review of the following separate effects in order to understand their influence onto mechanical properties:

- temperature;

- strain rate;

- oxygen concentration in cladding;

- mechanical anisotropy;

- dynamic strain aging;
- annealing;
- phase transformation and superplasticity.

Mechanical properties vs. temperature and strain rate

Data presented in Fig. 6.1 indicate that knowledge of the dependencies of mechanical properties versus temperature is the most important part for the respective data base, because strength of all Zr alloys decreases abruptly along with the temperature growth. Besides, analysis of the temperature dependencies for strength and ductility of the material indicates that worsening of strength and increase of ductility are not monotonic temperature functions. Hence in order to get the data base describing those parameters with good accuracy it is necessary to correctly select the pitch of the temperature variations.

Strain rate is a separate issue when the data base on mechanical properties intended to analyze fuel rod behavior under RIA conditions is reviewed. Unfortunately, there exists very little published data in order to characterize this aspect of the problem.

It is considered that zirconium alloys are very sensitive to the change of strain rate. In case of strain rate increase strength properties are improved, but the plastic ones decrease greatly. Measurements of dependence of strength and elongation versus strain rate in the axial direction indicated that the change of cross-head velocity from 1 mm/min to 16 mm/min leads to the decrease of the total elongation of Zr-1%Nb alloy by 10 – 12 %, in this case ultimate strength increases by approximately 9 %, main change of the alloy properties being in the interval 1 – 8 mm/min. It is also noted that for cross-direction tests strain rate increase leads to increase of the yield stress and ultimate strength, total elongation in this case does not change [1].

Oxygen concentration in the cladding

Presence of small amount of oxygen in zirconium alloys leads generally to the improvement of their strength, while good plastic properties are preserved. That is why oxygen was considered as the doping element for Zr-1%Nb alloy [1]. Table 6.2 lists the respective data characterizing oxygen influence onto mechanical properties of Zr-1%Nb VVER tubes.

Table 6.2. Mechanical properties of VVER tubes vs. oxygen concentration at 20°C [1]

Oxygen concentration (%)	Ultimate strength (MPa)		Yield stress (MPa)		Total elongation (%)	
	Axial direction	Cross direction	Axial direction	Cross direction	Axial direction	Cross direction
0.05	400 – 430	350 – 360	240 – 270	290 – 310	45 – 50	35 – 38
0.13	520 – 530	–	330 – 350	–	40 – 42	–

Comparison of the data listed in Table 6.2 indicates that the oxygen influence onto mechanical properties of Zr-1%Nb is approximately the same as for Zircaloy (fully recrystallized state of tubes) [1].

Analysis of these and other published results shows that strength parameters depend a lot on the oxygen concentration, hence this factor is to be considered when measuring mechanical properties of specific claddings.

Anisotropy of zirconium alloys

It is well known that mechanical properties of materials can significantly differ depending on the direction of measurement of these properties. This phenomenon is known as anisotropy of mechanical properties. Zirconium is a typical example of an anisotropic material. Technology of fabrication of zirconium items influences the material texture and this also influences differences in mechanical behavior for axial and cross-directions. α-phase is the basis for Zr-1%Nb alloy, that makes the alloy closer to zirconium from the standpoint of the texture and anisotropy [1]. It is important to note that plastic deformation of α-zirconium occurs in two different ways depending on the crystal axis to which the load is applied. In one case the deformation takes place by slipping, in the other case - by twinning [1]. VVER tube texture is such that its axial tension occurs mainly by slipping. Cross-tension leads to the situation, when part of the grains is

deformed by slipping, and part – by twinning. These differences result in differences in yield stress for different directions. Yield stress in the cross-direction exceeds significantly the yield stress in the axial direction. Other results characterize ultimate strength. Analysis indicates that the stage of necking and burst is characterized by the fact that the slip mechanism of strain is the main one for the material tension in both axial and cross- directions. That is why ultimate strength depends less on the direction. Study of the influence of anisotropy onto the material elongation parameters is a separate problem. In the work [1] it is shown that the results of measurement of the relative elongation, done in the cross- and axial directions, are not only the function of the property anisotropy, but of the test conditions as well. That is why we should treat interpretation of experimental data characterizing material elongation ratio in the axial and cross-directions very carefully. That is why in order to assess anisotropy parameters for Zr-1%Nb alloy Table 6.3 lists only the parameters of the alloy strength.

Table 6.3. Parameters of mechanical anisotropy for Zr-1%Nb alloy [1]

Material	Temperature of test (°C)			
	20		350 – 380	
	$K_B = \dfrac{\sigma_B^{\theta} \; ^{1)}}{\sigma_B^{z}}$	$K_{0.2} = \dfrac{\sigma_{0.2}^{\theta} \; ^{2)}}{\sigma_{0.2}^{z}}$	$K_B = \dfrac{\sigma_B^{\theta}}{\sigma_B^{z}}$	$K_{0.2} = \dfrac{\sigma_{0.2}^{\theta}}{\sigma_{0.2}^{z}}$
Zr-1%Nb tube for VVER reactor	0.9	1.33 – 1.38	0.95	1.5 – 1.7

[1) $\sigma_B^{\theta}, \sigma_B^{z}$ - ultimate strengths in the cross- and axial directions, respectively;

2) $\sigma_{0.2}^{\theta}, \sigma_{0.2}^{z}$ - yield stresses in cross- and axial directions, respectively.

The data listed in Table 6.3 indicate that anisotropy of Zr-1%Nb alloy is to be certainly considered for the calculations of the fuel rod deformation.

Dynamic strain aging

Dynamic strain aging is an important phenomenon influencing the profile of strength parameters versus temperature. For zirconium alloys this phenomenon is determined by the fact that in the certain temperature range atoms of gas impurities, such as oxygen atoms, start preventing dislocation movement [5]. In this case stabilization of the material strength parameters versus temperature occurs, and worsening of the material parameters characterizing its elongation. This effect disappears completely as the temperature increases further (see Fig. 6.2).

This phenomenon was registered for both Zr-1%Nb alloy and Zircaloy. Quantitative parameters of the dynamic strain aging depend on the great number of factors and according to the published data this effect is most vividly revealed in the range of 440 – 770 K [6, 7].

Annealing

Heat treatment of the cladding tubes determines greatly their mechanical properties. Annealing is the main kind of heat treatment of the cladding tubes for both VVER and PWR reactors.

Material recrystallization takes place during the process of annealing, this leads to better plasticity and worsening of strength. It was mentioned above that cladding tubes for VVER reactors are delivered in the fully recrystallized state (T = 580 K, t = 3 hours), at the same time Zry tubes are manufactured differently; tubes in the partially recrystallized state are used most often. That is why it is always important to remember that mechanical properties for one and the same material can differ greatly depending on the annealing procedure.
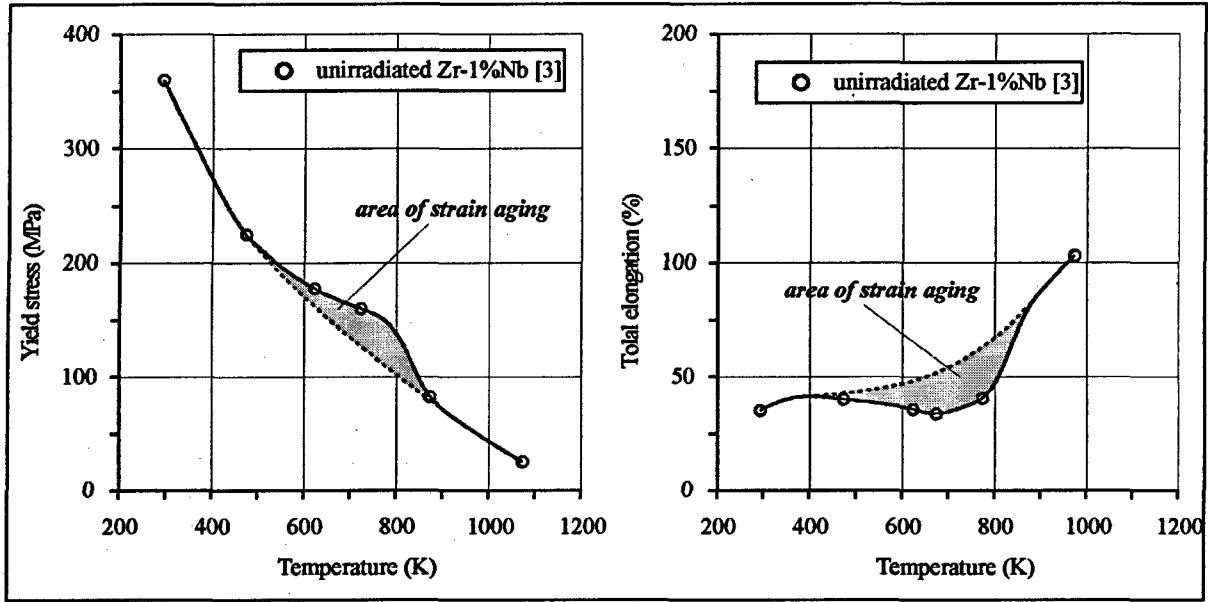
Fig. 6.2. Demonstration of dynamic strain aging effect for Zr-1%Nb alloy

Phase transformation and superplasticity

Zirconium and its alloys are allotropic materials. Low temperature α-phase has a hexagonal lattice. As the temperature increases phase transformation point is reached and the material is transformed into β–phase, which is characterized by the cubic volumetrically centralized lattice. Phase transformation for zirconium takes place when the temperature reaches 1135 K. Presence of impurities in zirconium alloys leads to the situation when two zirconium phases are present in the certain temperature range. At the bottom boundary of this range all the material is in the α–phase, and starting with the top boundary of this range the material is in β–phase, respectively (see Table 6.4). Impurities present in the alloys are responsible for the stabilization of α– and β–phases in the transition temperature range, which is not typical for pure zirconium [8].

Table 6.4. Parameters of allotropic transformation for Zry and Zr-1%Nb alloys

Parameter	Temperature (K)		
	Zr [1]	Zr-1%Nb [1]	Zry [8]
Initiation of α–β transformation	1135	883	1090
End of α–β transformation	1135	1163	1255

Phase transformation of zirconium alloys has an important effect on mechanical property. In particular abnormal change of elongation of these materials was observed in the number of tests [8, 1, 9]. Due to this effect known as the effect of superplasticity relative elongation up to 200 % was registered in the tests. Still detailed study of this phenomenon has not been arranged yet, despite the potential importance of this effect from the standpoint of mechanical behavior of the fuel claddings under accident conditions.

6.1.2. Analysis of peculiarities of irradiated VVER cladding

Experimental studies performed in order to validate the data base with mechanical properties of irradiated zirconium alloys has indicated that irradiation under reactor conditions leads to improvement of strength and worsening of ductility of the fuel rod claddings. Combination of the following main phenomena leads to those results:

- radiation damage and micro-doping with transmutants;
- corrosion;

- hydrating.

The works performed earlier in order to study the influence of irradiation onto mechanical properties of the fuel claddings lead to the fact that fluence of fast neutrons was generally used as the key parameter. Fig. 6.3 presents the data characterizing influence of irradiation onto mechanical properties of the fully recrystallized Zry-4.
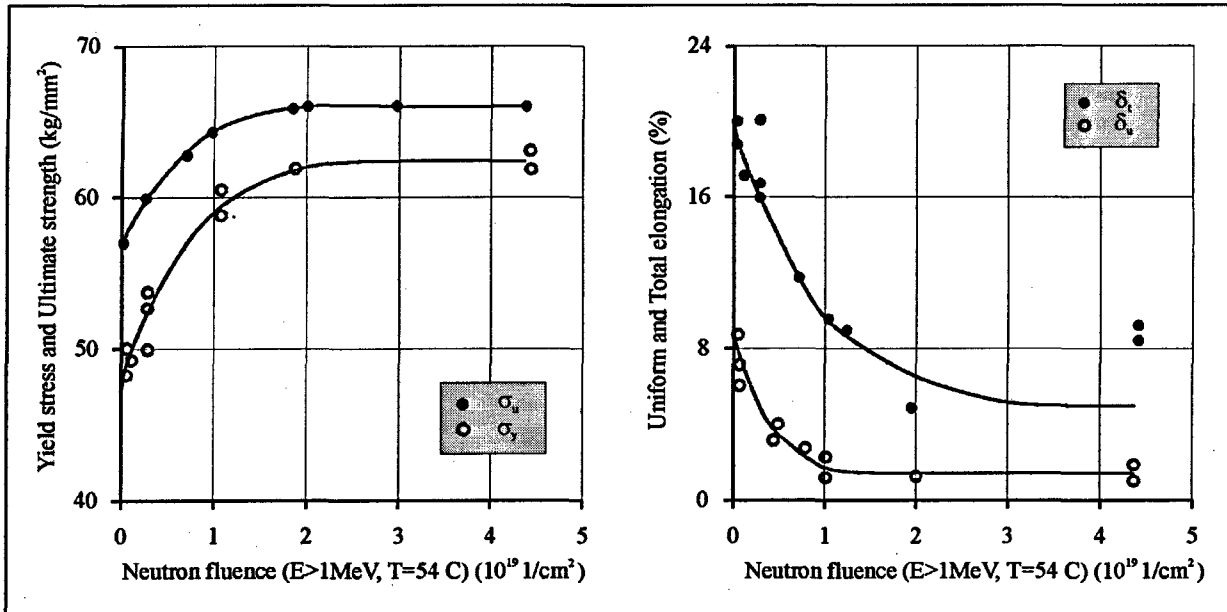
Fig. 6.3. Mechanical properties of Zry-4 vs. neutron fluence [1]

The presented data allow to assess the scope of effects connected with improvement of the material strength and worsening of its ductility in the process of irradiation. Besides, the data demonstrate that all the radiation effects are formed quickly enough, i.e. strength parameters change insignificantly after the neutron fluence reaches 10^{19} n/cm^2.

Research performed with Zr-1%Nb alloy allowed to find out that the transition process characterizing the change of Zr-1%Nb mechanical properties as the function of irradiation under the temperature 300-400°C takes place quickly. Comparative tests indicated that mechanical properties of the claddings tested in MR research reactor (RRC KI) up to the fluence of 10^{20} l/cm^2 (E>0.5 MeV) and mechanical properties of the claddings of commercial fuel elements irradiated at NV NPP up to 10^{22} l/cm^2 (E>0.5 MeV) do not practically vary [10, 11].

It is worth to review the two effects mentioned above in connection with the analysis of the irradiation impact onto mechanical properties:

- dynamic strain aging;
- annealing of irradiation damages.

It was shown in section 6.1.1 that the dynamic strain aging effect is present in the certain temperature range, this effect being valid for both Zry and Zr-1%Nb alloys. The research indicated that irradiation either suppresses this effect, or reduces it significantly, because interstitial atoms of oxygen are captured by radiation defects [5].

Annealing of irradiation damages is the other effect, which is very important for development of the data base with mechanical properties of irradiated claddings vs. temperature. This is the data base, which allows to analyze behavior of fuel elements under accident conditions.

The numerous tests allowed to state that initial mechanical properties of the alloy are recovered if the irradiated claddings are heated up to the temperature higher than 800 K. The rate of this process is the function of temperature and time and can be described by the corresponding equation [12]. Fig. 6.4 presents the set of solutions for this equation for Zry-2 alloy.
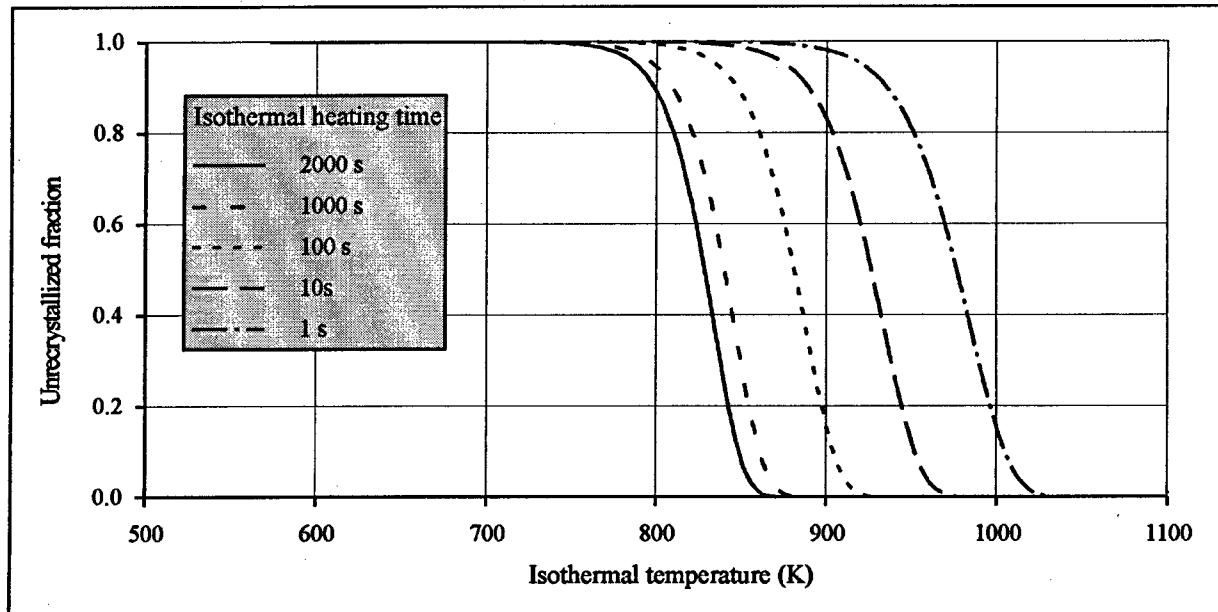
Fig. 6.4. Recrystallization rate of Zry-2 vs. temperature

Study of the influence of irradiation annealing onto Zr-1%Nb alloy has revealed approximately the same effects. Annealing of the irradiated material under the temperature of 600°C allows to recover its mechanical properties, so that they become the same as of the unirradiated material [1].

The above listed effects do not complete the list of phenomena which worsen the mechanical properties of the fuel claddings in the process of their irradiation in the commercial reactor. Oxidizing and hydrating of the claddings is to be reviewed separately in order to have complete information about those processes.

Oxidation of fuel claddings takes place over the fuel cycles as the result of chemical interaction of the fuel claddings and water coolant. This process results in the formation of ZrO_2 layer on the surface of the claddings and to the increase of oxygen concentration in the cladding material. It was noted in section 6.1.1 that reasonable oxygen concentration in the cladding is the useful factor, and oxygen is specially planned by the technological process as the doping element. Still, further increase of the oxygen concentration leads to embrittlement of the fuel claddings. Currently there exist no published data characterizing the influence of this effect onto the irradiated claddings, still certain conclusions can be made about the importance of this phenomenon on the basis of the analysis of results obtained for irradiated Zr-1%Nb tubes. Tube specimens were preliminary oxidized, then cut down, and the mechanical properties of them were determined in the cross-direction. Fig. 6.5 presents the results characterizing dependence of total elongation vs. temperature and weight gain of oxygen [13].

Hydrating of fuel claddings is another important effect, which is capable to influence mechanical properties of the claddings under irradiation. The reaction of zirconium oxidation in the water coolant is the source of hydrogen, which causes hydration of the cladding. Under the operating temperature hydrogen is present in the claddings partially in the form of solid solution and partially in the form of hydrides. Under normal conditions the total amount of absorbed hydrogen is in the form of hydrides. Hydride inclusions oriented along the cladding radius can provoke crack propagation, especially under low temperatures. On the whole, hydrating of the claddings of all zirconium alloys leads to improvement of strength and to worsening of ductility. This effect is significantly reduced if the temperature increases, but it is not fully eliminated under high concentrations of hydrogen (Fig. 6.6) [1]. It is also important to note that the presence of the temperature gradient at the fuel claddings leads to the situation that the major part of hydrides is concentrated on the outer surface of the cladding. This annular hydride layer influences the embrittlement of the cladding more actively than in case there takes place uniform hydrating of the cladding.
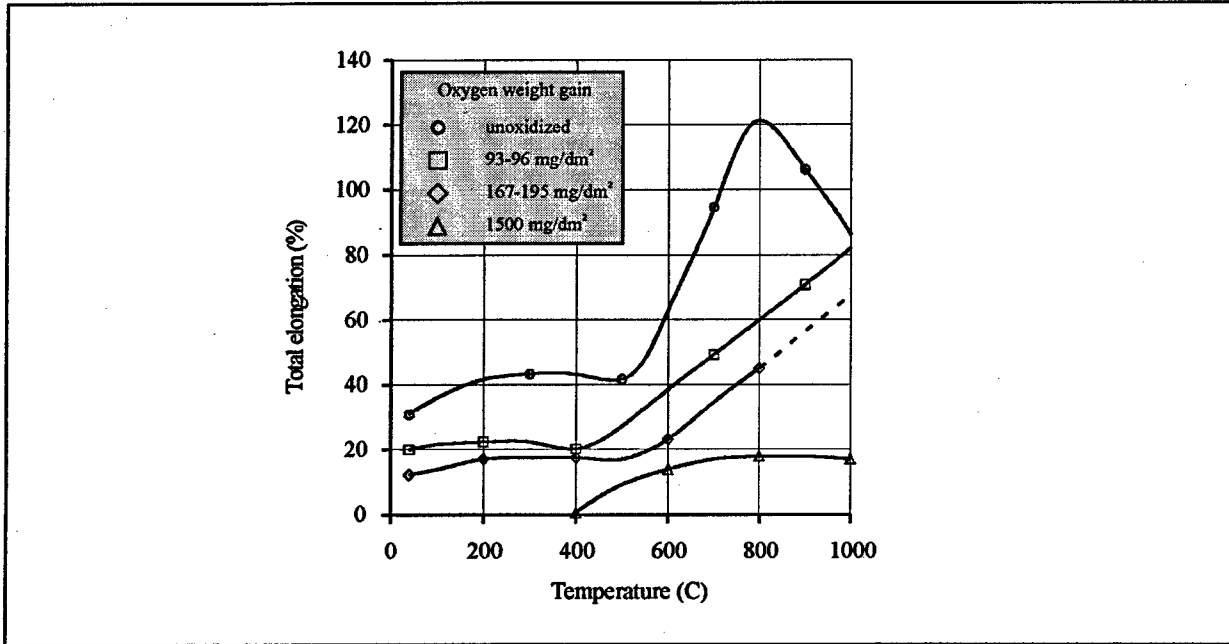
Fig. 6.5. Total elongation of Zr-1%Nb specimens vs. temperature and oxygen weight gain
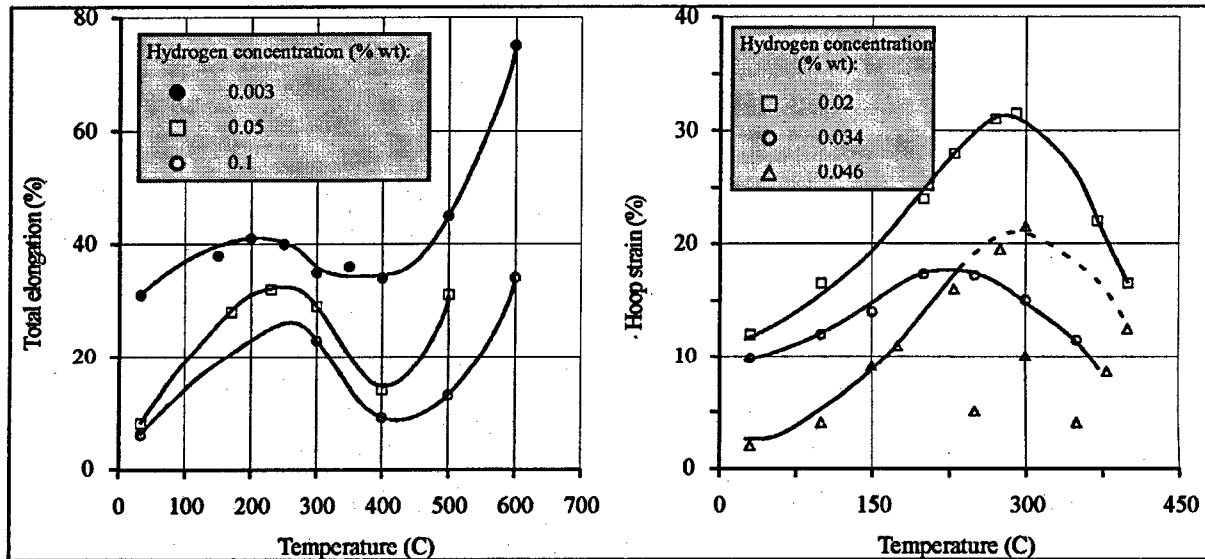
Fig. 6.6. Total elongation of Zr-1%Nb alloy (a) and hoop strain of pressurized zircaloy tubes (b) vs. hydrogen concentration and temperature

Hydride orientation is another principal issue to understand the influence of hydrogen onto the mechanical properties of claddings. It has already been noted that radial oriented hydrides significantly reduce the cladding ductility. This effect can be described with the help of the hydride orientation coefficient F_n, which is identified as the ratio of the amount of radial oriented hydrides to their total amount. Fig. 6.7 illustrates this effect for unirradiated Zr-1%Nb tubes [1].

6.8
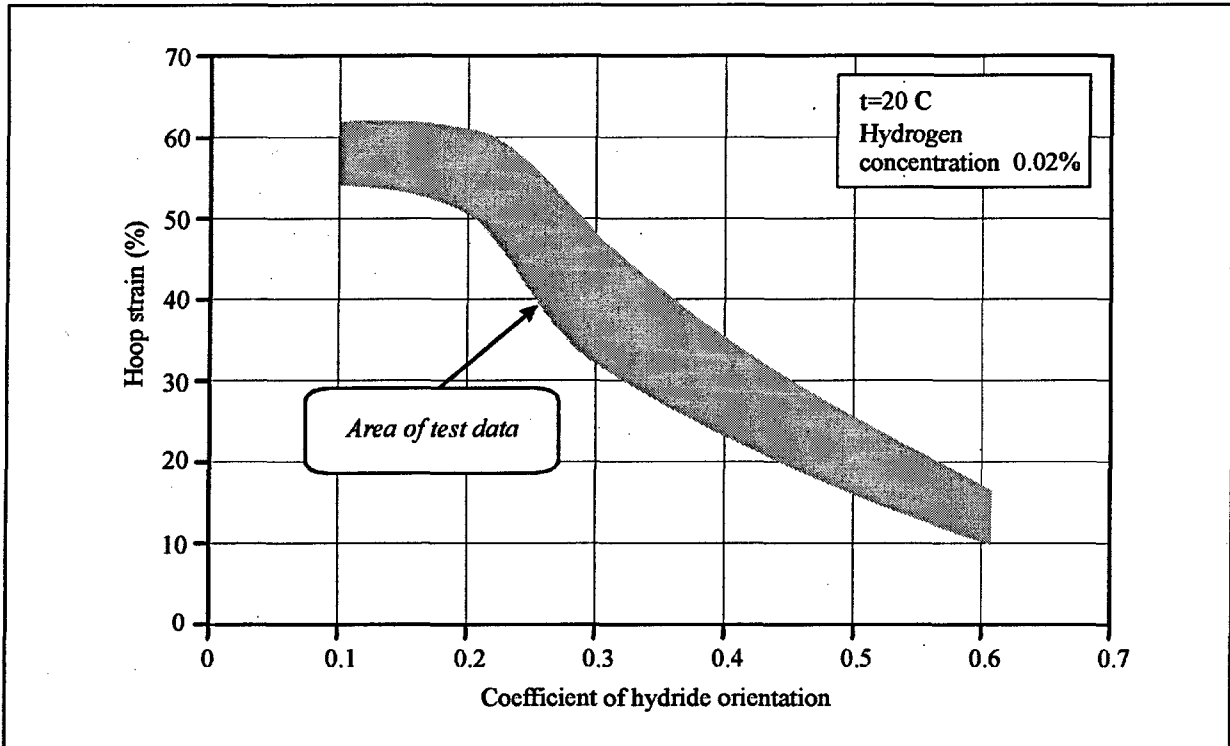
Fig. 6.7. Hoop strain of pressurized Zr-1%Nb tube vs. coefficient of hydride orientation

So analysis of the data obtained in the frames of separate effect tests has the logical connection to the question about the actual characteristics of the claddings of commercial fuel elements irradiated at NV NPP up to high burnup level. This is important for correct development of the approaches to measure their mechanical properties. Preliminary comparison of the PWR and VVER claddings (oxidation and hydrating levels) indicates that the parameters differ significantly.

Numerous data characterizing PWR claddings have been published recently. These data allow to characterize oxidation and hydrating of this cladding type as the function of burnup. Analysis of these data demonstrates that those parameters depend a lot on both type of alloy (Zry-2, Zry-4) and on the initial concentration of tin in the alloy. As an example we can review the parameters for commercial fuel elements of PWR type. Those fuel elements were used to fabricate fuel rods, which then were tested in NSRR (Japan), and in CABRI (France) reactors under RIA conditions. This example reflects certain tendencies, which can not though be generalized.

The published data are listed in Table 6.5 in accordance with the numbers of tests performed in NSRR and CABRI reactors [14, 15].

Table 6.5. Parameters of oxidation and hydriding for irradiated fuel rods of PWR type before CABRI and NSRR tests

Reactor	CABRI				NSRR			
Test No	Rep-Na1	Rep-Na3	Rep-Na4	Rep-Na5	HBO-1[*]	HBO-2[*]	HBO-3[*]	HBO-4[*]
Burnup (GWd/t)	64	53	62	64	50.4	50.4	50.4	50.4
Oxide thickness (μm)	80	40	80	20	43	35	23	19
Hydrogen concentration (ppm)	–[**]	–	–	–	190	150	145	90

[*] one mother element was used for refabrication of fuel rods

[**] no data

Analysis of the data demonstrates that, in the first place, there exists great spread between the characteristics, and, in the second place, that significant oxidation and hydrating of the claddings occurs over the fuel cycles. That is why we can expect that mechanical properties of he claddings will trace those tendencies.

A representative number of VVER type commercial fuel elements irradiated up to 50 MWd/kg U has been studied by now.

Post-test examination of those fuel elements has demonstrated that ZrO_2 film thickness on the surface of the cladding does not exceed 8 μm, hydrogen concentration is in the range of 3-6 10^{-3} % (by weight), the hydrides having random or tangential orientation [16].

Mechanical properties of ring specimens fabricated of the Zr-1%Nb claddings were also measured in the cross-direction. The respective data are presented in Table 6.6 [3].

Table 6.6. Mechanical properties of irradiated and unirradiated VVER claddings

Reactor type	Burnup (MWd/kg U)	Temperature (C)					
		20			350 – 380		
		σ_B (MPa)	σ_{02} (MPa)	δ_{tot} (%)	σ_B (MPa)	σ_{02} (MPa)	δ_{tot} (%)
VVER-440	24.2	580–610	460–535	16–20	360–430	325–375	16–20
	36.8	520–595	468–545	10–16	310–380	274–320	18–21
	46.2	595–614	550	14	361–426	329–395	18–30
	48.2	543–603	476–578	19–26	369–425	337–391	18–26
VVER-1000	36.7	590	435–520	12–27	316–400	270–340	16–26
	40.4	540–598	485–535	13–23	348	325	18–26
	44.7	585	460–530	13–19	380	344	20–28
	46.2	595	535	13	357–395	312–362	12
VVER cladding	0	370–465	310–410	29–40	190–210	160–195	30–41

The data listed in the table demonstrate the following:

- improvement of strength and worsening of ductility of the irradiated VVER cladding takes place despite of the low level of oxidation and hydrating;

- ductility of Zr-1%Nb alloy is preserved well enough;

- there exists spread of mechanical properties in the studied set of claddings.

In general, the presented data demonstrate that it is expedient to get the mechanical properties for irradiated VVER claddings in wide range of the temperature and other parameters in order to use the computer codes to model behavior of these fuel elements under RIA conditions.

6.1.3. Assessment of approaches developed in MATPRO and SCANAIR codes to characterize the data base with mechanical properties of cladding

In order to work out main provisions of the research program aimed at the measurement of mechanical properties of VVER claddings for computational analysis of IGR/RIA tests, it is necessary to analyze the set of parameters, which characterize these properties in computer codes. As was already noted in Chapter 5 two computer codes were used for calculations:

- FRAP-T6 code;

- SCANAIR code.

Specific feature of FRAP-T6 code is that the MATPRO package is used to introduce the input data characterizing material properties of fuel rods into FRAP-T6 code. SCANAIR code has its own data base to describe mechanical properties of the claddings. The features of data bases will be described in the further sections.

6.1.3.1. MATPRO package

MATPRO package is the complex multipurpose data base to analyze the behavior of LWR fuel elements under steady-state and transient conditions. This package was developed at the beginning of 80[es] and contains material properties of LWR fuel elements with the claddings of Zry-2 and Zry-4 up to the fuel burnup of 40 MWd/kg U. In the framework of this task MATPRO package proposes to describe parameters of elastic/plastic strain of the cladding as the function of:

- temperature;
- strain rate;
- cold work of the as received cladding;
- fast neutron fluence;
- oxygen concentration;
- annealing of irradiation and cold work effects;
- anisotropy coefficients versus temperature.

Besides, the parameters characterizing fuel element cladding failure due to ballooning are also included into MATPRO package. Local hoop burst stress is used in MATPRO as such a criterion. This is an empirical criterion and it was obtained with the help of great number of tests with pressurized tubes. The following test data are necessary to obtain the data base characterizing this criterion for the VVER cladding material not included into the MATPRO package:

- pressure and temperature at burst;
- axial radius of cladding curvature at burst;
- cladding peak circumferential elongation at burst;
- cladding thickness at burst.

Unfortunately, analysis of the MATPRO package indicates that it can be used to describe mechanical behavior of irradiated commercial claddings with great caution. This is caused by the fact that the respective correlations considering the influence of the base irradiation onto mechanical properties were mainly obtained from the research reactors, and the requirements to similarity of irradiation conditions were not always satisfied. There has not been any reassessment of the data base for a long time. Hence, specification and renew of the data characterizing mechanical properties of the claddings is an urgent task.

6.1.3.2. Input data base for the SCANAIR code

Models used in the current version of SCANAIR code to describe mechanical behavior of the claddings under RIA conditions are intended to calculate stress-strain state of cladding during the PCMI stage of an accident. Besides, as it was already noted this version of the code has no models to predict cladding failure. That is why the simplified stress strain law without consideration of strain hardening was used to model elastic and plastic behavior of the cladding. Young's modulus and Poisson's ratio are necessary to calculate elastic strain, and this part of mechanical properties has been already described in Chapter 5. SCANAIR code uses only yield stress versus temperature to describe cladding plastic strain. This dependence was obtained from the special tensile tests with irradiated PWR claddings under strain rates up to 1 l/s.

6.1.4. Justification of the program main provisions to obtain the data base with mechanical properties of Zr-1%Nb claddings for FRAP-T6 and SCANAIR codes

Justification of the research program is to be based, in the first place, on the analysis of peculiarities of the mechanical behavior of the claddings under IGR/RIA conditions. Analysis results demonstrate that two characteristic types of thermal mechanical behavior are of the key importance from the standpoint of deformation and failure of the cladding:

- pellet-cladding mechanical interaction (PCMI) stage;

- cladding ballooning and consequence rupture.

In order to understand specific parameters characterizing each of these stages in IGR tests it is possible to review time histories of some parameters obtained by FRAP-T6 and SCANAIR codes for the following types of VVER fuel elements tested in IGR reactor:

- unfailed high burnup fuel rod #H1T;

- failed high burnup fuel rod #H7T.

These time histories are presented in Fig. 6.8 and Fig. 6.9 in accordance with the data of Appendix G (Volume 3 of the Report).

So, scenario of mechanical behavior of the cladding of the fuel rod #H1T is characterized by 3 phases:

1. Closing of the gap.

2. PCMI stage.

3. Reopening of the gap.

Low stresses in the cladding are typical for the first phase, because those stresses are caused only by gas pressure inside the fuel rod. But the fuel temperature grows significantly over this phase, thus causing fuel expansion, which finally results in the situation when fuel-cladding gap disappears, and the PCMI stage of the scenario comes. The specific feature of this stage is that it consists of two parts too. The first is characterized by the continuous growth of the fuel temperature, and as the consequence, the fuel tends to increase its dimensions, but the cold cladding prevents this process. That is why abrupt increase of the hoop strain takes place in the cladding. In this connection it is necessary to mention three principal aspects:

- peak stress in the cladding of this fuel rod is just by 20 % less than the ultimate strength for this temperature;

- peak strain rate is 0.05 1/s;

- loading in the cross-direction is the key factor of this process.

The second part of the PCMI stage is characterized by the growth of the cladding temperature due to departure from the nucleate boiling, and the stresses in the cladding start to exceed the yield stress. Both of these factors lead to the beginning of the cladding plastic strain, thus the cladding stress decreases quickly.

Phase of the gap reopening is initiated by the cladding plastic deformation due to internal gas pressure. Besides, if the criterional correlations determining the conditions necessary to initiate cladding strain of ballooning type are not realized, the cladding cools down step by step and the accident scenario is completed.

Still, if the conditions necessary to begin ballooning of the cladding are realized, the further development of the phase of the gap reopening occurs according to the scenario presented in Fig. 6.9 for the fuel rod #H7T. Special BALON2 subcode starts to calculate time history of the cladding strain and other parameters in the local ballooning area. If, as in this case, local hoop stress is reached, the code predicts burst of the cladding.

FRAP-T6 code
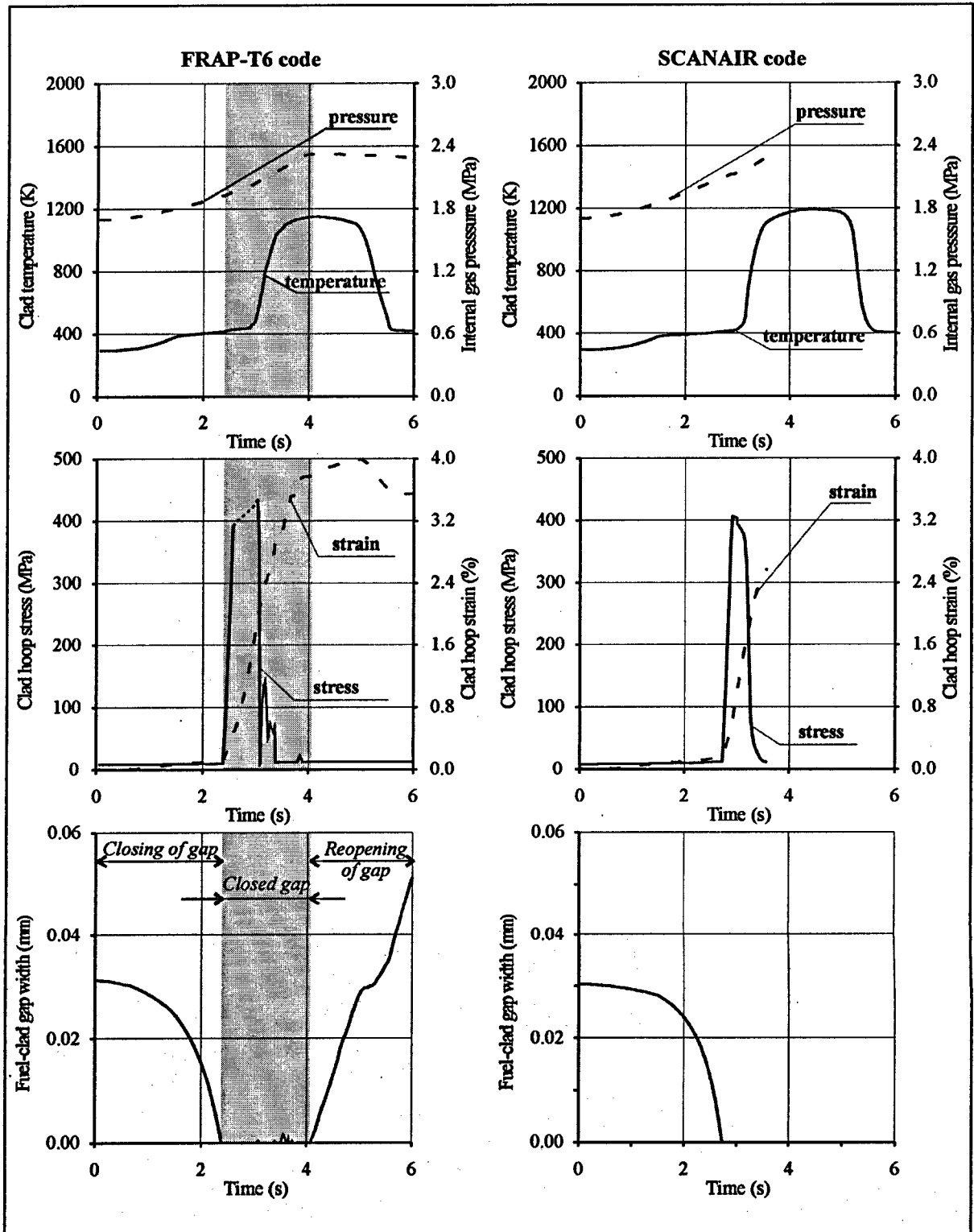

SCANAIR code

Fig. 6.8. Time histories of thermal mechanical behavior of fuel rod #H1T calculated by FRAP-T6 and SCANAIR codes
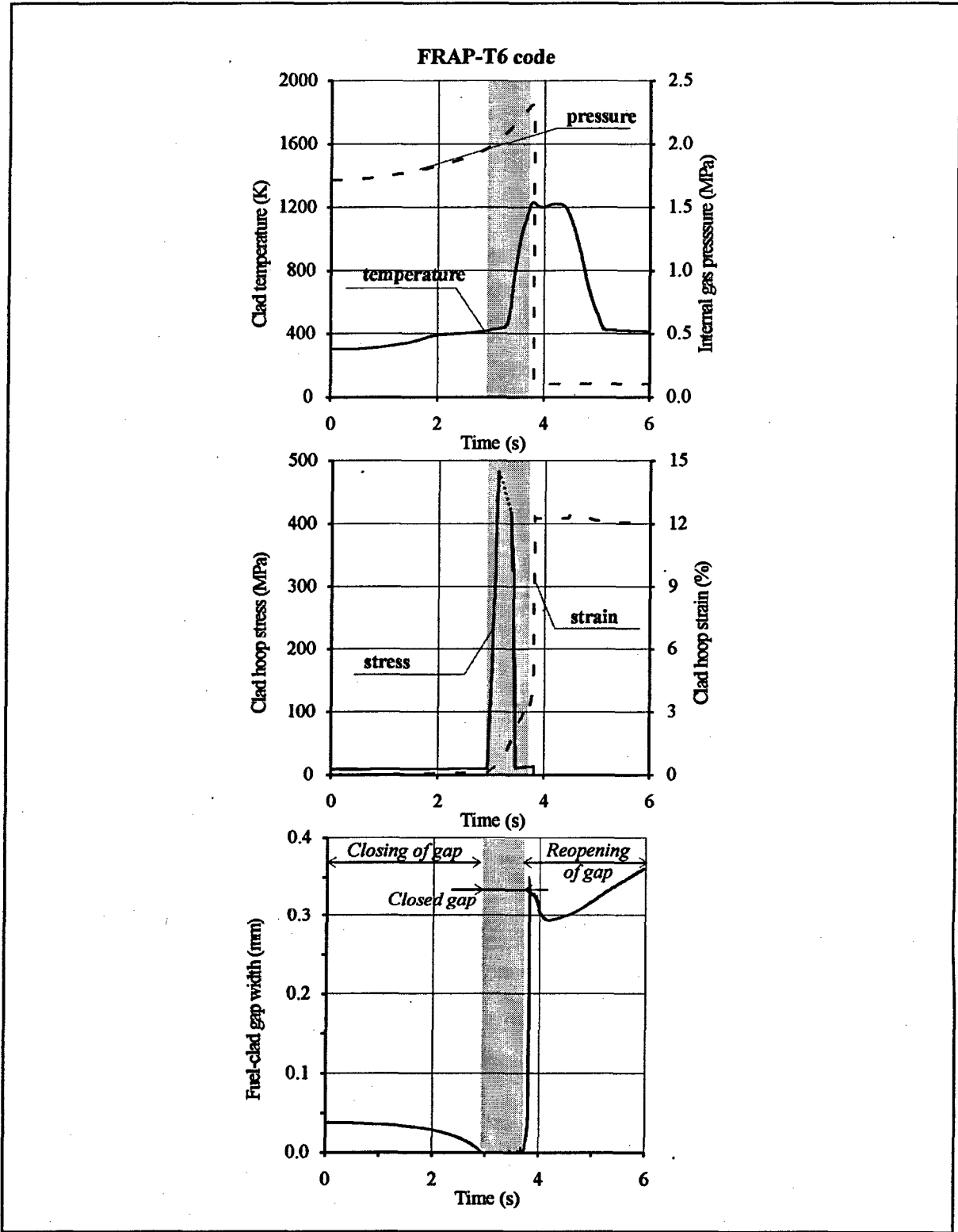
Fig. 6.9. Time history of thermal mechanical behavior of fuel rod #H7T calculated by FRAP-T6 code

Summarizing all the above mentioned we can formulate the following requirements to the mechanical properties of the claddings in order to predict the most important stages in the accident scenarios by computer codes:

- mechanical properties of the cladding material versus temperature and strain rate in the cross-direction up to 500 K are to be studied well in order to predict peak hoop stress during PCMI stage;

- mechanical properties of the cladding material versus temperature and strain rate in the cross-direction in the range of 500 – 1300 K are to be studied well in order to predict peak hoop stress during ballooning stage;

- experimental data base with gas pressure and cladding temperature for the burst of ballooning type is to be defined for the given material, and the criterion for the local burst stress is to be checked and specified.

Results of this analysis were used as the basis to justify the program of measuring mechanical properties of the VVER fuel rod claddings tested in IGR reactor, because it is evident that the development of the universal data base considering the whole complex of phenomena discussed in sections 6.1.1 - 6.1.4 is far beyond the frames of the specific task. That is why along with the conclusions made in the process of analysis of mechanical behavior of high burnup fuel rods ## H1T, H7T it was considered that only two types of the cladding were actually tested in IGR reactor:

- unirradiated claddings fabricated of commercial VVER tubes;

- irradiated claddings fabricated of the claddings of VVER-1000 commercial fuel elements irradiated at Unit 5 of NV NPP up to the average burnup of 48 MWd/kg U (average burnup in the sections used for refabrication).

That is why many of the phenomena influencing mechanical properties of the claddings can be inherently considered, if specimens fabricated of this type of fuel elements are used for measurements. Besides, analysis of the data shows that the problem number one to have the correct data base is to measure mechanical properties in the cross-direction. But, measurement of only this set of characteristics is not enough to get the parameters necessary for prediction of the ballooning strain and cladding failure of ballooning rupture. It is evident that to solve this problem it is necessary to perform testing of the corresponding pressurized specimens of claddings.

All the aspects of the problem were summarized taking into account of experimental equipment possibilities and the following provisions of the testing program were developed:

- it is necessary to measure such mechanical properties of the VVER claddings as yield stress, ultimate strength, uniform elongation, and total elongation;

- it is necessary to perform tests in the cross-direction using ring specimens fabricated of the standard VVER tubes, and irradiated claddings of commercial fuel elements from Unit 5 of NV NPP;

- it is compulsory to perform reassessment of the earlier obtained data base with mechanical properties of unirradiated VVER tubes, to compare the results with the results of current measurements, and to develop the combined data base;

- measurement of mechanical properties with the help of ring specimens is to be performed versus temperature - up to 1300 K and strain rate - up to 0.5 1/s;

- it is necessary to define the parameters characterizing ballooning and cladding failure due to ballooning using burst tests with pressurized tubes fabricated of irradiated VVER tubes and irradiated claddings of commercial fuel elements from Unit 5 of NV NPP;

- it is necessary to perform burst tests in the temperature range of 1000 – 1500 K.

The final stage of research to formulate requirements to the program of tests was directed to the development of the procedure to use the obtained data base of the MATPRO package and SCANAIR code. General principles of this procedure and brief justification of the respective stages are listed in Table 6.7.

Table 6.7. General principles to determine mechanical properties of Zr-1%Nb cladding for FRAP-T6 and SCANAIR codes

Principal phenomena	Measurements in the framework of present studies (Yes, No)	Comments
1. Initial state of cladding (type of material, cold work, heat treatment e.t.c)	No	*VVER claddings of standard initial state will be tested*
2. Parameters of stress-strain state vs.:		
2.1.temperature	Yes	*Two states of cladding will be*
2.2.strain rate	Yes	*considered:*
2.3.fast neutron fluence	Yes	*-unirradiated;*
2.4.oxygen content	Yes	*- irradiated (≈48 MWd/kg U)*
3. Anisotropy	No	*Test will be performed in cross direction. Anisotropy coefficients of Zry will be used.*
4. Annealing of irradiation damage	Yes	*Annealing is assumed to be completed during test procedures.*
5. Cladding ballooning and rupture, failure criteria (pressure, temperature, burst stress etc.)	Yes	*Burst tests of gas pressurized cladding specimens will be performed.*

6.2. Measurements of mechanical properties of Zr-1%Nb cladding by using simple ring specimens

6.2.1. Measurement procedure

6.2.1.1. Main provisions of the procedure of testing simple ring specimens

Mechanical properties of Zr-1%Nb cladding in the cross-direction were determined by tensile tests of simple ring specimens. This testing was arranged with the help of special machines equipped with semicylindrical mandrels. For each testing ring specimen was located around the mandrels, then the mandrels were drawn apart with the set cross-head velocity (V), thus ensuring tensile loading (P) of ring specimen (see Fig. 6.10).

Tensile loading of specimen was performed till the rupture of the specimen. During the test the following parameters were registered:

- temperature;
- cross-head velocity;
- tensile load;
- displacement of mandrels.

Testing of simple ring specimen was performed in the air environment under low temperatures, and in vacuum environment under high temperatures. Two types of simple ring specimen were tested:

- unirradiated;
- irradiated.
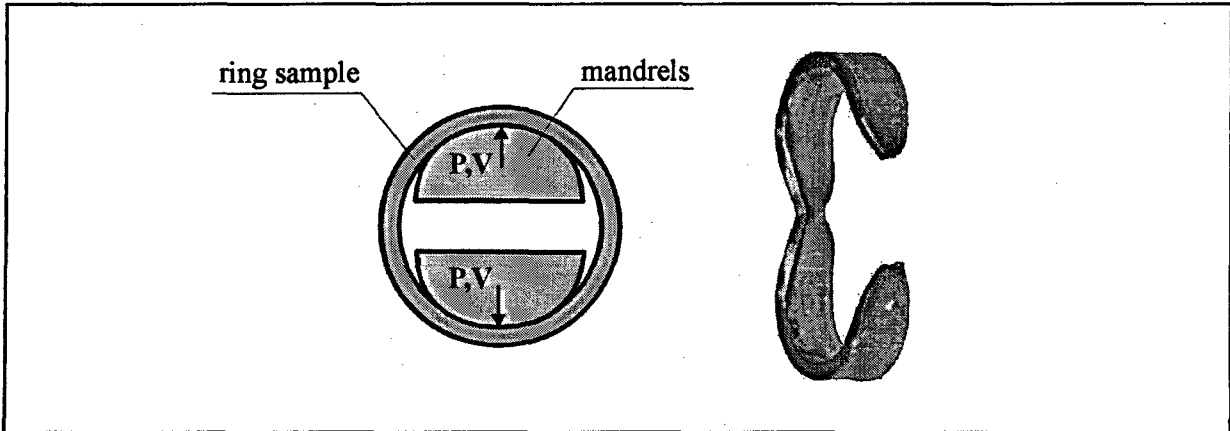
Fig. 6.10. Cross-section of mandrels with simple ring specimen and general view of simple ring specimen after the test

Unirradiated ring specimens were made of the standard tubes intended for VVER-1000 type fuel elements. Irradiated ring specimens were made of the cladding of the commercial fuel element, taken out of the core of Unit 5 NV NPP with the average burnup 48 MWd/kg U (within the section used for fabrication of ring specimens).

6.2.2. Methodological aspects of the tests with simple ring specimens

The objective of this type of tests was to determine mechanical properties of the cladding in the cross-direction. It is well known that measuring of mechanical properties with the help of ring specimens allows to determine yield stress and ultimate strength of material accurately enough. Still significant problems arise when it is necessary to determine uniform and total elongation. These two parameters are characterized respectively as:

- residual elongation of the material at maximum tensile load;

- residual elongation of the material after the rupture.

In practice these parameters are determined with the measured load-displacement diagrams. Fig. 6.11 presents the schematic view of such a diagram.
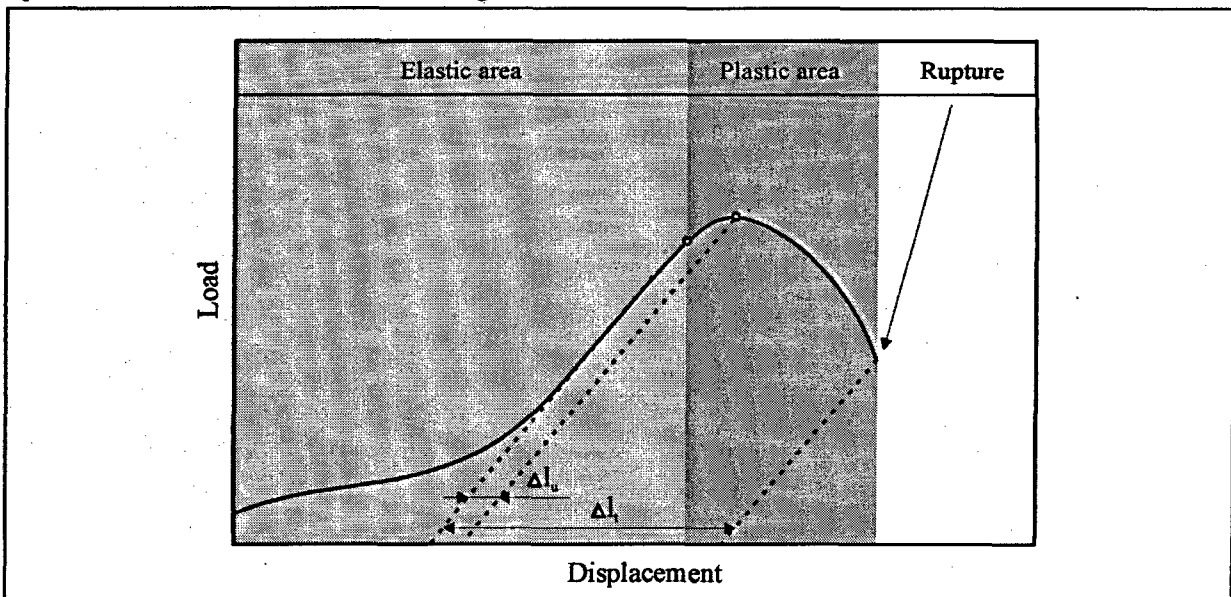
Fig. 6.11. Schematic view of load-displacement diagram

6.17

The following expressions are correct for the specimen of material subjected to tensile loading up to the rupture:

$$\delta_u = \frac{\Delta l_u}{l_s} \; ; \; \delta_t = \frac{\Delta l_t}{l_s} \, ,$$

where δ_u = uniform elongation;

δ_t = total elongation;

$\Delta l_u, \Delta l_t$ = absolute uniform and total elongation, respectively;

l_s = initial length of the specimen.

Certain methodological problems arise when the attempts are made to determine uniform and total elongation with the help of simple ring specimens. The main reason is that the tensile load caused by displacement of mandrels is not uniform along the perimeter of the simple ring specimen. Friction between the mandrels and the specimen makes the additional contribution into this effect. The epure of deformation distribution within the specimen semi-perimeter has the view presented in Fig. 6.12.
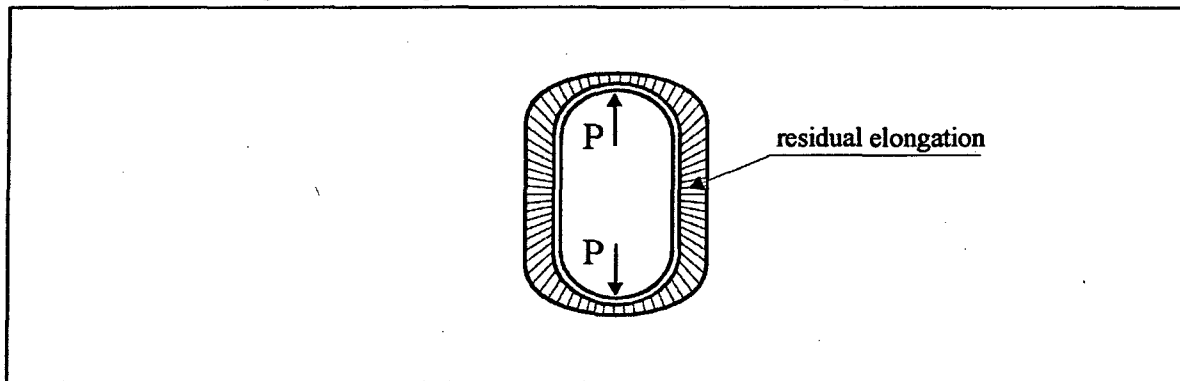
Fig. 6.12. Schematic view of azimuth profile of residual elongation for simple ring specimen

Thus, it is evident that tensile loads, non-uniform within the perimeter, lead to displacements non-uniform within the perimeter. Degree of non-uniformity decreases as the distance from the axis, along which the mandrel displacement takes place, increases. From the standpoint of procedure this effect can be considered in two ways:

• selection of the shape of machined ring specimen in order to concentrate the stress and elongation within well specified area (see Fig. 6.13);

• performance of special scoping tests allowing to empirically chose correlations that can correctly identify elongation parameters.
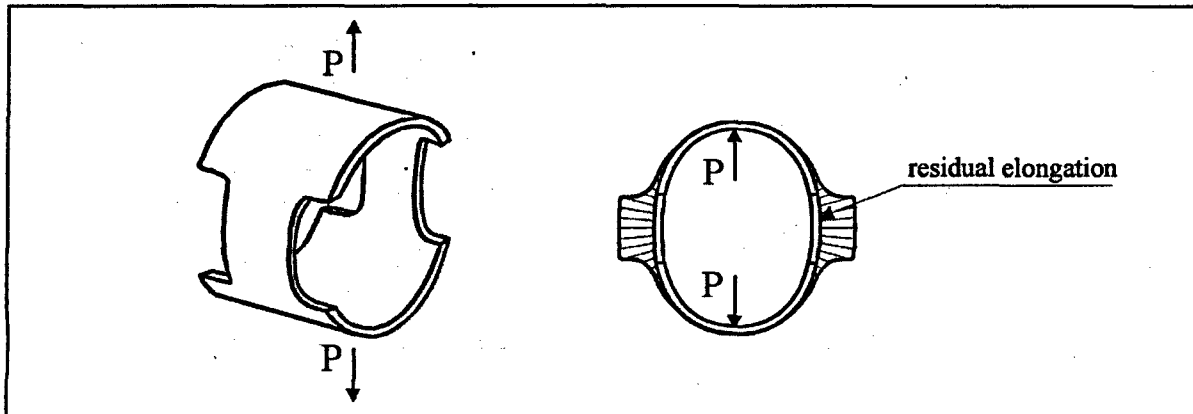
Fig. 6.13. Schematic view of machined ring specimen and azimuth profile of elongation for its

The historical background is that both approaches have been developed and used in practice in different countries. For example, the first method is being used in ANL (USA) and IPSN/CEA (France). The second method is in use in Russia. As the implementation of the new approach into practice is always an expensive and time consuming procedure, the second approach was used to understand the summary of main mechanical properties of the VVER cladding important for computational analysis of IGR/RIA tests. Simultaneously the specialists of NSI RRC KI (Russia), RIAR (Russia), ANL (USA), IPSN/CEA (France) made an effort to compare the results presented by each of these approaches. The approach developed in Russia is based on the fact that some effective length of the simple ring specimen, which is called gauge length, is used instead of the specimen length (l_S) in the procedure to calculate uniform- and total elongation. This length is defined by the following expression:

$$l_g = \frac{\pi \overline{D}}{2} - K \frac{\pi d_m}{2},$$

where l_g = gauge length of ring specimen;

$\overline{D}$ = average diameter of specimen;

d_m = diameter of mandrels;

K = empirical coefficient.

This expression allows to account for effects of non-uniformity of elongation with the help of empirical coefficient, which defines the effective specimen portion subjected to deformation.

A number of years ago special tests were performed at RRC KI to determine the value of K coefficient. The values of this coefficient were determined depending on the mandrel diameter. Recommended values for this case are K=0.85, d_m=4 mm. Besides, the special study was arranged in RIAR with the same objective, and a slightly corrected formula was obtained for l_g. Still, considering the importance of this problem, analysis and justification of the approach to define the value of gauge length were additionally performed in the framework of this research.

6.2.3. Program of research to obtain the data base characterizing mechanical properties of the VVER cladding tested in IGR reactor

In accordance with the main objective of the research it was necessary to obtain the data base characterizing mechanical properties of the claddings for the VVER fresh fuel rods, and fuel rods irradiated up to 48 MWd/kg U. As was mentioned in section 6.1 the respective parameters were to be defined as the functions of temperature and strain rate. As the time given for the work was not enough, it was decided to do it using the following main principles:

1. To arrange maximum use of the existing data base characterizing mechanical properties of unirradiated claddings.

2. To perform checking of the methods used to obtain data base for item1. To perform some tests with the VVER unirradiated claddings in order to be sure that these results agree with the results obtained for item1, and to compare the methods for measuring mechanical properties of LWR fresh claddings together with the specialists of ANL (USA) and IPSN/CEA (France).

3. To measure mechanical properties of irradiated claddings fabricated of the commercial fuel element from Unit 5 of NV NPP.

Three stages of research were performed in accordance with the presented principles.

Reassessment of the data base with mechanical properties of the VVER fresh cladding

Numerous measurements of mechanical properties of different claddings were performed by VNIINM (Russia) and RIAR (Russia), and presented in [3]. In the framework of this research we reviewed mechanical properties of Zr-1%Nb simple ring specimens with 9.15 mm OD diameter fabricated of the annealed tubes (T = 580°C, t = 3 hours). Reassessment of individual measurements of mechanical properties of the respective specimens was done by Dr. Kobyliansky, and the necessary initial data were transferred by the

author to those performing this work. The mentioned data base contains 65 measurements of mechanical properties of fresh claddings as the function of temperature (293 – 1273 K).

Comparative tests with unirradiated Zr-1%Nb ring specimens and additional tests with unirradiated Zr-1%Nb specimens

Considering the fact that measurement of mechanical properties of the LWR claddings is an important problem, specialists from Russia, and specialists from ANL (USA) and IPSN/CEA (France) decided to compare the methods to measure those properties. That is why the section of Zr-1%Nb tube was cut into three parts, each of them was sent to either RIAR, ANL, or IPSN/CEA. It was planned for this testing program to measure mechanical properties of the tube for two temperature levels 20 – (350 - 400)°C under different strain rates. The Russian part of the program was a little wider in order to simultaneously get the information to compare it with the earlier obtained data base.

The generalized analysis of results of comparative experiments and of comparisons between new data and the available data base allowed to develop a number of improvements of the procedure to process diagrams of the simple ring specimen deformation.

Program to obtain data base with mechanical properties of irradiated cladding

For this part of research program it was necessary to measure mechanical properties of irradiated claddings as the function of temperature and strain rate. As was previously mentioned, the approach had been used to reveal the influence of mainly temperature and strain rate onto mechanical properties. In other words the problem of representativity of results obtained for one commercial fuel element irradiated up to 48 MWd/kg U at Unit 5 of NV NPP was not the subject of research, because in order to perform computational analysis of fuel rods tested in IGR reactor it was necessary to have the data base with mechanical properties of the cladding of just such a fuel element.

Hence only two parameters varied in the framework of these tests:

- temperature (293 – 1223 K);

- strain rate (2 10^{-3} – 0.5 1/s).

Selection of the range to vary the loading rate was dictated by the capabilities of the test machines. Preliminary analysis was performed to develop the requirements assuring optimal accuracy of the statistical methods used to process the measured results. This analysis has indicated that the optimal temperature measurement step can be starting with 40-150 degrees up to different temperature levels. However, after the completion of these stages, the necessity of conducting additional studies in the following areas became obvious.

New measurements of mechanical properties of unirradiated claddings in the entire temperature range

The existing and generalized in [3] data base on unirradiated claddings was obtained using old equipment with analogue recording systems. The adjustment of this data base, performed at the first stage, did not allow to fully eliminate systematic differences with data obtained within the framework of the present work using modern equipment and a digital recording system. Moreover, since deformation diagrams are not fully available for all specimens, the procedure adjustment, taking into account modifications, is possible only using correction coefficients for the entire data base rather than individually for each specimen. Since the purpose of the present work is to create the data base to be used in computer codes, requirements on the relative accuracy of correlations developed on its basis is of a special significance. Thus, a decision was made to perform new measurements of mechanical properties of unirradiated claddings in the entire temperature range using the same equipment and procedures that were applied to irradiated claddings.

Special experiments to validate the new modified procedure

The use of diagram processing procedure upgrades that were proposed at the first stage confirmed their efficiency, and taking into account their future application prospect, it was appropriate to develop, on their basis, a new modified procedure. It is obvious that special experiments were required for a careful validation and confirmation of this modified procedure.

<u>Additional experiments with irradiated claddings to adjust mechanical properties, primarily, in the area of the superplasticity</u>

A strong alternating dependency of the total elongation on the temperature in the range of 800 – 1200 K and a large data spread required additional experiments to adjust the nature of studied dependencies and to improve the accuracy of correlation ratios.

6.2.4. Parameters of simple ring specimens used for tests

Two groups of simple ring specimens were used to obtain measurements results:

- specimens of unirradiated VVER tubes;

- specimens of irradiated VVER cladding.

Detailed characteristic of the tube sections and claddings used for this purpose is presented in Appendix J of Volume 3. Unirradiated specimens were fabricated of the fully recrystallized VVER tube ($t = 580°C$, $\tau = 3$ hours). Thickness of the ZrO_2 layer on the tube's surface did not exceed 1 µm, hydride orientation coefficient was 0.42. Measurements of the diametric tube dimensions were performed in two directions with the axial pitch of 7.5 – 8.5 mm. Accuracy of the measurements was 2 µm for the outer diameter, and 10 µm - for the inner diameter. The following results were obtained:

- VVER tube outer diameter 9.136 – 9.149 mm;

- inner diameter $7.72^{\pm 0.008}$ mm.

Commercial fuel element #165 of the fuel assembly #4108 irradiated in the reactor of Unit 5 NV NPP was used to fabricate simple ring specimens of the irradiated cladding. The following parameters were measured for this section of the fuel element #165:

- outer diameter – by profilometry;

- cladding thickness and ZrO_2 layer thickness – by using of 5 metallographic cross-sections;

- hydrogen concentration, hydride orientation and burnup – according to the procedures described in Chapter 3.

The measurement results have indicated that this section of the fuel element is characterized by the following parameters:

- burnup – 47 - 48 MWd/kg U;

- average outer diameter – 9.066 mm;

- cladding thickness – 0.69 ± 0.15 mm;

- hydrogen concentration in fuel elements – 0.049 – 0.058 % (by weight);

- hydride orientation coefficient – 0.36 - 0.42;

- ZrO_2 thickness on the cladding outer surface – 3 - 5 µm;

- ZrO_2 thickness on the cladding inner surface is less than 1 µm.

Both types of specimens were fabricated by cutting either VVER tube or VVER cladding. The height of simple ring specimens was 2.7 – 2.8 mm, individual height measurements for each specimen were performed with the accuracy of ±0.01 mm.

6.2.5. Types of procedures to obtain mechanical properties

The following expressions are generally used to define mechanical properties when testing simple ring specimen:

$$\sigma_u = \frac{P_{max}}{2ht}, \quad \sigma_y = \frac{P_{0.2}}{2ht},$$

6.21

$$\delta_u = \frac{\Delta l_u}{l_g} 100, \ \delta_t = \frac{\Delta l_t}{l_g} 100,$$

where $\sigma_u =$ ultimate strength;

$\quad P_{max} =$ maximum test loading of the specimen;

$\quad h =$ height of the specimen;

$\quad t =$ thickness of the specimen;

$\quad \sigma_y =$ yield stress;

$\quad P_{0.2} =$ load corresponding to residual strain equal to 0.2 %;

$\quad \Delta l_u =$ absolute uniform elongation;

$\quad l_g =$ gauge length of the specimen;

$\quad \Delta l_t =$ total displacement.

So the analysis of the expressions presented above indicates that two different groups of parameters are to be measured to determine the set of mechanical properties for each test:

- geometrical dimensions of specimens and mandrels (h, t, D_o, d_m);

- loading parameters (P_{max}, $P_{0.2}$, Δl_u, Δl_t).

Besides, the specimen temperature is to be measured in each test.

In framework of present studies the loading parameters are defined by computer processing of the measured load-displacement curves. Previously obtained data base on unirradiated Zr-1%Nb was developed by manual processing of such curves. As one of the tasks of the program was to reassess the previously obtained results, then both approaches are to be reviewed in this case. Fig. 6.14 presents the main principles used in both methods.
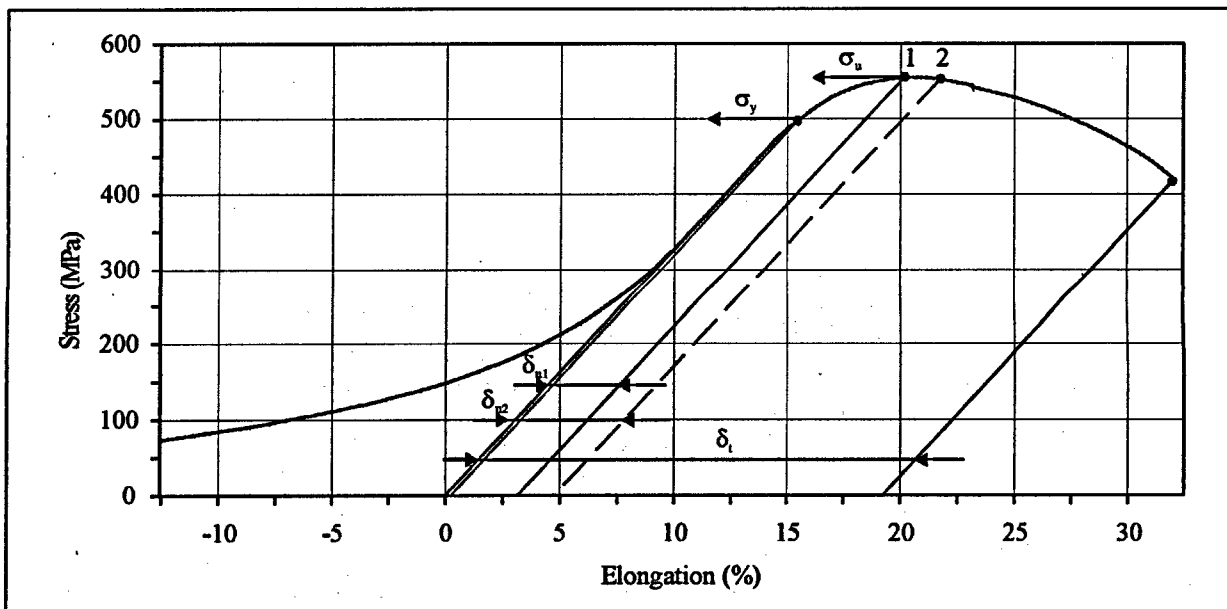
Fig. 6.14. Processing of stress-strain curve obtained with simple ring specimen of Zr-1%Nb

Processing of load-displacement curve starts with its transformation into the stress-strain. Then the curve slope angle is fixed in order to characterize the region of elastic strain, and thus to determine the beginning of coordinates in the elongation axis (0 %). This and other procedures are currently performed in RIAR by special computer tool. After that the line, parallel to the straight line fixing the region of elastic strain, is drawn through the point in the x-coordinate equal to 0.2 %. The point where this straight line crosses the stress-strain curve determines the yield stress value. Furthermore, the currently existing method of the curve

6.22

processing can identify point marked with "1", to which the maximum stress value, i.e. the ultimate strength corresponds. In accordance with the theory the line, parallel to the straight line fixing the elastic strain region, is drawn through this point, and the point where it crosses the elongation axis determines the value of the uniform elongation (δ_{ul}). The last stage of the method suggests the similar set of procedures to define total elongation (δ_t). In this case the respective straight line is drawn through the point where the rupture of specimen occurred.

The manual method of processing differed from the one described above by the procedure of δ_{u2} determination. Uniform elongation (δ_{u2}) was then determined with the help of the straight line drawn through the point marked with "2" in Fig. 6.14. The rule stated that this point is the point where one could start visually observe deviation of the curve from horizontal drawn through curve maximum. It is evident that this method always resulted in the overestimation of δ_u. For example, processing of the curve presented in Fig. 6.14 by this method indicated that δ_{u2}/δ_{ul} ratio was about 1.3. Hence practical application of the earlier obtained data base can be done only after all the files containing data on the uniform elongation are corrected, otherwise those date are to be excluded from the data base.

6.2.6. Validation of the procedure to measure mechanical properties with simple ring specimens

It was already noted that the main problem in measuring mechanical properties with the help of ring specimens are related to the non-uniformity of tensions and displacements along the specimen perimeter, and the uncertainty in the gauge length value. Moreover, it should be noted that while recording the diagram, changes in the linear distance between mandrels are measured as the displacement, rather than the elongation of the specimen working section. In case of ring specimens, when the tension process is accompanied by specimen shape changes, the difference between these values can be significant.

Despite the fact that the procedure of measuring mechanical properties with the help of simple ring specimens is generally accepted in Russia, and seems to be well justified in the past, special effort was made to check the obtained results. During the first stage of this checking we compared the results of measurements done by the specialists from RIAR (Russia), ANL (USA), and CE-Saclay (France). Section of the VVER tube was divided into three parts and each part was sent to one of these organizations. Specialists of each organization used their own original procedures to fabricate ring specimens and to measure mechanical properties of those specimens. Detailed comparison of the used procedures and obtained results is still planned for the future. But it is already possible to formulate one conclusion. It was clarified that the measured values of the uniform elongation for 20°C at the strain rate of 10^{-3} 1/s are in the range of 4 – 15 %, the corresponding range for the total elongation is equal to 35 – 87 %. These results have initiated the study targeted at finding the source of the potential methodical error.

The above research work (described in section 6.2.7) started after completion of theoretical analysis of results obtained in RIAR and ANL. This analysis was based on the assumption that true stress-strain curve can be described with the help of the power law presented as follows:

$$\sigma = K \, \varepsilon^n,$$

where σ = true stress;

ε = true plastic strain;

K, n = coefficients.

If the measurements were performed correctly, and Zr-1%Nb alloy follows the power law, then the true stress-strain curve are to be described by the straight line in the logarithmic coordinates. Fig. 6.15 presents the data illustrating the attempt to present in such a manner the results obtained in RIAR and ANL [18, 22].

- none of dependencies is a straight line;

- good agreement was observed only in the determination of the ultimate strength;

- difference in the determination of the yield stress between the RIAR and CE-Saclay is quite acceptable;

- ANL yield stress is quite different from RIAR and CE-Saclay data;

- uniform elongations are quite different between all three institutes.

6.23
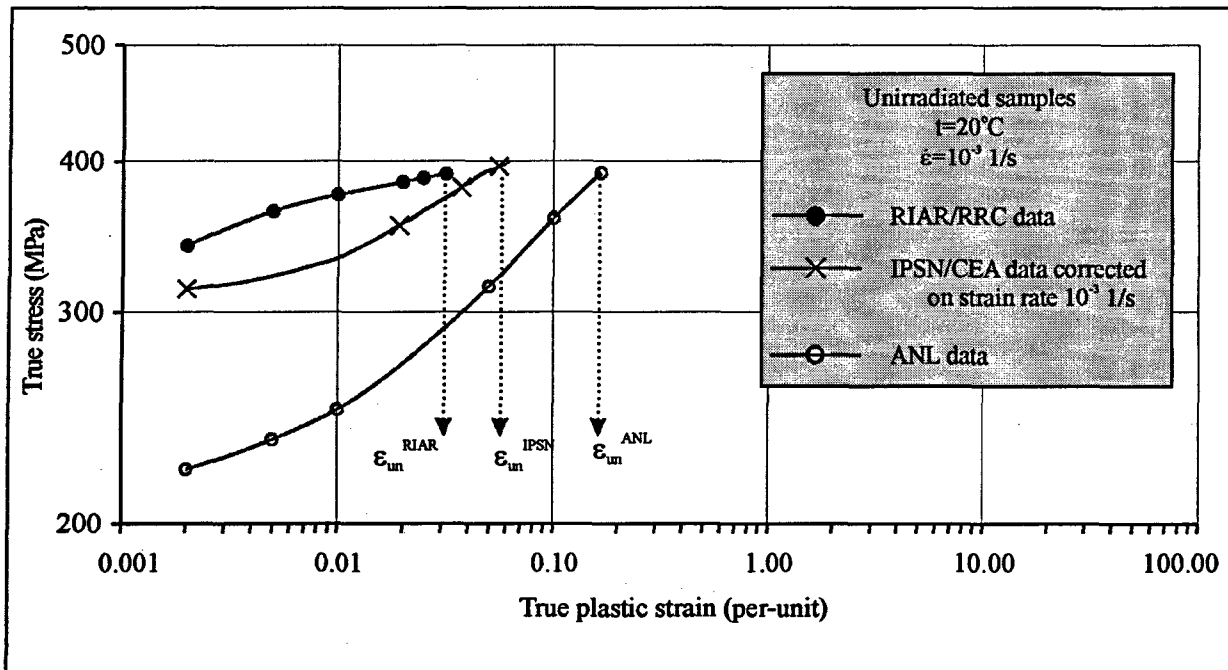
Fig. 6.15. Comparison RIAR, ANL and IPSN data for true stress-strain curve

At least two explanations can be given for the presented results:

- $\sigma = K \varepsilon^n$ law is correct for Zr-1%Nb alloy but not a single procedure allows to get probable results to characterize it;

- mechanical behavior of Zr-1%Nb cladding does not follow $\sigma = K \varepsilon^n$ law, and at least one curve presented in Fig. 6.15 is not correct.

In any case it is evident that the procedure described in section 6.2.5 needs to be additionally analyzed, and probably improved. A number of sequential upgrades of procedures, that allowed to develop a new modified procedure, was made on the basis of a detailed analysis of the existing data base, as well as results obtained within the framework of the present studies, including comparative trilateral experiments. The next Section covers the procedure description and validation.

6.2.7. Modified procedure to obtain mechanical properties using simple ring specimens

From the point of view of diagram processing procedures, the above physical causes of errors in the determination of mechanical properties during tests of ring specimens are related to the accuracy of determining two values:

- specimen absolute elongation;
- specimen gauge length.

6.2.7.1. Determination of the specimen absolute elongation

A special test was conducted to analyze causes of possible mistakes due to errors in measuring the absolute elongation that can occur in the determination of the uniform and total elongation.

Simple ring specimen was tested for the load much less than the yield stress, i.e. in correspondence with the tolerances adapted in the procedure residual strain was to be equal to zero, because the specimen was tested in the region of elastic strain. Fig. 6.16 presents cross-sections of the standard ring specimen before and after tests.

6.24
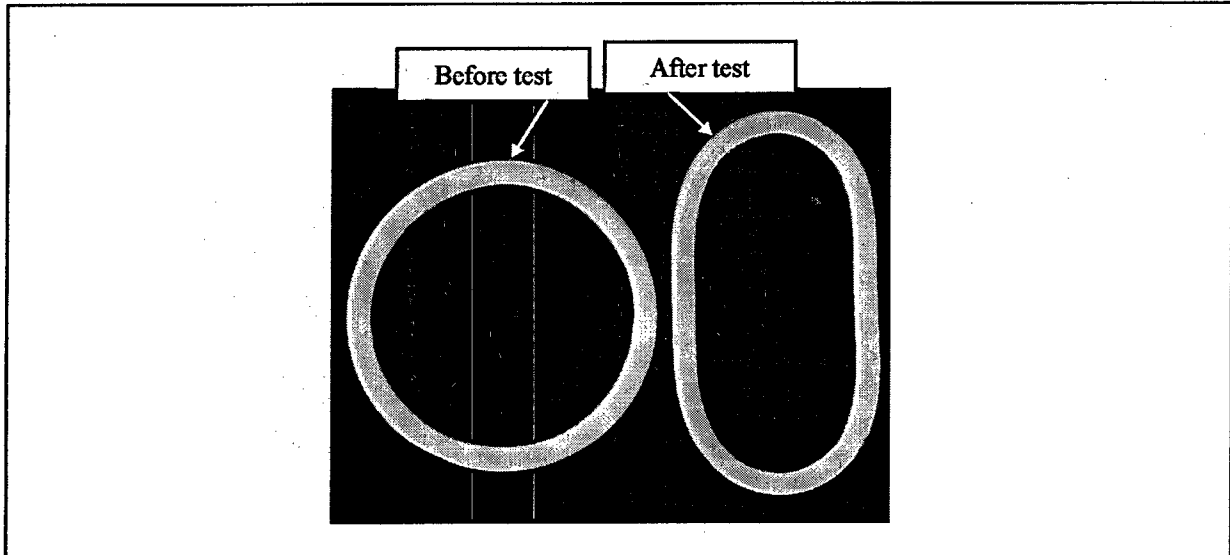
Fig. 6.16. Cross-sections of simple ring specimen before and after mechanical test with σ << σ_y

The respective measurements showed that the value of residual hoop strain was equal to 2 %. But in the framework of the existing procedure this elongation is not considered. Loading of the ring specimen causes not only its elastic tension, but also its bending and partial plastic deformation. Hence, when processing the stress-strain curve, in this case it is important to consider that this curve has not the linear, but the pseudo-linear section, which includes both elastic and plastic strain components. That is why the main task for the procedure modification is to determine the tangent of the slope angle of the actual elastic part for the stress-strain curve. Young's modulus characterizes this value according to the Hooke's law.

$$\sigma_s = E_s \delta_s ,$$ (1)

$$\delta_s = \frac{\Delta l_s}{l_s} ,$$

where σ_s = stress;

E_s = Young's modulus for the material of specimen;

δ_s = specimen relative elongation;

Δl_s = specimen absolute elongation;

l_s = specimen initial length.

Still, it is important to remember that the stretched specimen combines both mandrels of the machine, thus closing the kinematic circuit. That means that all the parts of the machine are subject to the same load as the specimen, and thus they are also displaced. Hence, the measured displacement of the machine mandrels characterizes the set of elastic deformations for the machine and specimen, and can be described by the following expression:

$$\Delta l_m = \Delta l_M + \Delta l_s ,$$ (2)

where Δl_m = measured mandrels displacement;

Δl_M = displacement of machine elements;

Δl_s = displacement of specimen.

If we express the Hooke's law for the kinematic circuit in the way similar to (1), and to change from the stresses to the measured load P, then we can have expression (2) as follows:

6.25

$$\Delta l_m = \frac{P l_s}{E_s S_s} \left(1 + \sum_{i=1}^{n} \frac{S_s \; l_{mi} \; E_s}{S_{mi} \; l_s \; E_{mi}} \right),$$ (3)

$$\sum_{i=1}^{n} \frac{S_s \; l_{mi} \; E_s}{S_{mi} \; l_s \; E_{mi}} = \theta,$$

> where P = measured load;
>
> S_s, S_{mi} = cross-section area of the specimen, and of the i machine element;
>
> l_{mi} = the length of the i machine element;
>
> E_{mi} = Young's modulus for the i machine element;
>
> θ = compliance of machine.

θ coefficient, called compliance of machine, characterizes the ratio of the absolute elastic strains of machine elements to the absolute elastic strain of the specimen and it depends only on ratios between the Young's modulus, and geometric dimensions of the specimen, and elements of the test machine. By arithmetic procedures we can transform equation (3) into the following:

$$\frac{\sigma_s}{\delta_s} = \frac{E_s}{1+\theta},$$ (4)

> where σ_s = stress of the specimen (MPa);
>
> δ_s = relative elongation of specimen (per-unit);
>
> E_s = Young's modulus for the specimen (MPa);
>
> θ = compliance of machine (per-unit).

Hence the theoretical tangent of the slope angle of the stress-strain curve linear part is to be equal to the ratio of the Young's modulus to the functional $1+\theta$. Machines used to measure mechanical properties are rigid enough, that is why θ value for them is equal to $4-6$ [9]. Really according to ring tensile test results the tangent of the slope angle of the stress-strain linear part is essentially less than Young's modulus. This is related to the fact that in case of simple ring specimens, at tensile loads below the yield point, the measured value of mandrels movement Δl_m consists not only of the sum of absolute elastic deformations of machines and the specimen, but of an additional movement of mandrels caused by changes in the specimen shape from the ring to an elongated loop as a result of the bending and partial plastic deformation.

In such case the follow expression could be written by analogy with expression (4):

$$\frac{\sigma_s}{\delta_s} = \frac{E_s}{1+\theta+\Delta},$$ (5)

$$\Delta = \frac{S_s E_s \Delta l_{sh}}{P l_g},$$

> where Δ = additional compliance as a result of specimen shape changes;
>
> Δl_{sh} = additional movement of mandrels as a result of specimen shape changes;
>
> l_g = gauge length of specimen.

The additional compliance Δ characterizes the ratio between the additional movement of mandrels as a result of specimen shape changes and the absolute elastic deformation of the specimen, and unlike the compliance θ, depends not only on the Young's modulus and geometric dimensions of the specimen, but also on the load. This is because of this dependence on the load, the starting section of the simple ring specimen stress-strain curve till the yield point is of pseudo-linear, rather than linear nature.

Graphical illustration of this approach is presented in Fig. 6.17. Part of an actual stress-strain curve obtained for one of the tested specimen was used for this purpose.
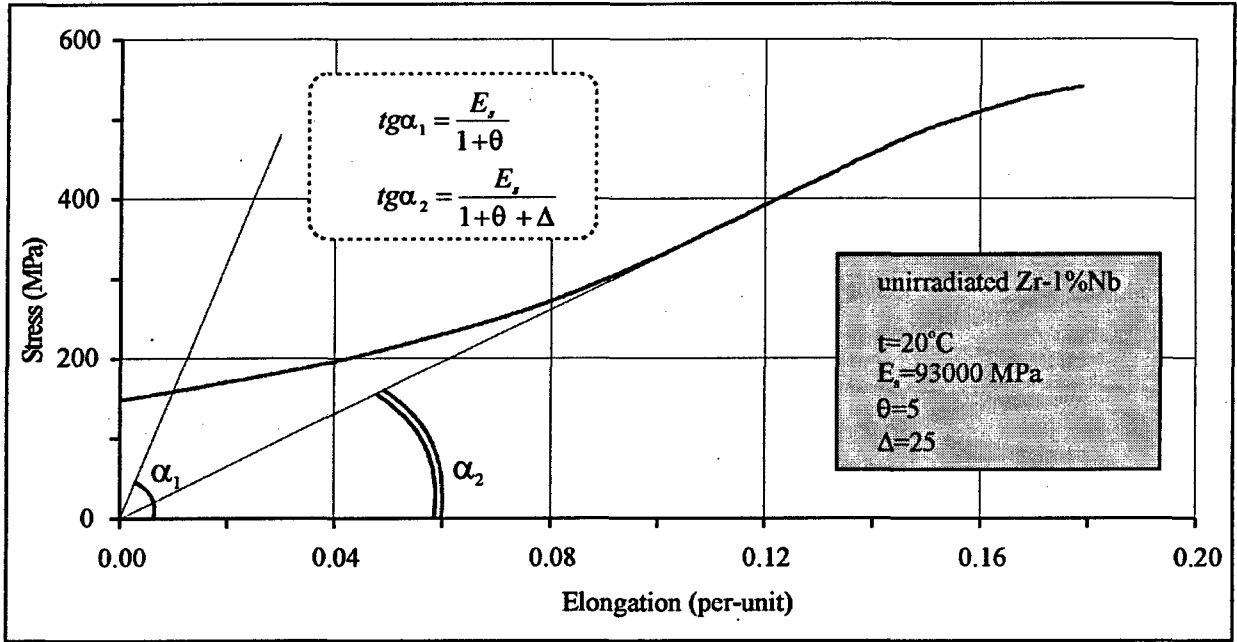
Fig. 6.17. Comparison of slopes for the linear part of stress-strain curve for ideal and imperfect specimens

So, the example presented in Fig. 6.17 has demonstrated the following:

- use of the pseudo-linear part of the stress-strain curve as the basis in order to determine uniform and total elongation results in underestimation of these parameters, because the slope angle of the respective straight lines (see Fig. 6.14) is determines with great error;

- in order to correctly calculate uniform and total elongation, taking into account only elastic deformation, the slope angle of the linear part of the stress-strain curve is to be calculated by the expression.(4) for the corresponding temperature of testing and the type of the specimen (unirradiated, irradiated). This is the angle to draw the straight lines necessary to determine uniform and total elongation.

The example of using this method is presented in Fig. 6.18.
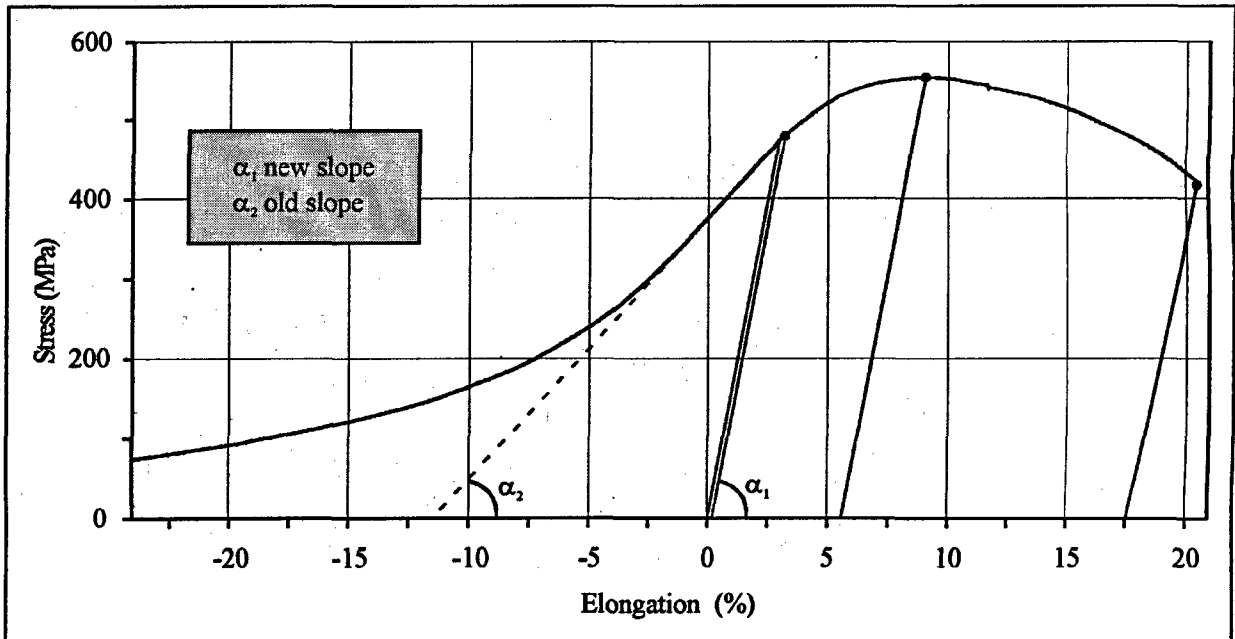
Fig. 6.18. Modified method to determine uniform and total elongation

6.27

Formally, in order to apply this method we need the data base characterizing Young's modulus versus temperature for both unirradiated and irradiated specimens. But the other procedure — more convenient and accurate can be used in practice in order to define the required slope angle of the straight part of the stress-strain curve for the ring specimen-machine system.

Determination of the real inclination angle of the diagram linear section

The main idea of this procedure is that the process of reduction of load for specimen in the elastic deformation area is described by the same straight line as the process of the specimen tension under the influence of the load. That is why the true slope angle of the straight part of the stress-strain curve can be determined if we reduce the load for the specimen at some point of this curve. Fig. 6.19 presents the example of realization of this procedure.
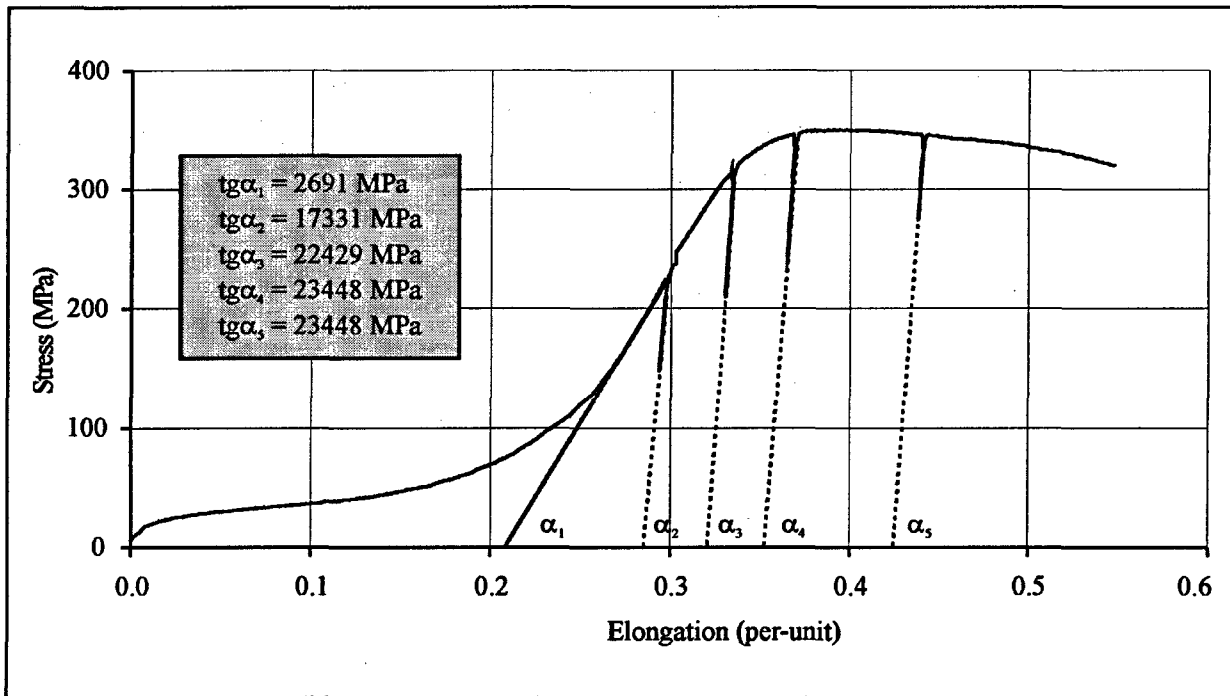

Fig. 6.19. Curve of the deformation with a partial relief

True inclination angles of relief lines were determined in experiments during which the test specimen was subjected to a partial relief at various stages of its deformation in the tensile process. In this case inclination angles of relief lines α_2–α_5 correspond to the expression (4), and the inclination angle of the pseudo-linear section α_1 corresponds to the expression (5). A significant (several times) difference between inclination angles of partial relief lines and the pseudo-linear section is caused by an additional compliance Δ during specimen shape changes from the original ring to an elongated loop due to a simultaneous bending and tension. A minor increase in inclination angles of partial relief lines is explained by a reduced compliance θ due to a certain increase in the specimen length during its shape changes (see expression 3).

The correspondence between the inclination angle of partial relief lines and the true inclination angle of the deformation diagram linear section in case of no specimen bending was experimentally verified using a cylindrical specimen of Zr-1%Nb alloy with the recording of the elongation to increase the accuracy by a strain transducer located in the working section of the specimen (see Fig. 6.20). The inclination of the starting section of the diagram practically coincides with partial relief lines.
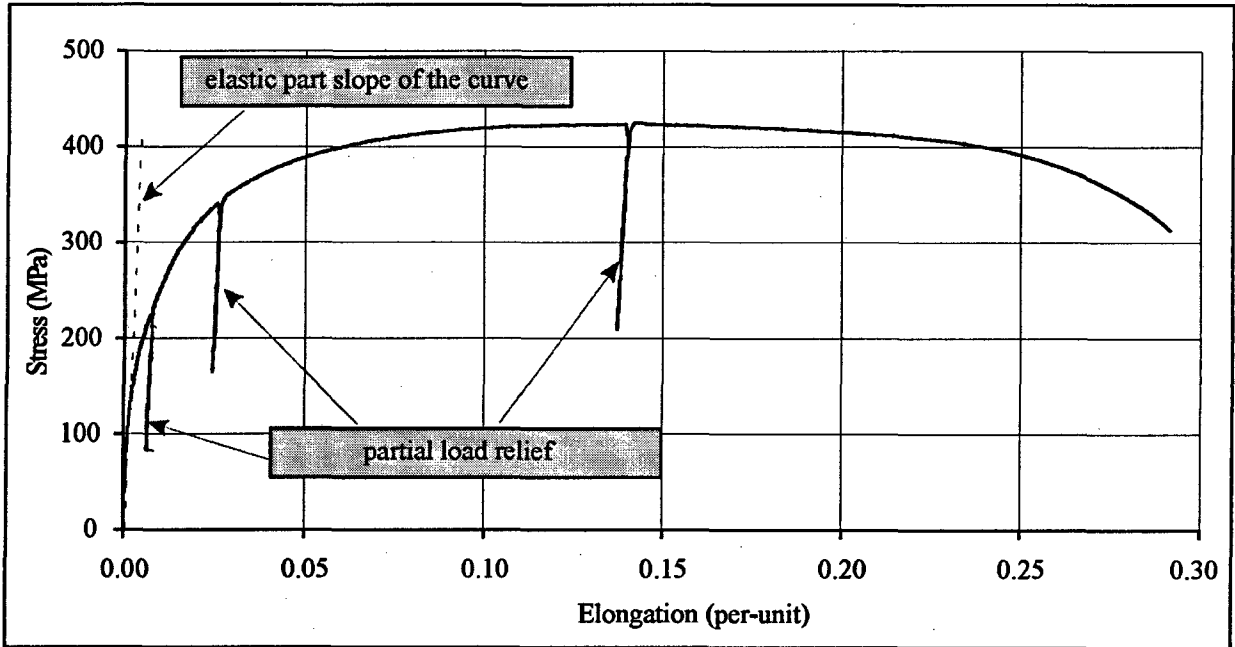
Fig. 6.20. Diagram of the cylindrical specimen deformation

Special experiments were performed to determine the dependence of the inclination angle of partial relief lines on the temperature; their results are presented in Fig. 6.21.
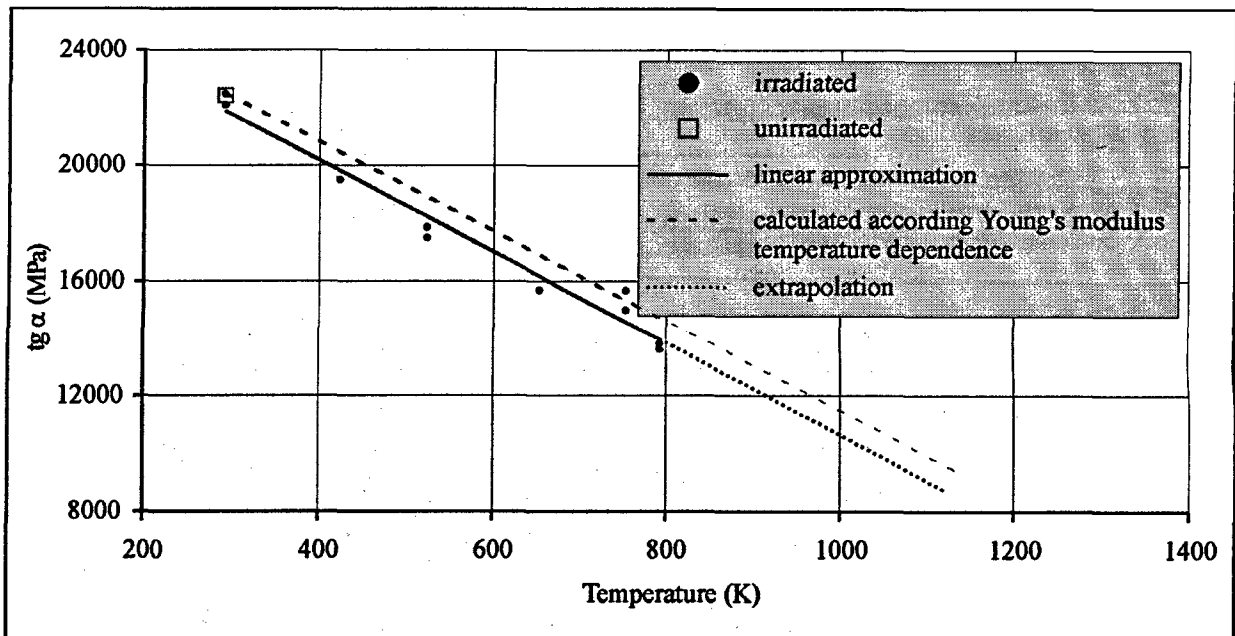
Fig. 6.21. Dependence of the inclination angle of partial relief lines on the temperature

The solid line represents the linear approximation of experimental data, and the dotted line corresponds to the Young's modulus dependence on the temperature (see section 5.6) related according to formula (4) to one of the experimental points. A good agreement between the calculated and experimental lines confirms the possibility of using partial relief lines for the determination of the elastic component of the ring specimen deformation in a wide temperature range. Above data are presented for irradiated specimens, however a weak irradiation influence on the Young's modulus [3] allows to use these data for unirradiated specimens; this is confirmed also by test results for an unirradiated specimen at the temperature of 293 K.

Due to a low accuracy of the load determination at high temperatures, experiments to determine the dependence of the inclination angle of partial relief lines on the temperature were performed only for the temperature up to 800 K, however the above noted good agreement of data with the calculated dependence that is of the linear nature allows to use the linear extrapolation in the temperature region of 800 – 1200 K.

The temperature dependence was further used to determine the real inclination angle of the linear section of the diagram.

Determination of the proportionality limit

It is obvious that the value of the residual elongation determined according to the diagram depends not only on the adopted inclination angle of the linear section, but also on the selected origin of the coordinates. Theoretically, this is the problem of determining the proportionality limit - the load at which a deviation from the linear law begins. In the standard procedure this problem was solved as shown in Fig. 6.14, by the continuation of the linear section until it crossed the abscissa axis. After this, the straight line, that was distant by 0.2 % from the coordinate origin, allowed to determine the yield stress without the determination of the proportionality limit in an explicit form. In the modified procedure the proportionality limit must be determined directly, since, to determine the coordinate origin, the point of the diagram corresponding to the limit must be used to draw the straight line with the real inclination angle that is significantly different from the inclination angle of the pseudo-linear section.

The analysis of deformation diagrams obtained within the framework of the present work allowed to develop a formalized approach for the determination of the proportionality limit on the basis of the following mathematical considerations.

Let us have an ideal diagram (Fig. 6.22 a), that has the linear form $y_1=kx$ at section $0<x<x_1$ and the arbitrary form $y_2=f(x)$ at section $x_1<x$, and conditions $y_1(x_1)=y_2$ (x_1) and $dy_1/dx(x_1) = dy_2/dx$ (x_1) are satisfied in the point x_1. It is obvious that the point x_1 for first derivative is the inflection point, and for second derivative - the point of discontinuity and of the maximum negative value (Fig. 6.22 b, Fig. 6.22 c).
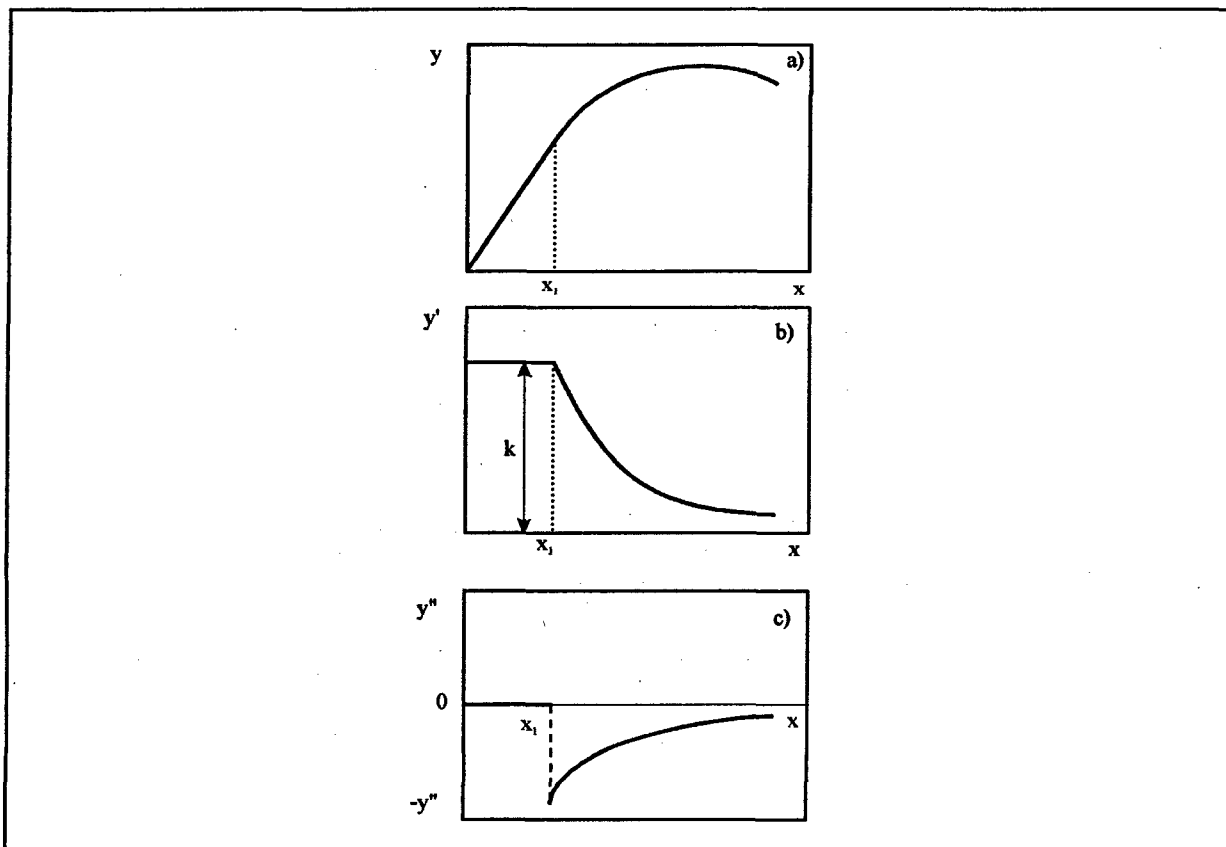
Fig. 6.22. Method to determine the proportionality limit using the second derivative

The real diagram of the ring specimen deformation and the dependence of its second derivative are presented in Fig. 6.23. As expected, at the pseudo-linear section of the diagram the second derivative is not equal to zero, but has positive values that reflect the change of the specimen shape, however a sharp reduction of the second derivative to maximum negative values is rather obvious. It is this approach to determine the proportionality limit in the point of the maximum negative value of the second derivative that was used for the processing of diagrams according to the modified procedure.
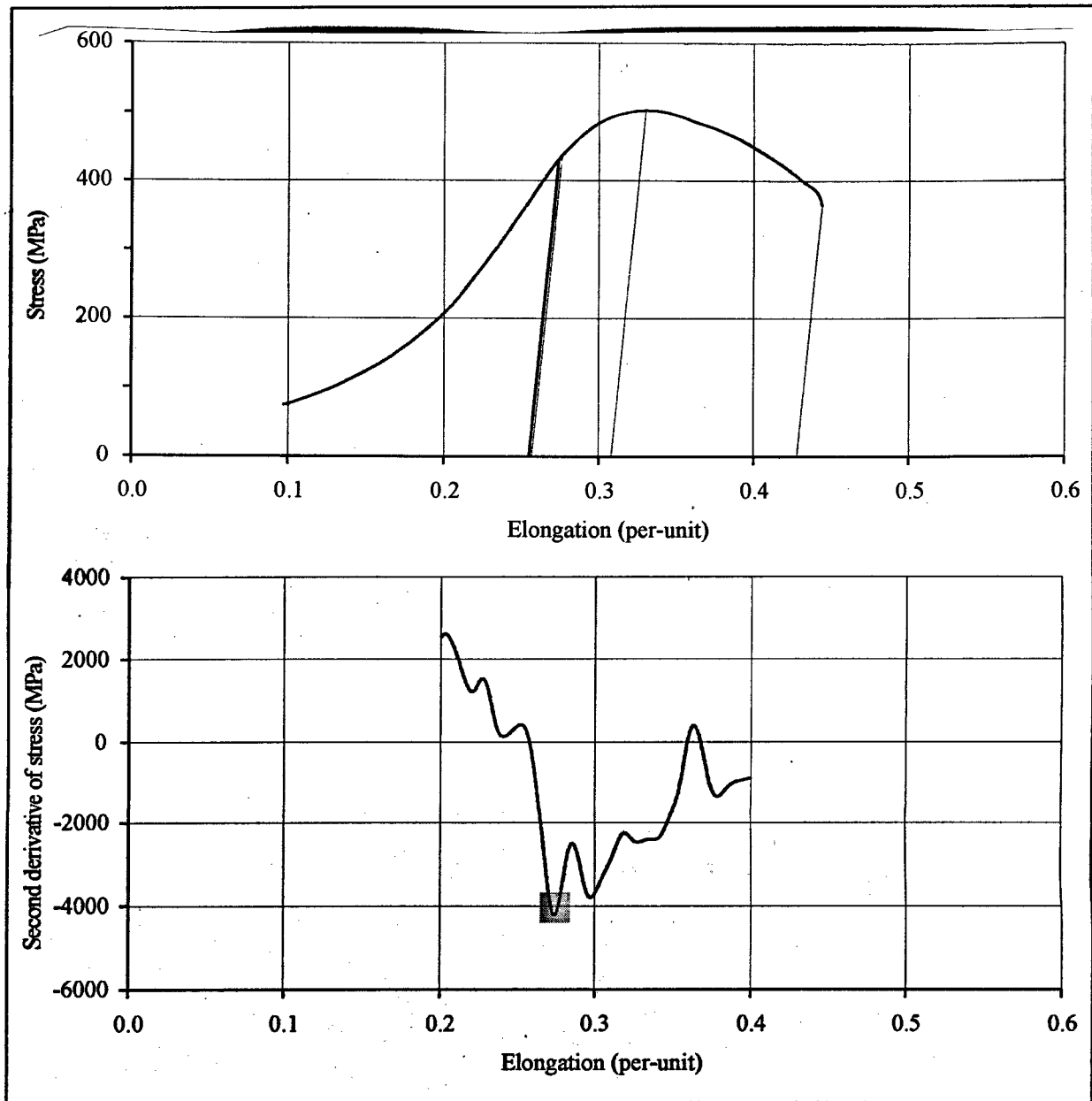
Fig. 6.23. Determination of the proportionality limit using the second derivative

6.2.7.2. Determination of the gauge length

As it has already been indicated, the formula to determine the gauge length l_g was obtained as a result of special studies at the end of 1970s, and since then has been used within the framework of the standard procedure. Nevertheless it was necessary to confirm it during current studies due to the following reasons:

6.31

- it is obvious that many changes and upgrades of both the test equipment, and cladding manufacturing technology took place since the conduct of the above studies;

- the standard procedure to determine short-term mechanical properties of simple ring specimens was developed and validated as a single complex that included the formula of l_g determination, and it would be inappropriate to believe that it is possible to adjust certain parts of the procedure while leaving other parts intact;

- due to significant differences obtained in results of comparative experiments with the participation of specialists from the USA and France it was necessary to perform a careful analysis of all provisions of the procedure.

However, since the problem of the validation of the gauge length of the simple ring specimen in a wide temperature range for various types and dimensions of specimens and mandrels requires a large scope of experiments, and taking into account a serious degree of studies of the past, in spite of above shortcomings, a decision was made to perform a selective verification of the applicability of the old formula to our conditions.

For this purpose, the polished face surface of the original specimen was marked using a micro hardness indentor. The marking is impressions near the internal and external surfaces at the distance of about 0.1 mm from the edge. The distance between the impressions is about 0.18 mm. The appearance of the specimens with marks is shown in Fig. 6.24.
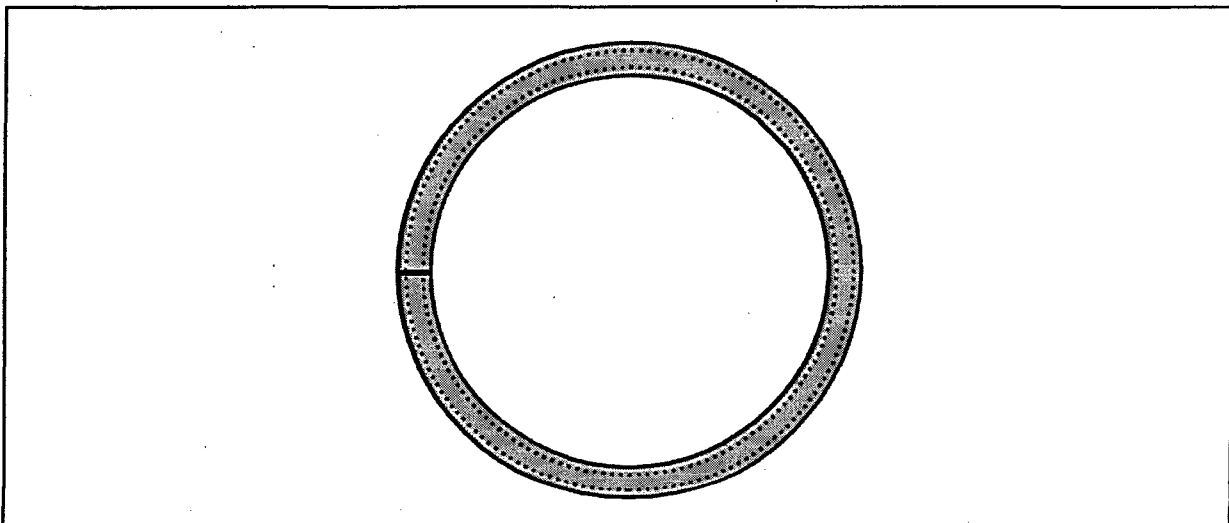
Fig. 6.24. Appearance of the original specimen with marks

The specimen tension was interrupted in several points of the diagram: approximately in the middle of the pseudo-linear section, in the region of the proportionality limit and ultimate strength limit. Changes in distances between analogous marks for various points of the diagram were measured for each specified point. The scheme of the processing of measurements to determine the specimen length, that participated in the elongation is presented in Fig. 6.25.
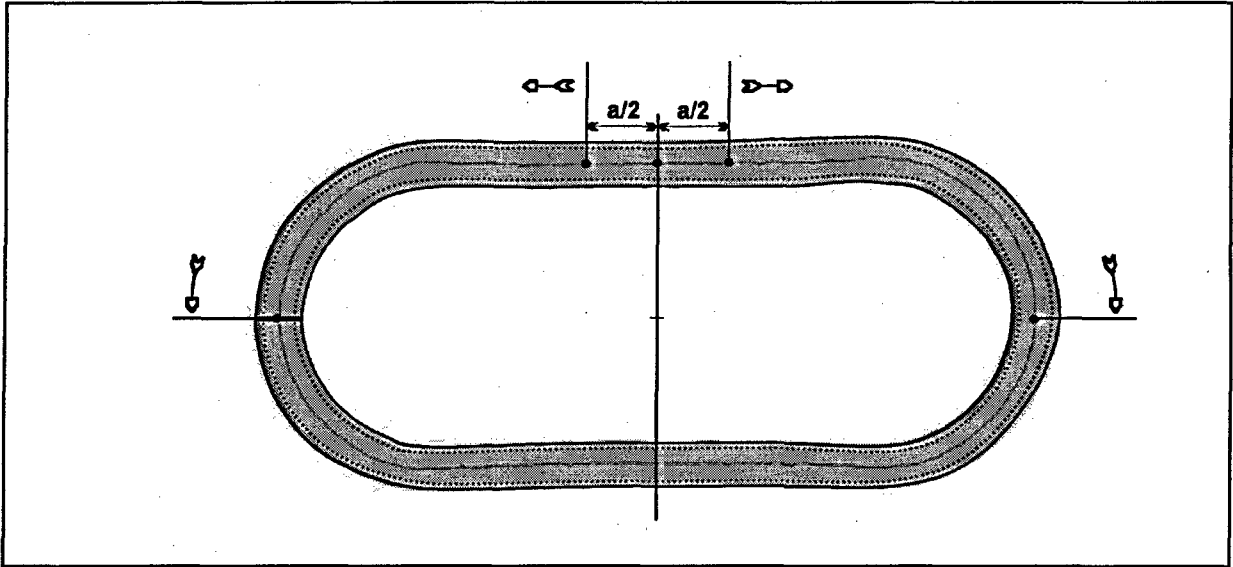
Fig. 6.25. Scheme of the processing of measurement results to determine the gauge length

It is obvious that with the increase in the length of the segment a, that changes symmetrically relative the specimen center in both directions, the share of the deformation occurring within this segment in comparison with the deformation of the entire specimen will increase and will reach 100 % when the length of the segment a becomes equal to the working length of the specimen. In this case, at sections with the uniform deformation, the dependence of the deformation share on the variable length of the segment must be of the linear nature. Results of the processing of the specimen elongation measurement according to this scheme are presented in Fig. 6.26.
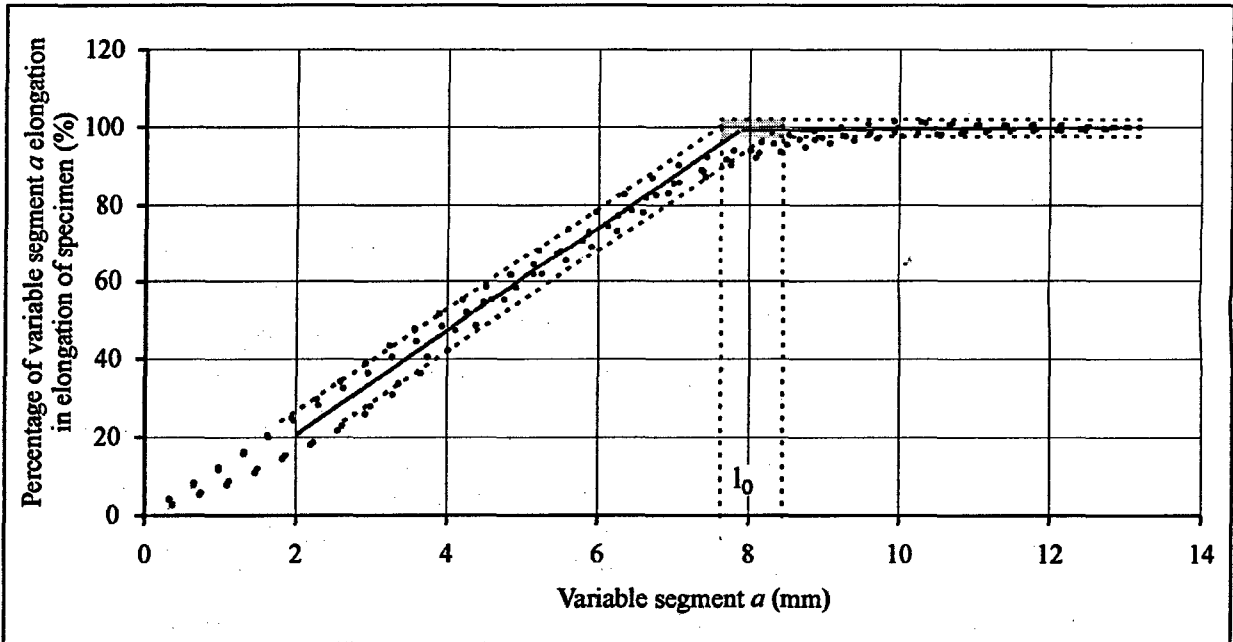
Fig. 6.26. Determination of the gauge length

As it can be seen from the above results, the dependence of the deformation share on the segment length is well approximated by a straight line, and the segment length that makes practically all the contribution to the elongation is close to the value of the gauge length of 7.85 mm determined according to the old formula. Fig. 6.27 shows results of determining the gauge length for various temperatures.

6.33
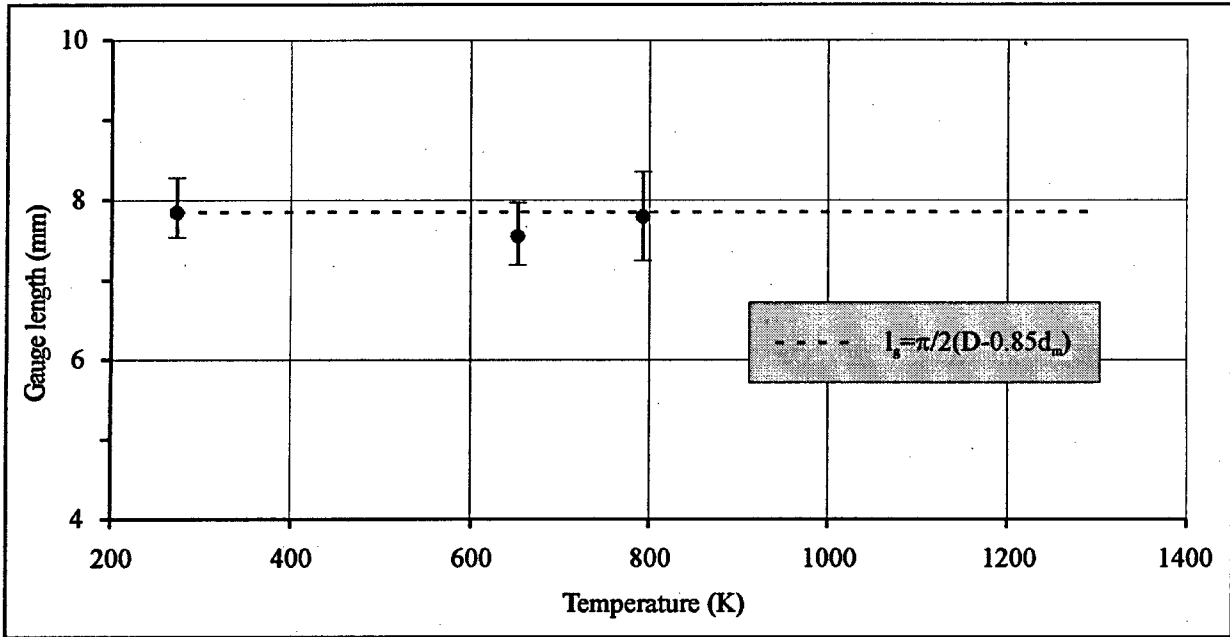
Fig. 6.27. Dependence of the specimen gauge length on the temperature

6.2.7.3. Confirmation of the modified procedure in general

A special test was conducted to confirm the modified procedure, its results are presented in Fig. 6.28. The unirradiated ring specimen A was tested in accordance with the standard approach. The unirradiated ring specimen B was pre-loaded to about 90 % of the yield point, i.e. the formation of the loop was practically completed. After that the specimen B was annealed at the temperature of 580°C during 3 hours, and then was subjected to another test till rupture. The curve B in Fig. 6.28 corresponds to the specimen loading after the annealing.

It is obvious that the annealing operation returns initial properties of the non-deformed specimen, and the comparison of curves A and B allows to detect the influence of specimen shape changes on mechanical properties.

UE(%)	TE(%)	YS(MPa)	US(MPa)	
6.7	33.1	284	328	(A)
8.6	31.3	267	322	(B)
8.8	31.0	280	329	(A$_{mod}$)
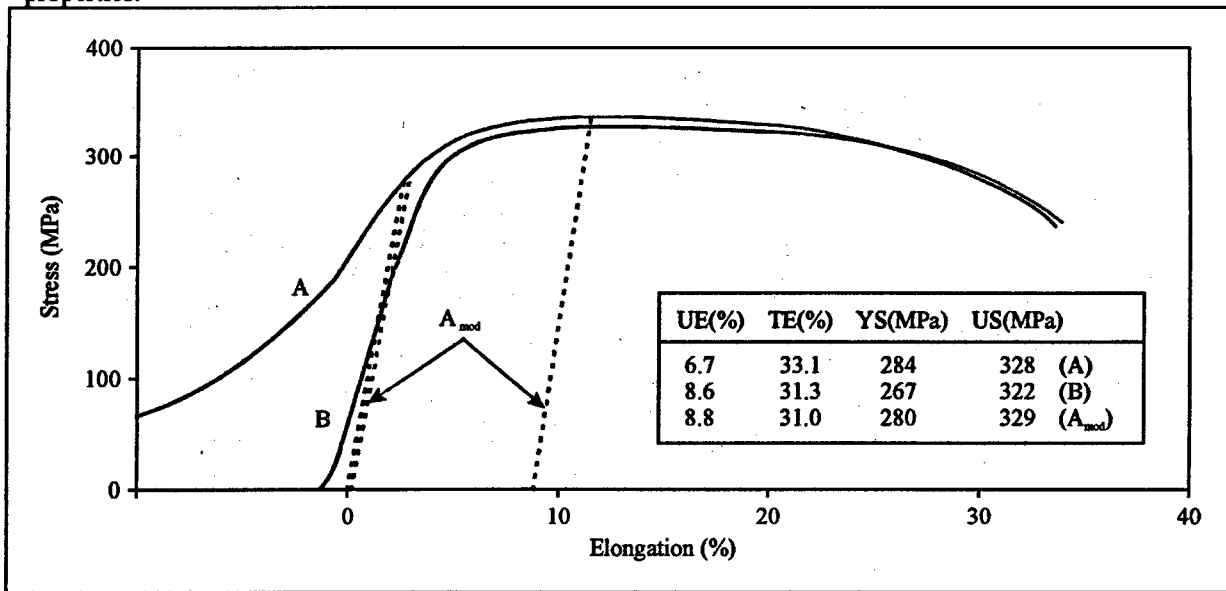
Fig. 6.28. Confirmation of the modified procedure on the test results for the specimen which was annealed after prestretching

6.34

The processing of curves A and B using the standard procedure revealed the 1.9 % difference in the relative uniform elongation. This difference corresponds to the partial plastic deformation in the process of specimen shape changes and is in a good agreement with the result of direct measurements of the residual circumferential deformation presented in the description of Fig. 6.16. The processing of the curve A using the modified procedure (dotted lines A_{mod}) results in the value of the uniform elongation, that is only by 0.2 % different from that for the curve B; in combination with a good agreement of the appearance of curves B and A_{mod}, this confirms the fact that the modified procedure allows to rather adequately determine mechanical properties based on tensile test results of simple ring specimens without the conduct of the intermediate annealing.

This modified procedure was used to obtain the data base with mechanical properties of unirradiated and irradiated Zr-1%Nb cladding. The last stage of this work was checking the results obtained with help of modified procedure for conformity to the power law $\sigma = K\varepsilon^n$. The result of application of the given procedure to the RIAR and CE-Saclay data (see Fig. 6.15) is presented in Fig. 6.29:

- the RIAR true stress-strain curve becomes quite linear;

- deviations of the CE-Saclay true stress-strain curve from a straight line are reduced;

- difference in the yield stress between the RIAR and CE-Saclay is negligible;

- the RIAR and CE-Saclay uniform elongations are coincided.
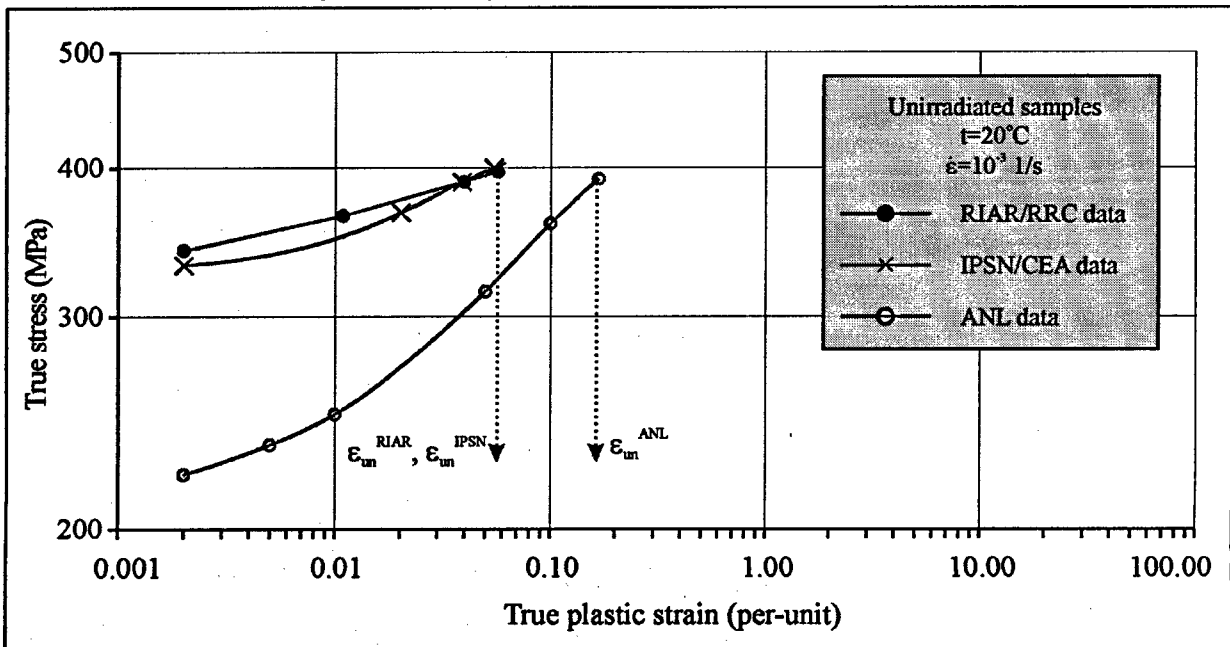
Fig. 6.29. Example of corrected stress-strain curve

6.2.8. Results of the tests to measure mechanical properties of Zr-1%Nb cladding

Data base characterizing results of the tests for unirradiated VVER tubes and irradiated VVER cladding is presented in Appendix J of Volume 3. This data base consists of the following data:

- parameters to characterize the state of the VVER unirradiated tube and VVER irradiated cladding, which were used to fabricate ring specimens;

- photographs of ring specimens after the tensile tests;

- data base with mechanical properties of Zr-1%Nb versus temperature and strain rate.

Main provisions of the procedure to measure mechanical properties with the help of simple ring specimens are presented in the previous section. This section describes data processing procedures, and systematization of the obtained results.

Measured types of mechanical properties

According to the final procedure the following properties were to be determined for each of the tested specimen:

- yield stress;
- ultimate strength;
- uniform elongation;
- total elongation.

The whole set of those properties was measured in accordance with initial procedure described in section 6.2.7. After the results of individual measurements of mechanical properties were generalized, correlation dependencies of mechanical properties versus temperature and strain rate were to be obtained. The following statistic procedure was worked out to perform this task.

Statistic procedure to obtain correlations for mechanical properties of Zr-1%Nb cladding

The first stage of this procedure was intended to exclude crude measurement errors from the data base. The following standard criterion was used for this purpose:

$$\frac{\left|x_{max(min)} - \bar{x}\right|}{S\sqrt{(n-1)/n}} \leq \tau_{1-p},$$

where $\bar{x}$ = sample mean;

$x_{max(min)}$ = such element of the sample that $\left|x_{max(min)} - \bar{x}\right| = \max$;

S = sample standard deviation;

n = number of measurements;

τ_{1-p} = distribution quantile;

$1-p$ = confidence level.

Confidence level was selected as 0.99, and crude measurements were removed from the measurement results. Then the regression analysis was used to obtain correlations for mechanical properties versus temperature.

It has been already noted in section 6.1 that mechanical properties depend complicatedly versus temperature. Different physical phenomena are revealed under certain temperature ranges, that is why it was considered not expedient to look for universal dependencies describing every type of mechanical properties in the whole range of the tested temperature (293 – 1223 K). Still, the approach based on development of certain correlations for each temperature subinterval calls for the necessity to determine the boundaries of those intervals. One formal method applied by the regression analysis for this class of tasks was used during the first stage of this studies. This method describes the files with the measurement results obtained for some random (but reasonable from the standpoint of researcher) temperature range with the help of the following equation:

$$\bar{b} = \left|\bar{X}^T \bar{X}\right|^{-1} \bar{X}^T \bar{Y},$$

where $\bar{b}$ = vector of regression coefficients;

$\bar{X}$ = action matrix;

$\bar{Y}$ = response vector;

T = sign of transposition of operation;

-1 = sign of inversion of operation.

This equation is transformed into the following regression equation:

$$y = b_o + b_1 x + b_2 x^2 + \ldots.$$

The power index for this equation was chosen by minimization of the sample standard deviation in accordance with the following expression:

$$S = \sqrt{\frac{\sum_{i=1}^{n}(y_{im} - y_{ir})^2}{n-1}},$$

where S = sample standard deviation;

y_{im} = measured value of the parameter;

y_{ir} = calculated value of the parameter using regression equation;

i = current measurement;

n = number of measurements.

The procedure was arranged in such a way that the boundary of the chosen temperature range was step by step shifted towards its broadening. This was done until abrupt increase of the sample standard deviation occurred. That was the sign that there existed breakpoint of some derivative, that is why the structure of the regression equation was to be changed [19]. Operations of this type performed for different sets of temperature sub-ranges, allowed to reveal all the breakpoints and to finally define the boundaries of temperature sub-ranges, for which the best regression equations for each mechanical property were obtained. Thus, it was recommended to describe ultimate strength with the help of correlation dependencies corresponding to four temperature sub-ranges:

1. 293 – 779.55 K

2. 779.55 – 903.55 K

3. 903.55 – 1123.99 K

4. 1123.99 – 1273 K

Those ranges were obtained for unirradiated cladding. Similar ranges were defined for irradiated cladding, and for other mechanical properties. Statistic processing of results characterizing mechanical properties versus strain rate was also performed with the help of regression analysis. Still, the volume of sample for each strain rate was limited in this case. That is why we used the a priory information that the straight line describes the dependence of strength versus strain rate in logarithm coordinates. Hence the linear regression analysis of the obtained data base was done, and the coefficients of respective regression equations were calculated. The result of statistic processing of all the measurement results was that correlation dependencies for all mechanical properties versus temperature and strain rate were obtained.

Correlations for mechanical properties of Zr-1%Nb cladding versus temperature

The set of correlations obtained by statistic processing of the measurement results is listed in Table 6.8, Table 6.9.

Fig. 6.30, Fig. 6.31 present the graphical view of correlations for the ultimate strength and yield stress.

Table 6.8. Correlations for mechanical properties of unirradiated Zr-1%Nb cladding vs. temperature

Parameter	Temperature range (K)	Property versus temperature
Engineering ultimate strength (MPa)	$293 < T \le 787.61$	$S_{ut} = 658.37 - 1.4605\,T + 0.00155977\,T^2 - 6.87908\ 10^{-7}\,T^3$
	$787.61 < T \le 903.55$	$S_{ut} = 11072.6\ \exp(-0.00555345\,T)$
	$903.55 < T \le 1123.99$	$S_{ut} = 308.857 - 0.260714\,T$
	$1123.99 < T \le 1273$	$S_{ut} = 32.6783 - 0.015\,T$
Engineering yield stress (MPa)	$293 < T \le 786.91$	$S_y = 502.9982 - 0.8738195\,T + 6.124696\ 10^{-4}\,T^2 - 1.418248\ 10^{-7}\,T^3$
	$786.91 < T \le 892.32$	$S_y = 10094.5\ \exp(-0.0055752\,T)$
	$892.32 < T \le 1125.38$	$S_y = 285.624 - 0.241928\,T$
	$1125.38 < T \le 1273$	$S_y = 44.4448 - 0.027619\,T$
Total elongation (%)	$293 < T \le 797.42$	$\delta_t = -18.9711 + 0.33792\,T - 0.000711456\,T^2 + 4.82512\ 10^{-7}\,T^3$
	$797.42 < T \le 921.36$	$\delta_t = 1.25035\ \exp(0.00442943\,T)$
	$921.36 < T \le 1128.97$	$\delta_t = -1193.07 + 2.52887\,T - 0.00125208\,T^2$
	$1128.97 < T \le 1223$	$\delta_t = 2052.89 - 3.3404\,T + 0.0014\,T^2$
Uniform elongation (%)	$293 < T \le 1223$	$\delta_u = 3.21877 + 0.0282662\,T - 0.460968\ 10^{-4}\,T^2 + 0.192154\ 10^{-7}\,T^3$

Table 6.9. Correlations for mechanical properties of irradiated Zr-1%Nb cladding vs. temperature

| Parameter	Temperature range (K)	Property versus temperature
Engineering ultimate strength (MPa)	$293 < T \le 742.27$	$S_{ut} = 608.908 - 0.0281736\,T - 0.000640119\,T^2 + 1.65407\ 10^{-7}\,T^3$
	$742.27 < T \le 847.04$	$S_{ut} = 7.63008\ 10^5\ \exp(-0.0105506\,T)$
	$847.04 < T \le 903.55$	$S_{ut} = 0.110726\ 10^5\ \exp(-0.00555345\,T)$
	$903.55 < T \le 1123.99$	$S_{ut} = 308.857 - 0.260714\,T$
	$112.99 < T \le 1273$	$S_{ut} = 32.6783 - 0.015\,T$
Engineering yield stress (MPa)	$293 < T \le 739.97$	$S_y = 690.3984 - 1.015694\,T + 0.001310936\,T^2 - 9.702603\ 10^{-7}\,T^3$
	$739.97 < T \le 846.56$	$S_y = 4.55945\ 10^5\ \exp(-0.0100762\,T)$
	$846.56 < T \le 892.32$	$S_y = 10094.5\ \exp(-0.0055752\,T)$
	$892.32 < T \le 1125.38$	$S_y = 285.624 - 0.241928\,T$
	$1125.38 < T \le 1273$	$S_y = 44.4448 - 0.027619\,T$
Total elongation (%)	$293 < T \le 750.35$	$\delta_t = -42.4625 + 0.392239\,T - 0.00083939\,T^2 + 5.80895\ 10^{-7}\,T^3$
	$750.35 < T \le 860.93$	$\delta_t = 0.289231\,T - 192.36$
	$860.93 < T \le 921.36$	$\delta_t = 1.25035\ \exp(0.00442943\,T)$
	$921.36 < T \le 1128.97$	$\delta_t = -1193.07 + 2.52887\,T - 0.00125208\,T^2$
	$1128.97 < T \le 1223$	$\delta_t = 2052.89 - 3.3404\,T + 0.0014\,T^2$
Uniform elongation (%)	$293 < T \le 749.01$	$\delta_u = 1.66205 + 0.0238493\,T - 0.512487\ 10^{-4}\,T^2 + 0.326065\ 10^{-7}\,T^3$
	$749.01 < T \le 870.67$	$\delta_u = -130.96 + 0.418691\,T - 4.21118\ 10^{-4}\,T^2 + 1.38229\ 10^{-7}\,T^3$
	$870.67 < T \le 1223$	$\delta_u = 3.21877 + 0.0282662\,T - 0.460968\ 10^{-4}\,T^2 + 0.192154\ 10^{-7}\,T^3$
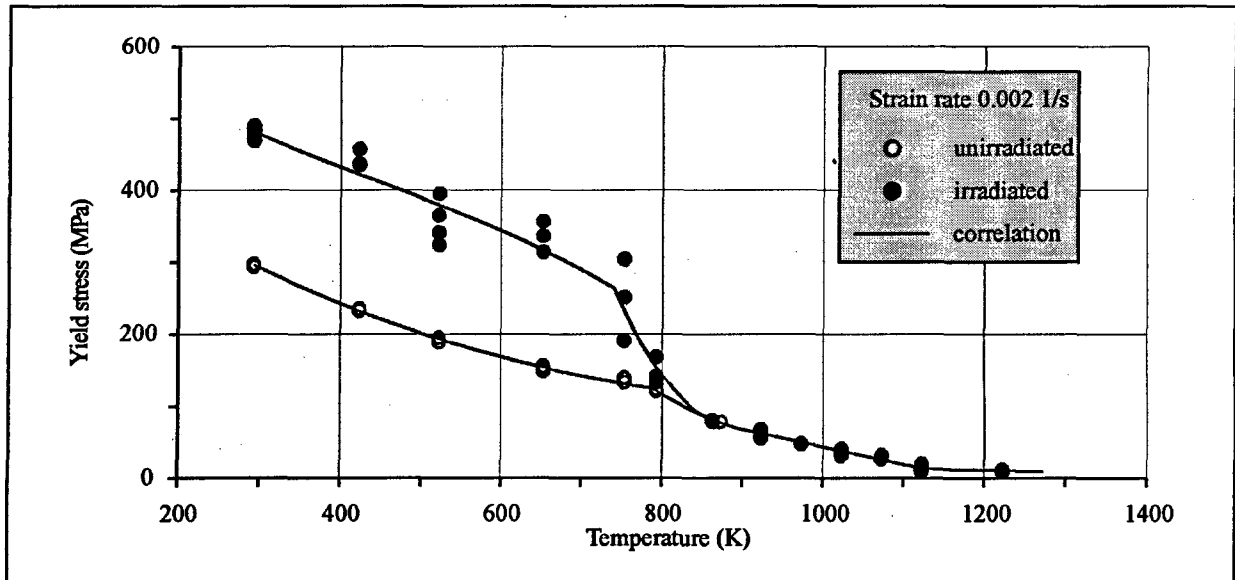
Fig. 6.30. Engineering yield stress vs. temperature for unirradiated and irradiated Zr-1%Nb cladding
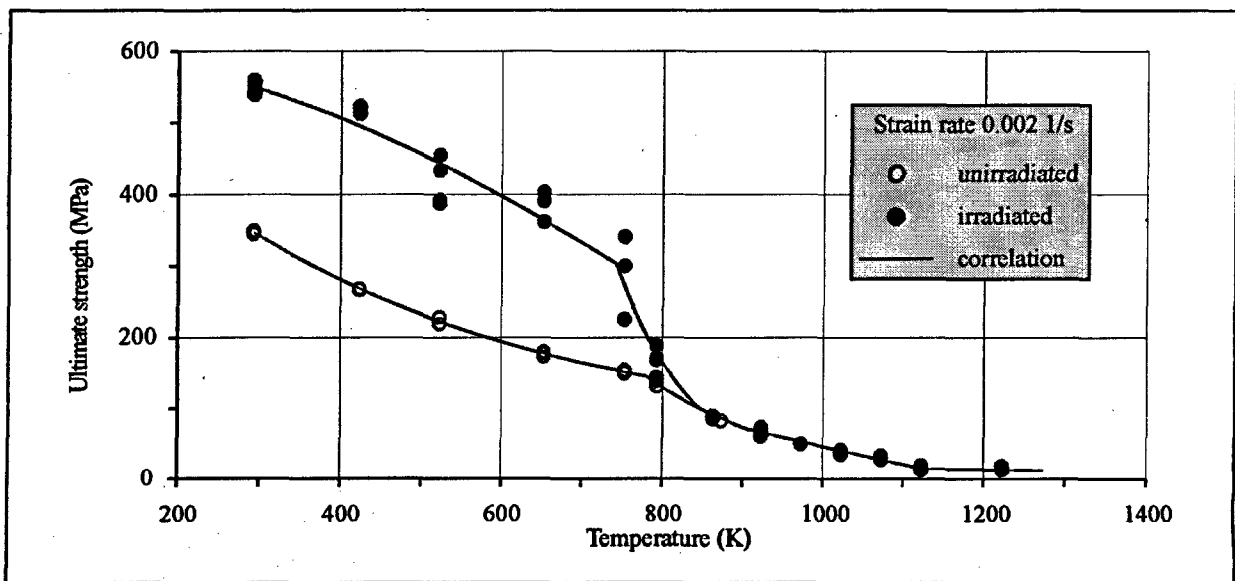
Fig. 6.31. Engineering ultimate strength vs. temperature for unirradiated and irradiated Zr-1%Nb cladding

Analysis of those correlations for unirradiated claddings allows to reveal the following important processes influencing mechanical properties of this cladding type versus temperature:

- lower temperature sub-range 293 – (780 - 790) K is characterized by monotonic reduction of strength properties;

- sub range (780 - 790) – (890 - 905) K reflects most probably the region of dynamic strain aging. In this case the strength of material at the beginning of this range depends slightly on the temperature, then it reduces greatly and reaches the value which could be obtained by extrapolation of correlations obtained for the lower temperature sub-range;

- the third temperature sub-range (890 - 905) – 1125 K practically coincides with the region of α - β phase transformation for Zr-1%Nb alloy. Additional analysis has demonstrated that the determined boundaries

6.39

of this range and the linear character of the dependence for strength parameters versus temperature satisfy the specified task with good accuracy;

- the fourth temperature region 1125 – 1273 K characterizes the strength of Zr-1%Nb alloy in the β phase. Linear approximation of experimental data was used, but the sample volume is not great, and it is not possible to insist that the correlations for this temperature sub-range could not be improved in the future.

It is also necessary to stress that the type of equations for original correlations obtained to describe strength of Zr-1%Nb cladding versus temperature coincides with the type of equations developed in MATPRO to characterize Zircaloy: polynomial of the third power, exponential function, linear functions. This fact objectively reflects the qualitative similarity of the mechanical behavior of these two alloys.

Analysis of the similar correlations for irradiated Zr-1%Nb cladding demonstrates significant strengthening of the cladding in the two lower temperature sub-ranges. This strengthening is obviously the effect of irradiation, because with the increase of temperature annealing of irradiation damages is revealed, and strength becomes worsened. The effects of annealing and dynamic strain aging are summed up in this temperature sub-range and their summarized influence determines the profiles of the corresponding curves. Shift of the point of the abrupt reduction of strength of irradiated claddings to the region of lower temperatures (in comparison with unirradiated claddings) corresponds well with the earlier obtained data that the maximum dynamic strain aging of irradiated claddings is shifted to the left because of the influence of annealing [5]. It is also interesting to note that the strength curves for irradiated claddings have the concave up shape in the temperature range of up to approximately 750 K, unlike the concave down shape of these curves for unirradiated claddings. Such change of the sign of the second derivative under the condition of approximately constant exposure time of the specimens under each of the specified temperatures can be explained by the increase of the rate of annealing of radiation defects under temperature growth.

Starting with 860 K strength parameters of irradiated and unirradiated Zr-1%Nb claddings practically coincide. According to the data presented in section 6.1 the total annealing time for the temperature of 860 K is about 2000 s, which corresponds to the exposure time of specimens in the given tensile tests. Statistic analysis of the two samples with the measurement results for irradiated and unirradiated specimens was performed for the temperatures higher than 860 K. The analysis has demonstrated that both samples belong to one general set, and, hence, can be combined. That is why unified correlation dependencies were developed for both types of specimens in this temperature sub-range.

Correlations for total elongation of unirradiated and irradiated specimens are graphically presented in Fig. 6.32.
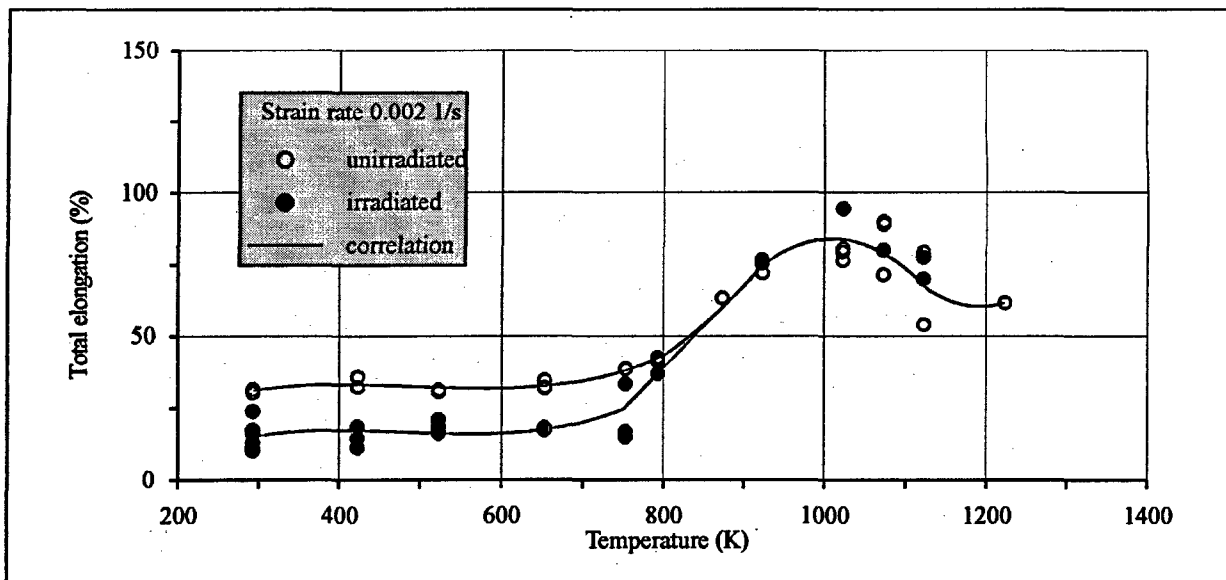

Fig. 6.32. Total elongation vs. temperature of unirradiated and irradiated Zr-1%Nb cladding

Statistic analysis allowed us to reveal three typical temperature sub-ranges for the total elongation of unirradiated Zr-1%Nb claddings:

6.40

- The first sub-range 293 – 797 K is characterized by the fact that the expected monotonic increase of the total elongation versus temperature is interrupted because of the influence of the dynamic strain aging effect. Slow down of the ductility increase, connected with this effect, starts to reveal under the temperature of 450 – 500 K. The maximum of this effect is observed at the temperature of 600 – 650 K. Under this temperature total elongation is almost equal to total elongation at 293 K. Comparison of the temperature, at which the maximum reduction of total elongation is observed, with the temperature, at which the maximum improvement of strength is noted, indicates that maximum of the plasticity reduction is displaced relative the maximum of the strength increase in the direction of lower temperatures. This corresponds with the earlier obtained data characterizing the influence of dynamic strain aging onto mechanical properties of claddings [7].

- The second temperature sub-range (797 – 1000 K) is the sub-range where we observe the abrupt increase of the total elongation caused by the superplasticity effect. This effect described in section 6.1 is connected with phase transformation in Zr-1%Nb alloy. Total elongation in the point T = 1073 K makes ≈ 100 %.

- The third temperature sub-range (1000 – 1223 K) is characterized by a reduction in the total elongation and its value stabilization at the level of ~70%.

The specific feature of irradiated claddings is that total elongation of this type of claddings is practically twice less than the total elongation of unirradiated claddings for the lower temperature sub-range. The nature of total elongation curve in the second temperature sub-range – 750 - 860 K is determined by the effects of annealing of irradiation damages and superplasticity. Total elongation of irradiated and unirradiated claddings practically coincide at the temperature of about 860 K, thus indicating that annealing of radiation defects is practically over by this temperature.

As in the case of strength characteristics, at temperatures above 860 K samplings of unirradiated and irradiated claddings were combined and are described by common correlation dependencies.

It should be specially noted that temperature dependencies of the total elongation in the superplasticity region, presented in Fig. 6.32, are significantly different from results obtained at the first stage [23] and from the existing data base on unirradiated claddings, for which the maximum value of the total elongation reached 200 %.

As it has already been mentioned, since existing data on irradiated claddings and results obtained at the first stage were characterized by a large spread and different behavior of unirradiated and irradiated claddings in the superplasticity region, a decision was made to conduct additional experiments in this temperature region. A joint analysis of methodologies and results of these and previous experiments allowed to reveal the following:

a. Previous experiments were performed in the temperature region above 800 K using an analogue recording system;

b. Two maximum values of the total elongation of 134 and 175 % for irradiated specimens were obtained as a result of an erroneous diagram interpretation when, due to small loads that were close to the sensitivity limit, the specimen was considered as failed in case of the failure of the second, rather than the first neck. With a correct processing of diagrams, these values are reduced to 94 and 115 %, respectively;

c. The application of the modified procedure of the diagram processing to all earlier obtained results leads to a reduction of the total elongation value by 10 – 15 relative percents;

d. New experiments were conducted at all temperatures for unirradiated and irradiated specimens using the same equipment with the digital recording, were processed according to the modified procedure and have a much smaller spread;

e. In case of possible adjustments of results of previous experiments according to items b and c, the old and the new data bases become closer, however such adjustments can be conducted only using correction coefficients for the entire data base since there are no diagram available for each test.

Taking into account above considerations, as well as the fact that the main purpose of developing this data base is to obtain correlations for the use in computer codes, it was decided to use results of only new experiments in the data base.

In the graphical form, correlations for the uniform elongation of unirradiated and irradiated specimens are presented in Fig. 6.33
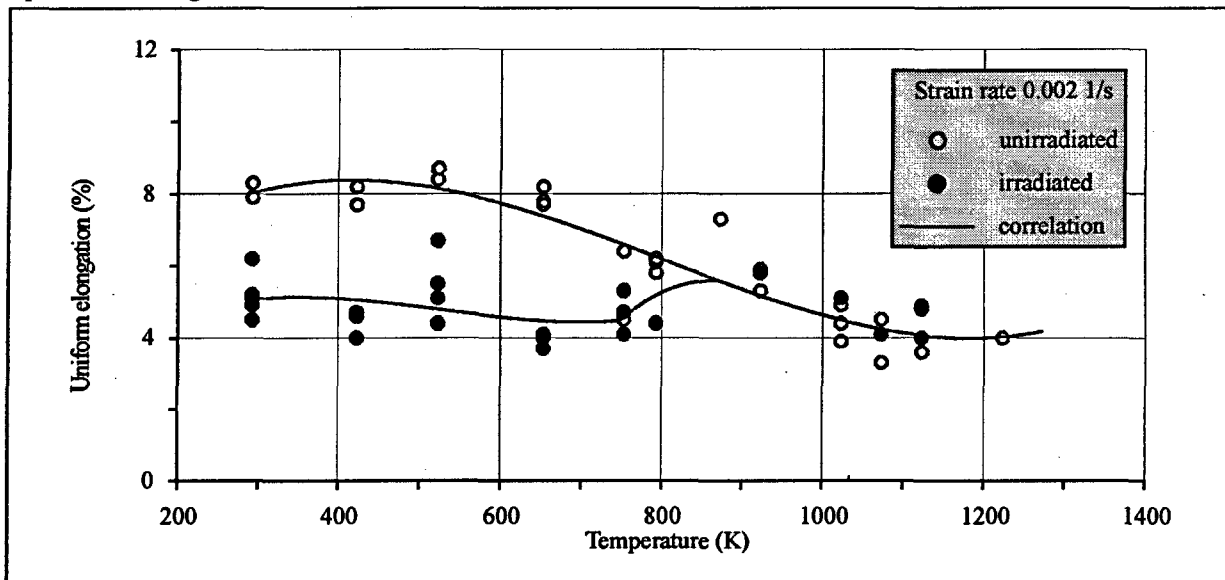

Fig. 6.33. Uniform elongation depending on temperature of unirradiated and irradiated claddings

As it has already been noted, a large spread of the relative uniform elongation in the existing data base and significant differences in results of the first stage of current studies and of trilateral comparative experiments were a reason of studies to improve the procedure and to conduct experiments of the second stage. Results of these studies allowed to obtain a rather consistent data base on the relative uniform elongation, described below.

Table files of all measurements, as well as of other mechanical properties are presented in Appendix J of Volume 3. The statistical analysis of data allowed to reveal three characteristic temperature subintervals for the relative uniform elongation of unirradiated claddings of Zr–1%Nb alloy:

- In the first subinterval (293 – 890 K), as in the case of the total elongation at temperatures 450 – 500 K, a slowdown of the plasticity growth is observed. Moreover, with a further temperature increase the uniform elongation decreases.

- The second subinterval (890 – 1073 K) practically coincides with the region of the α–β transition and is characterized by practically linear decrease in the uniform elongation.

- In the third subinterval (1073 – 1223 K) the value of the uniform elongation remains constant at the level of 4 %.

The temperature dependence of the uniform elongation of the irradiated cladding is similar to the nature of the unirradiated cladding dependence in the lower temperature subinterval, and as in the case of the total elongation it is 2 times smaller than for the unirradiated cladding. At temperature above 750 K, the annealing of radiation defects takes place, the value of the uniform elongation of the irradiated cladding increases, and at temperature 870 K the uniform elongation of irradiated and unirradiated claddings is the same.

Correlations for mechanical properties of Zr-1%Nb claddings vs. strain rate

Tabular files of all measurements are presented in Appendix J of Volume 3. According to the existing tradition it is accepted to describe the yield stress versus strain rate for Zr-1%Nb alloy by the equation [6]:

$$\ln \sigma_y = m \ln \dot{\varepsilon} + A ,$$

where σ_y = yield stress;

$\dot{\varepsilon}$ = strain rate;

m = strain rate sensitivity exponent;

A = constant.

6.42

I.e. yield stress in the double logarithmic coordinates is the straight line with the tangent of slope angle equal to m. Statistic processing of the measurement results according to this approach allowed to get correlation dependencies presented in Table 6.10 and in Fig. 6.34, Fig. 6.35. It is important to remember that comparison of the measurement results versus strain rate is to be performed for the same deformations of specimens. That is why it is usually yield stress to be used for this purpose, as this parameter always changes at the elongation equal to 0.2 %. The influence of strain rate onto other parameters is considered with the help of the law, which allows to consider dependence of these parameters versus strain rate. This approach will be described in detail in section 6.4.

Table 6.10. Correlations for yield stress vs. strain rate for unirradiated and irradiated Zr-1%Nb cladding

| Type of cladding	Temperature (K)	Yield stress (MPa) versus strain rate (1/s)
unirradiated	293	$\ln S_y = 0.0205123 \cdot \ln \dot{\varepsilon} + 5.94628$
	623	$\ln S_y = 0.0192842 \cdot \ln \dot{\varepsilon} + 5.20023$
	873	$\ln S_y = 0.104469 \cdot \ln \dot{\varepsilon} + 5.01359$
	923	$\ln S_y = 0.11364 \cdot \ln \dot{\varepsilon} + 4.80329$
	1023	$\ln S_y = 0.14491 \cdot \ln \dot{\varepsilon} + 4.57372$
	1073	$\ln S_y = 0.172774 \cdot \ln \dot{\varepsilon} + 4.53082$
	1123	$\ln S_y = 0.201979 \cdot \ln \dot{\varepsilon} + 4.18842$
	1223	$\ln S_y = 0.162062 \cdot \ln \dot{\varepsilon} + 3.02398$
irradiated	293	$\ln S_y = 0.0252894 \cdot \ln \dot{\varepsilon} + 6.29366$
	653	$\ln S_y = 0.0250984 \cdot \ln \dot{\varepsilon} + 5.90415$
	753	$\ln S_y = 0.0229939 \cdot \ln \dot{\varepsilon} + 5.7549$
	793	$\ln S_y = 0.0566845 \cdot \ln \dot{\varepsilon} + 5.26949$
	923	$\ln S_y = 0.131023 \cdot \ln \dot{\varepsilon} + 5.01256$
	1023	$\ln S_y = 0.19018 \cdot \ln \dot{\varepsilon} + 4.78353$
	1123	$\ln S_y = 0.180971 \cdot \ln \dot{\varepsilon} + 4.51703$
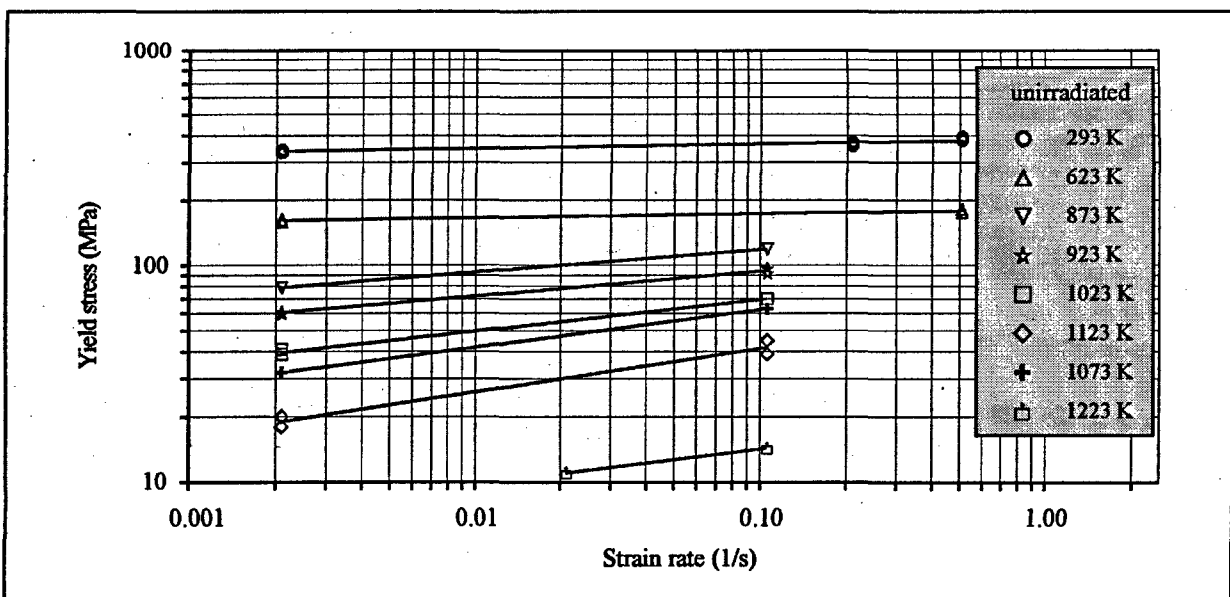
Fig. 6.34. Yield stress vs. strain rate for unirradiated Zr-1%Nb cladding
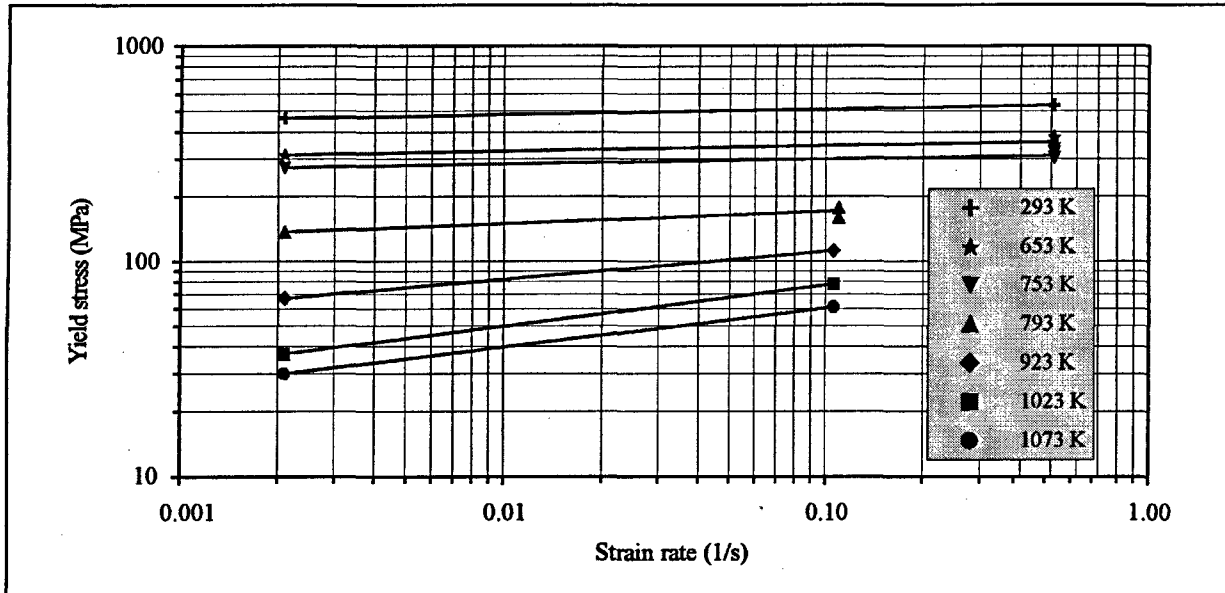
Fig. 6.35. Yield stress vs. strain rate for irradiated Zr-1%Nb cladding

Analysis of correlations presented in Table 6.10 indicated that strain rate sensitivity exponents for unirradiated and irradiated Zr-1%Nb claddings does not differ from the studied temperature range. Qualitative physical assessment of the strain rate influence onto mechanical properties can be done with the help of analysis of the data presented in Fig. 6.36, Fig. 6.37.

So, the obtained results demonstrate that the cladding strength increases significantly when the strain rate increases from 10^{-3} l/s to $0.1 - 0.5$ l/s. In the absolute sense the influence of rate is mostly important for the temperature range of $750 - 1273$ K.
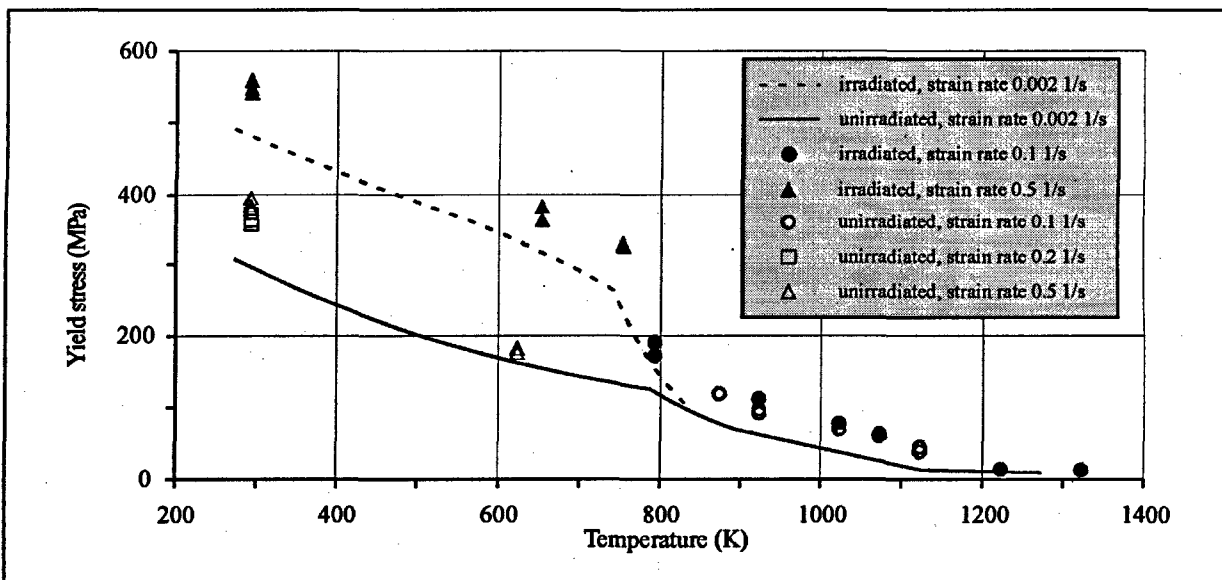

Fig. 6.36. Data base to characterize yield stress of Zr-1%Nb cladding vs. temperature and strain rate
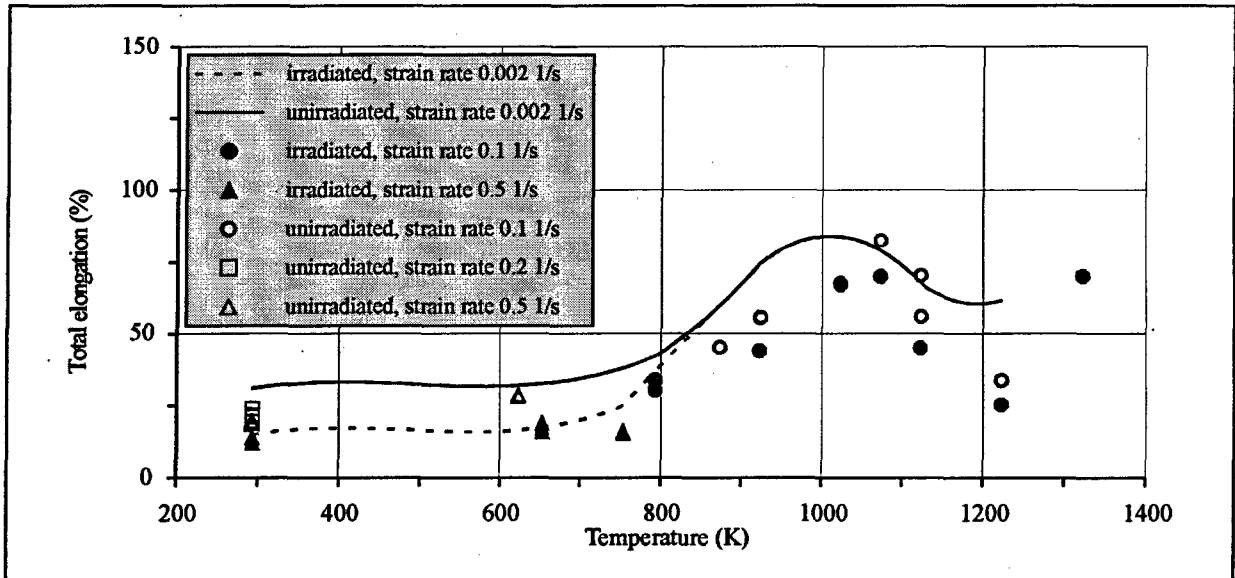
Fig. 6.37. Data base to characterize total elongation of Zr-1%Nb cladding vs. temperature and strain rate

Analysis of total elongation of unirradiated claddings is not completed yet. It is interesting, though, that total elongation of irradiated claddings demonstrates its insensitivity to the strain rate in the lower (up to 770 K) and upper (above 1100 K) temperature ranges. We still need to understand whether this is a real physical phenomenon or the deficiency of experimental data. Within $\alpha \rightarrow \beta$ transformation temperature range total elongation decreases significantly as the strain rate increases. But, it is necessary to perform additional measurements to reveal the tendency of the change of total elongation of β-phase of Zr-1%Nb alloy.

6.2.9. Summarizing of the obtained data base with mechanical properties of Zr-1%Nb cladding, and its analysis

The cycle of tensile ring tests allowed to obtain correlation dependencies describing mechanical properties of two types of claddings versus temperature (293 – 1273 K), and strain rate (0.002 – 0.5 l/s). The variation range of temperature and strain rate is sufficient to develop the MATPRO/VVER version necessary for computational analysis of IGR tests.

Analysis of the obtained data base has demonstrated the following:

- strength characteristics of Zr-1%Nb claddings versus temperature are original, and can not be described with the help of the data base for Zircaloy up to T = 860 K;

- under the temperatures higher than 860 K strength characteristics of Zr-1%Nb claddings do not depend on burnup and practically coincide with the properties of Zircaloy;

- total elongation of Zr-1%Nb claddings can reach 100 % for the superplasticity region, still additional measurements are to be done to improve accuracy of correlations for this region;

- total elongation of β-phase of Zr-1%Nb claddings versus temperature is to be also specified;

- the performed investigations have indicated that on the whole behavior of Zr-1%Nb specimens as the function of strain rate correspond to the behavior of Zircaloy specimens.

6.3. Measurements of parameters characterizing mechanical behavior of Zr-1%Nb cladding under ballooning conditions

6.3.1. Program and procedure of the burst tests

It has already been noted in section 6.1 that high temperature rupture of the cladding due to ballooning is the specific feature of testing VVER fuel rods under IGR conditions. It was important to obtain the data base to try to describe this process by computer codes. It should be mentioned that of the two considered codes only FRAP-T6 code allows to predict mechanical behavior of the cladding under ballooning conditions. That is why the program of special tests has been developed with consideration of FRAP-T6 code requirements to the respective data base. Still, the motivation targeted at better understanding of the ballooning key phenomena was also evidently present.

Burst tests of pressurized specimens are the classical type of tests to study ballooning phenomena. The special setup was developed for this (Fig. 6.38).

Each specimen 150 mm long was fabricated of the VVER tube, or irradiated VVER cladding. A special cap was placed in the bottom part of the specimen. The top part of the specimen was connected to the source of helium supply by the set of special technological elements. The whole assembly was located inside the protective capsule, which in its turn was put into electrical bakeout furnace. The history of temperature (T) and pressure (P) in the top part of the specimen was registered in the process of testing. Besides, the original structure of the furnace was designed to ensure video filming of the specimen surface during testing, and thus to obtain time history of the cladding hoop strain and burst. Fig. 6.39 presents the typical burst test scenario.
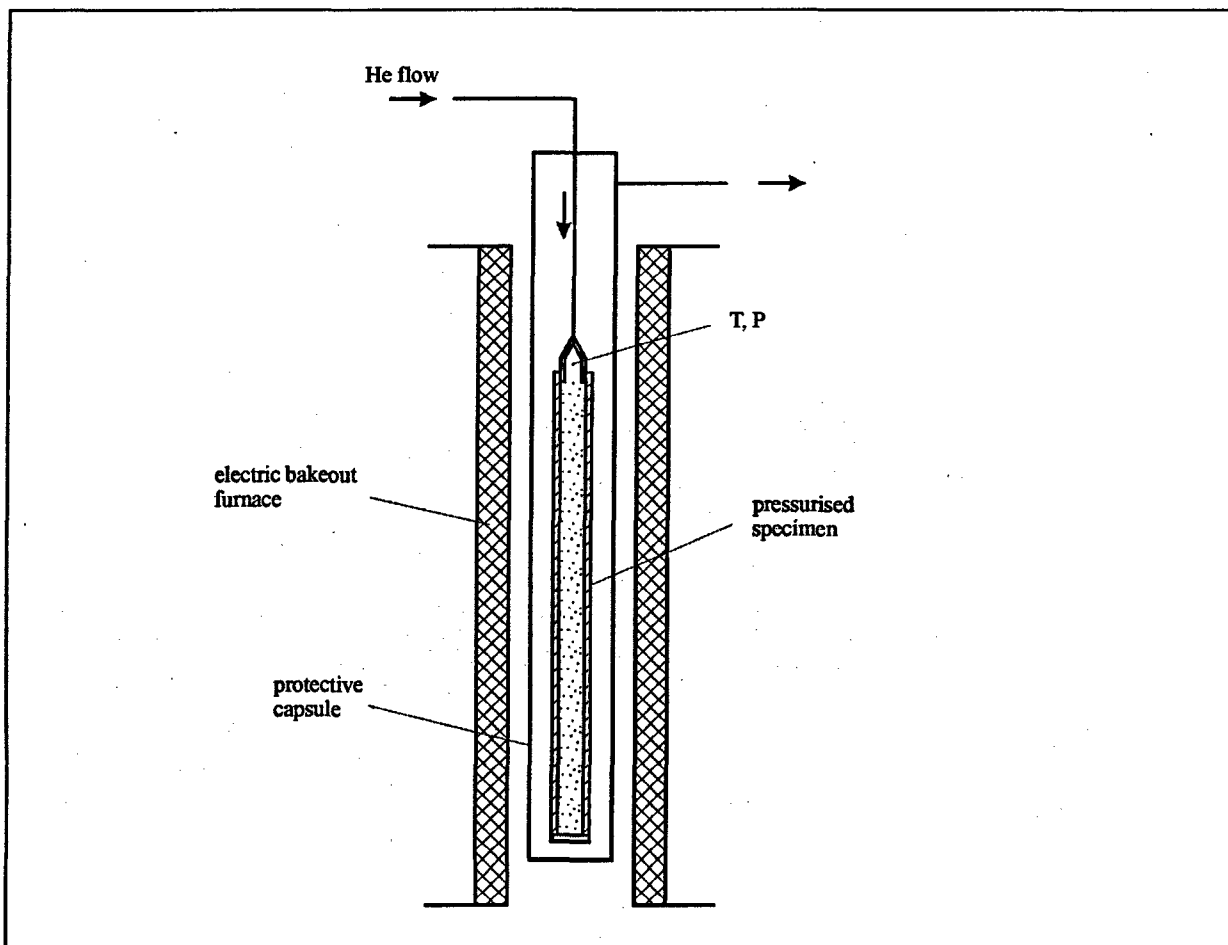

Fig. 6.38. Principle part of experimental setup for the burst tests

6.46
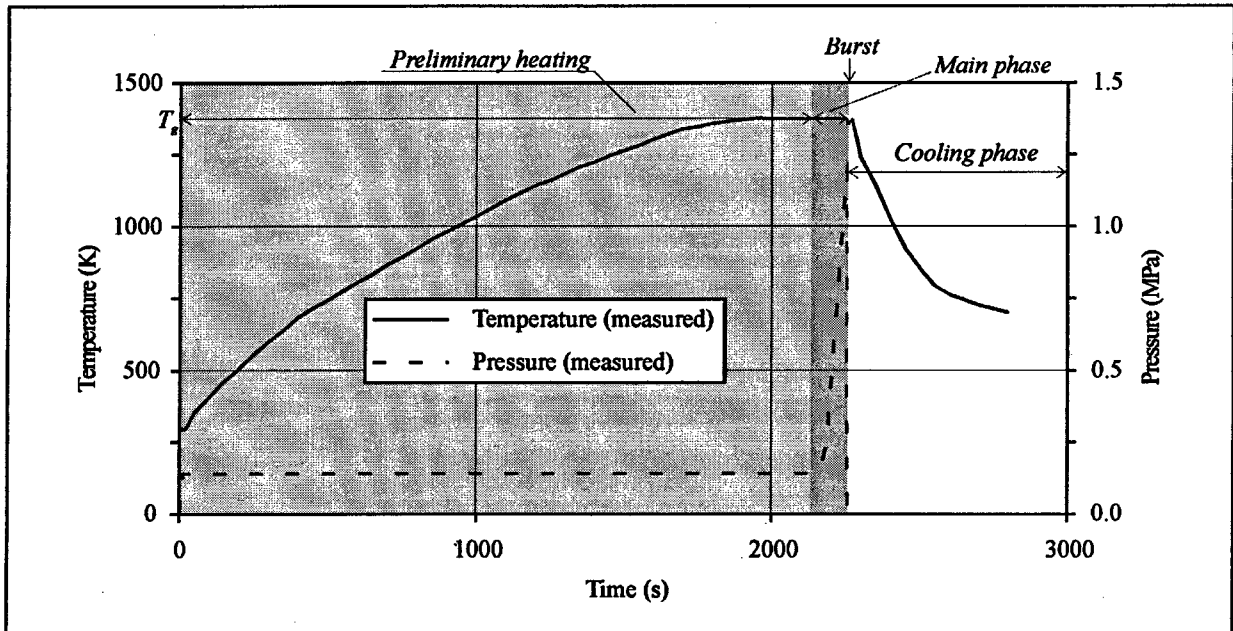
Fig. 6.39. Time history of the temperature and pressure for one of the burst tests

Preliminary heating stage of the scenario called for the step by step temperature increase of the specimen up to the specified T_g value under slightly excessive helium pressure inside the specimen. Non-uniformity of the temperature distribution along the specimen height and radius was not more than ±4°C. Then helium pressure inside the specimen was increased according to the specified value of the pressure increase rate up to the burst of specimen. After that the cooling phase took place.

The program of testing of unirradiated specimens called for measurement of the following parameters:

- pressure of the burst versus temperature and pressure increase rate;

- axial radius of the curvature of the cladding burst area versus temperature and pressure increase rate;

- circumferential elongation of the cladding burst area versus temperature and pressure increase rate.

The program of testing of irradiated specimens was the same but for the fact that no study of the influence of the pressure increase rate was planned.

Burst tests were performed for the following range of input parameters:

- temperature 1073 – 1473 K;

- pressure increase rate 0.01 – 1.0 MPa/s.

Two types of specimens were tested:

- specimens fabricated of unirradiated VVER tubes;

- specimens fabricated of the cladding of commercial VVER fuel element # 153 of the fuel assembly # 4108 irradiated at Unit 5 of NV NPP.

Two VVER tubes were used to fabricate unirradiated specimens for burst tests. Technological parameters of the tubes, and the methods used to measure their geometric dimensions were similar to the parameters and methods described in section 6.2.4 for simple ring specimens. The measured range of geometric dimensions variation was the following:

- specimen length – $150^{\pm1}$ mm;

- outer diameter – 9.136 - 9.149 mm;

- inner diameter – 7.712 - 7.735 mm;

- cladding thickness – 0.696 - 0.699 mm.

6.47

The data base characterizing parameters of unirradiated and irradiated specimens before burst tests is presented in Appendix K of Volume 3. The respective characteristics for irradiated specimens were obtained with the help of the following types of pre-test examinations:

- profilometry;

- eddy current examination;

- γ-scanning of fuel element.

These measurements showed that the outer diameter of irradiated cladding was equaled to $9.068 - 9.096$. Fuel burnup in the section used for fabrication of the specimens was $47.15 - 48.03$ MWd/kg U. The following parameters were measured with the help of metallographic cross-sections:

- cladding thickness $- 0.69 \pm 0.015$ mm;

- ZrO_2 thickness on the outer surface of the cladding $3 - 5$ μm;

- ZrO_2 thickness on the inner surface of the cladding < 1 μm;

- hydrogen concentration in the cladding $0.051 - 0.057$ % (by weight);

- hydrogen orientation in the cladding $- 0.36 - 0.41$.

After burst tests all the tested specimens were subjected to post-test examination to define specific ballooning parameters. The first stage of the work included making photographs of each specimen in different projections. Metallographic cross-sections were produced and their photographs made over the second stage of the post-test examinations, so that to get the view of the specimen in the center and at the boundary of the cladding rupture area. The third stage of examinations called for computer processing of the whole set of photographs according to the following issues:

- determination of the middle line profile for each cross-section of the cladding;

- measurement of the cladding thickness;

- measurement of the ballooning axial radius;

- measurement of the circumferential radius of the curvature;

- measurement of the peak circumferential elongation.

The necessary procedures, developed to measure every value are described further.

Determination of the middle line profile
Graphical illustration is presented in Fig. 6.40.
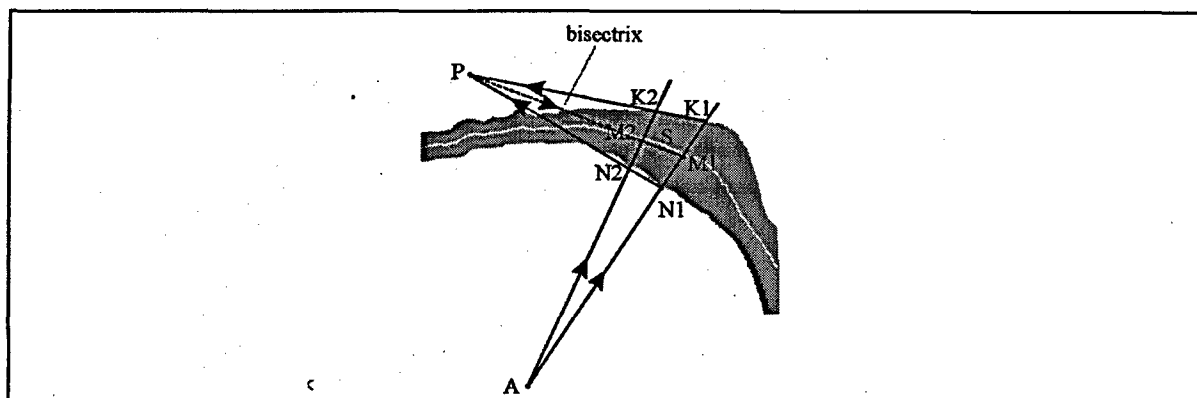
Fig. 6.40. Scheme to determine the middle line profile of the cladding cross-section

Geometric center, marked with point A is determined at the beginning. Then straight lines with the angle step equal to 0.5° are drawn from the geometric center of the figure. Two of these lines presented in Fig. 6.40 cross the cross-sections in points N_1, K_1 and N_2, K_2. Crossing of the two straight lines drawn through the points N_1, K_1 and N_2, K_2 determine the coordinates of the point P. Bisectrix of the angle formed by these two straight lines crosses the straight lines A-N_1-K_1 and A-N_2-K_2 in the points M_1 and M_2. The middle part of the section of the straight line connecting points M_1 and M_2 is defined as point S. This point lies in the middle line of the cross-section. Set of S_i points specifies the middle line profile.

Cladding thickness

Cladding thickness was determined versus azimuth angle by computer processing of the cross-section photograph. For each azimuth angle thickness measurement was made according to the normals for the cladding middle line. The example illustrating this procedure is presented in Fig. 6.41.
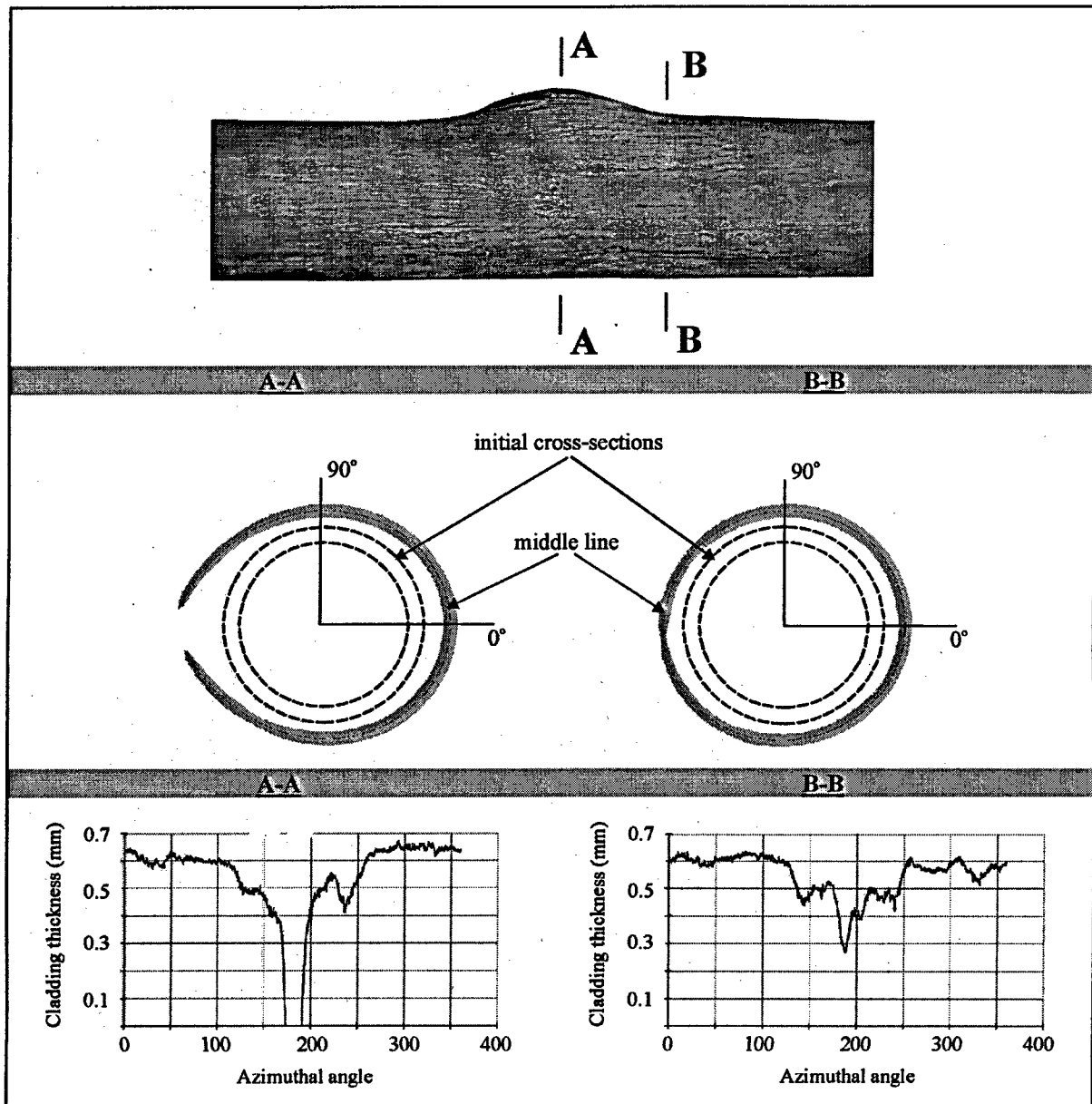

Fig. 6.41. Scheme of the procedure to determine cladding thickness vs. azimuth angle

It is important to note that A-A type of cross-section was fabricated for all specimens so that to characterize the cladding maximum hoop strain. This cross-section was made for the half of the cladding rupture length (Fig. 6.42). Cross-section of B-B type was cut so that to characterize the profile of the unfailed cladding for the part bordering the cladding rupture (Fig. 6.42).
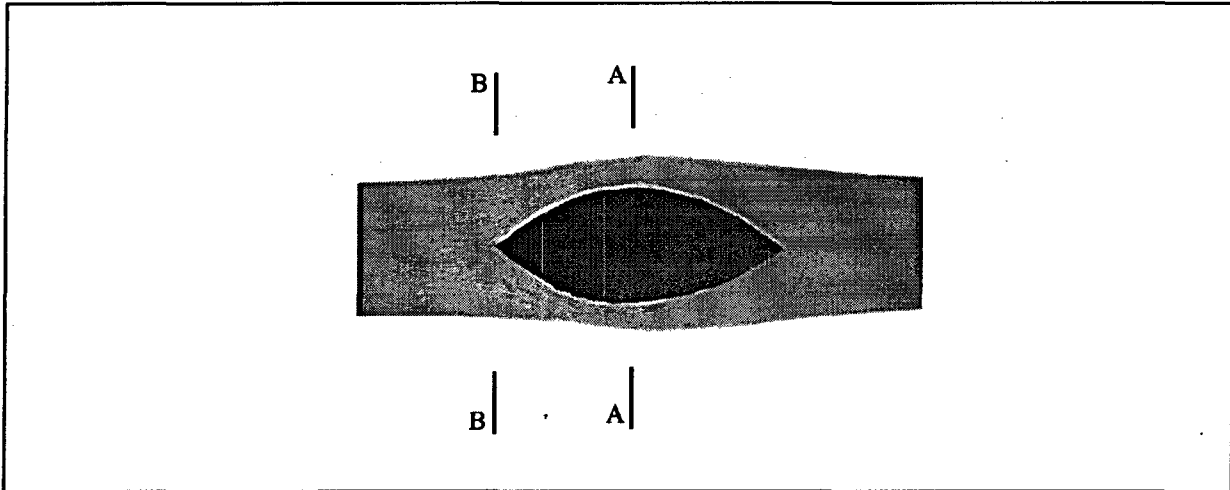
Fig. 6.42. Method to obtain cross-sections of A-A and B-B types

It will be shown in section 6.4.1 that the data base characterizing cladding thickness versus azimuth angle is not sufficient to calculate cladding failure. The special parameter called cladding thickness at the moment of burst (t_B) is to be also determined The special procedure was developed and described in MATPRO to determine this parameter using the results of burst test with Zry claddings. This procedure included measurement of the cleavage-like line (t_{cll}) presented in Fig. 6.43 for one of the cross-sections.
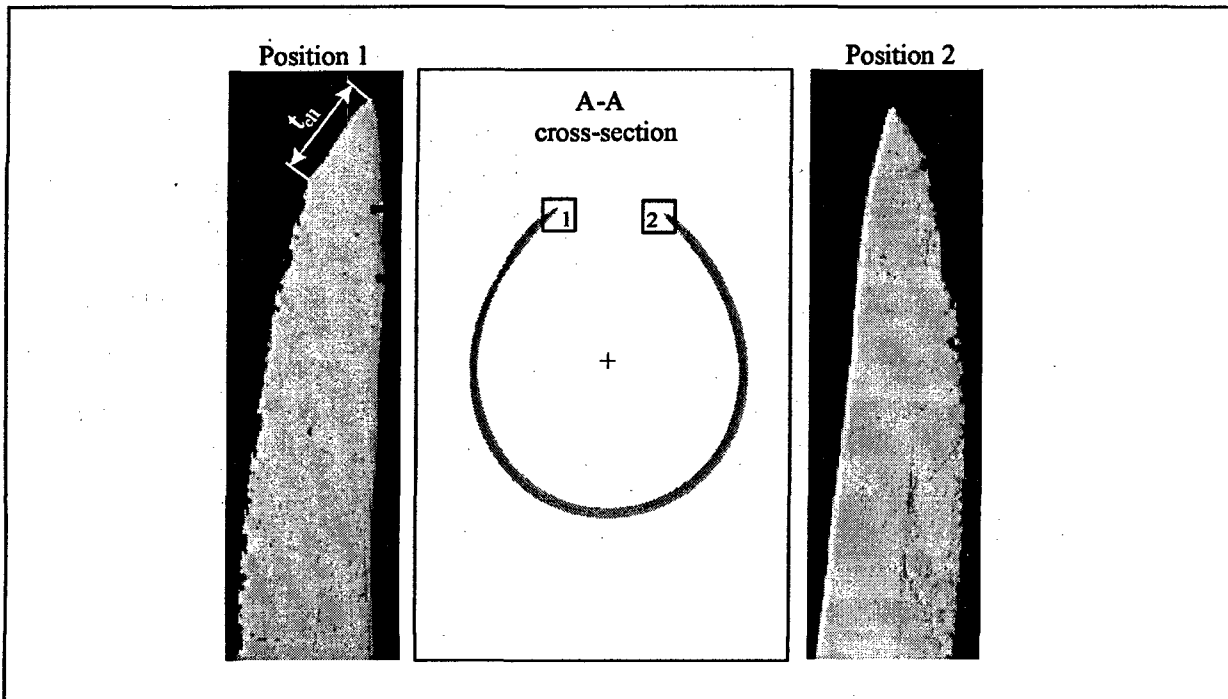
Fig. 6.43. MATPRO procedure to determine cleavage-like line presented for Zr-1%Nb specimen after the burst test

This example vividly illustrates that no clearly seen cleavage-like line is present in the tested specimens. The attempt to define t_{cll} for the part of the specimen presented in Position 1, and to compare this part with the part of the specimen presented in Position 2, indicates that it is either not possible to identify the cleavage-like line in Position 2, or the line is practically absent and the specimen rupture takes place at the nearly zero thickness of the cladding. Hence another approach was developed to determine cladding thickness at the moment of burst (t_B). This approach uses the following scenario of the cladding failure due to ballooning. The first phase of the process is characterized by the uniform reduction of the cladding thickness in all azimuth directions along with the increase of the pressure and temperature. Then the local necking of the cladding takes place. This process is schematically presented in Fig. 6.44.
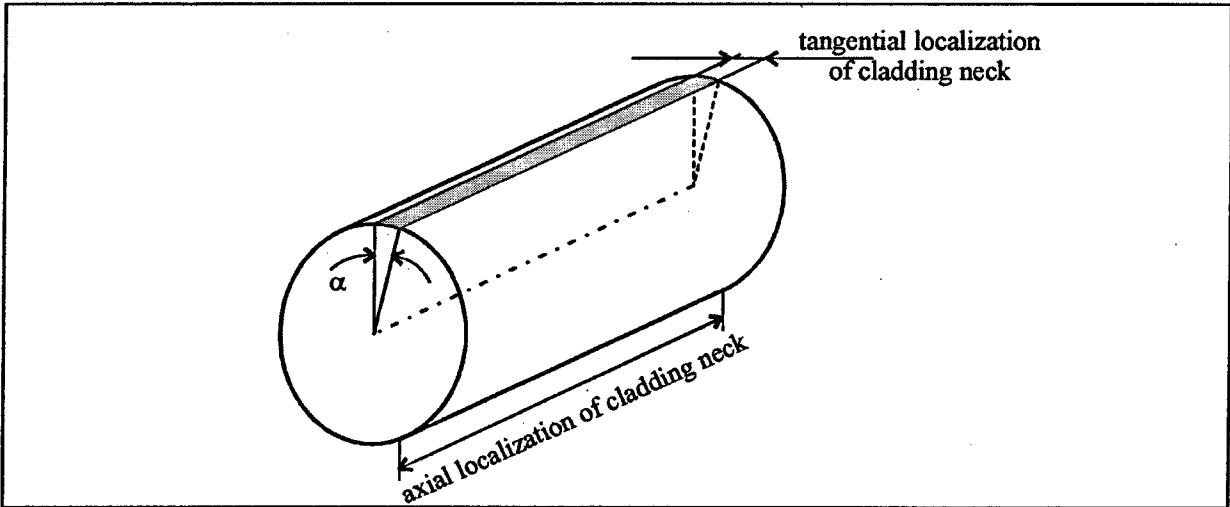
Fig. 6.44. Scheme of the cladding necking

In the part of the cladding with some length, limited by the α angle, neck is formed, which is characterized by the situation that neck thickness becomes less than the thickness of the rest cladding parts. The consequence of this is that circumferential elongation of the cladding in this part of it starts to increase quickly simultaneously with the continuous reduction of the cladding thickness. Maximum gradient of the change of both parameters is in the central part of the necking length. Cladding rupture is the final stage of this scenario. Analysis indicates that if the minimum thickness of the cladding neck is measured at the axial boundary between the ruptured and unfailed regions, we can get the criterion value of the cladding burst thickness (t_B). It has already been noted that the special set of B-B type cross-sections was intended for that purpose. Fig. 6.45 illustrates the procedure to determine t_B.
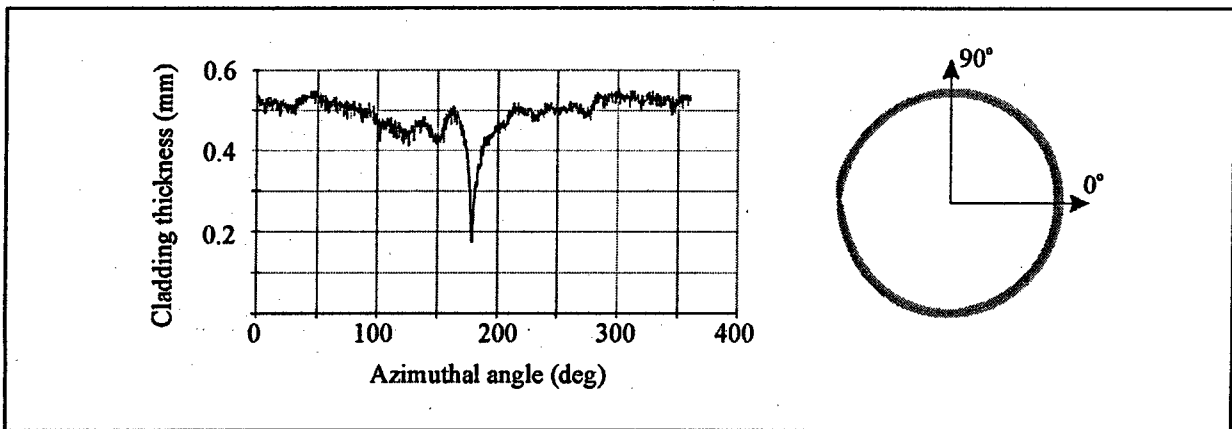
Fig. 6.45. Procedure to determine cladding burst thickness

Axial radius of ballooning

The procedure used to develop MATPRO package in order to determine axial radius of ballooning (r_Z) called for measuring of this parameter with the help of specimen photographs after burst tests. Fig. 6.46 presents this processing for Zr-1%Nb specimen.
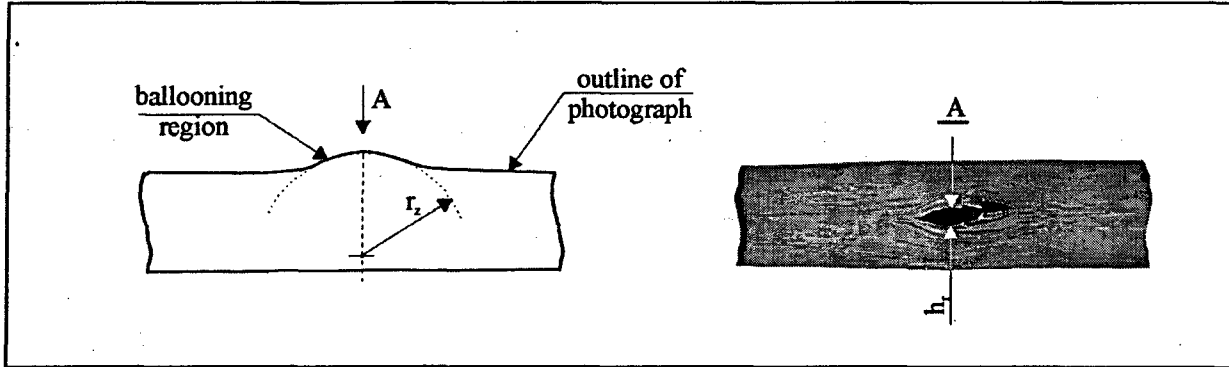
Fig. 6.46. Method to determine the axial radius of ballooning using MATPRO procedure

Analysis of this method indicates that it has a systematic error, because the axial radius of ballooning is to be determined before the edges of the cladding rupture tear are moved for h_r value. It is evident that if h_r value is not large in comparison with r_Z, this error can be neglected. Still the review of the respective data base indicates that it is not always that this requirement is satisfied. This issue is mostly important for the claddings tested under the parameters leading to significant strain (Fig. 6.47).
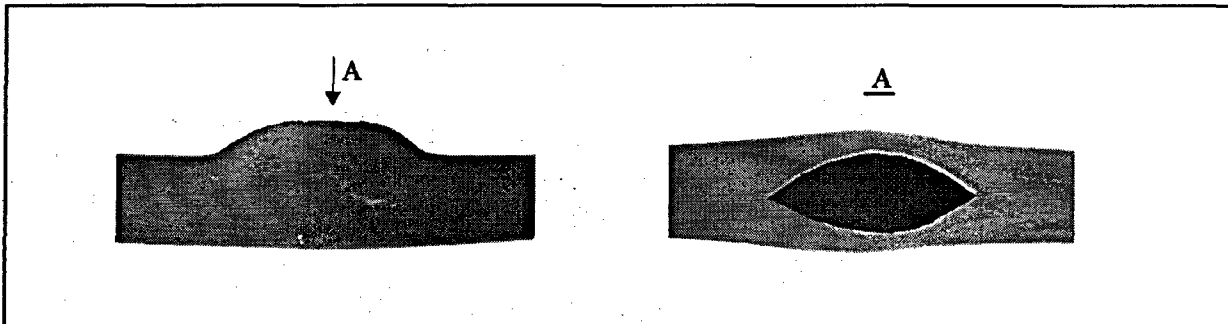
Fig. 6.47. View of Zr-1%Nb cladding burst under the superplasticity conditions

It is evident that the ballooning axial radius measured after the test and the ballooning axial radius just before the test differ greatly in this specific case. That is why another procedure was developed to determine r_Z. It was determined thus that the outlines of ballooning region for the tested specimens are characterized by the symmetry against the axis drawn along A arrow. That is why if the cross-sections of A-A and B-B types are fabricated for each specimen according to the procedure described above, r_Z value can be determined by the scheme presented in Fig. 6.48.

6.52

First step:

1.1. Restoration of shape of A-A cross-section at the burst.

1.2. Measurements of r_{A-A} and r_{B-B}.

Second step:

2.1. Two segments of the z length equal to the length between A-A and B-B cross-sections are plotted in the horizontal axis.

2.2. Vertical segments equal to r_{A-A} and r_{B-B} are plotted as shown in the graph.

2.3. The circle of r_z radius is drawn through the points 1, 2, 3.
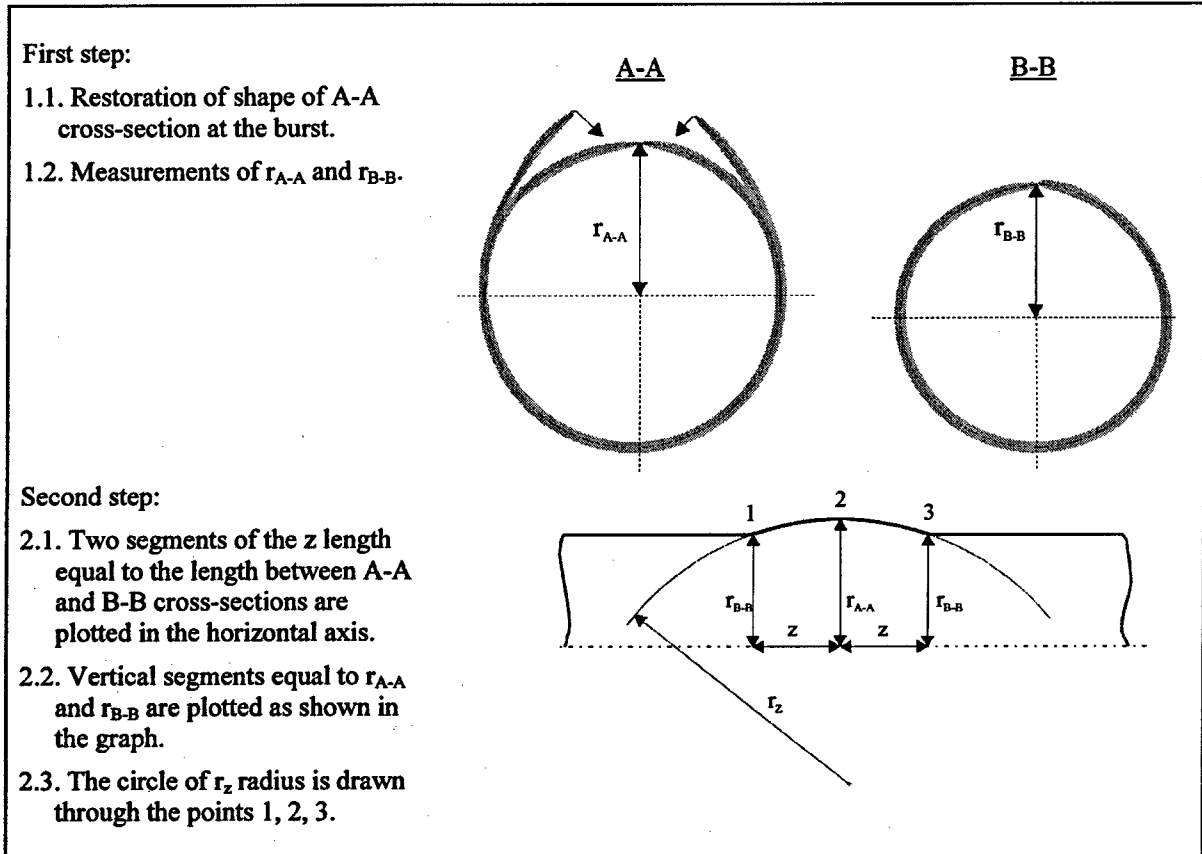
Fig. 6.48. Scheme of geometric procedures to determine axial radius of ballooning (r_z)

Circumferential elongation at the moment of burst

Measured length of the middle-line of the cladding cross-section in A-A position after the burst test (L_B), and the gauge length of the middle-line of the cladding cross-section before the burst test (L_o) were used to calculate circumferential elongation at burst by the following formula:

$$\varepsilon_\theta \; (\%) = \frac{L - L_o}{L_o} \, 100 \; \% \, .$$

Circumferential radius of curvature

According to the tolerances accepted in the MATPRO package circumferential radius of the curvature (r_θ) is the radius of such a circle for which the condition is correct that all the points of the middle line of the cladding cross-section, belonging to ballooning region in A-A position, are within this circle. With consideration of this definition the following expression was used to determine this radius:

$$r_\theta = r_{\theta o} \left(1 + \frac{\varepsilon_\theta}{100} \right),$$

where r_θ = circumferential radius of the curvature at the moment of burst (mm);

$r_{\theta o}$ = radius of the cladding middle line in the cross-section before the burst test (mm);

ε_θ = circumferential elongation at the moment of burst (%).

Fig. 6.49 illustrates the result obtained by this equation for one test of Zr-1%Nb cladding.
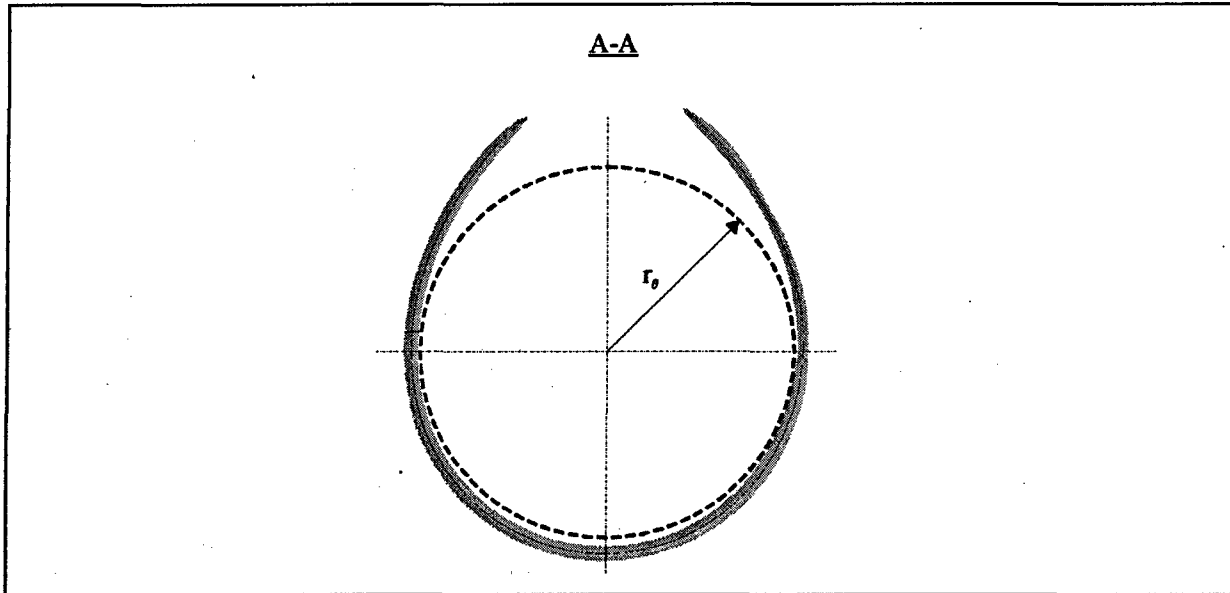
Fig. 6.49. Comparison of the cladding cross-section in A-A position after burst test and the restored profile of the cladding middle line at the burst moment

6.3.2. Results of burst tests

Data base to characterize burst tests is presented in Appendix K of Volume 3. It includes the following parameters:

- parameters of unirradiated and irradiated specimens before tests;
- photographs of specimens after tests;
- photographs of A-A and B-B type cross-sections of the specimens;
- tables with measured results.

Measurement results of burst pressure versus temperature are presented in Fig. 6.50.
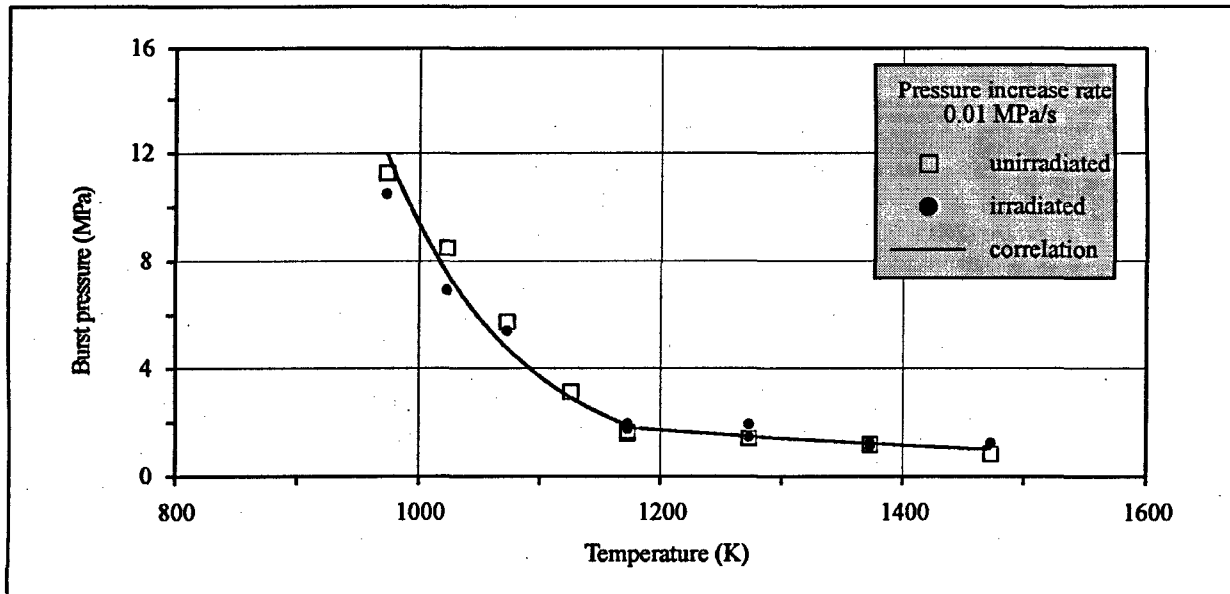
Fig. 6.50. Burst pressure vs. temperature for unirradiated and irradiated Zr-1%Nb cladding

These results confirm that mechanical behavior of unirradiated and irradiated specimens is identical under high temperatures. Statistic processing of obtained results allowed to get the following correlation for the burst pressure versus temperature. Analysis of this correlation indicates that in the temperature sub-range of 973 – 1173 K burst pressure decreases practically 6 times. This fact stresses the importance of studying the superplasticity temperature region for Zr-1%Nb alloy in order to reliably predict cladding failure due to ballooning. Burst pressure dependence versus temperature becomes less strongly expressed as the temperature continues to grow. Fig. 6.51 presents important results characterizing cladding hoop strain versus temperature.
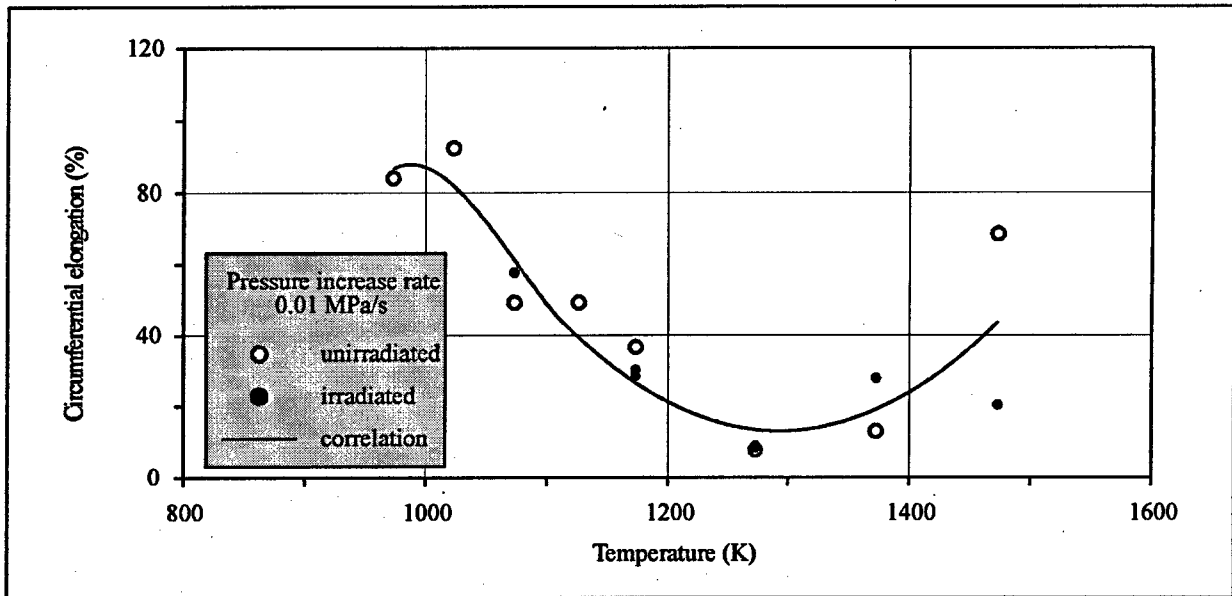

Fig. 6.51. Circumferencial strain at burst vs. temperature for unirradiated and irradiated Zr-1%Nb cladding

The obtained data indicate that as it has been already revealed with the ring specimens, cladding elongation decreases abruptly along with the $\alpha+\beta \rightarrow \beta$ phase transition. Beside that the tests indicate that beginning with 1273 K elongation of Zr-1%Nb starts to increase along with the increase of the cladding temperature. The correlations obtained for the burst pressure and cladding hoop strain are presented in Table 6.11.

Table 6.11. Correlations for burst pressure and maximum circumferential elongation vs. temperature

Parameter	Temperature range (K)	Correlation vs. temperature (K)
Burst pressure (MPa)	973<T≤1179	$P_B=94559.2 \exp(-0.0092216\ T)$
	1179<T≤1473	$P_B=19.1746 \exp(-0.200261\ 10^{-2}\ T)$
Circumferential elongation (%)	973<T≤1108	$\varepsilon_\theta=-25294.1 + 71.7577\ T - 0.067244\ T^2 + 0.0000208674\ T^3$
	1108<T≤1473	$\varepsilon_\theta=1589.11 - 2.43805\ T + 0.000942896\ T^2$

Moreover influence of pressurization rate on burst parameters was studied. Obtained results are presented in Fig. 6.52. As it was demonstrated for the case with ring specimens the results of the tests in logarithmic coordinates can be approximated by the straight lines. The tangent of the slope angle of these lines has the physical sense similar to the notion of strain rate sensitivity exponents that was introduced for ring

specimens. The data presented in Fig. 6.52 indicate that for all the tested temperature levels strengthening of the cladding, caused by pressurization rate growth, were observed.

This conclusion is in the agreement with the respective results obtained during testing of ring specimens.
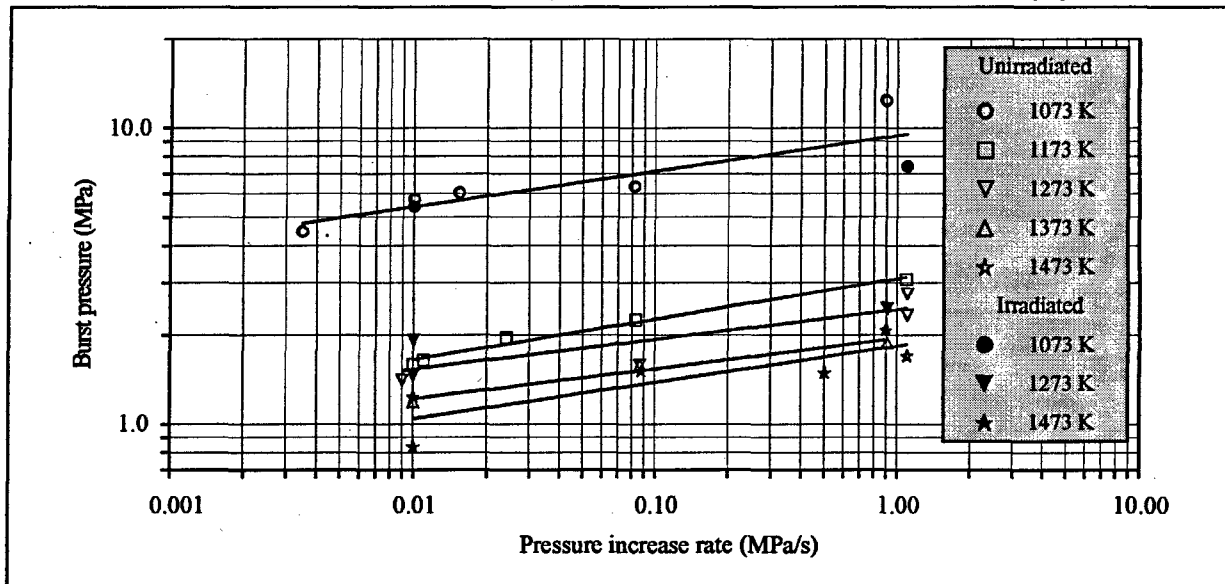
Fig. 6.52. Burst pressure vs. pressure increase rate at different temperatures for unirradiated and irradiated Zr-1%Nb cladding

6.3.3. Analysis of burst test results

It has been described in section 6.3.1 that burst tests with Zr-1%Nb specimens were performed with the help of a non-standard procedure. In this case the specimen was heated up to the specified temperature and then the gas pressure inside the specimen was increased until the cladding burst. The traditional testing procedure assumes that the cladding is loaded with the initial pressure, and then the specimen temperature, and as the consequence, pressure inside the specimen is increased until the cladding burst. Non-standard scenario was chosen to test Zr-1%Nb specimens, because the results of those tests were necessary to analyze the cladding behavior under RIA conditions. The proposed approach satisfies the main requirement to this data base, i.e. to exclude the influence of the cladding creep onto test results. This is the reason why the specimens were heated up to the specified temperature under the low pressure drop at the cladding. It is important to note that burst tests of unirradiated Zr-1%Nb specimens were performed earlier at VNIINM in the frames of the approach based on the controlled heating at the constant rate until the failure occurred [20].

In order to have the basis for formal analysis it is necessary to compare the results of different type of burst tests presented in Fig. 6.53. It is also important that the MATPRO data [2] are not uniform. Some part of it was obtained for the process of heating the specimens in inert environment, some specimens were tested in steam, heating rate was also different. Still, the generalized data base allows to make the following conclusions:

- abrupt decrease of the burst pressure is observed in the region of α–β phase transformation for both alloys;

- slight dependence of burst pressure versus temperature is noted for β-phase of Zr-1%Nb and Zry alloys.

6.56
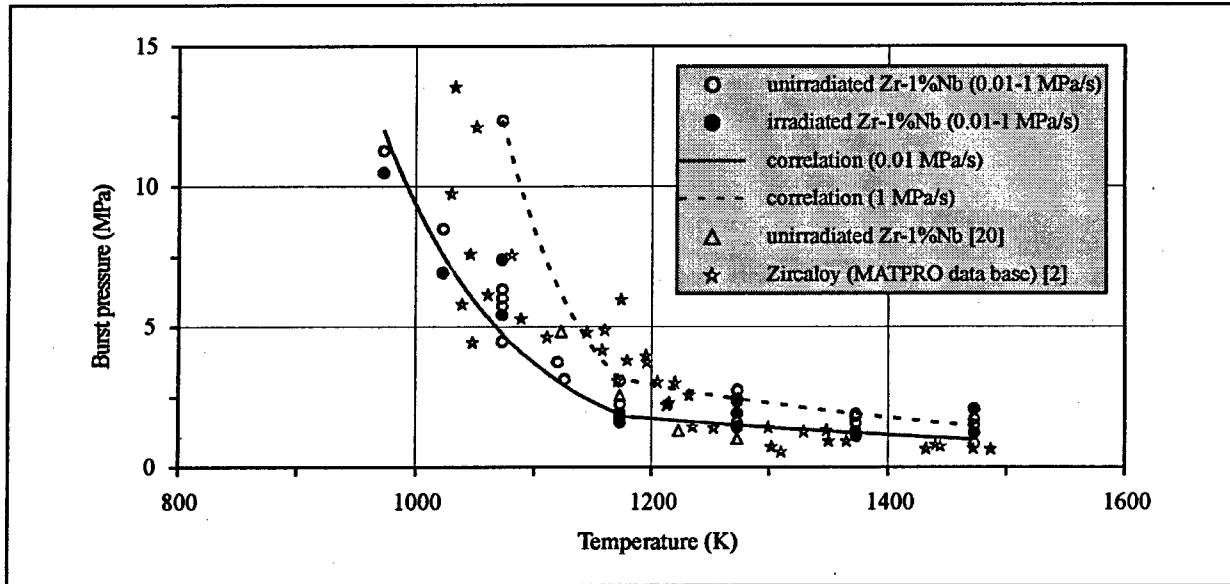
Fig. 6.53. Generalized data base to characterize burst pressure vs. temperature for Zr-1%Nb and Zry claddings

Additional analysis was performed to reveal the trends characterizing circumferential elongation versus temperature and pressure increase rate (see Fig. 6.54). Reduction of circumferential elongation is observed in the area of $\alpha+\beta\rightarrow\beta$ transition in the whole range of pressurization rates. In this case deformation rate does not practically depend on the pressurization rate. Along with the temperature growth in the β-phase, the higher pressurization rate leads to the higher elongation in comparison with the lower rate. Diffusion mechanisms of deformation (high temperature creep) at low loading rates can be most probable reason for this unexpected effect. This leads to the instability of plastic deformation and to the rupture at the circumferential elongation lower than in case of fast loading. In case of the higher pressurization rate there is no time for the diffusion creep to reveal, and strengthening caused by sensitivity to the strain rate becomes the prevailing factor. Hence, plastic instability and rupture take place in case of greater circumferential elongation of the cladding. Still, final explanation of the nature of this effect, which is most clearly revealed in 1273 – 1373 K temperature range, is the subject for the future investigation of the high temperature behavior of the Zr-1%Nb alloy.
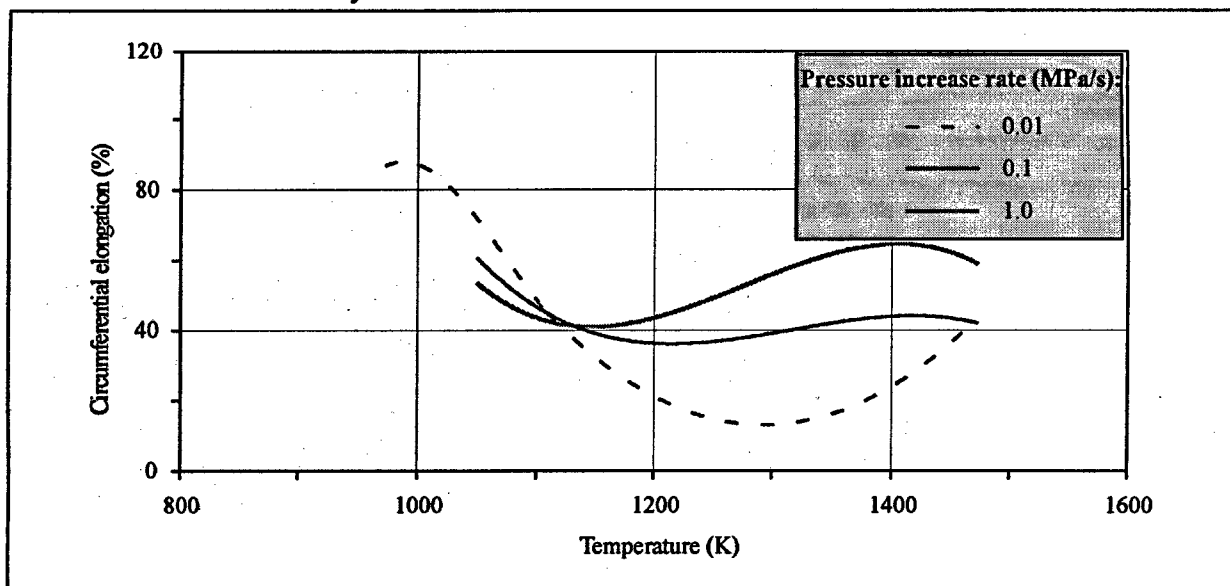

Fig. 6.54. Circumferencial elongation vs. temperature and pressure increase rate for unirradiated Zr-1%Nb cladding

6.57

Analysis of circumferential elongation (hoop strain) at burst, presented in Fig. 6.51 can become more interesting if we complete the results by the data obtained for ring specimens (Fig. 6.55)
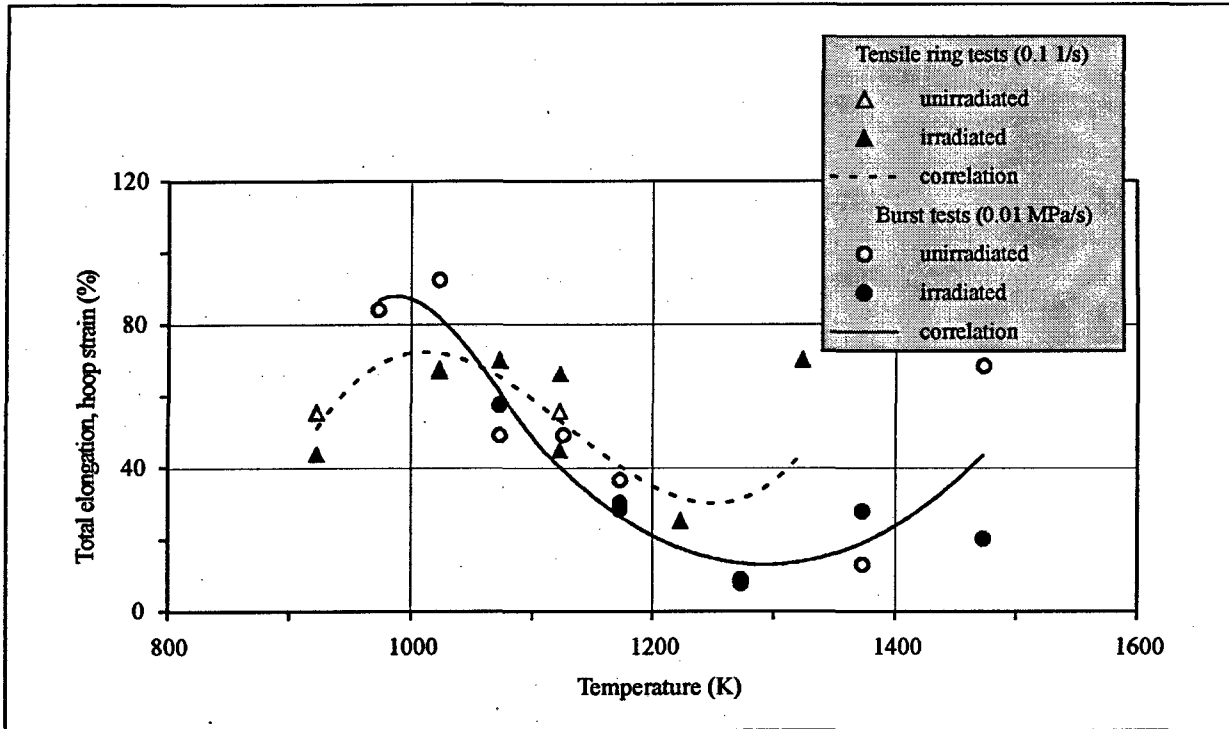
Fig. 6.55. Comparison of the Zr-1%Nb tensile and burst test results

It is obvious that comparison of these two data bases can be done with great caution, because unaxial and biaxial tests are compared.

Moreover, it is impossible to control the strain rate in the cause of burst tests with pressurized cladding specimens. The preliminary assessments indicate that the peaking rate of circumferential elongation in the burst tests with pressurization rate of 0.01 MPa/s is ~0.1 1/s. Circumferential elongation at burst, obtained in these tests and the total elongation of the tensile ring tests with strain rate of 0.1 1/s is presented in Fig. 6.55.

Still even the qualitative comparison allows to make the conclusion that values of the ductility parameters obtained in both types of tests are very close, and their temperature dependencies have similar trends in the high temperature area.

6.4. Development of the data base with mechanical properties of Zr-1%Nb for the MATPRO package and SCANAIR code

6.4.1. Data base for MATPRO package

MATPRO package uses the following basic equation to describe the correlation between the stress and strain depending on the loading conditions and the state of the cladding material:

$$\sigma = K\varepsilon^n \left(\frac{\dot{\varepsilon}}{\dot{\varepsilon}_o}\right)^m,$$

(6)

where $\sigma =$ true effective stress (MPa);

$K =$ strength coefficient (MPa);

$\varepsilon =$ true effective strain (per-unit);

6.58

$n =$ strain hardening exponent (per-unit);

$\dot{\varepsilon} =$ current strain rate (1/s);

$\dot{\varepsilon}_o =$ basic strain rate (1/s);

$m =$ strain rate sensitivity exponent (per-unit).

In their turn loading conditions and the state of the cladding are finally considered as follows:

$$K = f(K_T, \Delta K_f, \Delta K_{cw}, \Delta K_{ox}, \Delta K_A),$$

$$n = f(n_T, \Delta n_f, \Delta n_{cw}, \Delta n_{ox}, \Delta n_A),$$

$$m = f(m_T, \Delta m_{ox}),$$

where $K_T, n_T, m_T =$ strength coefficient, strain hardening exponent, strain rate sensitivity exponent vs. temperature, respectively;

$\Delta K_f, \Delta n_f =$ corrections to take into account the neutron fluence;

$\Delta K_{cw}, \Delta n_{cw} =$ corrections to take into account the cold work of cladding;

$\Delta K_{ox}, \Delta n_{ox}, \Delta m_{ox} =$ corrections to take into account the oxygen content in the cladding;

$\Delta K_A, \Delta n_A =$ corrections to take into account the annealing of fluence and the annealing of cold work.

Analysis of the presented above dependencies for K, n, m indicates that the approach formulated in section 6.1 allows to transform these correlations as follows:

$$K = K_U \quad K = K_I,$$

$$n = n_U \quad n = n_I,$$

$$m = m_{TU} \quad m = m_{TI},$$

where $U=$ index for the given Zr-1%Nb unirradiated tube;

$I=$ index for Zr-1%Nb irradiated cladding of the given commercial fuel element.

That means that formally the obtained data base will be correct only for the given tested tubes and claddings.

On the whole this approach calls for the development of correlations describing dependencies K, n, m versus temperature for both types of claddings. The procedure to describe these correlations starts with m_{TU} and m_{TI}. Taking into consideration according to the MATPRO approach strength coefficient (K) and strain hardening exponent (n) do not depend on the strain rate, strain rate sensitivity exponent (m) for the fixed temperature can be determined by the following expression:

$$m = \frac{\ln \dfrac{S_y(\dot{\varepsilon}_1)}{S_y(\dot{\varepsilon}_o)}}{\ln \dfrac{\dot{\varepsilon}_1}{\dot{\varepsilon}_o}}, \tag{7}$$

where $S_y(\dot{\varepsilon}_1), S_y(\dot{\varepsilon}_o) =$ engineering yield stress for $\dot{\varepsilon}_1$ and $\dot{\varepsilon}_o$ strain rate, respectively;

Expression (7) is obtained by taking the logarithm of the expression (6). In this case the condition of equality of true effective strains (ε) for two strain rates ($\dot{\varepsilon}_1$, $\dot{\varepsilon}_o$) is to be satisfied. That is why for this purpose it is convenient to use the data file characterizing engineering yield stress versus strain rate. Input data for this procedure are presented in Appendix J of Volume 3. Fig. 6.56 presents graphical illustration of the procedure for T = 1123 K.
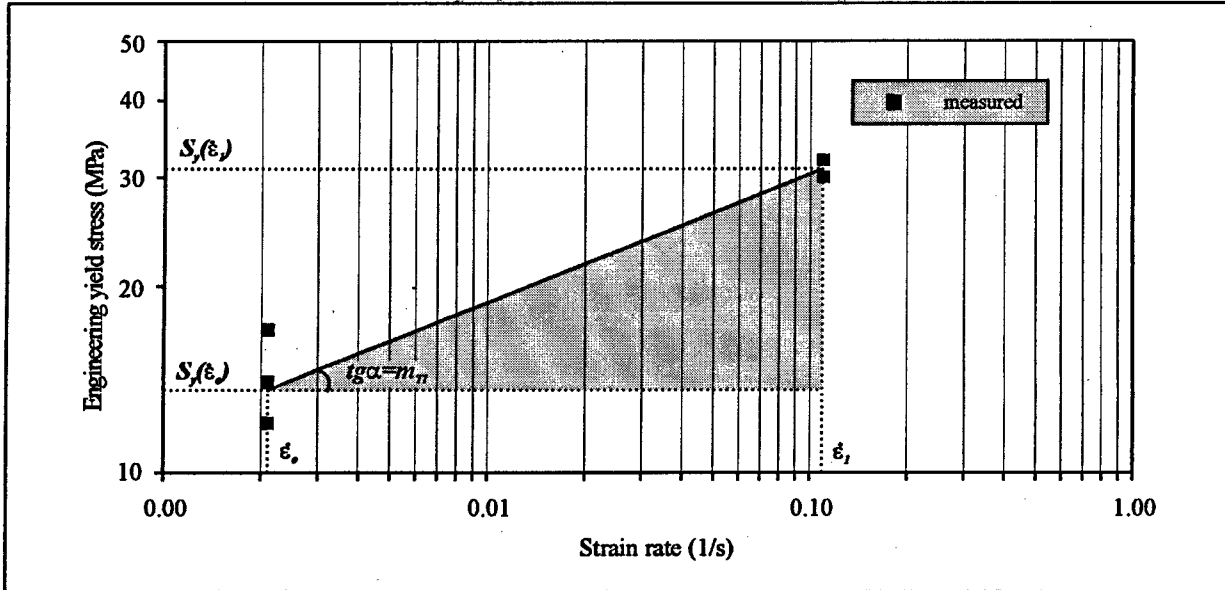
Fig. 6.56. Processing of the measured data to obtain strain rate sensitivity exponent of the irradiated Zr-1%Nb cladding for T = 1123 K

All the measured data were processed according with this procedure, and the values of m_{TU} and m_{TI} were obtained for different temperatures. Still, the analysis of the data base indicated that it was not sufficient. That is why we agreed that it were expedient to try to combine the obtained data base for Zr-1%Nb alloy with the data base used in the MATPRO package for Zircaloy. This combined data base is presented in Fig. 6.57.

It is seen that the MATPRO curve describes test results for Zr-1%Nb alloy well enough. That is why it was proposed not to develop the original curve for the VVER cladding, but to use the standard MATPRO approach to calculate strain rate sensitivity exponents.

The next stage was directed to defining strength coefficients (K_{TU} and K_{TI}) and strain hardening exponents (n_{TU} and n_{TI}) for the VVER cladding. The strict procedure of calculating these parameters requires that the data file characterizing uniform elongation was known. Unfortunately, the research work to study this issue has not been competed yet (sections 6.2, 6.3). That is why the indirect procedure has been developed to get the preliminary data characterizing strength coefficients and strain hardening exponents.
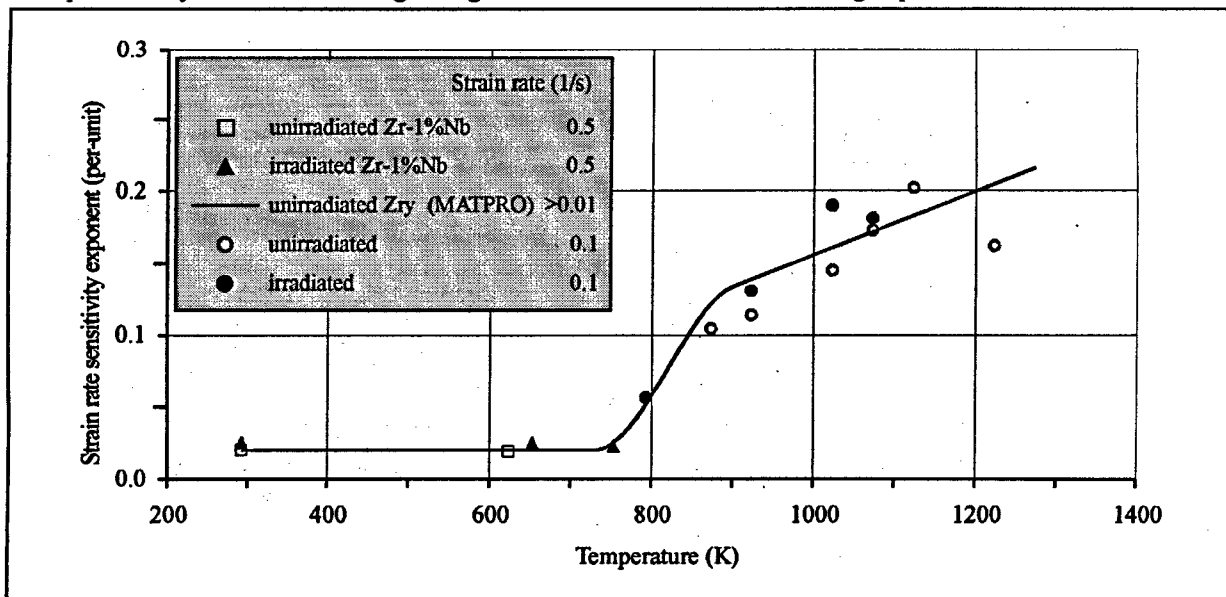

Fig. 6.57. Comparison of the strain rate sensitivity exponents for Zr-1%Nb alloy and Zircaloy

6.60

So, it is known that the following expression is correct for the point of the maximum load located in any of the measured stress-strain curves:

$$\frac{dS}{d\delta} = 0, \qquad (8)$$

where dS = differential of engineering stress;

dδ = differential of engineering strain.

If we put the engineering stress in the form of the power law according to equation (6) into equation (8), we can get the following equation:

$$\frac{d\left(K\varepsilon^{n}\left(\dfrac{\dot{\varepsilon}}{\dot{\varepsilon}_{o}}\right)^{m}\Big/(1+\delta)\right)}{d\delta} = 0.$$

This equation was solved according to the MATPRO procedure and expression for true strain at maximum load was derived:

$$\varepsilon_{ut} = ln(1+\delta_{un}) = \frac{n}{1+m}. \qquad (9)$$

From the power law at the basic strain rate ($\dot{\varepsilon} = \dot{\varepsilon}_{o}$) true ultimate strength can be presented as:

$$\sigma_{ut} = K\left(\frac{n}{1+m}\right)^{n}. \qquad (10)$$

It is evident that after that it is necessary to transfer from the true stress to the engineering stress by the following transformations:

$$\sigma_{ut} = S(1+\delta_{un}) = S_{ut}\exp(\varepsilon_{ut}) = S_{ut}\exp(\frac{n}{1+m}). \qquad (11)$$

It is evident that equations (10) and (11) allow to transfer to the following equation:

$$S_{ut}\exp(\frac{n}{1+m}) = K(\frac{n}{1+m})^{n}. \qquad (12)$$

Equations (9) and (12) were solved with respect to K and n for every temperature with the help of:

• measured S_{ut} and S_{y} presented in Appendix J;

• m defined according to the MATPRO correlation.

All of these calculations were performed for the basic strain rate ($\dot{\varepsilon} = 10^{-3}$ 1/s). The obtained data files for K_{TU}, K_{TI} and n_{TU}, n_{TI} were statistically processed in accordance with the procedure described in section 6.2.2, and the correlation dependencies were calculated for each parameter. Results of these calculations are presented in Fig. 6.58, Fig. 6.59, and in Table 6.12.

The focus of the next stage of research was to develop the data base necessary to calculate specific ballooning parameters. Formulation of the problem for this task required to determine the parameters necessary to be provided for the MATPRO package for BALON2 subcode installed into FRAP-T6 code [23].

6.61
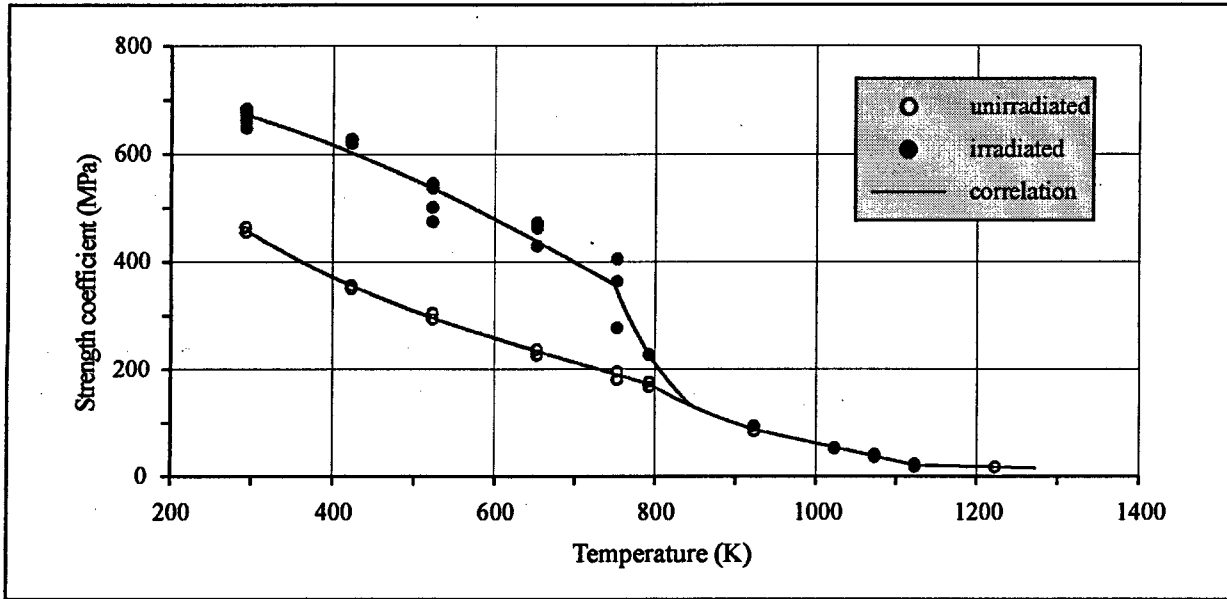
Fig. 6.58. Strength coefficient vs. temperature for unirradiated and irradiated Zr-1%Nb cladding

This subcode along with the traditional set of mechanical properties (K, n, m) uses such parameter as local burst stress. This is the parameter used as the cladding failure criterion. Equilibrium equation for a membrane element at failure lies in the foundation of the MATPRO approach to calculate local burst stress. This equation is used as follows:

$$\frac{\sigma_{ZB}}{r_Z} + \frac{\sigma_{\theta B}}{r_\theta} = \frac{P_B}{t_B},$$

where $\sigma_{ZB}, \sigma_{\theta B}$ = axial and tangential stress at the cladding burst, respectively;

r_Z, r_θ = axial and circumferential radius of curvature at burst, respectively;

P_B = pressure drop at burst;

t_B = cladding thickness at burst.
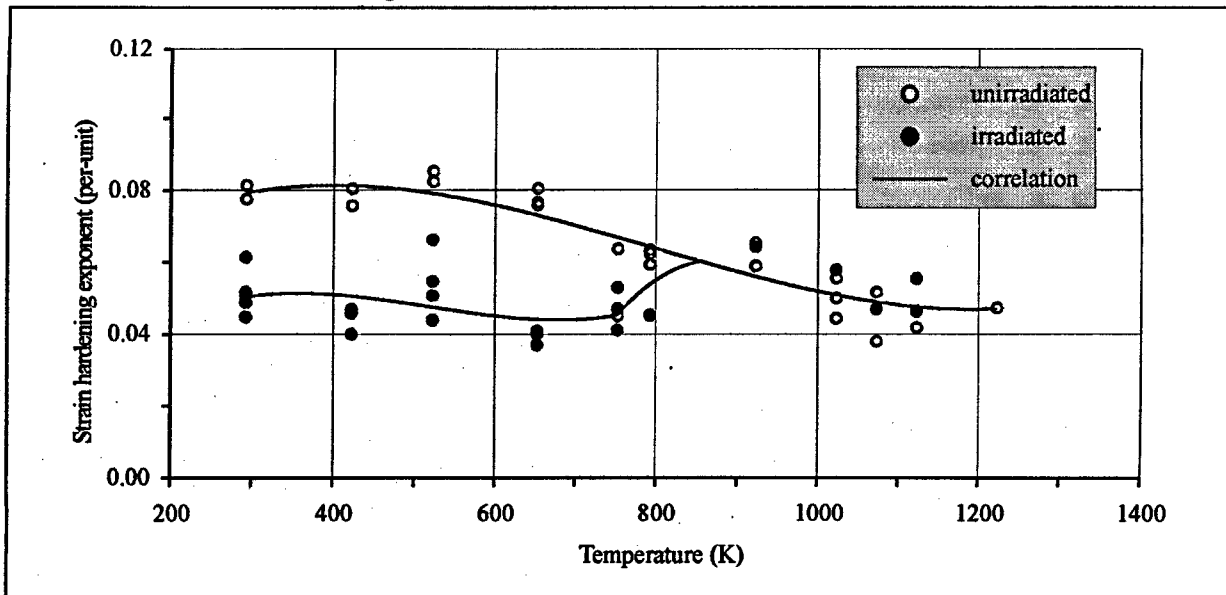
Fig. 6.59. Strain hardening exponent vs. temperature for unirradiated and irradiated Zr-1%Nb cladding

6.62

To solve this equation MATPRO approach calls for two assumptions:

- cladding shape in the cross-section is circular until the burst occurs;
- axial and tangential stresses are approximately equal at the moment of burst.

The respective procedures are presented in the MATPRO package to justify acceptability of these assumptions for each case. With consideration of the accepted assumptions equilibrium equation is transformed as follows:

$$\sigma_B = \frac{P_B}{t_B}\left(\frac{1}{1/r_z + 1/r_\theta}\right),$$

where σ_B = local burst stress.

Table 6.12. Correlations to calculate strength coefficient and strain hardening exponent vs. temperature for Zr-1%Nb cladding

Parameter	Type of cladding	
	unirradiated	irradiated
Strength coefficient (MPa)	293<T≤795.18 K	293<T≤749.45 K
	K=863.33 - 1.90882 T+0.00209374 T^2 - 9.91178 10^{-7} T^3	K=738.221+0.0395682 T-0.00100875 T^2 + 0.370178 $10^{-6}T^3$
		749.45 <T≤846.44 K
		K=8.34707 10^5 exp(-0.01035 T)
	795.18 <T≤926.62 K	846.44 <T≤926.62 K
	K = 1.08414 10^4exp(-0.00521825 T)	
	926.62 <T≤1123.54 K	
	K = 396.363 - 0.334806 T	
	T>1123.54 K	
	K = 56.6424 - 0.0324407 T	
Strain hardening exponent (per-unit)		293 <T≤752.37 K
		n = 0.0054616 + 3.12237 10^{-4} T - 0.668358 10^{-6} T^2 + 0.430236 10^{-9} T^3
		752.37 <T≤854.72K
		n = -1.58974 + 0.00500594 T - 4.99134 10^{-6} T^2 + 1.62978 10^{-9} T^3
	293 <T≤ 1223 K	854.72<T≤1223K
	n =0.0462842 + 0.000197952 T - 0.331487 10^{-6} T^2 +1.39133 10^{-10} T^3	
	T>1223 K	
	n = 0.047	

It is evident that all the parameters presented in this equation depend on temperature and state of the cladding. The data base characterizing P_B, t_B, r_Z, r_θ values under different temperatures for unirradiated and irradiated claddings is to be obtained in order to determine local burst stress versus temperature ($\sigma_B(T)$). The

measured values of P_B, t_B, r_Z, r_θ for different temperatures, described in section 6.3, were used to calculate the set of $\sigma_B(T_i) = f\left[P_B(T_i), t_B(T_i), r_Z(T_i), r_\theta(T_i)\right]$. The respective input data and obtained values of $\sigma_B(T_i)$ are presented in Table 6.13.

Table 6.13. Measured data base for local burst stress in Zr-1%Nb cladding

Types of cladding	Temperature (K)	Parameter				
		P_B (MPa)	t_B (mm)	r_z (mm)	r_θ (mm)	σ_B (MPa)
Unirradiated	973	11.27	0.38	49.6	7.77	199.1
	1023	8.49	0.36	59.3	8.12	166.6
	1073	5.75	0.27	149	6.30	128.8
	1126	3.13	0.18	141	6.30	104.9
	1173	1.6	0.23	70	5.77	37.1
	1273	1.42	0.26	62	4.55	23.1
	1373	1.19	0.30	10.6	4.77	13.1
	1473	0.84	0.25	51	7.11	21.0
Irradiated	1073	5.34	0.21	5.9	5.72	73.9
	1073	5.43	0.21	150	6.66	164.9
	1173	1.95	0.27	10.4	5.43	25.8
	1173	1.76	0.28	7.3	5.50	19.7
	1273	1.93	0.20	21.8	4.60	36.7
	1273	1.46	0.25	45	4.57	24.3
	1373	1.11	0.27	272	5.41	21.8
	1473	1.24	0.25	28.4	5.09	21.3

The standard statistic processing of the local burst stress files was used to get correlation dependencies describing $\sigma_B(T)$ for unirradiated and irradiated claddings. The correlations obtained this way are presented in Table 6.14 and Fig. 6.60.

Table 6.14. Correlations for local burst stress of Zr-1%Nb cladding

| Range of temperature (K)	Local burst stress (MPa) vs. temperature
973<T≤1176.44	$\sigma_B = 2.99522 \cdot 10^6 \exp(-0.00952232\,T)$
1176.44<T≤1473	$\sigma_B = 1.41537 \cdot 10^3 \exp(-0.00301426\,T)$
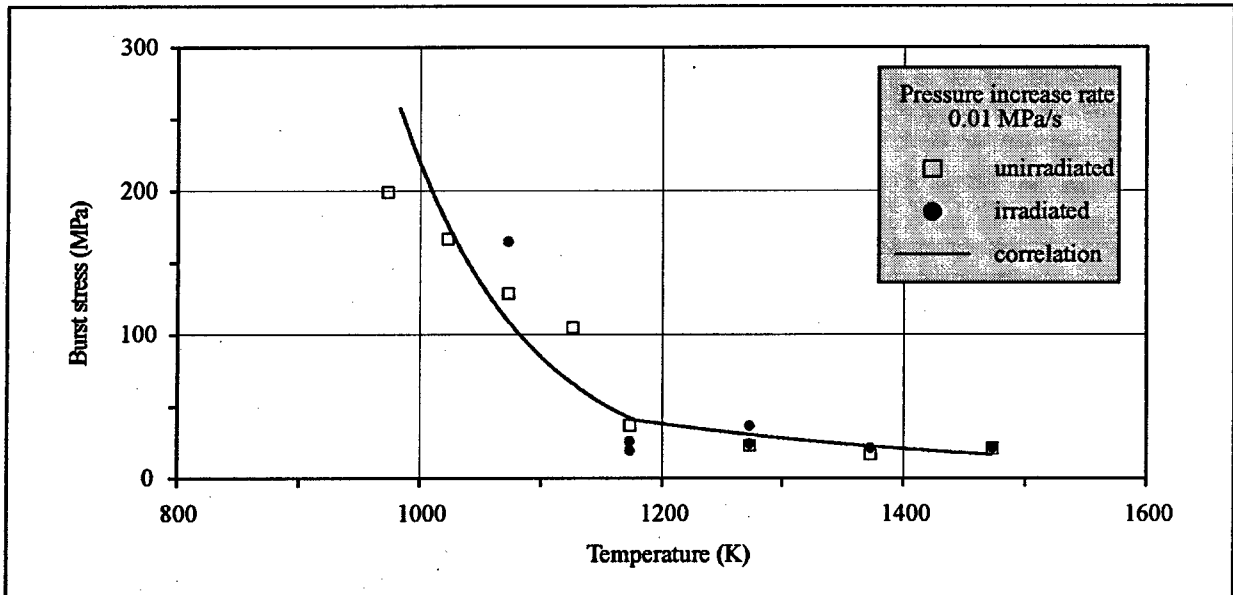
Fig. 6.60. Measured local burst stresses and new MATPRO correlation for Zr-1%Nb cladding

6.4.2. Data base for the SCANAIR code

It has been noted in section 5.6 that the current version of the SCANAIR code operates with three mechanical properties: Young's modulus, Poisson's ratio, yield stress. No original measurements of Young's modulus and Poisson's ratio were performed in the frames of this work. That is why the recommended correlations to calculate these properties for Zr-1%Nb alloy are presented in section 5.6. So of the whole measured set of mechanical properties only the correlations describing engineering yield stress versus temperature for unirradiated and irradiated Zr-1%Nb cladding are necessary for the SCANAIR code. The respective correlations obtained in section 6.2 for the basic strain rate ($\dot{\epsilon} = 10^{-3}$ 1/s) are presented in Table 6.15.

Table 6.15. Correlations to calculate engineering yield stress vs. temperature for Zr-1%Nb cladding

Type of cladding	Range of temperature (K)	Yield stress vs. temperature (MPa)
Unirradiated	$293 < T \le 786.91$	$S_y = 502.9982 - 0.8738195\ T + 6.124696\ 10^{-4}\ T^2 - 1.418248\ 10^{-7}\ T^3$
	$786.91 < T \le 892.32$	$S_y = 10094.5\ \exp(-0.0055752\ T)$
	$892.32 < T \le 1125.38$	$S_y = 285.624 - 0.241928\ T$
	$1125.38 < T \le 1273$	$S_y = 44.4448 - 0.027619\ T$
Irradiated	$293 < T \le 739.97$	$S_y = 690.3984 - 1.015694\ T + 0.00131 0936\ T^2 - 9.702603\ 10^{-7}\ T^3$
	$739.97 < T \le 846.56$	$S_y = 4.55945\ 10^5\ \exp(-0.0100762\ T)$
	$846.56 < T \le 892.32$	$S_y = 10094.5\ \exp(-0.0055752\ T)$
	$892.32 < T \le 1125.38$	$S_y = 285.624 - 0.241928\ T$
	$1125.38 < T \le 1273$	$S_y = 44.4448 - 0.027619\ T$

Altogether, the analysis demonstrates that the current version of the code allows to introduce the additional correction to consider the dependence of yield stress versus strain rate with the help of the following expression:

6.65

$$S_{ym} = S_{yo}\left(\frac{\dot{\varepsilon}}{\dot{\varepsilon}_o}\right)^m ,$$

where S_{ym} = engineering yield stress vs. strain rate;

S_{yo} = engineering yield stress at basic strain rate ($\dot{\varepsilon}_o = 10^{-3}$ 1/s);

$\dot{\varepsilon}$ = current strain rate;

$\dot{\varepsilon}_o$ = basic strain rate;

m = strain rate sensitivity exponent.

The following equation was used to practically determine strain rate sensitivity exponent:

$$m = \frac{\ln\dfrac{S_y(\dot{\varepsilon}_1)}{S_y(\dot{\varepsilon}_o)}}{\ln\dfrac{\dot{\varepsilon}_1}{\dot{\varepsilon}_o}} ,$$

where $S_y(\dot{\varepsilon}_1), S_y(\dot{\varepsilon}_o)$ = engineering yield stress for $\dot{\varepsilon}_1$ and $\dot{\varepsilon}_o$ strain rate, respectively;

$\dot{\varepsilon}_1, \dot{\varepsilon}_o$ = current and basic strain rate, respectively.

Thus, the obtained expression for the strain rate sensitivity exponent corresponds to the approach to determine this parameter, presented in section 6.4.1 for the MATPRO package. The respective analytical correlations to calculate S_{ym} of unirradiated and irradiated Zr-1%Nb claddings were obtained and put into ZYS module of the SCANAIR FORTRAN source.

6.5. References

[1] A.S.Zaimovskyi, A.V.Nikulina, N.G.Reshetnikov, "Zirconium Alloys in the Nuclear Industry". Moscow, Energoizdat, 1981 (rus).

[2] D.L.Hagrman, G.A.Reyman and R.E.Mason, "MATPRO-V.11 Revision 1: A Hand Book of Materials Properties for Use in the Analysis of Light Water Reactor Fuel Rod Behavior". NUREG/CR-0497 TREE-1280, Rev2, 1981.

[3] G.P.Kobyliansky, A.Ye.Novoselov, "Radiation Tolerance of Zirconium and Zirconium-Based Alloys". Edited by V.A.Tsycanov. GNC RF NIIAR, Dimitrovgrad, 1996 (rus).

[4] L.F.Van Swam, A.A. Strasser, J.D.Cook, J.M.Burger, "Behavior of Zircaloy-4 and Zirconium Liner Zircaloy-4 Cladding at High Burnup". *Proc. of Int. Topical Meeting on Light Water Reactor Fuel Performance*, Portland, 1997, p.421-431.

[5] I.I.Korobkov, "Investigations of Dynamic Strain Aging of Zirconium Alloys". In: "Zirconium and Its Alloys".Edited by V.S. Emelyanov and A.I. Efstiukhin. Moscow, Energoizdat, 1982 (rus).

[6] L.P.Loshmanov, V.D.Rudnev and O.A.Nechaeva, "Influence of Temperature and Strain Rate on Mechanical Properties of Zr-1%Nb Alloy". Atomnaya energia 2 (81) 1996 (rus).

[7] Sun Ig Hong, Woo Seog Pyn and Chang Saeng Kim, "Thermally Activated Deformation of Zircaloy-4". Journal of Nuclear Materials, 120 (1984) 1-5.

[8] D. Douglas, "Metallurgy of Zirconium". Moscow, Atomizdat, 1975 (rus).

[9] M.L. Bernshtein and V.A. Zaimovskyi, "Mechanical Properties of Metals". Moscow, Metallurgia, 1979 (rus).

[10] K.P. Dubrovin, A.V. Sukhikh and V.I. Kusmin, "First Qualitative Analysis of Fuel Irradiation Results Carried out in the MR Reactor on VVER-1000 Fuel". *Proc. Of Int. Seminar on VVER Reactors: Fuel Performance, Modeling and Experimental Support*. Varna, Bulgaria, 1994.

[11] Yu. Bibilashvily, K. Dubrovin and I. Vasilchenko, "Main Examination Results of VVER-1000 Fuel After Its Irradiation in Power Reactors". *Proc. Of Int. Seminar on VVER Reactors: Fuel Performance, Modeling and Experimental Support*. Varna, Bulgaria, 1994.

[12] C.E.L. Hunt and E.M. Schulson, "Recrystallization of Zircaloy-4 During Transient Heating". Journal of Nuclear Materials 92 (1980) 184-190.

[13] V. Tonkov, A. Kapteltsev, I. Golikov, Yu. Dolgov and A.B. Perepelkin, "Influence of Oxidation in Water Steam on Mechanical Properties of Zr-1%Nb Alloy at 20 -1000 C". Voprosy atomnoy nauki i tekhniki. Ser: Materialovedenie i novye materialy. 4 (38) 1990 (rus).

[14] T. Fuketa, K. Ishijima, Yu. Mori, H. Sasajima and T. Fujishiro, "New Results from the NSRR Experiments with High Burnup Fuel". *Proc. Of Twenty Third Water Reactor Safety Meeting*, 1995. NUREG/CP-0149 Vol.1.

[15] F. Schmitz, J. Papin, M. Haessler and N. Waeckel, "New Results from Pulse Tests in the CABRI Reactor". *Proc. Of Twenty Third Water Reactor Safety Meeting*, 1995. NUREG/CP-0149 Vol.1.

[16] A. Smirnov, K. Dubrovin, V.I. Kusmin, "VVER-1000 and VVER-440 Fuel Operation Experience". *Proc. Of Int. Topical Meeting on Light Water Reactor Fuel Performance*. Florida,USA 1994.

[17] V. Prokhorov, A. Finko and R. Mineev, "Evaluation of Gauge Length of the Ring Specimens from Fuel Claddings for Tensile Tests in Transverse Direction". Report NIIAR P-23317. Dimitrovgrad, 1977 (rus).

[18] A. B. Cohen, S. Majumdar, W.E. Ruther, M.C. Billone, H.M. Chung, and L.A. Neimark "Modified Ring Stretch Tensile Testing of Zr-1%Nb Cladding" *Proceeding of the Twenty - Fifth Water Reactor Safety Information Meeting*, Bethesda, Maryland, October 20-22 1997. NUREG/CP-0162

[19] N.R. Draper and H. Smith, "Applied Regression Analysis". John Wiley and Sons. New York,1981.

[20] V.Solyany, Yu. Bibilashvily, V. Tonkov, "High temperature oxidation and deformation of Zr-1%Nb alloy claddings of VVER fuels", *IWGFRT-16 IAEA Specialist Meeting on Water Reactor Fuel Safety and Fission Product Release in off-Normal and Accident Conditions*, Denmark,1983.

[21] D.L. Hagrman, "Zircaloy Cladding Shape at Failure (BALON2)". EGG-CDAP-5379, 1981.

[22] V.David CEA/DRN/DMT-Saclay "Hoop Tensile Tests on Unirradiated VVER Cladding (Zr-1%Nb)". Work performed under IPSN contract.

[23] V.Asmolov, L.Yegorova, E.Kaplar, K.Lioutov (NSC RRC KI), V.Smirnov, V.Prokhorov, A.Goryachev (RIAR) "Development of Data Base with Mechanical Properties of Un– and Preirradiated VVER Cladding", *Proceedings of the Twenty – Fifth Water Reactor Safety Information Meeting*, Bethesda, Maryland, October 20-22, 1997. NUREG/CP-0162

U.S. NUCLEAR REGULATORY COMMISSION

BIBLIOGRAPHIC DATA SHEET

(See instructions on the reverse)

1. REPORT NUMBER
(Assigned by NRC, Add Vol., Supp., Rev., and Addendum Numbers, if any.)

NUREG/IA-0156
Volume 2

2. TITLE AND SUBTITLE

Data Base on the Behavior of High Burnup Fuel Rods with Zr-1%Nb Cladding and UO2 Fuel (VVER Type) under Reactivity Accident Conditions

Volume 2   Description of Test Procedures and Analytical Methods

3. DATE REPORT PUBLISHED

MONTH	YEAR
July	1999

4. FIN OR GRANT NUMBER

W6500

5. AUTHOR(S)

L. Yegorova, V. Asmolov, G. Abyshov, et. al.
A. Bortash, L. Maiorov, et. al.
V. Smirnov, A. Goryachev, V. Prokhorov
V. Pakhnitz, A. Vurim

6. TYPE OF REPORT

IPSN 99/08-2   NSI RRC KI-2179

7. PERIOD COVERED *(Inclusive Dates)*

manuscript completed Dec 1998

8. PERFORMING ORGANIZATION - NAME AND ADDRESS *(If NRC, provide Division, Office or Region, U.S. Nuclear Regulatory Commission, and mailing address; if contractor, provide name and mailing address.)*

Russian Research Center "Kurchatov Institute" Moscow 123182 Russia

State Research Centre "Research Institute of Atomic Reactors" Dimitrovgrad Russia

Institute of Atomic Energy of NNC Semipalatinsk Kazakhstan

9. SPONSORING ORGANIZATION - NAME AND ADDRESS *(If NRC, type "Same as above"; if contractor, provide NRC Division, Office or Region, U.S. Nuclear Regulatory Commission, and mailing address.)*

Division of Systems Analysis and Regulatory Effectiveness
Office of Nuclear Regulatory Research
U.S. Nuclear Regulatory Commission
Washington, DC 20555-0001

10. SUPPLEMENTARY NOTES

11. ABSTRACT *(200 words or less)*

This volume of the report contains the following information on test conditions and basic procedures used to develop the data base:
· objects and conditions of the IGR reactor tests;
· test parameters of fuel rods before, during and after the RIA tests;
· parameters of fuel rods during RIA tests calculated by FRAP-T6 and SCANAIR computer codes;
· measured mechanical properties of Zr-1%Nb cladding obtained due to special tests;
· parameters of Zr-1%Nb cladding failure of the ballooning type measured under the burst test conditions;
· input data with original material properties of Zr-1%Nb cladding for the MATPRO package and SCANAIR code.

12. KEY WORDS/DESCRIPTORS *(List words or phrases that will assist researchers in locating the report.)*

reactivity initiated accident
impulse graphite reactor (Kazakhstan Atomic Energy Agency)
Zirconium-1% Niobium alloy
FRAP-T6 & SCANAIR computer codes
material properties
cladding strain and ballooning
energy deposition
post-test examinations

13. AVAILABILITY STATEMENT

unlimited

14. SECURITY CLASSIFICATION

(This Page)

unclassified

(This Report)

unclassified

15. NUMBER OF PAGES

16. PRICE

Printed
on recycled
paper

Federal Recycling Program